A Study of Muon Neutrino Oscillation with Low Energy Spectrum in a Long Baseline Experiment

Yosuke Takubo
Department of Physics, Osaka University

February, 2006

Abstract

The KEK-to-Kamioka (K2K) experiment is a long baseline neutrino oscillation experiment by using an accelerator, which was performed to confirm muon neutrino oscillation observed by the study of atmospheric neutrinos in Super-Kamiokande. In the K2K experiment, a number of the neutrino events and the energy spectrum were measured by the near detectors at KEK site and Super-Kamiokande. As an effect of neutrino oscillation, the decrease of neutrinos events and the distortion of the energy spectrum are observed at SK, comparing to the expectation by measurement of the near detectors. In particular, distortion of the energy spectrum is expected to become larger in low energy region below 1 GeV. Therefore, precise spectrum measurement in low energy region at the KEK site, is necessary for the confirmation of neutrino oscillation. For this purpose, a full active scintillator bar (SciBar) detector was constructed and installed in 2003, summer. The data of 2.04×10^{19} protons on target (POT) were taken by the SciBar detector, while a total of 9.2×10^{19} POT had been taken for the K2K experiment from June 1999 to November 2004. In this thesis, the energy spectrum, especially in low energy region, is studied by using SciBar. The spectrum measurement in the low energy region by SciBar is improved with the low energy samples. After consistency check of the spectrum measurement by SciBar and the other near detectors, the neutrino energy spectrum at the KEK site was measured by using the all near detectors. By using the neutrino spectrum measured by the near detectors, the effect of neutrino oscillation at Super-Kamiokande was studied. In a two-flavor neutrino oscillation case, the best fit value of the oscillation parameter was obtained as $(\Delta m^2, \sin^2 2\theta) = (2.8 \times 10^{-3}[\mathrm{eV}^2], 1.0)$. This result is consistent with the 90% C.L. allowed parameter region obtained at Super-Kamiokande, $(1.5 \times 10^{-3} < \Delta m^2 < 3.4 \times 10^{-3}$ [eV^2], $\sin^2 2\theta > 0.92)$.

Acknowledgments

I would like to express my great appreciation to my supervisor Prof. Yoshitaka Kuno. He introduced and encouraged me to study high energy physics.

I also would like to express gratitude to Prof. Koichiro Nishikawa for accepting my participation to the K2K experiment. I am very thankful to Prof. T. Nakaya and Dr. M. Yokoyama, who invited me to the SciBar group and gave helpful and sevior suggestions for my study.

I would like to thank Dr. M. Yoshida, who gave a lot of helpful advice and supported me to write this thesis.

I thank you for all people in SciBar detector group. The SciBar detector has been realized with a lot of efforts by Dr. H. Maesaka as a leader. I thank Dr. M. Hasegawa and Dr. S. Yamamoto, who worked to construct the SciBar detector and spent a lot of time to discuss about our analysis together. Dr. A. Ichikawa, Dr. K. Nitta, Mr. T. Sasaki, Mr. T. Morita devoted considerable efforts to the construction. K. Hiraide operated SciBar detector and helped the beam test (T551). Dr. H. Tanaka made effort to analyze SciBar data. Prof. S. B. Kim, Dr. K. K. Joo, Dr. E. Jeon, and Ms. M. J. Lee manufactured and tested the electronics. Dr. Y. Hayato cooperated closely with us in preparing the online data handling program and in doing the neutrino interaction simulation. Prof. L. Ludovici, Prof. P. Loverre, Prof. U. Dore, and Mr. C. Mariani brought the electro-magnetic calorimeter from CERN. Dr. F. Sanchez developed the track finding algorithm. Dr. K. Kobayashi created the slow monitor system. Prof. S. Aoki, Dr. A. Suzuki, Dr. M. Iinuma, Mr. S. Nawang, Mr. K. Hayashi, Mr. S. Ueda, Mr. J. Kubota, Mr. D. Kerr, Mr. Eric J., Mr. P. Rovegno, Ms. M. Tuchscher, Mr. K. Shiraishi, Prof. I. T. Lim, Dr. S. S. Choi, Prof. M. Khabibullin, and Mr. M. Oleg kindly helped us to install the SciBar detector. Prof. T. Takahashi dispatched students to KEK, and they assisted us voluntarily in the construction. Analysis contributions have been provided by Ms. L. Whitehead, Mr. F. Nova, G. Jover, Ms. E. Aliu, Mr. X. Espinal, Ms. A. Rodriguez, Ms. S. Andringa, Ms. A. M. Tornero-Lopez, and Mr. G. V. Sitjes. I would like to thank people in the electronics group at KEK. Especially, I was supported by Prof. M. Tanaka, Mr. S. Shimazaki and Mr. T. Murakami to develop the trigger board and the timing distributor. I am also helped by Dr. Y. Ushirada in the Belle experiment at KEK to check the electronics. Mr. M. Taino and Mr. N. Tanaka in KEK, Mr. H. Sukegawa and Mr. M. Odakura from Kikka Setsubi Engineering Company, and all the people of Wachi Kensetsu Company, Hokuto Company, Futaba Kogyo Company, Suzuno Giken Company, CI Kogyo Company, and REPIC Corporation exerted energetic efforts to construct the structure and the hardware of the SciBar detector.

In addition, my study is supported by all the K2K collaborators. Prof. Y. Totsuka, Prof. K. Nakamura, Prof. Y. Suzuki, Prof. C.K. Jung, and J. Wilkes have administrated the K2K experiment with the best efforts. The beamline monitors have been supported by Dr. T. Hasegawa, Dr. T. Maruyama, H. Sato, and the other beamline group members. The 1KT detector has been maintained and analyzed by the 1KT group, especially by Prof. Y. Itow, Prof. M. Shiozawa, Dr. M. Miura, Dr. J. Kameda, Dr. I. Kato, and R. Terri. The SciFi detector has been supported and studied by Prof. M. Sakuda, Dr. T.

Ishida, Dr. R. Gran, Dr. T. Iwashita, and Dr. H. Yokoyama, Mr. A. Ikeda, Ms. M. Sekiguchi and the other SciFi group people. Prof. T. Kobayashi have controlled the LG detector. The Super-Kamiokande data have been provided by Prof. K. Kaneyuki, Dr. Y. Obayashi, and Dr. S. Yamada.

I also gratefully acknowledge all the people of the KEK 12GeV PS group, the beam channel group, the Super-Kamiokande collaboration, and Kamioka Mining and Smelting Company, for the generous cooperation to carry out the K2K experiment.

I would like to thank all the members in the high energy physics group of Kyoto university. They accepted me to study in their office for two years. Especially, I enjoyed a lot of time with people in the neutrino group, Mr. K. Ezawa, Mr. Y. Kurimoto, Mr. Y. Kurosawa, Mr. T. Nobuhara, Mr. M. Taniguchi, and Mr. K. Matsuoka. The other members are also kind to me, Dr. T. Nomura, Dr. H. Nanjo, Mr. T. Sumida, Mr. H. Morii, Ms. N. Taniguchi, Mr. Y. Nakajima and Mr. T. Shirai.

I am sincerely grateful to all the member in Kuno group of Osaka university. I wish to express my gratitude to Prof. M. Aoki, Dr. A. Sato, Dr. Y. Arimoto, Prof. T. Itahashi, Dr. T. Ohki, who gave me a lot of usefull suggestions. I thank all the students, Mr. S. Takano, Mr. N. Nosaka, Mr. M. Harada, Mr. Y. Arakawa, Mr. Y. Kuriyama, Mr. F. Maeda, Mr. K. Nakahara, Mr. J. Ishii, Mr. H. Sakamoto, Mr. S. Nakaoka, Mr. A. Horikoshi, Mr. K. Yamada, Mr. T. Takayanagi, Mr. S. Araki, Mr. N. Miyamoto and Mr. A. Muroi. I was also supported by Ms. M. Torikoshi. All of them helped me not only my study but also my graduate school life.

Finally, I would like to express the special appreciation to my parents. I could complete my graduate course with their continuous support.

Contents

Chapter 1

Introduction

1.1 Neutrinos in the standard model

In the standard model of particle physics, left-handed components of the charged lepton (ℓ_L) and neutrino ($\nu_{\ell L}$) fields are defined as an isospin doublets of the group $SU(2)_L$,

$$\phi_{\ell L} = \begin{bmatrix} \nu_{\ell L} \\ \ell_L \end{bmatrix}, \qquad \ell = e, \mu, \tau, \tag{1.1}$$

while the right-handed components of the charged lepton fields (ℓ_R) are singlets. The right-handed components of the neutrino fields ($\nu_{\ell R}$) have no SU(2) interaction due to their singlet nature, and no U(1) interaction due to zero value of weak hypercharge, $Q = I_3 + Y$, where Q, I and Y shows charge, the 3rd component of isospin and weak hypercharge, respectively. In addition, the Yukawa coupling of $\nu_{\ell R}$ with Higgs is very weak due to the small mass of $\nu_{\ell L}$s. From these reasons, a $\nu_{\ell R}$ behaves as a sterile neutrino. Since the effect of the neutrino mass is very small, it is treated as zero in the standard model. However, the recent experimental results of the neutrino oscillation indicates the existence of the neutrino mass. Since only the neutrino oscillation experiment is sensitive to the neutrino mass and its mixing angles for the present, it would give important information to the elementary particle physics. The physics characteristics of the neutrino oscillation is described in the next section.

1.2 Neutrino oscillation

1.2.1 Neutrino oscillation in vacuum

If the neutrinos have masses, the weak eigenstates produced in weak interaction (ν_α) are expressed in general as linear combinations of the mass eigenstates (ν_i),

$$|\nu_\alpha\rangle = \sum_{i=1}^{n} U^*_{\alpha i} |\nu_i\rangle, \tag{1.2}$$

where n is a number of light neutrino species and U is the mixing matrix. Information on the neutrino mixing is obtained by the study of neutrino oscillation [1]; a quantum mechanical interference effect resulting from the mixing. The neutrino oscillation is described in this section.

After traveling a distance L which is equivalently time (t) for relativistic neutrinos, the neutrino originally produced with flavor of α evolves as follows.

$$|\nu_\alpha(t)\rangle = \sum_{i=1}^{n} U^*_{\alpha i}|\nu_i(t)\rangle. \tag{1.3}$$

The component of flavor β can be detected in the charged-current interaction $\nu_\beta(t)N' \to \ell_\beta N$ with probability of

$$P_{\alpha\beta} = |\langle\nu_\beta|\nu_\alpha(t)\rangle|^2 = \left|\sum_{i=1}^{n}\sum_{j=1}^{n} U^*_{\alpha i}U_{\beta j}\langle\nu_j(0)|\nu_i(t)\rangle\right|^2. \tag{1.4}$$

In vacuum, propagation of the mass eigenstates can be written as plane waves with relativistic formula,

$$|\nu_i(t)\rangle = \exp^{-iE_i t}|\nu_i(0)\rangle = \exp^{-i\sqrt{p_i^2+m_i^2}t}|\nu_i(0)\rangle \simeq \exp^{-i(p_i+\frac{m_i^2}{2E_i})t}|\nu_i(0)\rangle, \tag{1.5}$$

where E_i and m_i are the energy and the mass of the neutrino mass eigenstate of ν_i, respectively.

Then we obtain the following transition probability

$$P_{\alpha\beta} = \delta_{\alpha\beta} - 4\sum_{i=1}^{n-1}\sum_{j=i+1}^{n} Re[U_{\alpha i}U^*_{\beta i}U^*_{\alpha j}U_{\beta j}]\sin^2 x_{ij}, \tag{1.6}$$

where $x_{ij} \equiv \Delta m^2_{ij}L/(4E)$ with $\Delta m^2_{ij} \equiv m_i^2 - m_j^2$. L is the distance between the source (that is, the production point of ν_α) and the detector (that is, the detection point of ν_β). x_{ij} is written as

$$x_{ij} = 1.27\frac{\Delta m^2_{ij}}{\mathrm{GeV}^2}\frac{L/E}{\mathrm{km/MeV}}. \tag{1.7}$$

The transition probability in Eq. 1.6 has an oscillatory behavior, with oscillation length of $\frac{4\pi E}{\Delta m^2_{ij}}$, and the amplitude that is proportional to the elements in the mixing matrix. Thus, in order to have oscillations, the neutrinos must have different masses ($\Delta m^2_{ij} \neq 0$) and they must mix ($U_{\alpha i}, U_{\beta i} \neq 0$).

1.2.2 2 flavor mixing

The neutrino oscillation between only two flavor neutrinos is considered. In this case, the mixing matrix depends on a single parameter and can be given as

$$U = \begin{bmatrix} \cos\theta & \sin\theta \\ -\sin\theta & \cos\theta \end{bmatrix}, \tag{1.8}$$

and there is single mass-squared difference Δm^2. Then, $P_{\alpha\beta}$ in Eq. 1.6 takes the well-known form

$$P_{\alpha\beta} = \delta_{\alpha\beta} - (2\delta_{\alpha\beta} - 1)\sin^2 2\theta\sin^2 x. \tag{1.9}$$

The physical parameter space is covered with $\Delta m^2 \geq 0$ and $0 \leq \theta \leq \pi/2$ (or, alternatively, $0 \leq \theta \leq \pi/4$ and either sign for Δm^2).

1.2.3 3 flavor mixing

The mixing matrix of 3 neutrinos is parameterized by three angles, conventionally denoted as θ_{12}, θ_{13}, θ_{23}, one Dirac phase δ and two Majorana phases α_1, α_2. Here, Dirac phase and Majorana phases are CP-violating phases. Using c for the cosine and s for the sine, we write U as ,

$$\begin{bmatrix} \nu_e \\ \nu_\mu \\ \nu_\tau \end{bmatrix} = \begin{bmatrix} c_{12}c_{13} & s_{12}c_{13} & s_{13}e^{-i\delta} \\ -s_{12}c_{23} - c_{12}s_{23}s_{13}e^{i\delta} & c_{12}c_{23} - s_{12}s_{23}s_{13}e^{i\delta} & s_{23}c_{13} \\ s_{12}s_{23} - c_{12}c_{23}s_{13}e^{i\delta} & -c_{12}s_{23} - s_{12}c_{23}s_{13}e^{i\delta} & c_{23}c_{13} \end{bmatrix} \begin{bmatrix} e^{i\alpha_1/2}\nu_1 \\ e^{i\alpha_2/2}\nu_2 \\ \nu_3 \end{bmatrix}. \quad (1.10)$$

By convention the mixing angle θ_{12} is associated with the solar neutrino oscillations, hence the masses m_1 and m_2 are separated by the smaller interval $\Delta m^2_{\rm sol}$ (we shall assume, again by convention, that $m_2 > m_1$) while m_3 is separated from the 1, 2 pair by the larger interval $\Delta m^2_{\rm sol}$, and can be either lighter or heavier than m_1 and m_2. The situation where $m_3 > m_2$ is called “normal hierarchy”, while the “inverse hierarchy” has $m_3 < m_1$. From Eq. 1.6, the oscillation probability is independent of the Majorana phase α. The oscillation pattern is identical for Dirac or Majorana neutrinos.

The general formula can be simplified for the practical importance. Using $\Delta m^2_{\rm atm} \gg \Delta m^2_{\rm sol}$ and considering distances comparable to the atmospheric neutrino oscillation length, only three parameters are relevant in the zeroth order, which are the angles θ_{23} and θ_{13} and $\Delta_{\rm atm} \equiv \Delta m^2_{\rm atm}L/4E_\nu$. However, corrections of the first order in $\Delta_{\rm sol} \equiv \Delta m^2_{\rm sol}L/4E_\nu$ should be also considered and are included below (some of the terms with $\Delta_{\rm sol}$ are further reduced by the presence of the empirically small $\sin^2 2\theta_{13}$):

$$\begin{aligned} P(\nu_\mu \to \nu_\tau) &\simeq \cos^4\theta_{13}\sin^2 2\theta_{23}\sin^2\Delta_{\rm atm} \\ &- \Delta_{\rm sol}\cos^2\theta_{13}\sin^2 2\theta_{23}(\cos^2\theta_{12} - \sin^2\theta_{13}\sin^2\theta_{12})\sin 2\Delta_{\rm atm} \\ &- \Delta_{\rm sol}\cos\delta\cos\theta_{13}\sin 2\theta_{12}\sin 2\theta_{13}\sin 2\theta_{23}\cos 2\theta_{23}\sin 2\Delta_{\rm atm}/2 \\ &+ \Delta_{\rm sol}\sin\delta\cos\theta_{13}\sin 2\theta_{12}\sin 2\theta_{13}\sin 2\theta_{23}\sin^2\Delta_{\rm atm}, \qquad (1.11) \\ P(\nu_\mu \to \nu_e) &\simeq \sin^2 2\theta_{13}\sin^2\theta_{23}\sin^2\Delta_{\rm atm} \\ &- \Delta_{\rm sol}\sin^2\theta_{23}\sin^2\theta_{12}\sin^2 2\theta_{13}\sin 2\Delta_{\rm atm} \\ &+ \Delta_{\rm sol}\cos\delta\cos\theta_{13}\sin 2\theta_{13}\sin 2\theta_{23}\sin 2\theta_{12}\sin 2\Delta_{\rm atm}/2 \\ &- \Delta_{\rm sol}\sin\delta\cos\theta_{13}\sin 2\theta_{12}\sin 2\theta_{13}\sin 2\theta_{23}\sin^2\Delta_{\rm atm}, \qquad (1.12) \\ P(\nu_\mu \to \nu_\mu) &= 1 - P(\nu_\mu \to \nu_e) - P(\nu_\mu \to \nu_\tau) \qquad (1.13) \end{aligned}$$

where δ is the CP phase of Eq. 1.10 and

$$\begin{aligned} P(\nu_e \to \nu_x) &\simeq \sin^2 2\theta_{13}[\sin^2\Delta_{\rm atm} - \Delta_{\rm sol}\sin^2\theta_{12}\sin 2\Delta_{\rm atm}] \\ &+ \Delta^2_{\rm sol}\cos^4\theta_{13}\sin^2 2\theta_{12}, \qquad (1.14) \end{aligned}$$

where the term linear in $\Delta m^2_{\rm sol}$ is suppressed by the factor $\sin^2 2\theta_{13}$ and therefore the quadratic term is also included. The ν_e disappearance probability is independent of the CP phase δ. Some terms of the first order in $\Delta_{\rm sol}$ depend on the sign of $\Delta_{\rm atm}$, i.e., on the hierarchy. Therefore, the neutrino oscillation in the 3 flavor mixing has information of CP and the neutrino mass hierarchy as well as the mixing angle and mass-squared difference. In addition, the precise study may gives suggestion of CPT-invariance and existence of the sterile neutrinos.

1.3 Neutrino oscillation experiments

Before reach to the experimental sensitivity to physics of CP and the neutrino mass hierarchy, some experiments are performed to study the mixing angle and mass-squared difference in 2 flavor mixing.

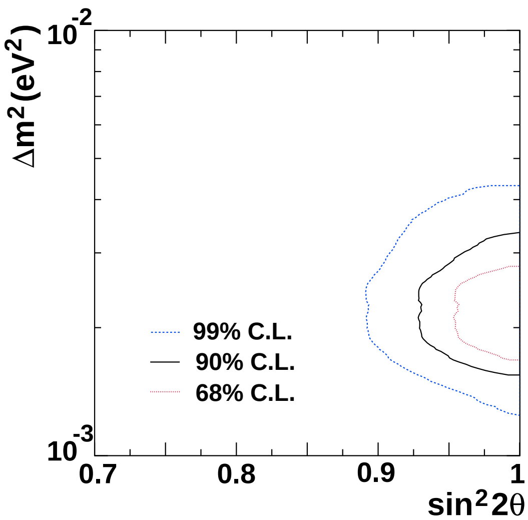

Figure 1.1: Allowed region of oscillation parameters in the atmospheric neutrino study at Super-Kamiokande.

The neutrino oscillation experiments are categorized into four types according to the neutrino sources, which are atmospheric neutrino experiment, solar neutrino experiment, reactor neutrino experiment, and accelerator neutrino experiment. There are three possible regions remaining for the neutrino oscillation parameters.

- Atmospheric neutrino region : $\Delta m^2 \sim 10^{-3}$ eV^2
- Solar neutrino region : $\Delta m^2 \sim 10^{-5} - 10^{-4}$ eV^2
- LSND region : $\Delta m^2 \sim 10^{-1}$ eV^2

1.3.1 Atmospheric neutrino region

At first, neutrino oscillation was observed in the measurement of atmospheric neutrinos at Super-Kamiokande (SK) [2]. The atmospheric neutrinos are generated by decays of pions and kaons which are produced by collision of primary cosmic rays with atmosphere. The experiments to measure oscillation of atmospheric neutrinos is sensitive to $\nu_\mu \to \nu_x$ oscillation. Since the energy of atmospheric neutrino is $1 \sim 100$ GeV and the flight length of $10 \sim 13,000$ km, it is sensitive to $\Delta m^2 = 10^{-4} \sim 1$ eV^2. The parameters of Δm^2 and $\sin^2 2\theta$ were measured with 90% C.L. by SK, as

$$\begin{aligned} &1.5 \times 10^{-3} < \Delta m^2_{\mathrm{atm}} < 3.4 \times 10^{-3} \mathrm{eV}^2, \\ &\sin^2 2\theta_{\mathrm{atm}} > 0.92. \end{aligned} \tag{1.15}$$

The allowed region of oscillation parameters (Δm^2, $\sin^2 2\theta$) is shown in Fig 1.1.

1.3.2 Solar neutrino region

Solar neutrinos are created by nuclear fusion reactions at the center of the Sun. Only electron neutrinos are produced. Therefore, solar neutrino experiments are sensitive to $\nu_e \to \nu_x$ oscillation. The neutrino

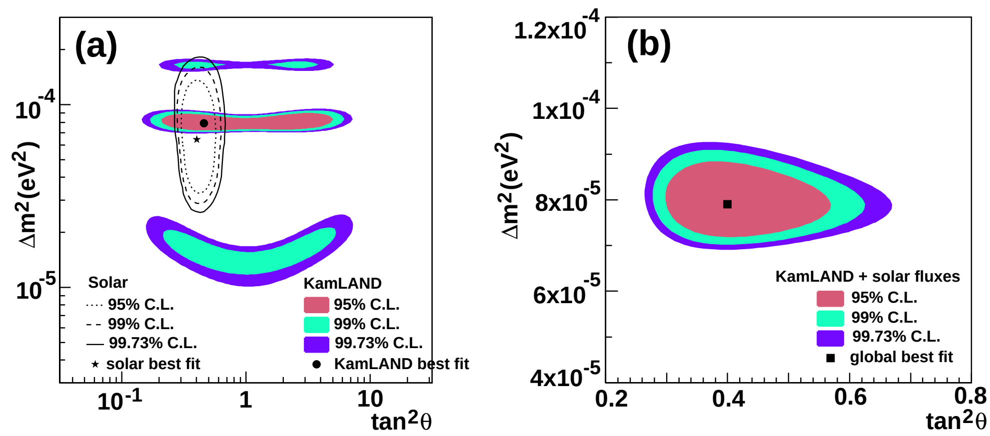

Figure 1.2: (a) Neutrino oscillation parameter allowed region from KamLAND anti-neutrino data(colored regions) and solar neutrino experiment (lines) [6]. (b) Result of a combined two-neutrino oscillation analysis of KamLAND and the observed solar neutrino fluxes under the assumption of CPT invariance. The fit gives $\Delta m^2 = 7.9^{+0.6}_{-0.5} \times 10^{-5}$ eV^2 and $\tan^2\theta = 0.40^{+0.10}_{-0.07}$ including the allowed 1-sigma parameter range.

energy spectrum distributes from 0 to 15 MeV. Since the distance between the Sun and the Earth is 1.5×10^8 km, the sensitivity to Δm^2 reaches down to 10^{-11} eV^2 in case of vacuum oscillation. Solar neutrino experiments can measure Δm^2 up to 10^{-3} eV^2, if we take MSW (Mikheyev-Smirnov-Wolfenstein) effect [3] into account. Here, the MSW effect is the phenomenon that the effective mass eigenvalue is shifted when neutrinos travel through matter.

Recent solar neutrino experiments, such as Super-Kamiokande [4] and SNO [5], reported that the electron neutrino flux from the Sun is significantly smaller than the expected flux while the total neutrino flux is consistent with the expectation. The mass square difference and the mixing angle are measured to be $\Delta m_\odot \simeq 5.0 \times 10^{-5}$ eV^2 and $\tan^2\theta_\odot \simeq 0.45$, respectively.

The neutrino oscillation in the solar neutrino region has been studied by a reactor neutrino experiment, KamLAND [7]. This experiment observes electron anti-neutrinos produced by β-decays of nuclear fission products. KamLAND has observed smaller neutrino flux than the expectation. As shown in Fig. 1.2, the combined analysis of both solar and reactor experiments shows that the allowed intervals of the oscillation parameters are

$$\Delta m^2_\odot = 7.9^{+0.6}_{-0.5} \times 10^{-5} [eV^2], \tan^2\theta_\odot = 0.40^{+0.10}_{-0.07}. \tag{1.16}$$

The solar neutrino oscillation has been established by using two neutrino sources with different systematics.

1.3.3 LSND region

$\bar{\nu_\mu} \to \bar{\nu_e}$ oscillation was observed in the LSND (Liquid Scintillator Neutrino Detector) experiment [8], which was performed to study $\bar{\nu_e}$ appearance by using $\bar{\nu_\mu}$ beam at LANSCE (Los Alamos Neutron Science Center). The best fit value for $\bar{\nu_\mu} \to \bar{\nu_e}$ oscillation is obtained as ($\sin^2 2\theta$, Δm^2) = (0.003, 1.2 eV^2). To confirm the results of the LSND experiment, the MiniBooNE experiment has been in operation at Fermi National Accelerator Laboratory since the summer in 2002.

1.4 Motivation of the K2K experiment

Neutrino oscillation in the atmospheric region is observed only by the atmospheric neutrino experiments before the K2K experiment. To confirm the atmospheric neutrino oscillation, the other types of experiments with different systematics is desired. From this reason, the K2K (KEK to Kamioka) experiment is performed. The K2K experiment is the first dedicated long baseline experiment with muon neutrinos generated by an accelerator. The experimental features and analysis methods to study the neutrino oscillation are described in the next chapter.

Chapter 2

The K2K Experiment

2.1 Overview

The K2K experiment was proposed to confirm atmospheric neutrino oscillation [9] and to measure the oscillation parameters. An almost pure muon neutrino (ν_μ) beam produced by a 12 GeV proton beam at KEK, was detected by Super-Kamiokande (SK), a 50 kt water Cherenkov detector after 250 km flight as shown in Fig. 2.1. In addition to the SK measurement, the near detectors (ND) at KEK measured the ν_μ beam properties just after ν_μ production. By comparing the results between ND and SK, the neutrino oscillation in the atmospheric region is studied.

The K2K experiment is also investigating $\nu_\mu \rightarrow \nu_e$ oscillation by searching for electron neutrino events in SK. A study of $\nu_\mu \rightarrow \nu_e$ oscillation is described in [12].

2.2 Evidence of the neutrino oscillation

In the $\nu_\mu \rightarrow \nu_x$ oscillation in the atmospheric region, ν_x could be likely ν_τ. For $\nu_\mu \rightarrow \nu_\tau$ oscillation at the K2K experiment, ν_τ does not have the scattering amplitude for charged current interaction, because the neutrino energy is below the threshold of tau production (~ 3.5 GeV). Therefore, the effect of neutrino oscillation is observed as disappearance of the muon neutrinos. In addition, since the baseline is constant of 250 km in the K2K experiment, the oscillation probability of ν_μ in Eq. 1.9 is a function of only the neutrino energy. For these reasons, two features for ν_μ disappearance would be observed in the K2K experiment as below,

- Distortion of the neutrino energy spectrum shape.
- Deficit of a number of events at SK from its expectation.

Figure 2.2 shows oscillation probability as a function of neutrino energy (E_ν) (top) and the ν_μ energy spectrum at SK with and without neutrino oscillation (bottom). A typical parameter set suggested by the atmospheric neutrino experiments is used in Fig. 2.2. A large dip at around 0.6 GeV and decrease of overall statistics can be seen with neutrino oscillation in Fig. 2.2. For a study of the atmospheric neutrino oscillation at SK, the neutrino energy and flux at the generated point is expected by using the MC simulation. In the K2K experiment, a number of neutrino events and the energy spectrum at SK is estimated from the measurement by ND without the uncertainty on the neutrino flight length. Therefore, the neutrino oscillation is investigated suppressing the systematic errors by comparison with the observation at ND and SK.

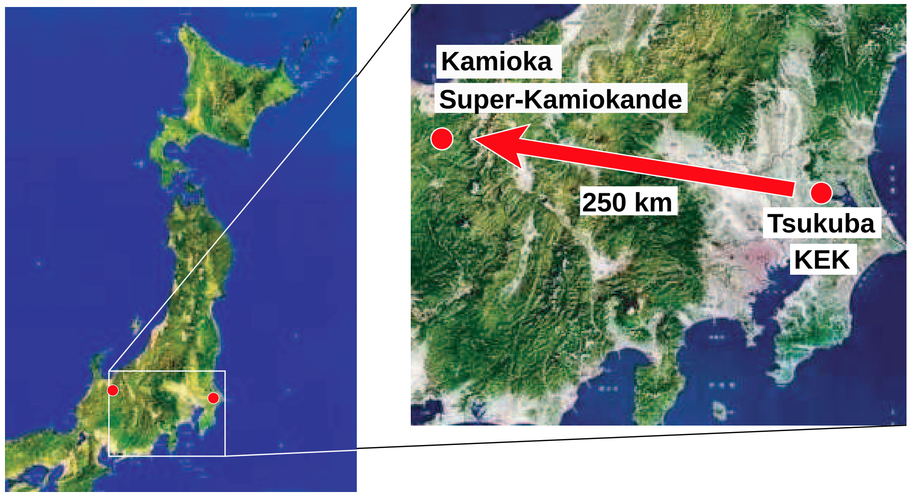

Figure 2.1: Overview of the K2K experiment. The $\nu_\mu$beam produced at KEK is detected by Super-Kamiokande after 250 km flight.

2.3 Analysis strategy

In the K2K experiment, neutrino oscillation is studied by comparing the observation and the expectation of a number of neutrino events and the energy spectrum at the SK site. The analysis procedure in the K2K experiment is summarized as follows.

- Measurements at the near detectors
- Extrapolation from ND to SK
- Measurements at SK
- Study of neutrino oscillation

Each analysis procedure is described briefly as below.

2.3.1 Measurement at the near detectors

As described in Section 2.2, the effect of neutrino oscillation appears in the shape of the energy spectrum at SK. Therefore, the neutrino energy spectrum was measured at the ND to expect that at SK. The neutrino energy spectrum was measured with the relation between momentum and angle of muons from charged current (CC) interaction. Especially, charged current quasi-elastic (CC-QE) interaction,

$$\nu_\mu + n \to \mu^- + p, \tag{2.1}$$

have an important role in the measurement of the neutrino energy spectrum, which is a dominant process in the K2K experiment. Since the CC-QE interaction has only two particles (a muon and a proton) in the final state, neutrino energy can be reconstructed by using the muon momentum and its angle. Therefore, it is important to increase the purity of CC-QE interaction in data sample.

In addition, a number of neutrino events is also measured at a near detector. Multiplying the flux ratio between ND and SK, a number of events at SK is expected.

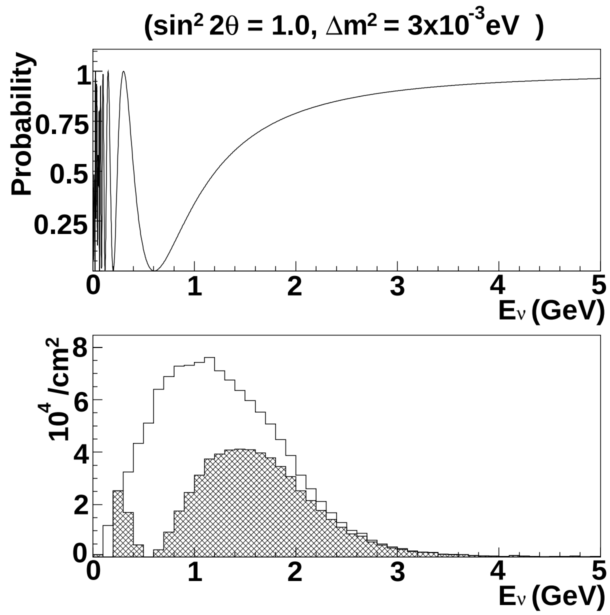

Figure 2.2: The oscillation probability as a function of E_ν (top) and E_ν spectrum with and without neutrino oscillation (bottom). The oscillation parameters are selected as ($\Delta m^2 = 3 \times 10^{-3}$ [eV^2], $\sin^2 2\theta = 1.0$).

2.3.2 Extrapolation from ND to SK

To study neutrino oscillation, the energy spectrum and a number of the neutrino events observed at SK are compared with the expectation by the measurement at ND. To extrapolate those measurements at ND to SK, the flux ratio from the near site to SK for each neutrino energy ($R^{\mathrm{F/N}}(E_\nu)$) is estimated. The expected neutrino spectrum and a number of events at SK can be obtained by multiplying $R^{\mathrm{F/N}}(E_\nu)$ to the results of the measurement at ND.

2.3.3 Measurements at SK

The neutrino energy spectrum and a number of the events could be measured at SK. This result would be compared with the expectation from the measurement results at ND in the neutrino oscillation study.

2.3.4 Study of neutrino oscillation

The neutrino energy spectrum and a number of events observed at SK are compared with the expectation by using a maximum likelihood method. In this study, the effect of the atmospheric neutrino oscillation experiment and the oscillation parameters are investigated.

2.4 Requirements to the experiment

The requirements to the K2K experiment are summarized as below.

- **Neutrino beam :**
  To study the neutrino oscillation in the atmospheric neutrino region, the neutrino beam must

cover the parameter region of the atmospheric neutrino oscillation. In the K2K experiment, the ν_μ beam energy spreads widely around mean energy of 1.3 GeV. Therefore, the K2K experiment is sensitive to the range of $\Delta m^2 \sim 10^{-3} - 10^{-2}$ [eV^2], which covers the atmospheric neutrino oscillation parameters ($\Delta m^2 \sim 3 \times 10^{-3}$ [eV^2], $\sin^2 2\theta \sim 1$).

- **Near detectors :**
  To expect the neutrino energy spectrum and a number of events at SK, the near detectors must have good performance for the measurements at the near site. For the spectrum measurement, they should have sufficient performance to identify each neutrino interaction to separate CC-QE and the other interaction mode which is backgrounds for the energy measurement. For comparison of the number of events with the observation at SK, one of them is desired to be the same water Cherenkov detector as SK to cancel out the uncertainties with the same neutrino cross-section and detector systematics. For these purpose, the near detectors are designed as described in Section 3.2.

- **Far detector :**
  With the oscillation parameters of $\Delta m^2 = 3 \times 10^{-3}$ [eV^2] and $\sin^2 2\theta = 1$, the observed number of SK events corresponds to 65% of that of the null oscillation case. Therefore, at least 100 events (10% statistical error) is required to exclude the null oscillation hypothesis by three standard deviations (99.7% C.L.) with only statistical error. SK has sufficient mass to accumulate neutrino events, whose event rate is expected to be 0.4 event/day without neutrino oscillation. Therefore, the requirements for the statistics (more then 100) is satisfied by a run time of a few hundred days.

2.5 History of the K2K experiment

A brief history of the K2K experiment is summarized. The neutrino data taking was started in June 1999 with a horn current of 200 kA (80% of design value). This period is named "K2K-Ia". In November 1999, the horn current increased to 250 kA (design value), and the data had been accumulated until July 2001 (K2K-Ib). The results from K2K-Ia and K2K-Ib were published for the $\nu_\mu \to \nu_x$ oscillation [10, 11] and for the $\nu_\mu \to \nu_e$ oscillation [12].

In November 2001, a severe accident happened in Super-Kamiokande, and many PMTs were crashed. After the reconstruction of SK with a half PMT density, the experiment was resumed in January 2003, and data was taken until June 2003 (K2K-IIa). In the K2K-IIa period, there was no lead glass calorimeter. Then, a new near detector, SciBar, was installed in the summer 2003. The neutrino data was taken again from October 2003 to February 2004 (K2K-IIb) and from October 2004 to November 2004 (K2K-IIc).

Fig. 2.3 shows a number of delivered protons on target (POT). A total of 10.5×10^{19} POT have been delivered. POT recorded by SK are 9.2×10^{19}, which were analyzed to examine neutrino oscillation.

2.6 The purpose for this thesis

In the K2K experiment, the effect of the neutrino oscillation becomes larger in low energy region below 1 GeV, as shown in Fig. 2.2. The precise spectrum measurement in low energy region by the near detector is necessary to confirm neutrino oscillation.

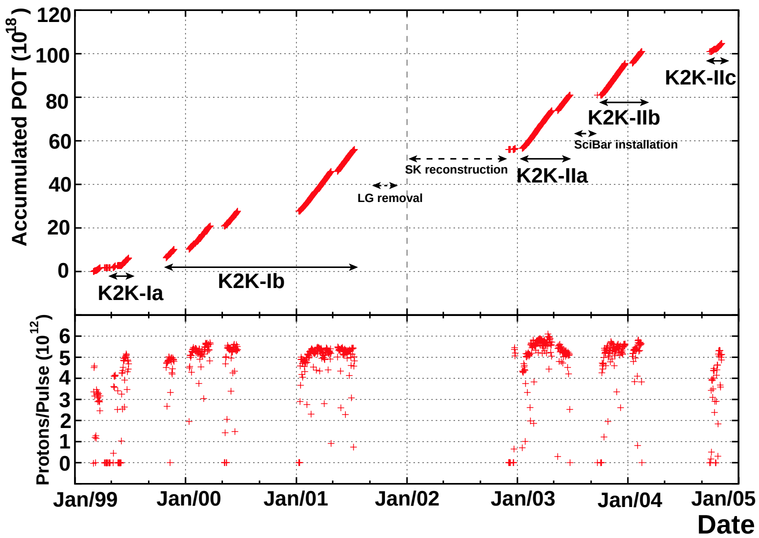

Figure 2.3: The accumulated number of protons delivered to the target since the beginning of the experiment (upper). The lower figure shows the number of protons per spill (bottom).

The 1KT detector which is one of the near detectors has performance enough to detect low energy CC-QE events. However, it can not identify CC-QE from the events of the other interaction modes (nonQE), since only muons after neutrino interactions can make Cherenkov rings. Therefore, the contamination of nonQE interaction in the sample is estimated without any constraint. For this reason, the near detector is desired to be able to identify CC-QE events even in the low energy region. To separate CC-QE interaction from nonQE interaction, the detector had better observe both muons and protons from the CC-QE events and other particles from the nonQE events. In particular, to identify short track from other low energy events, detector structure is segmented without any dead region.

Therefore, the SciBar detector was constructed in 2003 summer, which is a fully active detector composed of fine scintillator strips. It can detect short tracks made by low energy events and separate CC-QE and nonQE events by using both muon and proton tracks. In addition to that, SciBar can observe both low energy events ($>$ 1 GeV) and high energy events ($<$ 1 GeV). By using SciBar, the energy spectrum for all energy region is determined by only one detector.

In this thesis, the neutrino oscillation is studied with the measurement of the low energy neutrino spectrum by SciBar. The purpose of this thesis is summarized as below.

- **Study of the low energy spectrum in SciBar :**
  The neutrino energy spectrum especially in low energy region, was measured by using SciBar. In this analysis, the low energy samples were made to make the energy threshold lower and increase low energy events by SciBar. The method to investigate the low energy region by SciBar is established.

- **Measurement of the energy spectrum at the near site :**
  The consistency of the spectrum measurement was studied with each near detector. The contamination of nonQE interaction was estimated by SciBar. The energy spectrum in low energy region measured by 1KT, was studied to be consistent with that from SciBar. Then, the energy spectrum at the near site was measured by using all the near detectors.

- **Study of neutrino oscillation :**
  Finally, the neutrino energy spectrum measured by all near detectors, is used for a study of the neutrino oscillation. The effect of the neutrino oscillation was investigated.

Chapter 3

The Experimental Setup

The setup for the K2K experiment is composed of the KEK-12GeV proton synchrotron, the neutrino beamline, the near detectors, and the far detector (Super-Kamiokande), as shown in Fig. 3.1. In this chapter, each experimental component is described.

3.1 Beamline

The neutrino beam is produced by primary protons accelerated by the KEK-12GeV proton synchrotron. Fig. 3.2 shows a schematic overview of the KEK-12GeV proton synchrotron and the neutrino beamline. The beam monitors are installed in the beamline to measure the properties of primary protons and their secondary particles. In this section, the production of a neutrino beam and the beam monitors are described.

3.1.1 Production of the neutrino beam

Primary proton beamline

The KEK-12GeV proton synchrotron (KEK-PS) is used to accelerate protons. In the main ring, more than 7×10^{12} protons are accelerated up to kinetic energy of 12 GeV. A number of the beam bunches

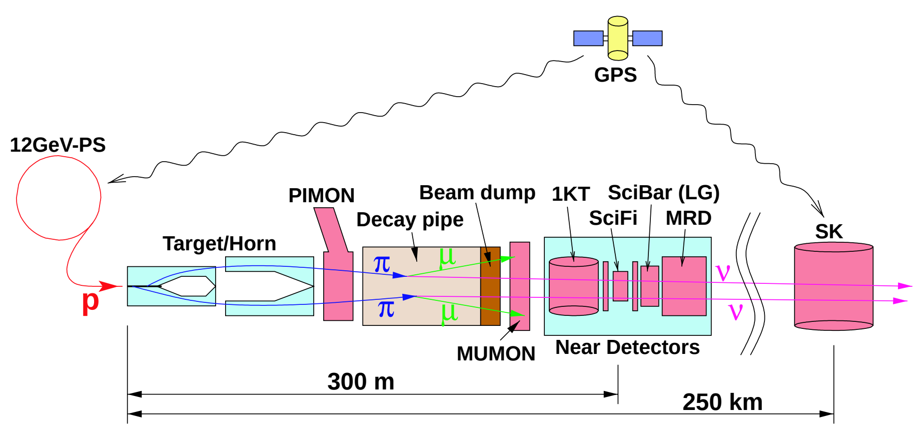

Figure 3.1: Schematic overview of the K2K experiment.

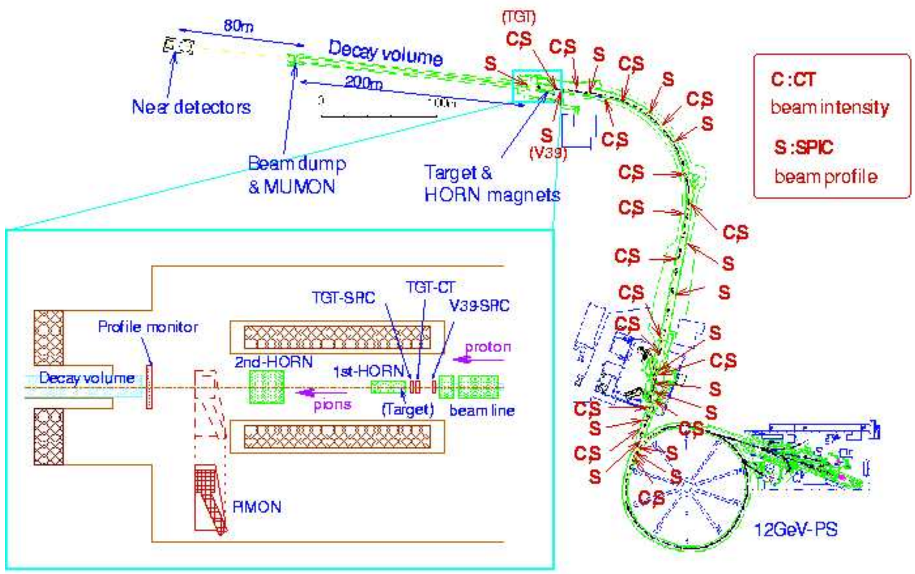

Figure 3.2: Schematic overview of KEK-12GeV proton synchrotron and neutrino beam line.

in a single spill is nine, which corresponds to the harmonic number of the main ring.

The accelerated protons are extracted from the KEK-PS in a fast extraction mode whose repetition time is 2.2 sec and spill time is 1.1 μsec. After extraction from the KEK-PS, the proton beam is bent toward Super Kamiokande (about 90° to the west) at the arc section. The proton beam is focused on the neutrino production target located just after the arc section. The transportation efficiency from the extraction point to the production target is about 85%, and the beam intensity just before the target is about 5×10^{12} protons in one spill.

Production target and horn magnet

Secondary pions are generated by hadron interaction of primary protons in the production target [13]. Two magnetic horns are used to focus pions. The production target is embedded in the first horn in order to focus the pions efficiently. The target is made of an aluminum alloy 6061-T, which is a rod of 66 cm in length and 3 cm in diameter.

The pulsed coaxial electrical current is supplied to the inner and outer conductors of the horn magnets with its duration of 2 msec and its amplitude of 250 kA. This current makes a toroidal magnetic field between the inner and outer conductors. The maximum magnetic field is 33 kG at the rod surface with a current of 250 kA. This magnetic field focuses the positive charged particles into the forward direction, whereas the negative charged particles are swept out. The two horn systems enhance the neutrino flux above 0.5 GeV by 22 times more than the bare target case as shown in Fig. 3.3

During the period of K2K-Ia, a peak current of 200 kA was applied to the horn magnets, and the production target of 2 cm was used. The target of 3 cm diameter has been used with a peak current of 250 kA since Oct. 1999.

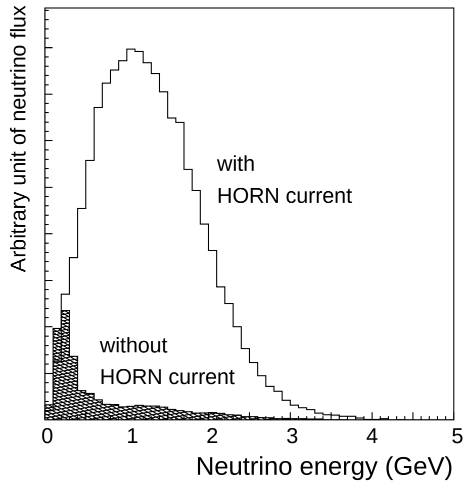

Figure 3.3: The neutrino flux at Super-Kamiokande with and without the horn systems, estimated by the MC simulation. The open histogram shows the neutrino flux with the horn current of 250 kA, and the hatched one shows that without the horn current.

Decay volume and beam dump

After the horn magnets, the pions go into the decay volume, which is a cylindrical pipe of 200 m long. The decay volume is filled with helium gas of 1 atm to avoid a possible loss of pions by absorption. In the decay volume, π^+ decay into μ^+ and ν_μ. Since pions are strongly boosted in the laboratory frame, neutrinos are emitted toward Super-Kamiokande within the decay angle of 10 mrad. After the decay volume, the beam dump is located to stop all the particles except for neutrinos. It consists of 3.5 m thick iron shield, 2 m thick concrete, and about 60 m long soil. All the particles other than neutrinos are absorbed by iron, concrete, and soil shields.

3.1.2 Primary beam monitors

The intensity of the proton beam and the beam transportation efficiency is monitored by the current transfers (CTs), which are a kind of pick-up coil sensitive to an induced current by the protons. Measuring the integrated induced current, a number of the protons on the target (P.O.T.) is monitored by the TARGET-CT located just before the target as shown in Fig. 3.2. The profiles of the proton beam are measured by the segmented plates ionization chambers (SPICs) [14]. In total, 13 CTs and 28 SPICs are installed in the beam line.

3.1.3 Secondary beam monitors

The pion monitor and muon monitor are used for the secondary beam monitors. Here, they are summarized briefly, and the detail descriptions are found in Appendix A.1 and A.2.

Pion monitor (PIMON)

The momentum and divergence of the secondary pions are measured by the pion monitor (PIMON) [96], which is located just after the second horn magnet. The PIMON is a gas Cerenkov detector, which consists of a gas vessel, a spherical mirror, and a photo detector. For rejection of severe backgrounds

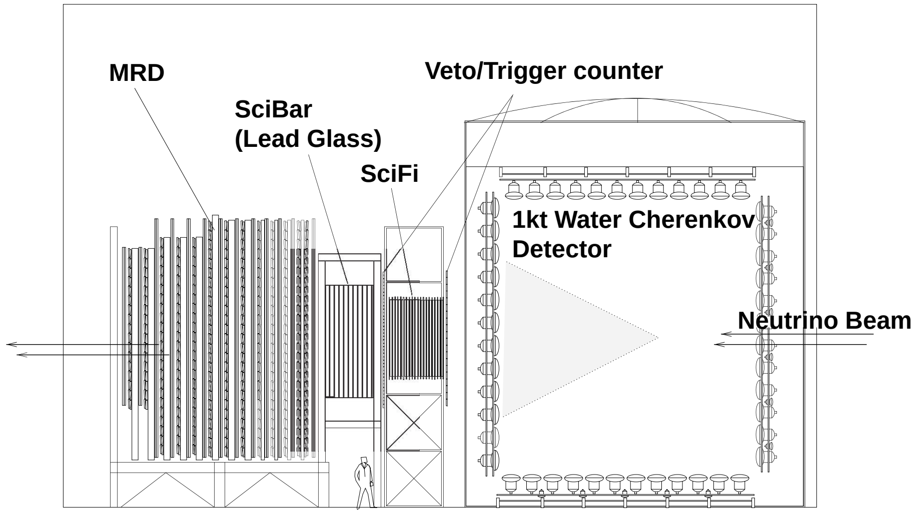

Figure 3.4: The experimental setup of the near detectors.

from primary protons, the momentum threshold of PIMON for the pions is determined to be 2 GeV, which corresponds to 1 GeV for the neutrinos.

Up to now, the data taking of PIMON had been performed twice, in June 1999 and November 1999, for different experimental configurations. The PIMON measurement was done with a target of 2 cm in diameter and the horn current of 200 kA in June 1999, and with a target of 3 cm in diameter and the horn current of 250 kA in November 1999.

Muon monitor (MUMON)

Muon monitor (MUMON) is placed in a pit at the downstream of the beam dump, which monitors the distribution and the intensity of the neutrino beam by measuring the muons spill by spill. MUMON consists of two detector parts, an ionization chamber (ICH) and a silicon solid detector (SSD) array. Only muons with the momentum above 5.5 GeV/c can reach the pit due to the beam dump, where the flux is roughly 10^4 muons per 1 cm^2. Since such high energy muons is more sensitive to the overall neutrino beam direction, it works well as a monitor for the overall beam steering toward SK.

3.2 Near detectors

The near detectors at the KEK site are composed of the 1kt water Cherenkov detector (1KT), a scintillating fiber detector (SciFi), a lead glass calorimeter (LG) for K2K-Ia and K2K-Ib, the scintillator bar detector (SciBar) for K2K-IIb and K2K-IIc, and a muon range detector (MRD). Fig. 3.4 shows the experimental setup of the near detectors. Since the beam center is about 10 m underground, the near detectors are installed in the cylindrical hole with the dimension of 16 m in depth and 24 m in diameter.

3.2.1 1kt water Cherenkov detector

The 1kt water Cherenkov detector (1KT) is located at the most upstream part of the experimental hall. Fig. 3.5 shows a schematic view of the 1kt detector. It consists of the cylindrical tank of 10.8 m in diameter and 10.8 m in height, which is filled with approximately 1,000 tons of pure water.

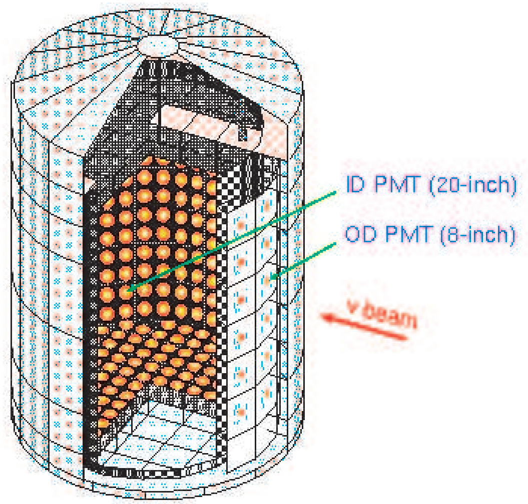

Figure 3.5: Schematic overview of the 1kt water Cherenkov detector.

The inside of the tank is optically separated into two parts, the inner detector (ID) and the outer detector (OD). The ID is a cylindrical water Cherenkov detector, which is 8.6 m in diameter and 8.6 m in height. There are 680 20-inch PMTs mounted on the support frame facing inward. The OD is also a water Cherenkov detector, whose thickness is 1 m for barrel and 0.6 m for the bottom. There are 68 8-inch PMTs facing outward on the support frame.

The neutrino events are detected by using Cherenkov ring images made by muons from CC interaction. The advantage of the 1kt detector is to cancel out the systematic uncertainties with SK, since they have the same target material (H_2O), the same detection principle and the same analysis algorithm.

3.2.2 SciFi detector

The Scintillating Fiber (SciFi) tracking detector is located just behind the 1KT. A schematic view of the SciFi detector is shown in Fig. 3.6. The SciFi consists of water filled aluminum target and scintillating fiber layers.

A scintillating fiber used for the fiber layers is a Kuraray SCSF78M multi-cladding fiber, which is 0.692 mm in diameter and 3.7 m in length. One layer consists of a set of horizontal and vertical fiber planes. Each plane has 6 bundles which compose 1142 scintillating fibers. In total, 274,080 fibers are used for the SciFi with 20 fiber layers.

19 water target layers are inserted between each SciFi layer. Water is contained in an aluminum tank of 0.18 cm thick, whose size is $240 \times 240 \times 6$ cm^3. Water is used as a target material to minimize systematic uncertainties in the neutrino cross-section when the event rates are compared between SciFi and SK. Signals from the scintillating fiber is read by electrostatic image intensifiers (IIT). Each fiber bundle is connected to the photo-cathode of the IIT. Amplified signals by IIT are recorded by a CCD camera with 768×493 pixels.

The trigger/veto counter (TGC), which is a plastic scintillator hodscope, is installed upstream and downstream of SciFi to obtain timing information of a track.

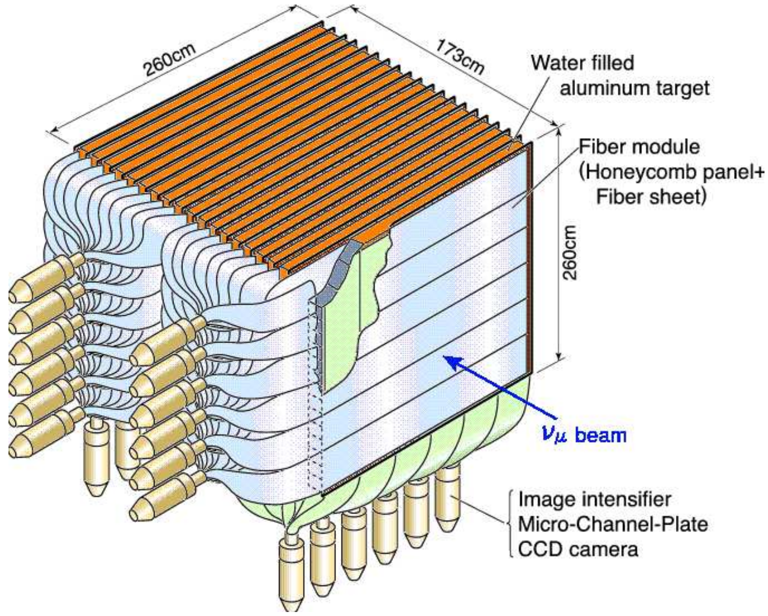

Figure 3.6: Schematic overview of the SciFi tracking detector.

3.2.3 Lead glass Cherenkov calorimeter

A lead glass Cherenkov calorimeter (LG) was located downstream of SciFi until 2001 [19]. The purpose is to measure the contamination of the electron neutrinos in the beam [20]. LG was removed in fall 2001 to reduce material behind SciFi and to install a new detector, SciBar.

3.2.4 SciBar detector

A full-active scintillator detector, “SciBar”, was installed at the same place as LG, in 2003 summer. The detail of SciBar is described in Chapter 4.

3.2.5 Muon range detector

The muon range detector (MRD) is used to measure muon energy by its range [21, 22]. The MRD consists of 12 layers of iron absorber sandwiched between vertical and horizontal drift-tube layers. The size of a layer is approximately 7.6×7.6 m^2. In order to have a good energy resolution for the whole energy region, the upstream four iron plates are 10 cm thick and the downstream eight are 20 cm thick. A total iron thickness of 2 m covers up to the muon energy of 2.8 GeV.

Each drift-tube module consists of 8 drift tubes, which are arranged as shown in Fig.3.7 (right). Active aria of the drift-tube is $5 \times 7 \times (245 \sim 760)$ cm^3. The anode wire is a tungsten wire of 70 μm diameter, stretched with around 390 g wire tension. Ideally, a drift-tube layer should be arranged by 25 modules of 7.6 m length with 2 cm gap between consecutive modules. However, for some horizontal drift-tube layers shorter modules are combined end-to-end to make the full 829 modules in total: 377 modules of 7.6 m length, and 452 shorter ones. The setup of the MRD is shown in Fig.3.7 (left). The total weight of iron is 864 tons. Including the aluminum drift-tubes, the total mass is 915 tons.

P10 gas with a mixture of 90% argon and 10% methane is filled in the modules. Applied high voltage is 2.7 kV.

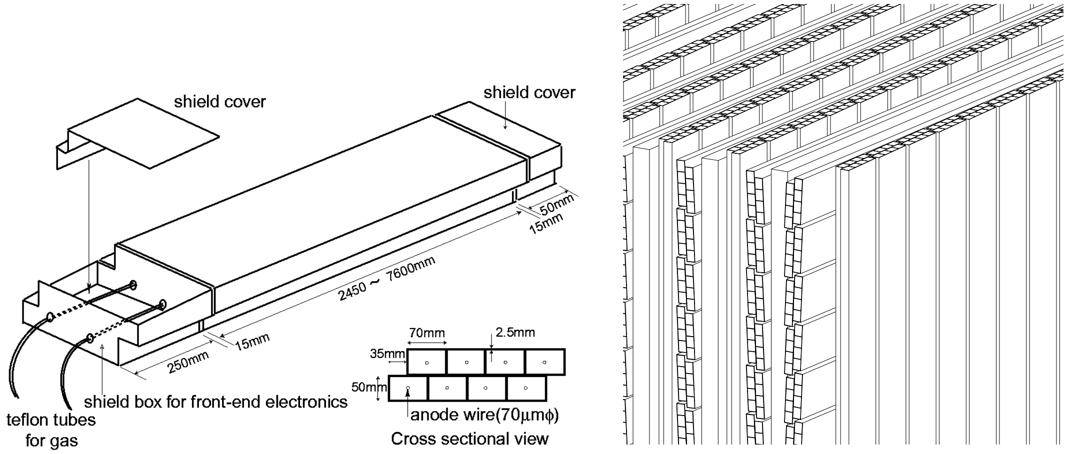

Figure 3.7: Schematic overview of the MRD detector.

Hit efficiency and tracking efficiency is studied by using cosmic ray. The hit efficiency of each module is 97.5%. The tracking efficiency is above 95% if a particle penetrates more than 3 layers, as shown in Fig. 3.8.

3.3 Far detector

The Super-Kamiokande (SK) detector [23] is employed as the K2K far detector (Fig. 3.9), which is located at the Kamioka observatory of Institute for Cosmic Ray Research, University of Tokyo, in the Kamioka mine in Gifu prefecture. Here, SK is described briefly, and the detail description for SK is found in Appendix A.3.

The SK is a cylindrical water tank whose size is 41.4 m in height and 39.3 m in diameter, instrumented with photomultiplier tubes (PMTs), electronics, an online data acquisition system and a water purification system. The water tank to be filled with 50,000 tons of pure water, is made of stainless steel. The detector has two PMT layers, inner detector (ID) and outer detector (OD). The ID is 33.8 m in diameter and 36.2 m in height. The total mass is 32 kton. 11,146 20-inch PMTs are used for the ID. The OD is 2.0 m for the side and 2.2 m for the top and bottom, and 1,885 8-inch PMTs are mounted. As 1KT, the neutrino events are detected by using Cherenkov ring image made by the muons.

The K2K data has been taken since 1999 with 11,146 20-inch PMTs for the ID. However, about 60% of PMTs were broken in 2001, fall. SK was rebuilt with a half of PMT density. The experimental period is called “SK-I” before the accident, and “SK-II” after the rebuilding. The overall efficiency for SK-I and SK-II are 77.2% and 77.9%, respectively. Regardless of the reduction of PMTs, the efficiency for SK-II is higher than that for SK-I as described in Section 9.2.4.

3.4 Timing synchronization

To identify the K2K neutrino events from the atmospheric neutrino backgrounds, the timing synchronization between the KEK site and SK is necessary. The global position system (GPS) [24] is used for the timing synchronization. Two independent GPS receivers was used in parallel in both the KEK and SK sites for hardware backup as well as their quality check with each other. They are compared and

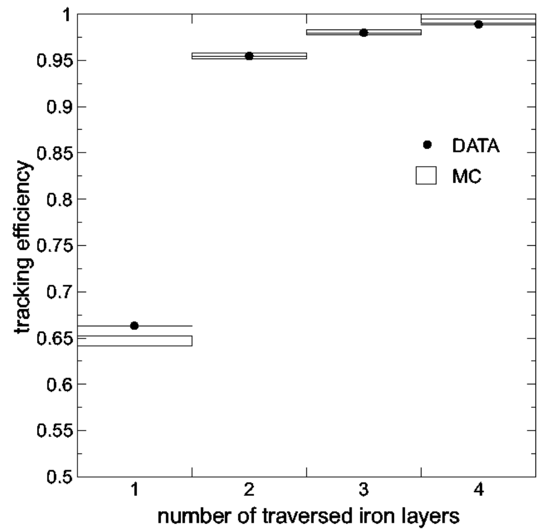

Figure 3.8: Tracking efficiency as a function of the traversed iron layers. The boxes show the Monte-Carlo result, with a size representing the errors.

agreed with each other within 100 nsec (FWHM). Detail description for the GPS system is found in Appendix A.4.

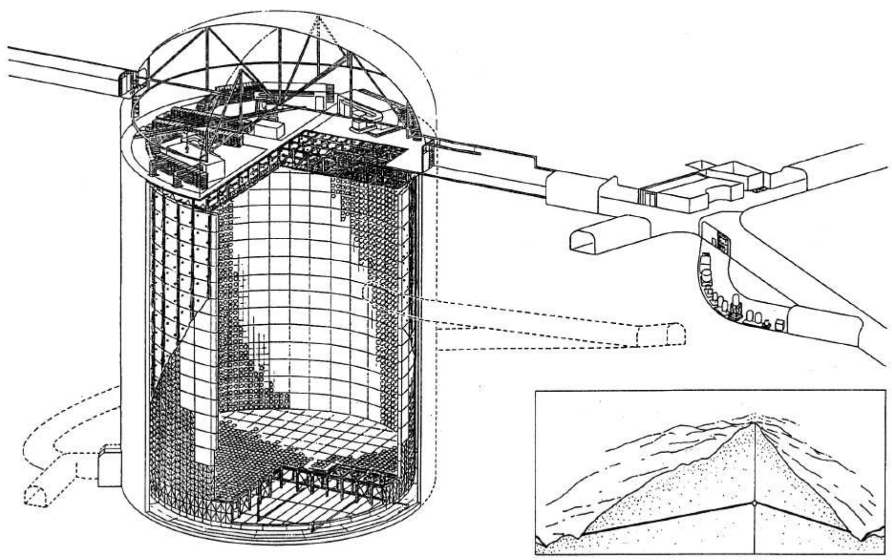

Figure 3.9: Schematic view of the Super-Kamiokande detector.

Chapter 4

SciBar Detector

4.1 Introduction

In the K2K experiment, the effect of neutrino oscillation is expected to be maximum in energy region below 1 GeV The neutrino energy is measured by using charged-current quasi-elastic scattering (CC-QE) events, which is $\nu_\mu n \rightarrow \mu p$. Since CC-QE is a two-body process, the neutrino energy can be determined by the muon momentum and angle. For energy measurement, the other interactions than CC-QE (nonQE) are also detected, such as charged-current 1π production ($\nu_\mu N \rightarrow \mu\pi N'$). Since the muon momentum and angle in non-QE events can not lead to the exact energy information, the nonQE interaction behaves as backgrounds for energy measurement. To separate CC-QE and nonQE events, the following performances are required for a detector.

- Measurement of muon energy.
- Detection of both muon and proton tracks.
- Identification of protons and muons (and pions).

Since the muons have a long range in material, we can detect them above 0.3 GeV/c in momentum easily. On the other hand, the protons from CCQE interaction by low energy neutrinos make only a short track (for example, 20 g/cm^2 for the momentum of 0.6 GeV/c). Therefore, fine detector segmentation is required, for instance a few cm level with small amount of dead material. In addition, since the neutrino interaction cross-section is very small, a neutrino detector should be massive. To measure precise neutrino energy spectrum in low energy region at near-site, we designed and constructed a full-active scintillator detector, “SciBar”.

4.2 Detector overview

A schematic view of the SciBar detector (SciBar) is shown in Fig. 4.1. SciBar consists of approximately 15,000 extruded scintillator strips with each dimension of $1.3 \times 2.5 \times 300$ cm^3. The scintillator strips are arranged in 64 layers. Each layer consists of two planes with 116 strips glued together by Cemedine PM-200, to give horizontal and vertical position. A total size and weight are $2.9 \times 2.9 \times 1.7$ m^3 and 15 tons, respectively. Scintillation photons from each strip are read out by a wavelength shifting (WLS) fiber, which is inserted into a hole of the strip as shown in Fig. 4.2. These photons are transported to a photo-detector, 64-pixel multi-anode photo-multiplier tube (MA-PMT). The charge and timing

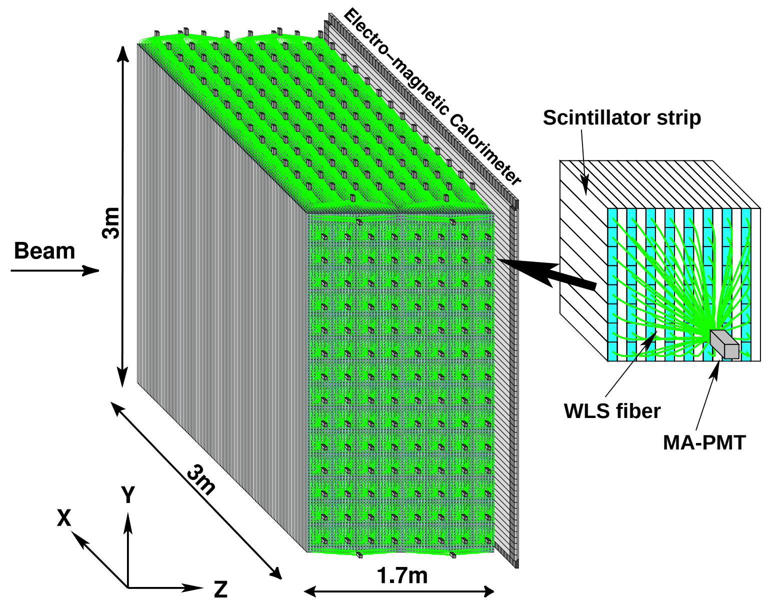

Figure 4.1: Schematic view of SciBar.

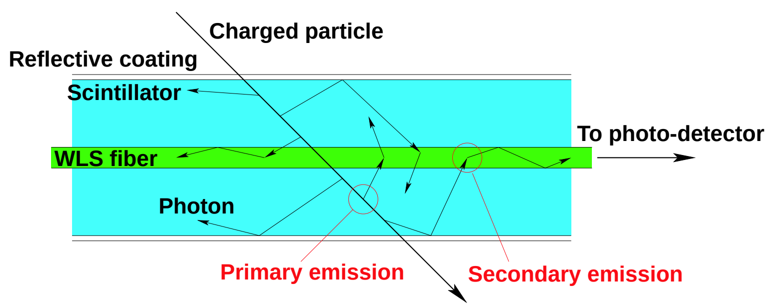

Figure 4.2: Schematic view of a scintillator strip and WLS fiber.

information are recorded by the readout system as shown in Fig. 4.3 and Fig.4.4. An electro-magnetic calorimeter (EC) is also installed just downstream of SciBar to measure the ν_e contamination in the beam and π^0 yield. During the summer shutdown in 2003, the SciBar detector was constructed and placed at the site of Lead glass Cherenkov calorimeter. Neutrino data have been taken with SciBar since October 2003.

We summarize the characteristics of the SciBar detector as follows.

- A full active detector with no dead region.
- SciBar detects tracks as short as 8 cm, corresponding to 0.45 GeV/c for a proton, with requirement of 3 layers penetration.
- Protons are distinguished from charged pions and muons with energy deposit (dE/dx).

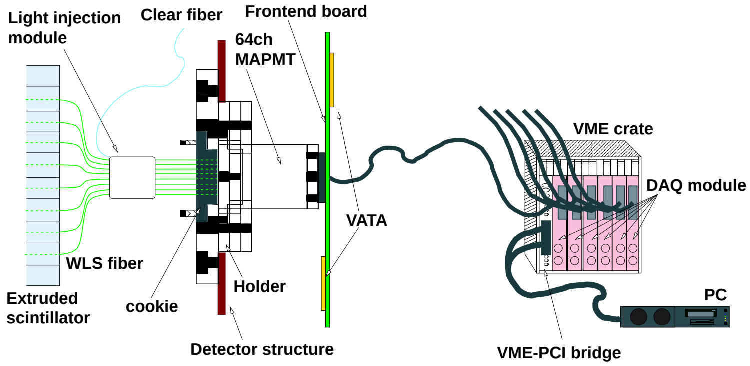

Figure 4.3: Schematic view of the readout system.

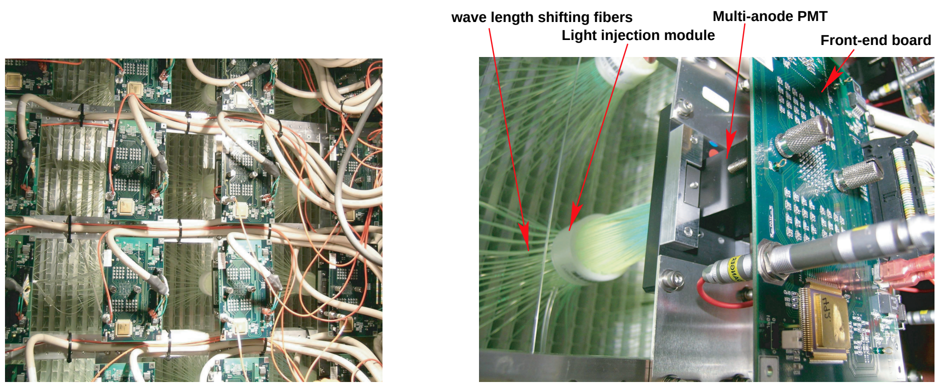

Figure 4.4: Pictures of the SciBar readout electronics.

4.3 Detector components

4.3.1 Extruded scintillator

The extruded scintillator strips are made of polystyrene, infused with the fluor PPO (1% by weight) and POPOP (0.03%). The extruded scintillator was developed and produced by Fermilab [25], whose composition was the same as scintillators used by the MINOS experiment [26]. The wavelength of the scintillators is 420 nm (blue) at the emission peak. This compound is melted and extruded in the shape of rectangular bar with a hole at the center. The scintillator strip has a dimension of 2.5 cm wide, 1.3 cm thick, and 300 cm long. The diameter of the hole is 1.8 mm, that is sufficient to insert a 1.5 mm diameter WLS fiber. A white reflective coating of 0.25 mm thick in which TiO_2 is infused in polystyrene (15% by weight), surrounds the entire scintillator bar. The coating improves light collection efficiency, and it acts as an optical isolator. The basic quantities of the scintillator strips are summarized in Table 4.1. During the installation, 10% of strips were sampled and the dimensions and weight were measured. Their mean value and root-mean-square (RMS) are also shown in Table 4.1.

4.3.2 Wave-length shifting fiber

The wavelength shifting (WLS) fibers are used to collect scintillation light. Blue scintillation lights emitted by scintillator strips are absorbed by Y11 flour (wavelength shifter) in a fiber, and re-emitted as

Table 4.1: Basic quantities of the SciBar scintillator. The errors for the dimension and weight are assigned their RMS, which are measured by using 10% of all strips.

Scintillator	Polystyrene with PPO (1%) and POPOP (0.03%)
Emission wavelength	420 nm (blue)
Dimensions	width : 2.5 ± 0.021 cm
	thickness : 1.287 ± 0.026 cm
	length : 302.2 ± 1.0 cm
Hole diameter	1.8 mm
Reflector material	TiO_2 (15%) infused in polystyrene
Reflector thickness	0.25 mm
Weight	994.6 ± 8.4 g
Number of strips	14,848

Table 4.2: Basic characteristics of WLS fiber.

Diameter	1.5 mm (OD 1.2 mm)
Core	Polystyrene ($n = 1.59$)
Inner clad	Acrylic ($n = 1.49$)
Outer clad	Polyflour ($n = 1.42$)
Wavelength shifter	Y-11 flour (200 ppm)
Absorption wavelength	430 nm (peak)
Emission wavelength	476 nm (peak)
Attenuation length	350 cm

green lights. Basic characteristics of the WLS fiber are summarized in Table 4.2. As shown in Fig. 4.5, the absorption spectrum has only a little overlap with the emission spectrum, so that the probability of self-absorption in the fiber is small.

The WLS fibers of 1.5 mm diameter are used to fit the pixel size of the photo-detector (2 × 2 mm^2) within the alignment precision of 0.2 mm, whereas those of 1.2 mm diameter are used for the outer detector (OD), which is the two strips at the edge of each plane. The fibers are double-clad type to give a maximum trapping fraction for green light. the inner core is polystyrene with the WLS flour of 200 ppm (refractive index $n_1 = 1.59$), a thin intermediate layer is acrylic ($n_2 = 1.49$), and the thin outer cladding is a polyflour ($n_3 = 1.42$). The green light with reflective angle less than 26.7 degree is trapped and transported along the fiber. Before the installation, the attenuation length of all WLS fibers were measured around 350 cm by using blue LED lights [27]. In addition, it was checked by cosmic rays after the installation.

Each 64 WLS fibers were bundled with an alignment fixture, “cookie” [28], to attach the photo-detector (64-pixel MA-PMT) as shown in Fig. 4.6. After glued WLS fibers with a cookie by epoxy resin, the surface of cookie was polished by a diamond blade. The cookie holes are precisely aligned with 64 pixels on the MA-PMT. The fiber bundle and MA-PMT were connected with alignment pins on the cookie and cookie holder attached to MA-PMT. The fibers were aligned to pixels on the MA-PMT within 0.2 nm precision.

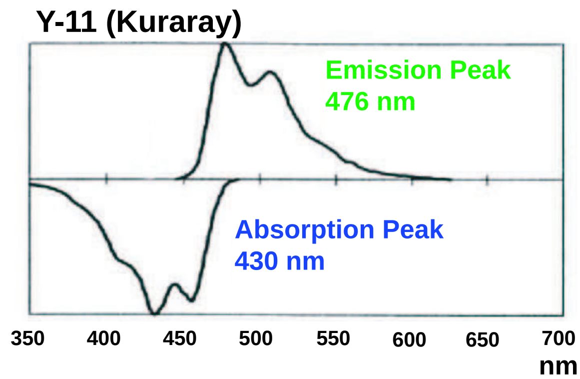

Figure 4.5: Absorption and emission spectrum of a Y-11 WLS fiber.

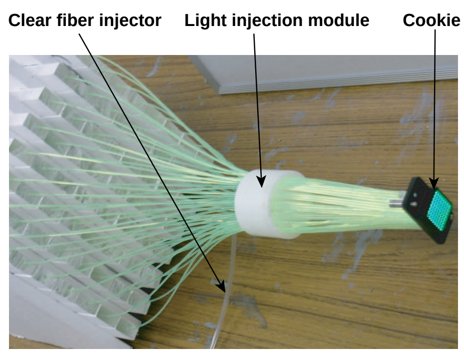

Figure 4.6: A picture of the fiber bundle.

4.3.3 Photo sensor

The 64-pixel MA-PMTs manufactured by Hamamatsu Photonics are used for a photo-sensor of the SciBar detector. MA-PMT has the same performance as H8804, whose package is modified to fix with cookie and the front-end electronics. The specifications of MA-PMT is summarized in Table 4.3. A cross-talk with a 1.5 mm diameter fiber is measured to be 4% for adjacent pixels and 1% for othogonally opposite pixels. The pixel-to-pixel gain uniformity is measured to be 21% in RMS. The high voltage value was adjusted so that the average gain is 6×10^5. With this gain, the response linearity within 5% up to the input signal of 200 photo-electrons was obtained. The single-anode PMTs are used for the photo sensor of OD, which read every 64 fibers together.

4.3.4 Gain monitor

The gain of all the MA-PMT channels was monitored by the gain monitor system during the detector operation [29]. 64 WLS fibers were assembled with "light injection module" to illuminate LED light uniformly as shown in Fig. 4.6. A blue LED was used as a light source, and pulsed blue light was distributed to each fiber bundle through a clear fiber (1 mm diameter). In order to measure the light intensity of each pulse, the LED also illuminated a pin photo-diode and a 2 inch PMT which was calibrated by an Am-NaI stable light source. By comparison with the MA-PMT outputs and the pin photo-diode or the 2 inch PMT, the relative gain drift is measured with 0.1% precision. The performance

Table 4.3: Specifications of the MA-PMT.

Photo-cathode	Bi-alkali
Quantum efficiency	12% for 500 nm photons
Number of pixels	64
Pixel size	2×2 mm^2
Typical gain	6×10^5 at ~ 800 V
Response linearity	200 p.e. at PMT gain of 6×10^5
Cross talk	4% (adjacent pixel)
Number of MA-PMTs	224

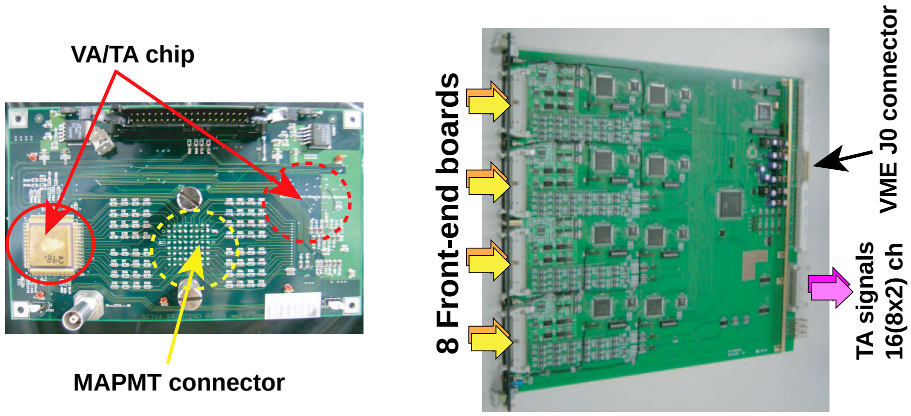

Figure 4.7: Pictures of the front-end board (left) and DAQ board (right).

of the gain correction is discussed in Section 4.5.3.

4.3.5 Readout electronics

The readout electronics, the front-end board (FEB) and the DAQ board [84], was developed to deal with 15,000 readout channels of the SciBar detector, as shown in Fig. 4.7. The FEB board was directly connected to a MA-PMT, which reads the signals with VA/TA chips developed by IDEAS. Since one VA/TA chip has 32 inputs, a pair of VA/TA's was mounted on the FEB. The model numbers of VA and TA are VA32HDR11 and TA32CG, respectively. The DAQ boards is 9U VME modules, which were developed to control FEBs and read charge and timing information. Since one DAQ board controls eight FEBs that corresponds to 512 channels, all the channels in SciBar detector (14,336 channels) can be read by only 28 DAQ boards.

Signals from MA-PMT are read by the VA/TA chips on FEBs. TA makes an OR-ed signal over 32 channels, which produces a narrow pulse peak with a duration time of 80 nsec and discriminates signal at a threshold given by the DAQ board. The threshold was set to 0.7 photo-electron equivalent. The VA amplifies the PMT signals and shapes them into slowly rising signals, whose peaking time is 1.2 μsec. If the DAQ board receives the TA signal, it provides a hold signal to VA, by which its pulse height proportional to a PMT charge is kept for reading. Just after holding, the DAQ board sends readout

Table 4.4: Basic quantities of the SciBar readout system.

VA/TA chip (at PMT gain of 6×10^5)		AMT	
Shaping time	VA : 1.2 μsec	TDC resolution	0.78 nsec
	TA : 80 nsec	TDC full range	50 μsec
Noise level	0.3 p.e.		
Response linearity	300 p.e.		
TA threshold	0.7 p.e.		

pulses and receives the pulse heights from VA one by one. Finally, the flush ADC on the DAQ board digitizes the VA outputs. If the PMT gain is 6×10^6, the VA output is sufficiently linear up to 300 photo-electrons and the noise level was measured to be 0.3 photo-electron level.

TA signals were also sent to time-to-digital converters (TDC) and cosmic ray trigger boards. The AMT board developed by the ATLAS TGC group [31] was used as a TDC module, which has multi-hit capability with timing resolution of 0.78 nsec and 50 μsec in full range.

The basic quantities of the system are summarized in Table 4.4.

4.3.6 Electro-magnetic calorimeter

To study $\nu_\mu \rightarrow \nu_e$ oscillation, the ν_e contamination in a beam and π^0 production from neutrino interaction are dominant backgrounds. Detection of electro-magnetic shower is required to study ν_e and π^0 events. The scintillator part of SciBar covers only four radiation length (X_0) along the beam direction. It is not sufficient to measure an energy of electrons and photons around 1 GeV. Therefore, an electro-magnetic calorimeter (EC) was installed downstream of the scintillator part. EC is an array of “spaghetti modules” [32] which were used for the CHORUS experiment [33]. Fig. 4.8 shows a schematic drawing of EC. EC is made of scintillator fibers and lead sheets. Scintillating fibers of 1 mm diameter are embedded in grooves on the 1.9 mm thick lead sheets. The module consists of a pile of 21 layers with 740 scintillating fibers. The pile has the dimensions of $4.0 \times 8.2 \times 262$ cm^3, which is kept together by a steel box. On the both sides, fibers are arranged in two groups, which correspond to 4×4 cm^2 cross-section. Each fiber group is read by a 1 inch PMT. EC is composed of a vertical plane (32 modules) and a horizontal plane (30 modules), providing an additional 11 X_0 along the beam direction. The energy resolution of EC is $14\%/\sqrt{E_e(\mathrm{GeV})}$, where E_e is electron energy.

4.4 Data acquisition system

Four types of data (beam, pedestal, LED, and cosmic) were taken for the SciBar detector, whose timing diagram is shown in Fig. 4.9. The neutrino beam was produced every 2.2 seconds at 1.1 μsec duration pulse. The timing of beam triggers was provided by the accelerator. After the beam trigger, one pedestal and one LED triggers were generated. Until 1.5 seconds after the beam, the cosmic ray data was taken, whose trigger signal was made by the trigger boards. The cosmic ray data was collected approximately 15 events per spill. The LED and cosmic ray data are used to monitor the PMT gain and the light yield. The cosmic ray data is also used for the calibration of timing information as described in Section 4.5.1. Trigger timing and its type is managed by timing distributors. Specification of the trigger board and the timing distributor is described as follows.

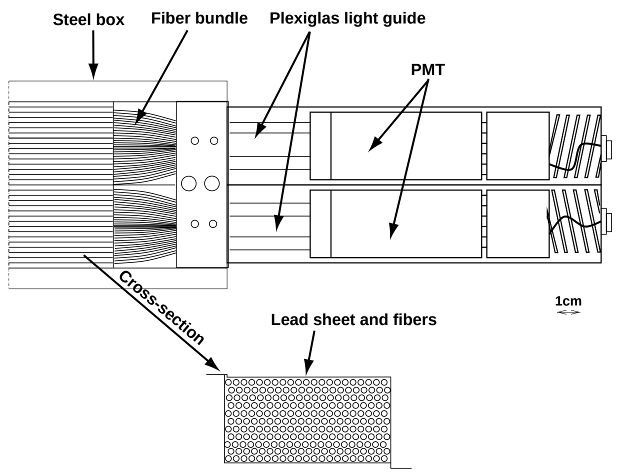

Figure 4.8: The time difference between adjacent TQ channels along a cosmic ray track after TQ correction. The standard deviation of the fitted Gaussian is 1.9 nsec.

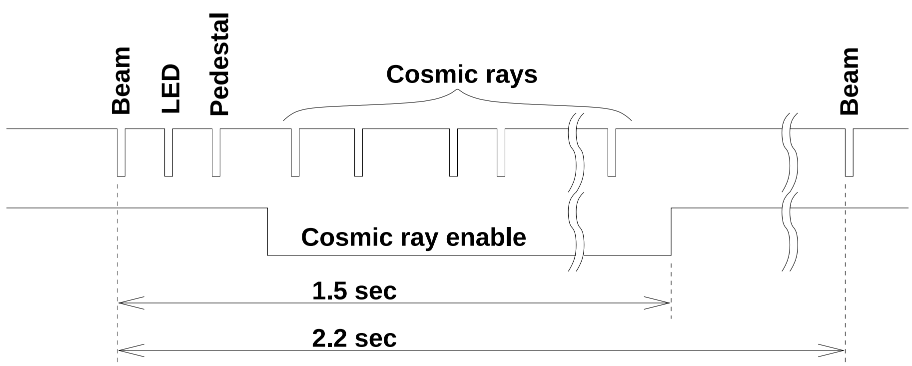

Figure 4.9: The time difference between adjacent TQ channels along a cosmic ray track after TQ correction. The standard deviation of the fitted Gaussian is 1.9 nsec.

Trigger board

Cosmic rays were used for energy calibration, timing calibration, cross checks of the gain monitor system in the SciBar detector. Since the trigger system must handle many timing signals, it should have flexibility so that the trigger logic can be easily modified. To achieve the requirements, the trigger board was developed, which is a 9U standard VME module as shown in Fig. 4.10 (left) [34]. The trigger board has 128 ch inputs and one FPGA (Field Programmable Gate Array) to implement trigger logic. A schematic diagram of the cosmic ray trigger is shown in Fig. 4.11. The TA channels were arranged in 8×28 for each projecting plane. The trigger board receives the signals from every other TA layers. It was programmed to make a trigger when a cosmic ray penetrates all the layers. Fig. 4.12 (left) shows an event display of the cosmic ray event. The trigger conditions can be changed easily by modification of the program implemented in FPGA. For example, stopping muon events can be taken as shown in Fig. 4.12 (right).

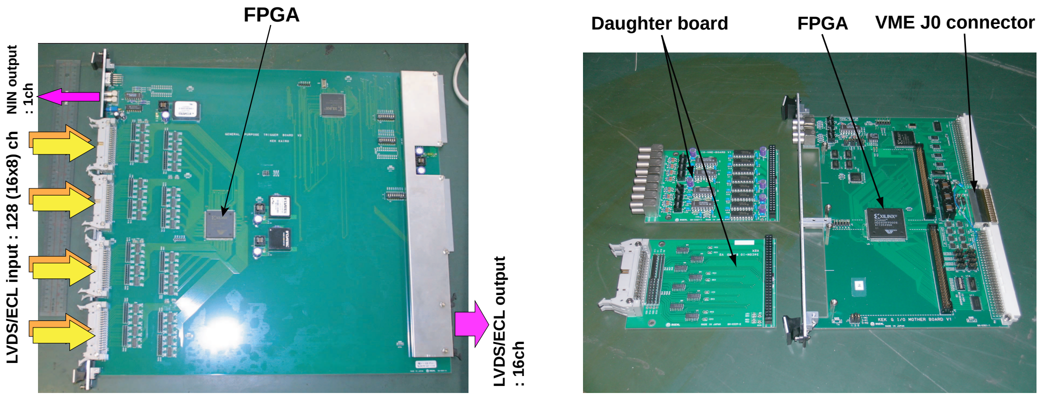

Figure 4.10: Pictures of a trigger board (left) and a timing distributor (right).

Timing distributor

The trigger timing was distributed to the DAQ boards and AMTs by the timing distributor, which are 6U VME modules as shown in Fig. 4.10 (right). A timing distributor consists of one mother board and two daughter boards which were attached to the mother board. One daughter board has sixteen channels of the NIM connectors, which can be changed the inputs or outputs by toggle switches. The trigger signal and the trigger ID are read by NIM inputs and controlled by using FPGA. These signals are distributed to the DAQ boards through VME J0 bus lines and AMTs by NIM outputs. The other board has two 16 channel ECL/LVDS inputs, which read an event count provided by the VME-TRG module.

4.5 Basic performance

4.5.1 Timing resolution

Timing resolution is estimated by using cosmic ray data. Fig. 4.13 (left) shows a timing difference between the adjacent TA channels as a function of ADC channels which correspond to the amount of charges. Since the timing information has correlation with charge, the TQ correction was applied. The light velocity in a fiber was also estimated. Fig. 4.13 (center) shows a timing after the TQ correction as a function of their position along the fiber for one TA channel. From this measurement, average light velocity in a fiber is estimated as 17.1 ± 0.3 cm/nsec. After TQ correction and subtraction of the light propagation time in a fiber, An average timing resolution of 1.3 nsec was obtained, as shown in Fig. 4.13 (right).

4.5.2 Dead channel

A number of the dead channels were checked by the gain monitor system. There are only six dead channels. A fraction of the active channel is 99.96% ($= 1 - 6/14,336$) for K2K-IIb. Since five dead channel is in two MA-PMTs, these MA-PMTs were replaced during the shutdown period between K2K-IIb and K2K-IIc. Therefore, the fraction of the active channel become 99.99% ($= 1 - 1/14,336$) for K2K-IIc.

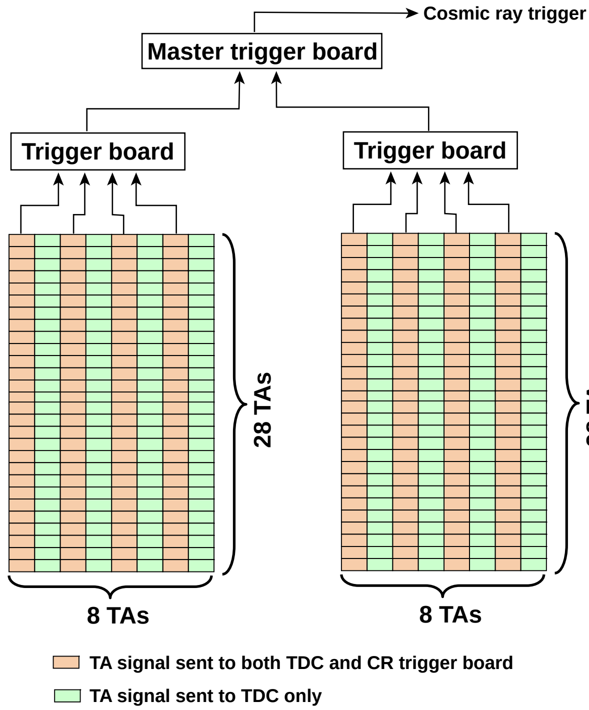

Figure 4.11: Schematic diagram for cosmic ray trigger.

4.5.3 Light yield

The light yield was measured by using cosmic ray data. A typical light yield of the strip is shown in Fig. 4.14(a). The path length in each cell and the attenuation of the fiber were corrected.

Fig. 4.14(b) shows the distribution of the mean light yield for each cell. The average light yield is 18 photo-electrons for a muon track of 1 cm long, which corresponds to 9 p.e./MeV. The time variation of the light yield was also checked by cosmic ray data. The light yield is stable within 0.7% level after the PMT gain correction with the monitor system.

4.5.4 Momentum scale

Momentum scale in SciBar is studied in beam test, T551 at KEK T1 beamline, by using test-SciBar detector. Fig. 4.15 shows the ratio of proton range between data and MC simulation as a function of the momentum. It is consistent within 1% with data and MC simulation.

4.5.5 Particle identification

The Proton/Muon(Pion) separation was performed by using the information of the energy deposit in the scintillator strips. As the index of the particle type, the muon confidence level (MuCL) function was defined with the energy deposit in each scintillator plane. The distribution of muon (pion) energy deposit in each scintillator plane is obtained by cosmic-ray muons as shown in Fig. 4.16 (top). Integrating the distribution from right to left, the fraction of events above a particular energy deposit can be calculated as shown in Fig. 4.16 (bottom), which is defined as a MuCL for one plane. Since the energy deposit in

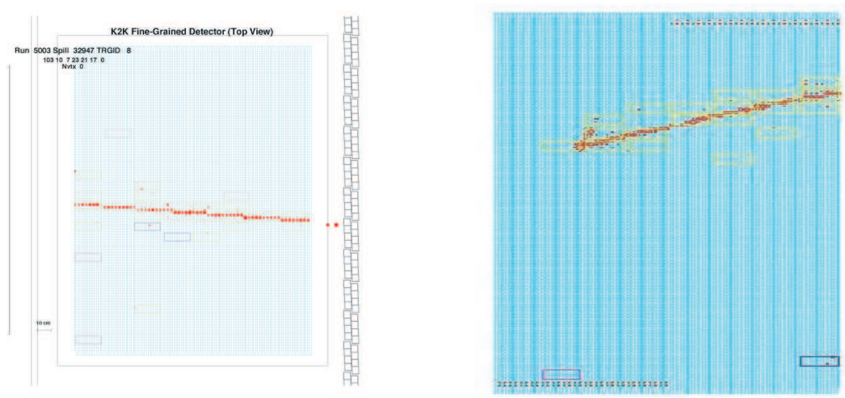

Figure 4.12: Event display of through cosmic ray muon, through going muon (left) and stopping muon in SciBar (right).

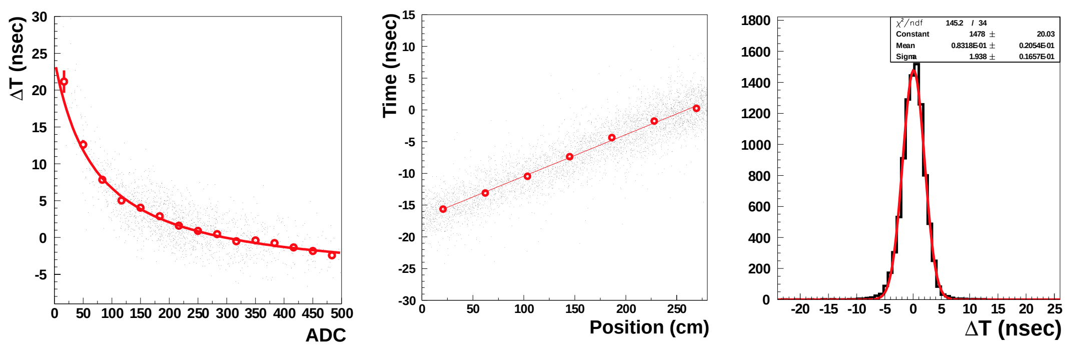

Figure 4.13: (left) Relation between ΔT and the amount of charges , where ΔT the time difference between adjacent TA channels. (center) The timing after TQ correction as a function of their position along a fiber for one TA channel. (right) The time difference between adjacent TQ channels along a cosmic ray track after TQ correction and subtracting the light propagation time in a fiber. The standard deviation of the fitted Gaussian is 1.9 nsec. In this case, the timing resolution is 1.4 $(= 1.9/\sqrt{2})$ nsec.

a scintillator strips by protons is larger than that of muons, value of MuCL for protons become smaller. Therefore, a proton and a muon (pion) can be separated by using MuCL function.

To use the information from all planes, we combine the MuCLs obtained by all planes. All MuCLs obtained are sorted sequentially from bigger one, and truncated CLs of 20% from the larger ones and that of 50% from the smaller ones to avoid the effect from inefficiency of scintillator and track overlapping in one view. Therefore, 30% in the all MuCL are used to make the final MuCL function. Finally, MuCL function is expressed as

$$MuCL = \prod_i CL_i \times \sigma_j \frac{(-\ln \prod_i CL_i)^j}{j!}, \tag{4.1}$$

where CL_i is a MuCL of the i-th plane.

The MuCL values for muons distribute close to 1, and those for protons distribute close to 0. If we require 90% efficiency for protons, the muon miss-identification probability is 1.7%.

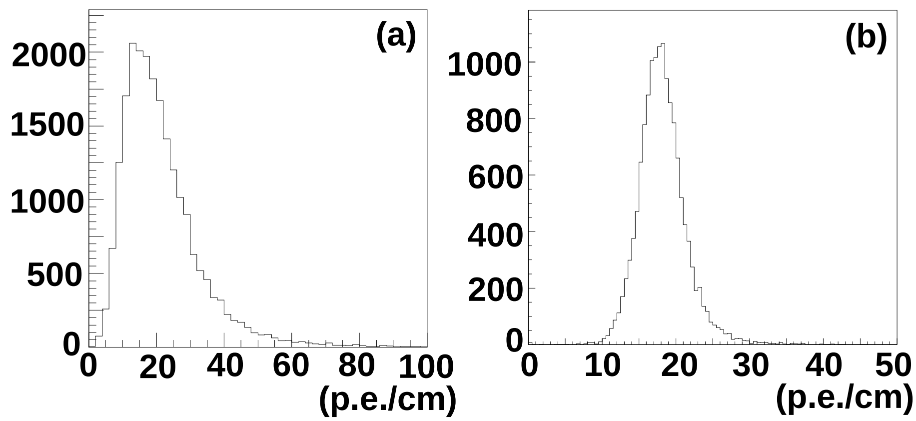

Figure 4.14: (a) A typical light yield of a strip. The path length in each cell and the attenuation of the fiber are corrected. (b) The mean light yield of each strips.

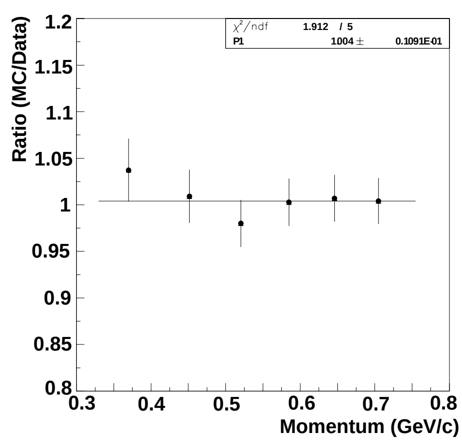

Figure 4.15: Ratio of proton range between data and MC simulation as a function of the momentum. It is consistent within 1% with data and MC simulation. Systematic error of momentum scale for SciBar is 1% with momentum measurement by the range.

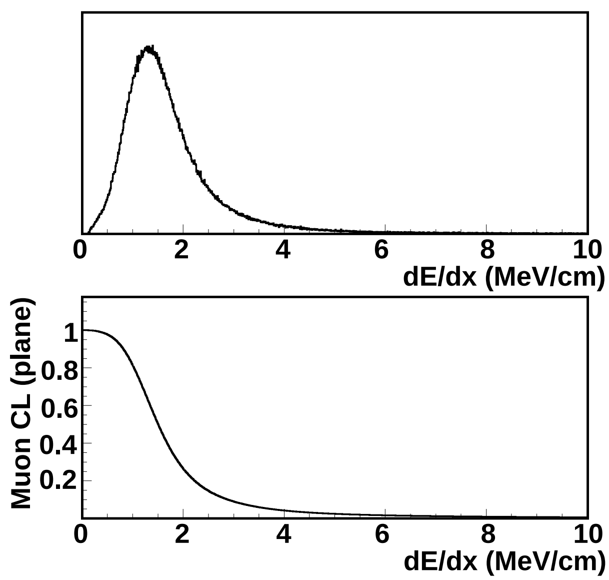

Figure 4.16: A distribution of the energy deposit in scintillator strips of cosmic ray muons (top), and the muon confidence level as a function of energy deposit in each scintillator plane (bottom).

Chapter 5

Monte Carlo Simulation

Monte Carlo (MC) simulations for the K2K experiment consist of three parts, which are the neutrino beam simulation (Beam-MC), neutrino interaction simulation (Neut-MC), and detector simulation (Detector-MC). In this chapter, the components of these simulation tools are described.

5.1 Neutrino beam simulation

The MC simulation for the neutrino beam (Beam-MC) reproduces the primary proton beam, the secondary meson production in the target, and the decay of secondary mesons into neutrinos.

5.1.1 Secondary pion production

There are various pion production experiments in the energy region of the K2K experiment, whose results are inconsistent with each other. That remains the possibility of some kinds of the MC simulation for the application. From this reason, the following three kinds of pion production models are compared.

- **GCALOR/FLUKA model** [38, 39]
  The package of hadron simulation provided in a GEANT simulation [40].

- **Sanford-Wang model**
  This is an experimental parameterization with the compilation of Lundy *et al.* [41], Dekkers *et al.* [42], and Baker *et al.* [47]. Yamamoto's measurements [84] agrees well with this model.

- **Cho-ANL and Cho-CERN compilation**
  The Cho-ANL compilation [85] is the fitting results of the Sanford-Wang formula with several experimental data [87, 85, 88, 89]. The another result of compilation, which gives almost the same differential cross-section with Cho-ANL compilation, is Cho-CERN [86] compilation.

Since the PIMON measurements favor the Cho-CERN model, it is selected as the standard pion production model. However, the other models are also consistent with the PIMON measurements within their errors. They are used for systematic error estimation.

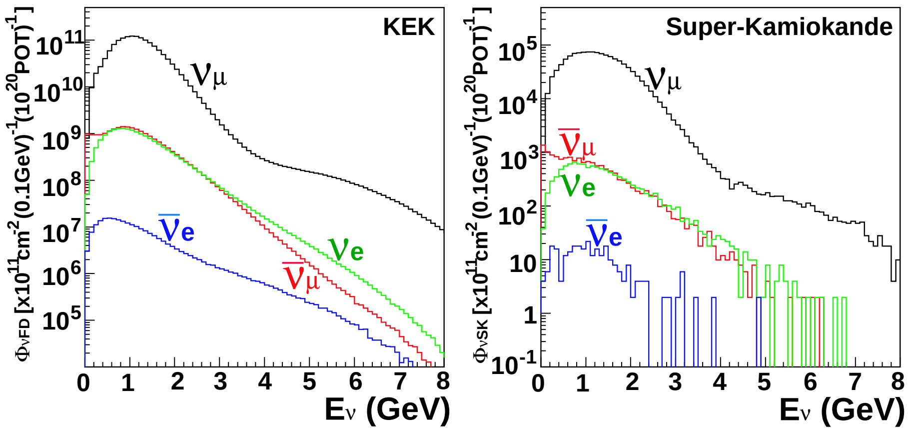

Figure 5.1: Neutrino energy spectrum of each neutrino type for near and SK site with the horn current of 250 kA.

5.1.2 Simulation in the horn magnets and the decay volume

GEANT with the GCALOR hadron simulator is used to trace survived primary protons and generated secondary particles. It simulates the particles' behavior in the two horn magnets and the decay volume until their decay or absorption in a material. The focusing effect of the magnetic field is also simulated. The decay channels and kinematics of pions, kaons, and muons are computed by our original codes.

5.1.3 Neutrino energy spectrum

Since the decay tunnel have the finite volume against the near site, the energy spectrum are different between near and far sites. Fig. 5.1 shows the energy spectrum of each neutrino type for near and SK site with the horn current of 250 kA. The fraction of ν_μ, ν_e, $\bar{\nu}_\mu$, and $\bar{\nu}_e$ at Super-Kamiokande are 97.9%, 0.9%, 1.2% and 0.02%, respectively.

5.2 Neutrino interaction simulation

"NEUT" [44] is used for the Monte Carlo simulation of neutrino interactions, which is originally developed in the atmospheric neutrino analysis in SK [45]. NEUT generates the final state particles from neutrino-nucleus interaction. The target materials are H_2O for water Cherenkov detectors and SciFi, and $(CH)_n$ for SciBar.

Neutrino interaction channels are summarized as follows.

- CC quasi-elastic scattering $\nu + N \to l^- + N'$ ($\sim$ 27%)
- NC elastic scattering $\nu + N \to \nu + N$ ($\sim$ 13%)
- CC resonance production $\nu + N \to l^- + N' + \text{meson}$ ($\sim$ 28%)
- NC resonance production $\nu + N \to \nu + N' + \text{meson}$ ($\sim$ 10%)
- CC multi-pion production $\nu + N \to l^- + N' + \text{hadrons}$ ($\sim$ 14%)

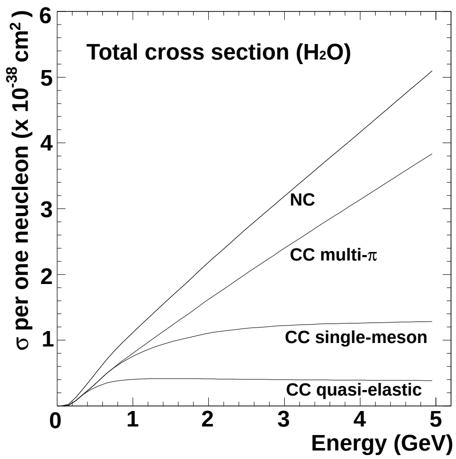

Figure 5.2: The cross-section of each neutrino interaction channel in water as a function of incident neutrino energy, which is calculated by NEUT. The CC resonance production and CC coherent pion production modes are assorted into "CC single-meson".

- NC multi-pion production $\nu + N \to \nu + N^{-} + \mathrm{hadron}$ ($\sim 4\%$)
- CC coherent-pion production $\nu +^{16}\mathrm{O}(^{12}\mathrm{C}) \to l^{-} +^{16}\mathrm{O}(^{12}\mathrm{C}) + \pi^{+}$ ($\sim 2\%$)
- NC coherent-pion production $\nu +^{16}\mathrm{O}(^{12}\mathrm{C}) \to \nu +^{16}\mathrm{O}(^{12}\mathrm{C}) + \pi^{0}$ ($\sim 1\%$)

where N and N' show nucleons and l^{-} shows a charged lepton. The fraction of each mode is also shown in the parentheses. Fig. 5.2 shows the cross-section of each interaction mode with water, obtained by NEUT. The model of each interaction mode is described in the following sections.

5.2.1 CC quasi-elastic scattering and NC elastic scattering

The charged-current quasi-elastic (CC-QE) and neutral-current elastic (NC-el) interactions are two-body scattering on a nucleon. Their simulations are based on Llewellyn Smith's formula [90]. Since the neutrino interacts with nucleus through the V-A weak interaction, the cross-section is written by the combination of the vector form factors and the axial form factor as shown in Eq. B.12. The axial form factor (F_A) is given by

$$F_A(Q^2) = \frac{-1.23}{\left(1 + \frac{Q^2}{M_A^2}\right)^2}, \tag{5.1}$$

where M_A is the axial vector mass and Q^2 is a four-momentum transfer. Although the past electron-nucleon and neutrino-nucleon scattering experiments give 1.0-1.1 GeV/c for M_A of (quasi-)elastic scattering [91], 1.11 GeV/c is employed from our previous analysis [81, 82].

The Fermi motion and Pauli blocking effect are considered for the target nucleons bound in ^{16}O or ^{12}C. The Fermi gas model is adopted to reproduce the Pauli blocking effect. The final nucleon momentum is required to be larger than the Fermi surface momentum (225 MeV/c in ^{16}O and 217 MeV/c in ^{12}C), which is estimated by an electron-^{12}C scattering experiment [50]. The cross section depends on the target nucleus because of the Pauli blocking effect. The difference of the cross section between ^{16}O and ^{12}C is less than 1.5% in the neutrino energy region of $E_\nu > 0.5$ GeV.

5.2.2 Resonance production channel

The resonance production interaction produces one lepton and one pion which intermediates a baryon resonance state N* as

$$\begin{aligned} \nu + N &\rightarrow l^- + N^* \\ N^* &\rightarrow N' + \pi(\eta, K). \end{aligned} \tag{5.2}$$

This is the dominant process when the invariant mass of the hadron system is less than 2 GeV/c^2.

The simulation of the resonance production mode is based on the Rein-Sehgal model [52]. Although the cross-section with $M_A = 1.11$ GeV/c^2 is approximately 10% higher than that with $M_A = 1.01$ GeV/c^2, it is consistent with the past experiments. Therefore, M_A of 1.11 GeV/c^2 is employed for our MC simulation.

5.2.3 Coherent pion production

The charged-current (CC) coherent pion production in neutrino-nucleus scattering, $\nu_\mu + A \rightarrow \mu^- + \pi^+ + A$, is a process in which the neutrino scatters coherently off the entire nucleus with a small energy transfer. Since the measurement by SciBar in the K2K experiment is consistent with the non-existence of CC coherent pion production in the energy region of a few GeV, it is removed from our MC simulation.

5.2.4 Deep inelastic interaction

The charged current deep inelastic scattering (CC-DIS) produces more than one meson with the invariant mass of the hadronic system greater than 1.3 GeV/c^2. The cross-section of CC-DIS is calculated based on Bjorken scaling [65] with modification by Bodek and Yang [67]. The cross-section of the NC deep inelastic scattering is calculated by scaling the that of CC-DIS according to the experimental results [72].

5.2.5 Nuclear effects

Mesons and nucleons generated in the neutrino interactions often cause secondary interaction with nucleons ("nuclear effect") before leaving ^{16}O or ^{12}C nucleus. The nuclear effects of pions, nucleons, and Δ resonance are considered in NEUT. The position of neutrino interaction in a nucleus is calculated by using the Wood-Saxon type density distribution, which is defined as

$$\rho(r) = \frac{Z}{A}\rho_0 \left\{ 1 + \exp\left(\frac{r-c}{a}\right) \right\}^{-1}, \tag{5.3}$$

where $\rho = 0.48 m_\pi^3$, $a = 0.41$ fm, and $c = 2.69$ fm are used for our simulation. The nuclear effect is taken into account as follows.

Pion

The nuclear effects for pions are classified into inelastic scattering, charge exchange, and absorption. The cross-section is calculated by the model of L. L. Salcedo *et al.* [73]. The Fermi motion and the Pauli blocking effect of nucleons are taken into account in the similar way as the CC-QE interaction.

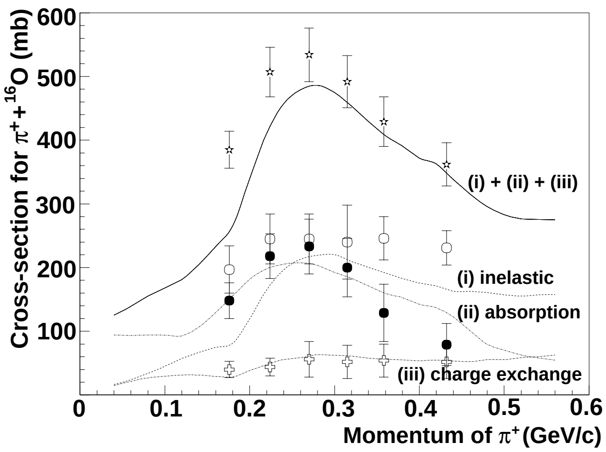

Figure 5.3: The cross-section of π^+-^{16}O interactions. The lines shows the results of our calculation based on [73], and the symbols show the experimental data [74].

Fig. 5.3 shows the calculated π^+-^{16}O interaction cross-section together with experimental data from C. H. Q. Ingram *et al.* [74]. Since uncertainties in the past measurements are approximately 30%, a systematic error of 30% is assigned on the nuclear effect for pions.

Nucleon

The cross-section of nucleon-nucleon elastic scattering implemented in NEUT is based on the measurement by H. W. Bertini [75], which is used in GCALOR. The pion production interaction is also taken into account, according to the isobar production model by S. J. Lindenbaum *et al.* [76].

The effect of these models are compared with the past experiment by K. V. Alanakian *et al.* [77], which measured the yield of scattered protons in electron scattering on a ^{12}C target. This experiment is reproduced with NEUT by replacing the incident electron by an electron neutrino. Since a number of scattering protons are generated 10% larger than the measurement in NEUT, the nuclear effect for nucleons is rescaled by multiplying 0.9 to the cross-section, and the error of 0.1 is assigned to the factor.

Δ resonance

Approximately 20% of the Δ resonance are lost by the absorption effect [78]. The absorption is taken into account.

5.3 Detector simulation

Particles generated by NEUT are processed by a detector simulator, in which GEANT-3.2.1 package is used. The materials of each detector component are implemented in the code. DetSim reproduces the passage of a particle through a matter, and simulates the detector response.

Chapter 6

Charged-Current Event Selection in SciBar

6.1 Overview of SciBar event selection

In this chapter, neutrino event selection in SciBar is described. The neutrino energy spectrum is measured by using charged-current (CC) interaction, especially charged-current quasi-elastic (CC-QE) interaction. Therefore, muon tracks from SciBar are selected as SciBar CC event sample. In addition, the selection of the low energy neutrino events is required since the neutrino oscillation effect becomes large in the low energy region below 1 GeV, assuming the oscillation parameters indicated by the atmospheric neutrino oscillation.

The procedure of the event selection is summarized as follows.

1. **Track reconstruction :**
   Tracks are reconstructed after requiring the hit definition in SciBar.

2. **Selection of the neutrino events in SciBar :**
   The selection of tracks is performed to identify neutrino interactions inside SciBar. In this procedure, particles from the outside of SciBar are rejected effectively.

3. **CC event selection :**
   CC events are selected from the neutrino event samples. Two event categories, “SciBar-contained events” and “SciBar-exiting events”, are defined for SciBar data, according to whether the track stops inside SciBar or exits from SciBar.

4. **Event classification for the spectrum measurement :**
   SciBar-exiting events and SciBar-contained events, are used for the spectrum measurement by SciBar. They are divided into four event samples, which are“1-track sample”, “2-track CC-QE enriched sample”, and “2-track nonQE enriched sample” for SciBar-exiting events, and “SciBar-contained sample” for SciBar-contained events.

In the following section, each selection procedure is described in detail.

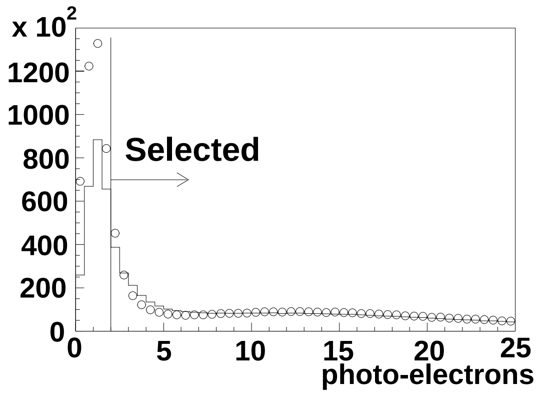

Figure 6.1: Distribution of a number of photo-electrons for SciBar hits. The open circle shows data and the solid line shows MC simulation. The MC distribution is normalized by the entries from 2 to 25 photo-electrons.

6.2 Track reconstruction

The track reconstruction is performed by using hit information in SciBar. At first, requirement for real hits is defined to identify from the fake hits. After that, a track is reconstructed by the tracking code with the cellular automaton tracking algorithm. The track reconstruction procedure of SciBar is summarized as follows.

6.2.1 Hit definition

To identify the real hits on scintillator strips from the fake hits, the hit selection of SciBar is defined. At first, the hits greater than three standard deviation of the pedestal distribution, are selected.

An MA-PMT used in SciBar has cross-talk around a hit channel. For the rejection of the fake hits by the cross-talk, a cross-talk correction is applied. Since the MA-PMT has 64 channels, the cross-talk is expressed by a linear transformation of a 64×64 matrix. Therefore, the cross-talk is corrected by its inverse transformation. We represents 2.8% cross-talk to adjacent pixels, and 0.7% to diagonal pixels. Figure 6.1 shows the distributions of a number of photo-electrons after the cross-talk correction. Finally, a threshold is set at 2.0 photo-electrons to reject fake hits which exist in the small photo-electron region in Fig. 6.1.

6.2.2 Track reconstruction

A cellular automaton tracking (CAT) algorithm is used to look for two-dimensional (2D) tracks in each projecting plane. After searching for the hit clusters, they are fitted with a straight line by a least square method. A couple of 2D tracks are combined into a three-dimensional track, if they satisfy the requirements to their edge position along the beam axis and timing. The detail of tracking method is described in [36].

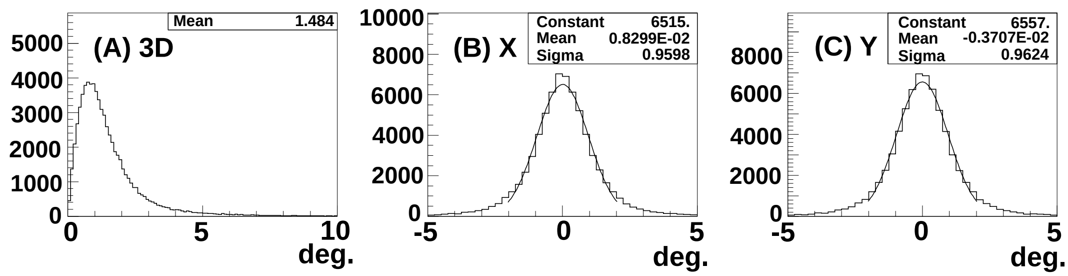

Figure 6.2: The angle difference between the true muon direction obtained by the MC simulation and the reconstructed muon direction for three-dimensional view (A), and the projection to X-view (B) and Y-view (C), respectively.

6.2.3 Tracking performance

Angular resolution

The angle between the reconstructed muon direction and the true direction is shown in Figure 6.2. The three-dimensional angular resolution of the muon is 1.6 degrees, where the resolution is defined as one standard deviation. We also define the two-dimensional angular resolution of the muon as the standard deviation of Fig. 6.2 (B) and (C), which is 1.0 degree.

The systematic error on the angular measurement is estimated by comparing the direction of a SciBar track with a MRD track. The average of the angular difference between SciBar track and the MRD track is 0.19 degree for X projection and 0.06 degree for Y projection.

Tracking effi ciency

Muon tracks from SciFi are used to check tracking efficiency of SciBar. Tracks exiting from SciFi are required to match his on TGC, and the starting point must be in the upstream half of SciFi to avoid the mis-fitting of the SciFi track finder. If the extrapolated track from SciFi matches with the hits on both the first layer and the fifth layer of SciBar, the track is identified as a muon from SciFi. The position difference between the extrapolated track from SciFi and the SciBar hit, is required to be less than 50 cm on each projection. We define $N_{\mathrm{SF}\to\mathrm{SB}}$ as a number of these events. We look for a reconstructed track in SciBar matching to the SciFi track. The matching condition is that the distance between the extrapolated SciFi track and the start point of a SciBar track should be less than 50 cm, and the angle difference is less than 0.4 radian. A number of events with SciBar tracks matching with SciFi track is defined as N_{SB}. The tracking efficiency is defined as $N_{\mathrm{SB}}/N_{\mathrm{SF}\to\mathrm{SB}}$. The track finding efficiency of the particle passing through more than four layers of SciBar is estimated to be 99.2%.

The track finding efficiency for neutrino events is also estimated by using the MC simulation. We use the ratio between a number of the true hits and that of the hits used for the track reconstruction. The MC tracks with the ratio above 0.7 are judged as the reconstructed tracks. The track finding efficiency is defined as the percentage of the reconstructed tracks and estimated as 89.3%. Figure 6.3 shows the track finding efficiency as a function of the number of layers for muons, protons and charged pions. Since most of the charged particles are generated from a common vertex, the track finding efficiency for short tracks decreases due to the overlapping of the tracks.

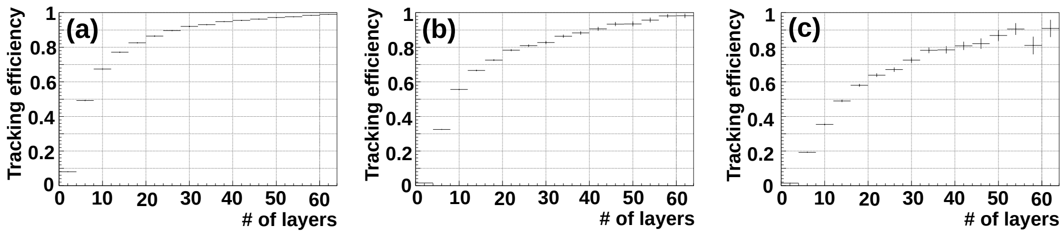

Figure 6.3: A tracking efficiency as a function of a number of layers for muons (a), protons (b), and charged pions (c). Only the statistical error is assigned to the error bar.

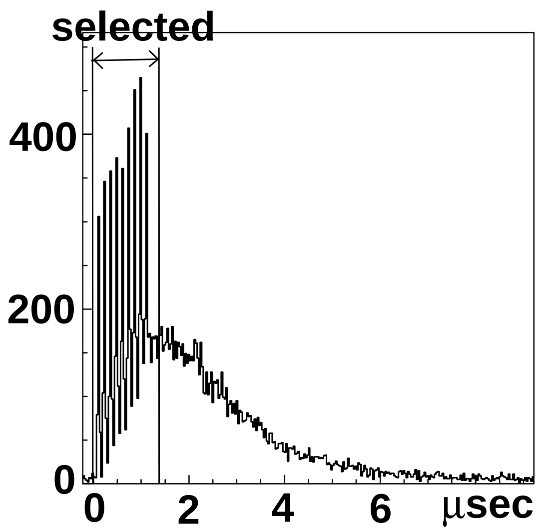

Figure 6.4: A timing distribution of SciBar tracks. The micro-bunch structure of the beam is clearly seen. The events of $-0.1 < t < 1.3$ μsec is selected as a beam timing window. The sky-shine backgrounds are seen in the beam spill.

6.3 Selection of neutrino interactions in SciBar

6.3.1 Timing cut

Fig. 6.4 shows a timing distribution of SciBar tracks. We select the events within beam spill window of $-0.1 < t < 1.3$ μsec. Here, the origin of the time (t) is defined as roughly 0.1 μsec before the first bunch. The peak of events after the bunch timing is seen in Fig 6.4. They are called sky-shine backgrounds [37], which are thought to be induced by neutrons from the production target, decay volume, and other components on beam line. The details on the sky-shine background are described in Section 6.4.2.

6.3.2 First layer veto

A particle which is generated by a neutrino interaction or a cosmic ray, often comes from upstream of SciBar. In order to select neutrino events in SciBar, we require no hits on the most upstream layer of SciBar. If there are any hits above five photo-electrons on either X-plane or Y-plane of the first layer,

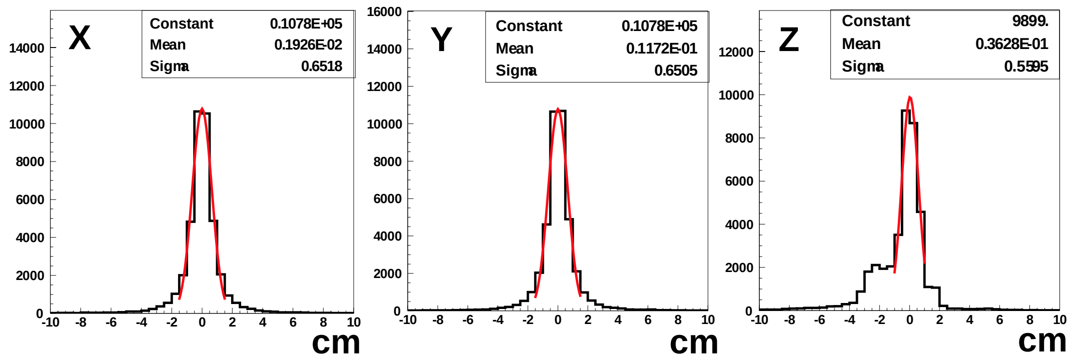

Figure 6.5: Distributions of the distance between a true vertex and a reconstructed vertex for the MC simulation.

Table 6.1: Reduction summary for SciBar data.

	Data	MC			
		Total	CCQE	CC-nonQE	NC
Beam spill	190,523	147,118	48,160	58,820	40,138
SciBar track existing	92,938	118,371	44,026	53,379	20,966
Timing cut	92,759	118,350	44,025	53,364	20,961
First layer veto	47,986	113,662	42,745	50,850	20,067
Vertex cut	27,680	82,449	30,417	37,080	14,952

we do not use any tracks within 50 nsec from the hits.

By using the reconstructed tracks in SciBar, the rejection performance of the incoming particles is estimated to be 99.6%. According to the MC simulation, 2.7% of neutrino events are lost by the first layer veto, owing to backward scattering particles.

6.3.3 Vertex reconstruction

The starting point of a SciBar track is defined as a vertex of the neutrino interaction. The vertex is required to be inside the fiducial volume which is defined by 260 cm (height) $\times$ 260 cm (width) $\times$ 135.2 cm (depth), corresponding to the target mass of 9.38 tons.

Figure 6.5 shows the distance between a true vertex and a reconstructed vertex by using the MC simulation. The resolution for X and Y view is almost the same as the expectation, which is $2.5/\sqrt{12} \sim 0.7$ cm. However, the Z resolution is worse than the expectation, which is $1.3/\sqrt{12} \sim 0.4$ cm, and the second peak is observed in the upstream. The discrepancy is explained by the cross-talk of the MAPMTs. Since the light yield at the vertex position becomes large by the energy deposit of protons, the fake hits at the upstream cells caused by the cross-talk are reconstructed as the vertex.

6.3.4 Summary of the neutrino event selection in SciBar

The reduction summary of the neutrino event in SciBar is shown in Table 6.1. In total, 27,680 events are selected as the neutrino interactions in SciBar.

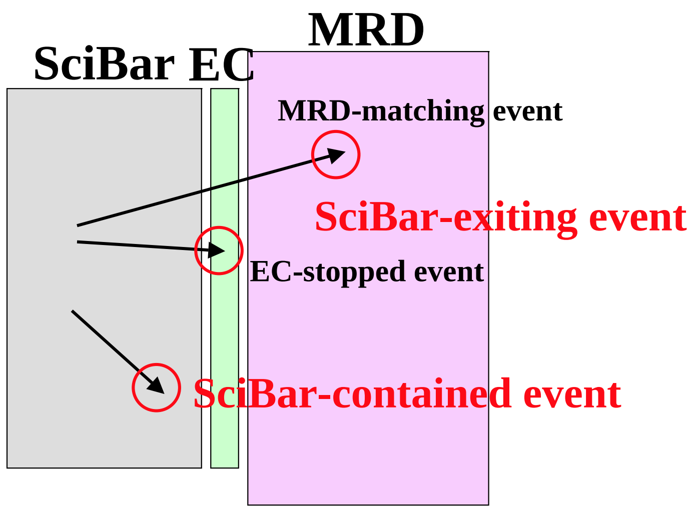

Figure 6.6: Event categories of SciBar data.

6.4 CC event selection

Fig. 6.6 shows the event categories of SciBar data. A selection of the CC events is studied for SciBar-contained events and SciBar-exiting events. In SciBar-exiting event, two event categories, “MRD-matching events” and “EC-stopped events”, are contained. In MRD-matching events, the efficiency for CC-QE interaction is 80% for neutrino energy above 1 GeV. Since CC-QE is the dominant (∼60%) interaction for neutrino energy below 1 GeV, detection of low energy CC-QE events is important to measure low-energy neutrino spectrum. In MRD-matching evens, the efficiency for CC-QE events is ∼40% in low energy region below 1 GeV. To enhance low energy events, SciBar-contained events and EC-stopped events are selected in this analysis.

6.4.1 SciBar-exiting condition

To identify whether a SciBar track stops inside SciBar or exits from SciBar, the SciBar track exiting condition is defined as follows.

- $Z_{\rm down}$ is on the most downstream layer of SciBar,
- $|X_{\rm down}| > 130$ cm or $|Y_{\rm down}| > 130$ cm,

where $X_{\rm down}$, $Y_{\rm down}$ and $Z_{\rm down}$ are the position of the downstream edge of a SciBar track. The origin of the coordinate is the center of SciBar.

The tracks which satisfy the exiting condition are identified as “SciBar-exiting events”, and the others are classified as “SciBar-contained events”. Since the tracking area of the XY plane is $|X_{\rm down}, Y_{\rm down}| <$ 140 cm, 10 cm margin is left for exiting condition of the XY plane to reject the sky-shine backgrounds in the SciBar-contained events, which is described in the following sections.

6.4.2 SciBar-contained events

Events whose track stops inside SciBar, are selected as “SciBar-contained events”. In the previous analysis, SciBar-contained events are not used, since they have contamination of the sky-shine backgrounds

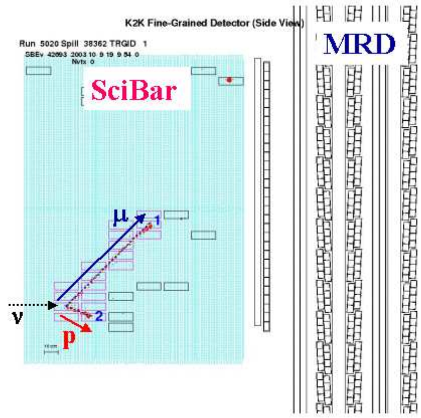

Figure 6.7: A event display of typical SciBar-contained event.

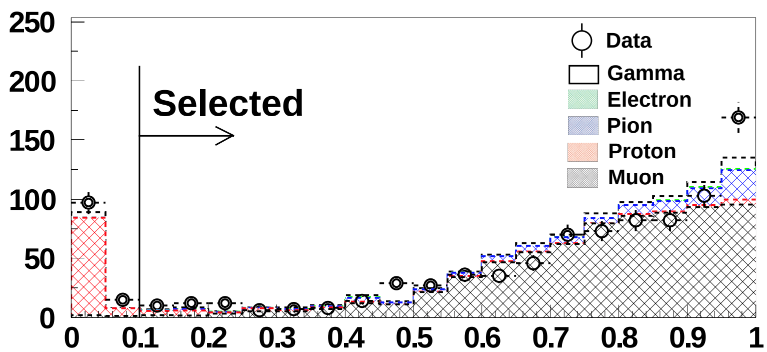

Figure 6.8: MuCL (Muon Confidence Level) distribution for the primary tracks of SciBar-contained events when tracks longer than 60 cm are selected to reject sky-shine background. The histograms of the MC simulation are normalized by a number of events of MRD-matching events.

and neutral current (NC) events. In particular, contamination of NC events worse the measurement of the neutrino energy spectrum. In this section, the rejection of such background events is described.

Muon track selection

To obtain muon tracks from CC interaction, the longest track inside SciBar is selected as a muon track candidate for SciBar-contained events. In addition, the rejection of the proton tracks are performed by using dE/dx information. For the particle identification, a valuable of MuCL (Muon Confidence Level) are defined. Details of the definition are described in Section 4.5.5. Figure 6.8 shows the MuCL distribution of SciBar-contained tracks when the tracks longer than 60 cm are selected to reject the sky-shine backgrounds which make short tracks as described in the next section. The MuCL distribution of data is well consistent with that of the MC simulation. In the definition of MuCL, a track with larger value up to 1 is defined as a muon-like track. The tracks with MuCL less than 0.1 are rejected as proton-like tracks.

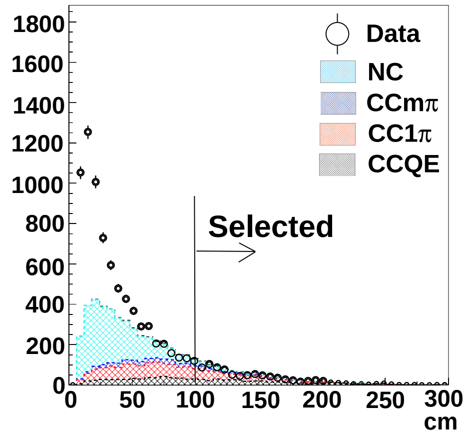

Figure 6.9: The track length distribution of SciBar-contained events after the muon track selection. The normalization between data and the MC simulation is done by a number of events of MRD-matching events. Excess of sky-shine background is seen in the region of track length shorter than 60 cm.

Rejection of sky-shine backgrounds and NC events

Figure 6.9 shows the track length distribution of SciBar-contained events after the muon track selection. The sky-shine backgrounds and NC events contaminate in the short track events. The sky-shine backgrounds are events synchronizing with the accelerator cycle, which make a large excess in the region of track length shorter than 60 cm. In addition, contamination of NC events becomes about 30%, even after the muon-like track selection. Since the spectrum measurement is performed by using CC events, the rejection of NC events is necessary. Therefore, the tracks longer than 100 cm are used in the spectrum measurement to reject both sky-shine background and NC events. By this procedure, $\sim 93\%$ of NC events are rejected, and NC contamination is reduced to 8% in SciBar-contained events. The problems of the sky-shine backgrounds and NC events is described below.

Sky-shine background

In SciBar-contained events, backgrounds synchronizing with the accelerator cycle (sky-shine backgrounds) contaminate. Fig. 6.4 shows timing distribution of SciBar tracks. We can see incoming sky-shine backgrounds in the beam spill. According to the MC simulation, the sky-shine backgrounds are recognized protons and gammas from π^0 decay, which are made by interaction of neutrons from the accelerator with nucleus in the atmosphere as shown in Fig. 6.10. Fig. 6.11 and Fig. 6.12 show the proton-like and gamma-like sky-shine background candidates, respectively, which are observed in the off-bunch timing. In Fig. 6.11, large light yield can be seen, whereas a gamma behaves as a MIP-like track in Fig. 6.12.

Although tracks made by the sky-shine protons can be rejected by using dE/dx information, those of the sky-shine gammas remain as MIP-like tracks. Figure 6.13 shows the reconstructed vertex distribution of Y-axis after the proton rejection. Large background events made by the sky-shine gammas are seen in the upper region.

NC contamination

There are four NC interactions which contaminate in SciBar-contained events after the muon track selection, as follows.

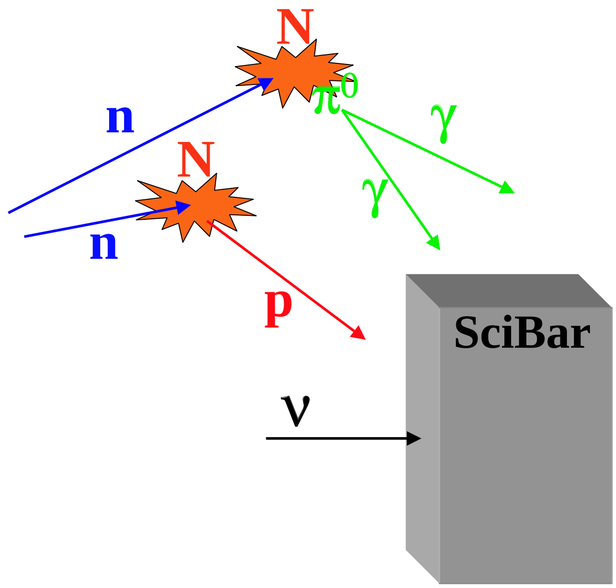

Figure 6.10: A schematic view of the sky-shine events.

- NC 1 $\pi^{\pm}$ production (NC1$\pi^{\pm}$) : $\nu + N \to \nu + N' + \pi^{\pm}$ (29%)
- NC 1 π^{0} production (NC1π^{0}) : $\nu + N \to \nu + N' + \pi^{0}$ (38%)
- NC multi π production (NCmπ) : $\nu + N \to \nu + N' + m\pi^{\pm}$ (22%)
- NC elastic scattering (NCES) : $\nu + N \to \nu + N(N' + p$ or $n)$ (11%)

Figure 6.14 shows the neutrino energy spectrum of NC and CC-QE interactions for SciBar-contained events after the proton rejection, which is estimated by the MC simulation. Most of the NC events contaminating in SciBar-contained events come from the energy region above 1 GeV, whereas the neutrino energy of CC-QE events is below 1 GeV. The neutrino energy spectrum may not be measured correctly by mis-identification of NC events as low energy CC-QE events.

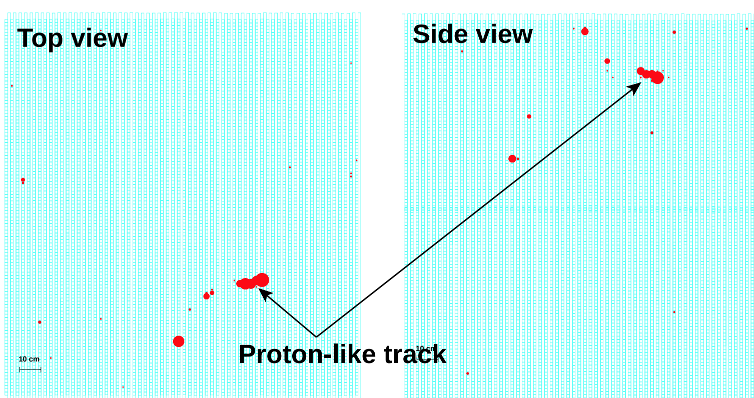

Figure 6.11: An event display of a proton-like sky-shine event.

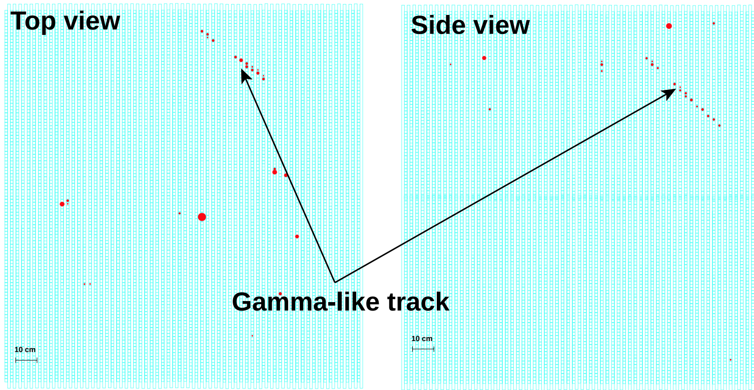

Figure 6.12: An event display of a gamma-like sky-shine event.

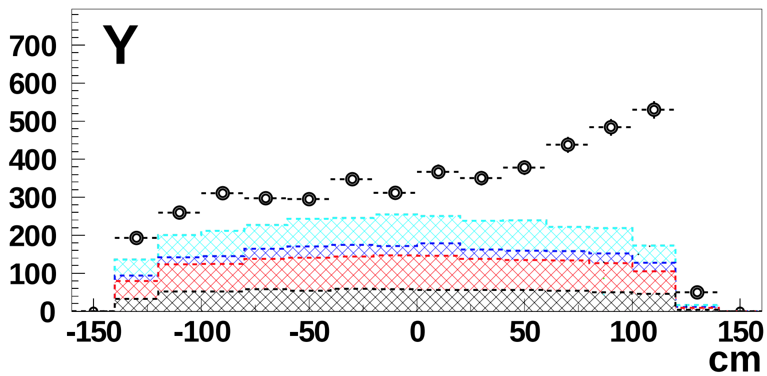

Figure 6.13: The reconstructed vertex distribution of Y-axis after the rejection of the protons by using dE/dx information. The normalization between data and the MC simulation is done by a number of events of MRD-matching events. Excess made by sky-shine gammas can be seen in the upper region.

The neutrino spectrum is measured by using the muon momentum and angle from CC interaction. Since tracks of $\pi^{\pm}$ and gammas from π^{0} generated by NC interaction behave like muon tracks, their momentum is reconstructed as muon track. Figure 6.15 (A, B) shows momentum distribution of $\pi^{\pm}$ and gamma from π^{0}, respectively, which are reconstructed as muons by using their range. The distributions overlap with that of muons from CCQE as shown in Fig. 6.15 (C). Therefore, the spectrum measurement gets worse by the uncertainty of NC cross-section. If we assume 30% uncertainty in NC cross-section, its systematic error is larger than statistical error on CCQE events in energy region below 1 GeV. For this reason, NC events should be reduced to less than statistics error of CCQE, that is required 93% rejection of NC events.

A fraction of particles which make muon track candidates induced by NC interaction, is as follows.

- gamma shower : 45%
- $\pi^{\pm}$: 35%
- proton : 16%
- others : 4%

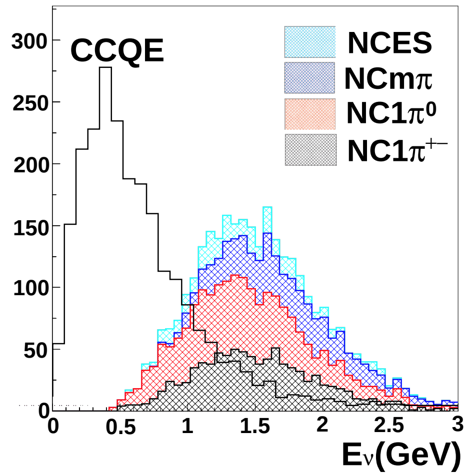

Figure 6.14: The neutrino energy spectrum of NC interaction for SciBar-contained events after the rejection of the protons by using dE/dx information, which is estimated by the MC simulation. That of CC-QE events are also overlaid.

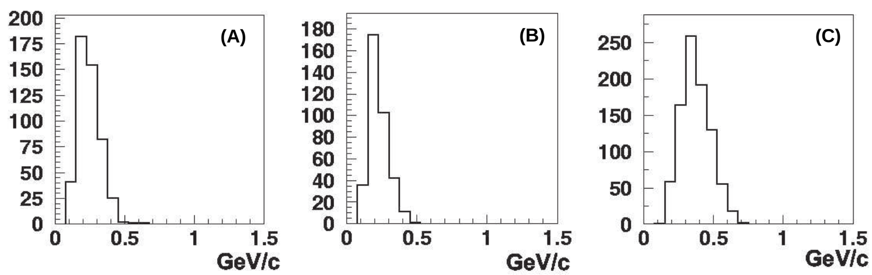

Figure 6.15: Momentum distributions of $\pi^{\pm}$ from NC interaction reconstructed as a muon (A), gamma tracks from π^0 by NC interaction reconstructed as muons (B), and muons from CCQE (C).

Figure 6.16 shows the range of protons from NCES in SciBar simulated by MC simulation. Even after the proton rejection by using dE/dx information, we still have protons in short track region. This is due to the reaction of $p + N \rightarrow n + N'$ by high energy protons. Since the high-energy protons generate MIP-like tracks, the rejection by the track length is necessary to separate from muon tracks.

A reduction summary of SciBar-contained event

A reduction summary of SciBar-contained events is shown in Table 6.2. 821 events are obtained for SciBar-contained events. Assuming 30% uncertainty on NC cross-section, the systematic error caused by the remaining NC contamination (8% contamination in the sample) is comparable to the statistical error of CC-QE events in the energy region below 1 GeV. Therefore, SciBar-contained events have enough purity as CC event sample.

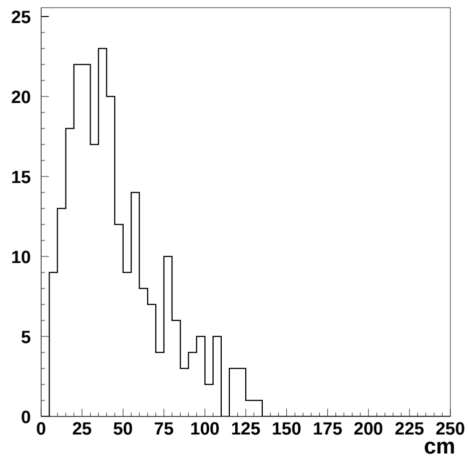

Figure 6.16: A range distribution of protons from NCES in SciBar estimated by the MC simulation.

Table 6.2: A reduction summary for SciBar-contained events.

	Data	MC			
		Total	CCQE	CC-nonQE	NC
SciBar contained	8,946	18,557	2,861	6,319	9,377
MuCL greater than 0.1	4,609	9,799	2,060	4,652	3,087
Track longer than 100 cm	821	3,105	1,148	1,719	238

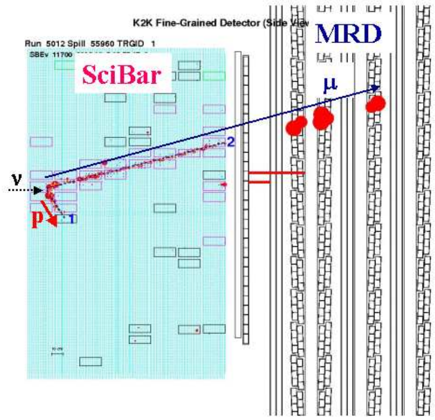

Figure 6.17: An event display of a typical MRD3D-matching event.

6.4.3 MRD-matching event selection

Electro-magnetic calorimeter (EC) and muon range detector (MRD) are located downstream of SciBar. A track from SciBar which matches an MRD track or MRD hits, is selected as an MRD-matching event. Since MRD and EC are mainly made of lead and iron, they are good muon filters. Consequently, charged current (CC) events are mainly selected as MRD-matching events. We select two kinds of MRD-matching events, “MRD3D-matching events” and “MRD first layer (MRD1L) matching events”. The events with SciBar tracks matching with MRD tracks are identified as MRD3D-mathcing events. If there is no track in MRD matching with SciBar track, we look for MRD hits which satisfy matching condition with a SciBar track. An event display of a typical MRD3D-matching event is shown in Fig. 6.17. The event selection procedure is described in the following sections.

3D track matching

The MRD3D track matching condition is summarized as bellow.

- An MRD track is required to start from the first chamber plane of MRD.
- $|\Delta X| < 20$ cm and $|\Delta Y| < 20$ cm,
- $|\Delta\theta| < 0.5$ rad.,

where ΔX (ΔY) shows the residual between the extrapolation position of the SciBar track at the MRD first layer and the starting point of the MRD track on X (Y) view (Fig. 6.18). $\Delta\theta$ is the residual of the angle as shown in Fig. 6.19. If there are MRD tracks to satisfy this requirement, the events are categorized as MRD3D-matching events.

Matching with hits on the MRD fi rst layer

If no MRD3D-matching tracks are found, hits on the MRD first layer matching with the SciBar track are looked for. The difference between the extrapolation of a SciBar track and MRD first layer hits is required to be less than 20 cm for both X and Y in the previous analysis [36], as shown in Fig. 6.20. To increase the efficiency for low energy events, the effect of the multiple scattering in EC is also

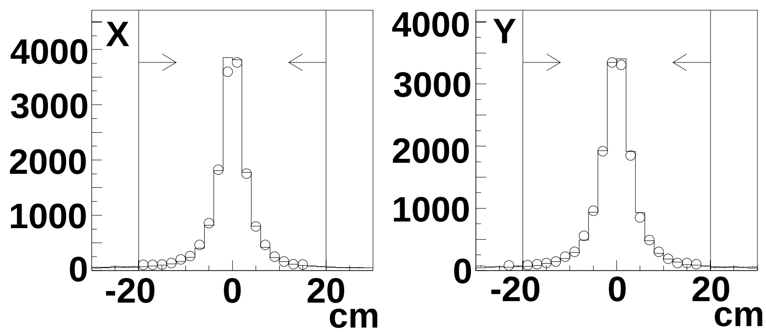

Figure 6.18: A residual distribution of the position between a SciBar and a MRD track. The circles show data and the histogram shows the MC simulation. The matching condition is within $\pm$20 cm.

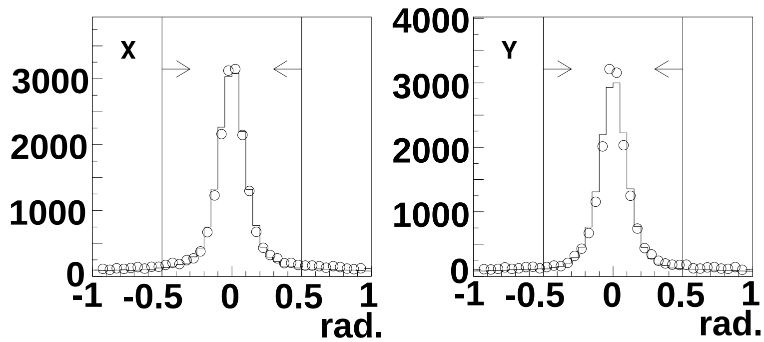

Figure 6.19: A residual distribution of the direction between a SciBar and a MRD track. The circles show data and the histogram shows the MC simulation. The matching condition is within $\pm$0.5 radian.

considered. The muon momentum just before the EC is calculated, assuming that the muon stops inside the first layer of MRD. By using the Moliere formula [35], the scattering angle on EC is calculated. Three standard deviation of the scattering angle distribution is taken into account to matching condition.

Since the MRD tracking efficiency is very low for short tracks (only 65% for tracks passing two chamber layers, as shown in Fig. 3.8), the MRD1L track may also have hits in the second layer or more. To obtain correct muon range for MRD1L-matching events, we look for the downstream hits associated to an MRD1L track. To search for the matching hit in the second layer, we draw a line from the first layer hit to one of the second layer hits. The angle between the line and the MRD1L track is required to be less than 0.5 radian so far. In this analysis, the effect of multiple scattering on MRD plane are also considered by additional three standard deviation of the scattering angle distribution. The distribution of the angle is shown in Fig 6.21. Similarly, for the third layer hits, the same procedure is applied to the angle between the lines from the first layer to the second and from the second to the third. The same is true for more downstream layers.

By taking account of multiple scattering effect to the MRD1L-matching condition, 362 events are recovered, where 3,121 events are obtained as MRD1L event in total as shown in Table. 6.3.

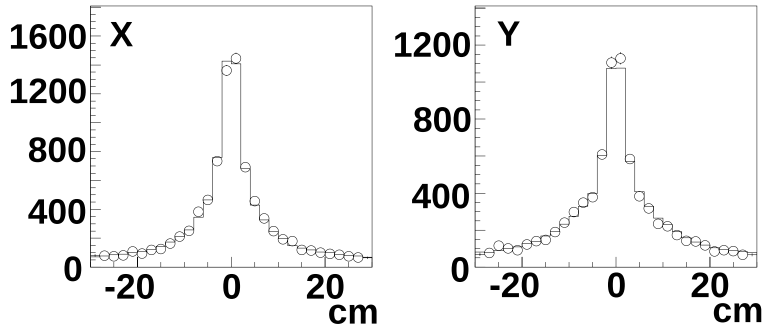

Figure 6.20: A residual distribution of the position between a SciBar track and a MRD first layer hit. The circles show data and the histogram shows the MC simulation.

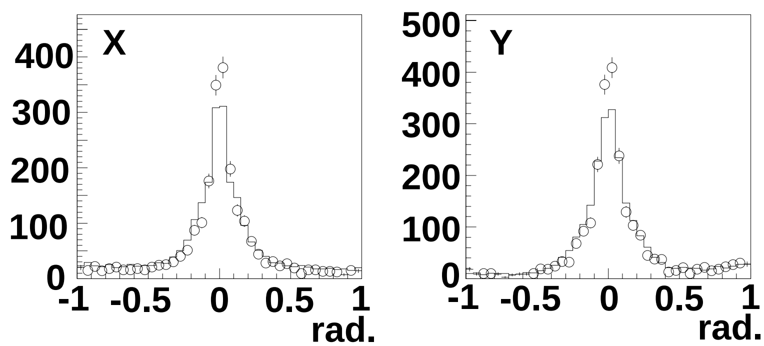

Figure 6.21: A residual distribution of the direction between a SciBar track and the line of a MRD first layer hit to a second layer hit. The circles show data and the histogram shows the MC simulation.

Muon track selection

A muon track is selected by selecting an MRD matched track which has the longest track in MRD. Since MRD are mainly made of iron, most hadron events are rejected by the requirement.

Reduction summary of MRD-matching event

The reduction for MRD-matching events is summarized in Table 6.3. We obtain 8,441 events for MRD3D-matching events and 3,121 events for MRD1L-matching events. The CC events are effectively obtained by requiring MRD matching condition.

Table 6.3: A reduction summary for MRD-matching events.

	Data	MC			
		Total	CCQE	CC-nonQE	NC
SciBar exiting	18,734	63,892	27,694	30,922	5,276
MRD3D matching	8,441	30,992	18,237	12,602	153
MRD1L matching	3,121	9,609	3,059	5,808	742

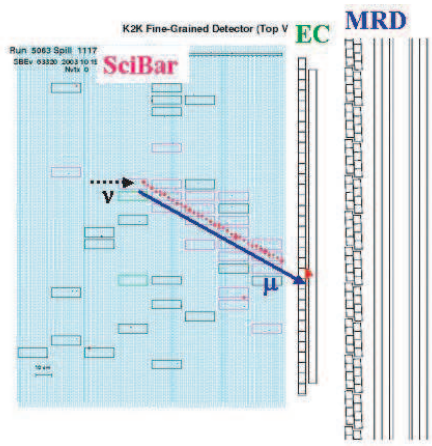

Figure 6.22: Event display of a typical EC-stopped event.

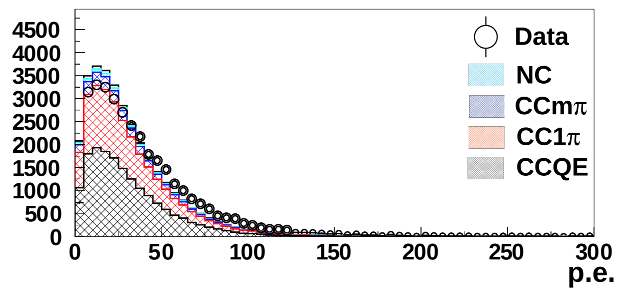

Figure 6.23: The photo-electron distribution obtained by EC when MRD3D-matching tracks are within EC volume. The normalization between data and MC is done by a number of events of MRD-matching events.

6.4.4 EC-stopped event selection

Events with track stopping in EC, are selected as "EC-stopped events". Figure 6.22 shows a event display of a typical EC-sopped event. To search for EC-stopped events, EC matching criteria is applied to the SciBar-exiting events which do not match with MRD tracks. In this section, the selection cuts are explained.

EC matching condition

After selection of SciBar track, we require EC matching condition to ensure that there are real hits on EC by exiting track from SciBar.

Hit threshold : Figure 6.23 shows a photo-electron distribution obtained by EC when an extrapolated position of MRD3D-matching track is within EC volume. Hit threshold of 5 p.e. is required to identify real hits by SciBar-exiting particles.

Fiducial volume : Fig. 6.24 shows a hit distribution on EC. The fiducial volume of EC is defined as

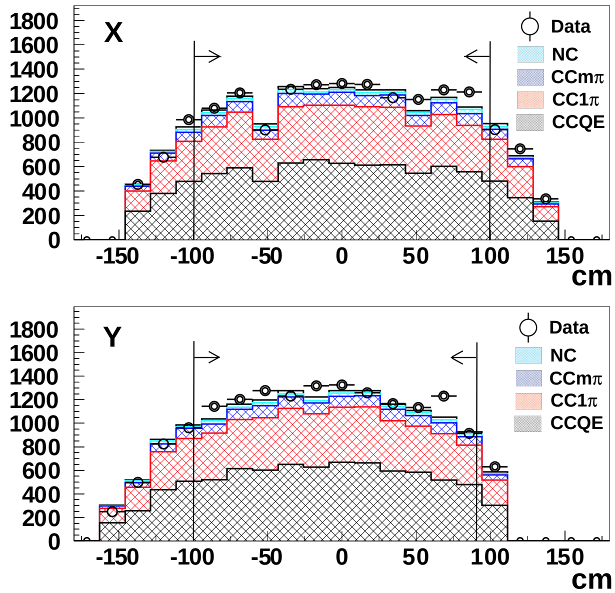

Figure 6.24: Hit distributions on EC for the vertical plane (top) and the horizontal plane (bottom). The normalization between data and the MC simulation is done by a number of events of MRD-matching events.

$-100 < |X| < 100$ cm and $-100 < |Y| < 80$ cm to ensure the real hit on EC.

Matching condition : Fig. 6.25 shows the distribution of the distance between an expected hit position on EC by a SciBar track and a real EC hit position. We require the residual to be within 6 cm.

MRD 1st plane veto

Tracks which stop in MRD first plane or do not satisfy MRD 1st layer condition by the effect of multiple scattering, may be identified as EC-stopped events. Fig. 6.26 shows a hit distribution on MRD first plane when tracks from SciBar satisfy EC matching condition. To reject migration from the mis-matching of MRD1L events, no hits on MRD first plane within 40 cm from extrapolated position of SciBar track are required.

Muon track selection

A muon track is selected by using an EC-matched track which has the longest track in SciBar. Since SciBar is constructed with scintillator strips, the mass is small to reject hadron tracks from NC events. Therefore, some hadron tracks remain in EC matched tracks. The rejection of the hadron track from NC events are described in the next section.

Rejection of NC events

As the situation in SciBar-contained events, NC events contaminate in EC-stopped events (25% in the sample). Figure 6.27 shows track length distribution in SciBar for EC-stopped events. We can see large fraction by NC events in the short track region. To reject such NC events, the track longer than 100

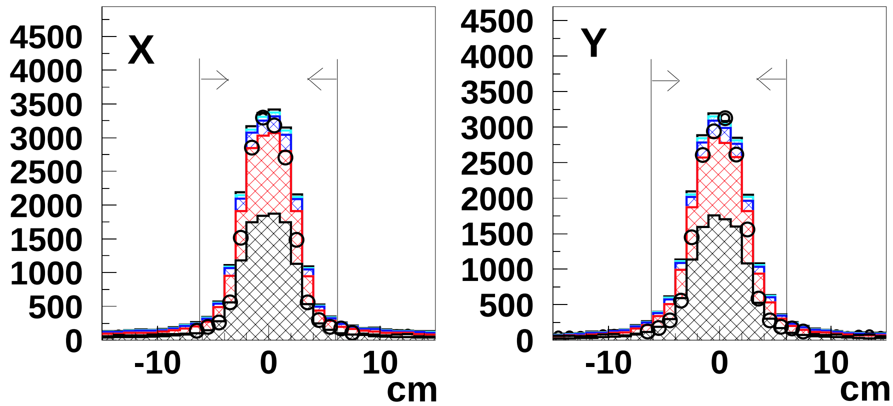

Figure 6.25: A residual distribution between the expected hit position on EC by SciBar track and real EC hit position. The normalization between data and MC is done by a number of events of MRD-matching events.

Table 6.4: A reduction summary for EC-stopped events.

	Data	MC			
		Total	CCQE	CC-nonQE	NC
SciBar exiting	18,734	63,892	27,694	30,922	5,276
MRD mis-matching	7,433	23,423	6,561	12,493	4,369
EC fi ducial	709	2,827	594	1,522	711
EC matching	521	2,054	437	1,102	515
MRD fi rst plane veto	512	2,005	429	1,070	506
Track longer than 100 cm	203	805	260	482	63

cm is required. As a result, contamination of NC events is reduced to 7%. This is comparable to the statistical error of CC-QE events. Therefore, the uncertainty of NC cross-section becomes negligible in the spectrum measurement and EC-stopped events can be used as CC event sample.

Reduction summary of EC-stopped events

A reduction summary of EC-stopped events is shown in Table 6.4. In the final reduction stage, 203 events are selected.

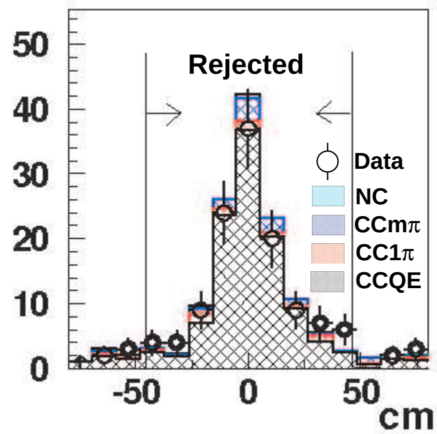

Figure 6.26: A hit distribution on MRD first plane when tracks from SciBar satisfy EC matching condition. The normalization between data and MC is done by a number of events of MRD-matching events.

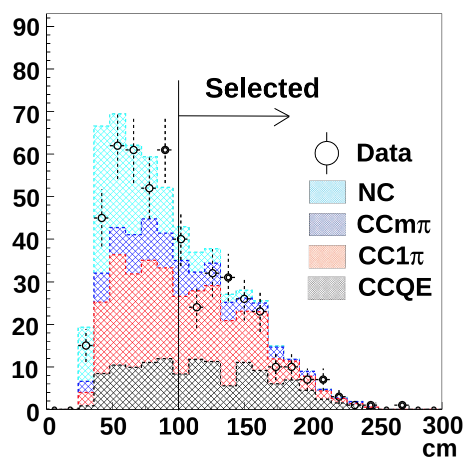

Figure 6.27: The reconstructed muon track length distribution of EC-stopped events in SciBar. The histogram of the MC simulation are normalized to data by a number of events of MRD-matching events.

Table 6.5: A selected number of events and the neutrino interaction mode estimated by the MC simulation in each event category.

	# of event	CCQE	CC1π	CCmπ	NC
MRD-matching event	11,562	54%	35%	9%	2%
SciBar-contained event	821	37%	43%	12%	8%
EC-stopped event	203	34%	46%	13%	7%

Table 6.6: The list of particle species making tracks in each event category estimated by the MC simulation.

	muon	proton	$\pi^{\pm}$	γ
MRD-matching event	91%	4%	3%	1%
SciBar-contained event	82%	3%	10%	5%
EC-stopped event	79%	12%	7%	2%

6.4.5 Summary of CC event selection

Two events categories, SciBar-contained events and SciBar-exiting events, are prepared for SciBar data. In SciBar-exiting events, MRD-matching events and EC-stopped events are selected. In total, 12,586 events are obtained, where MRD-matching events are 11,562 events, SciBar-contained events are 821 events, and EC-stopped events are 203 events. A number of events and the interaction mode in each event category are summarized in Table 6.5.

Table 6.6 shows a fraction of particles making tracks in each event categories for each event category, which is estimated by the MC simulation. Since the hadrons stop easily in EC by comparison with muons, high-energy protons remain 12% in EC-sopped events. However, the uncertainties of the proton and pion contamination are enough small comparing to the statistical error of CC-QE events, which are described in Section 7.2.2. Therefore, the muon tracks are selected sufficiently for each event sample.

The number of events and the fraction of CC-QE interaction in low energy region below 1 GeV is summarized in Table 6.7. A selected number of CC-QE events in low energy region increases by a factor of 1.3 by adding SciBar-contained events and EC-stopped events to MRD-matching events.

Table 6.7: A number of events in the energy region below 1 GeV for each event category expected by the MC simulation.

	Total	CCQE
MRD-matching event	1,083	992
SciBar-contained event	289	240
EC-stopped event	54	40

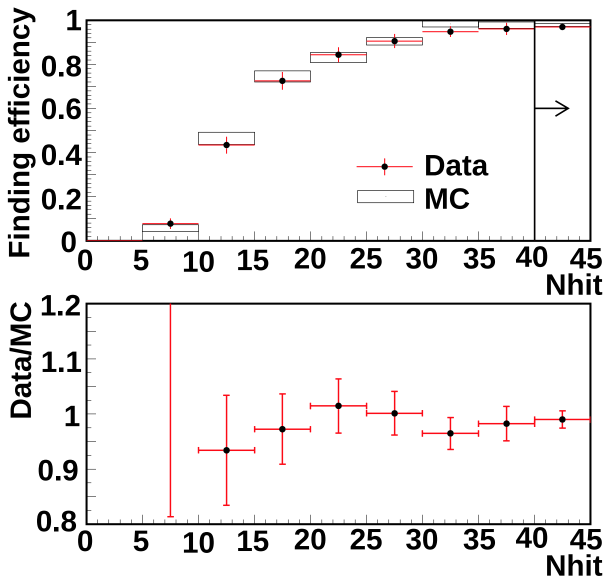

Figure 6.28: The efficiency to find extra tracks in SciBar (top) and the ratio of data to MC simulation (bottom).

6.5 Event classifi cation for the spectrum measurement

Two CC event samples (SciBar-contained events and SciBar-exiting events) are classified into the sub-samples for the spectrum measurement. In this section, the procedure is described.

6.5.1 Event classification of SciBar-contained event

The statistics of SciBar-contained events is too small to divide into sub-samples. Therefore, without any other selections like a number of tracks, all SciBar-contained events are used as one sample ("SciBar-contained sample").

6.5.2 Event classification of SciBar-exiting event

Track counting

If the extra tracks other than a muon track associated with the vertex are found, CC-QE interactions and the other CC interactions (nonQE) can be separated by using their kinematics. Therefore, the extra track search is studied.

Eye scan is performed to study the finding efficiency of the extra tracks other than the muon tracks. We check the existence of the reconstructed extra tracks and count the number of hits along the extra tracks. Figure 6.28 shows the efficiency to find extra tracks and the ratio of data to MC simulation. The efficiency exceeds 80% at 20 hits. Data and MC simulation is well consistent.

To find the other tracks associating with the vertex, the vertex matching conditions is defined as below.

- $|\Delta X, \Delta Y| < 9$ cm

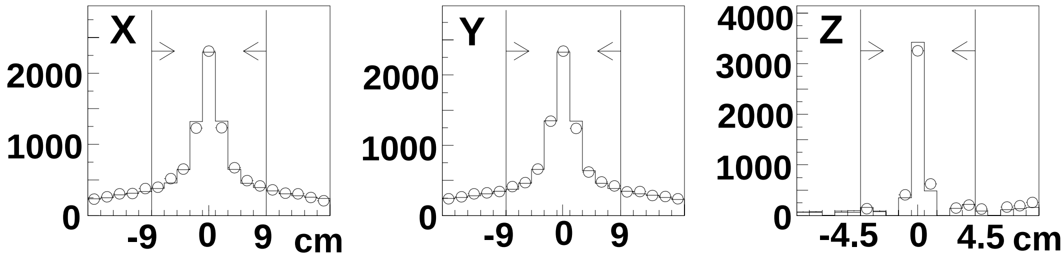

Figure 6.29: Distributions of the position difference between the track edge and the reconstructed vertex. Open circle and solid histograms show data and MC simulation, respectively.

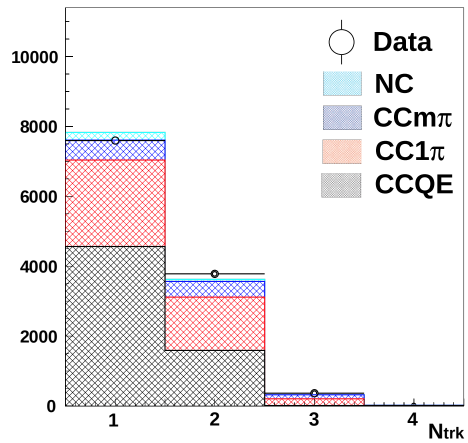

Figure 6.30: The number of track distribution of SciBar-exiting events.

- $|\Delta Z| < 4.5$ cm,

where ΔX, ΔY and ΔZ is the position difference between the track edge and the reconstructed vertex as shown in Fig. 6.29. The reconstructed vertex is defined as the upstream edge of muon track. Figure 6.30 shows the distribution of a number of tracks ($N_{\rm track}$) starting from the muon vertex of SciBar-exiting events. The events with more than 2 tracks are rejected to increase CC-QE purity in the sample.

CC-QE/nonQE separation for the 2-track events

The 2-track events are divided into 2-track-QE and 2-track-nonQE events. If CC-QE interaction is assumed, the proton track direction can be estimated with the momentum and direction of muon tracks by the following equation.

$$\tan\theta_p = \frac{p_\mu \sin\theta_\mu}{E_\nu^{\rm rec} - p_\mu \cos\theta_\mu}, \tag{6.1}$$

where p_μ, θ_μ and $E_\nu^{\rm rec}$ are the muon momentum, the muon angle with respect to the beam, and the reconstructed neutrino energy assuming CC-QE interaction, respectively.

Since CC-QE has two-body kinematics, the azimuthal angles of the proton (ϕ_p) is opposite to that of the muon (ϕ_μ) as

$$\phi_p = \phi_\mu + \pi. \tag{6.2}$$

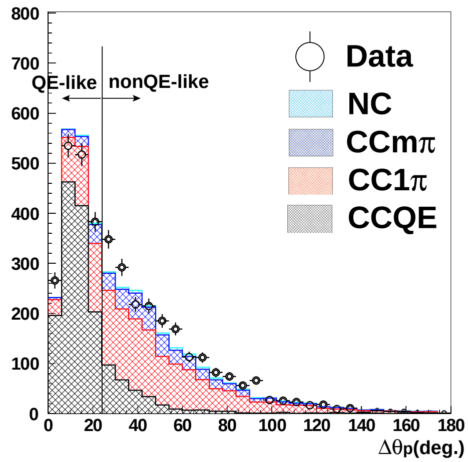

Figure 6.31: The angle between an observed second track and the expected proton direction by assuming CC-QE interaction.

Therefore, the angle between the observed second track and the expected proton direction ($\Delta\theta_p$) is obtained by

$$\cos\Delta\theta_p = \sin\theta_p \sin\theta_2 \cos(\phi_\mu + \pi - \phi_2) + \cos\theta_p \cos\theta_2, \tag{6.3}$$

where θ_2 and ϕ_2 are zenith and azimuthal angles of the observed second track, respectively. The events with small $\Delta\theta_p$ are classified in QE-like, and the other events are categorized in nonQE-like. Fig. 6.31 shows the angle between an observed second track and the expected proton direction by assuming CC-QE interaction. The events with $\Delta\theta_p$ less than 25 degree are classified to 2-track QE-enriched (2-track-QE) sample, and the other events are classified to 2-track nonQE-enriched (2-track-nonQE) sample. The 2-track-QE sample and 2-track-nonQE sample are used to determine the ratio of nonQE cross section to that of CC-QE in the spectrum measurement.

6.5.3 Summary of the event classification

SciBar-exiting events and SciBar-contained events are divided into four event samples, which are“1-track sample”, “2-track-QE sample”, and “2-track-nonQE sample” and “SciBar-contained sample” as summarized below.

- **SciBar-exiting events (SBEXT)**
  - 1-track sample (1-track)
  - 2-track CC-QE enriched sample (2-track-QE)
  - 2-track CC-nonQE enriched sample (2-track-nonQE)
- **SciBar-contained events (SBCNT)**
  - SciBar-contained sample

A number of events, the fraction of CC-QE and efficiency for CC-QE interaction in these event samples are summarized in Table 6.8, where the fraction and efficiency of CC-QE interaction for each event sample are estimated by MC simulation. The efficiency is defined as the ratio of the number of

Table 6.8: The observed number of events, the fraction of CC-QE and the efficiency for CC-QE interactions in each SciBar event sample, which are estimated by the MC simulation.

Event category	1-track	2-track-QE	2-track-nonQE	SBCNT	Total
Number of events	7,598	1,752	2,031	821	12,202
Purity of CC-QE [%]	58	73	16	37	-
Efficiency for CC-QE [%]	50	15	3	4	72

reconstructed events to that of generated events in the fiducial volume. The event samples of SciBar spectrum analysis have 72% efficiency for CC-QE in total.

6.6 Muon momentum reconstruction

The muon energy (E_μ) for each event category is reconstructed as follows.

$$\begin{array}{ll} E_\mu = E_\mu^{\mathrm{SciBar}} + m_\mu & \text{SciBar-contained event,} \\ E_\mu = E_\mu^{\mathrm{SciBar}} + E_\mu^{\mathrm{EC}} + m_\mu & \text{EC-stopped event,} \\ E_\mu = E_\mu^{\mathrm{SciBar}} + E_\mu^{\mathrm{EC}} + E_\mu^{\mathrm{MRD}} + m_\mu & \text{MRD-matching event,} \end{array} \tag{6.4}$$

where E_μ^{SciBar}, E_μ^{EC}, E_μ^{MRD} and m_μ are the energy deposit in SciBar, EC, MRD, and the muon mass, respectively. The energy deposit in each detector is calculated from the range by the conversion tables obtained by the MC simulation. By using the energy deposit in each detector, the muon momentum (p_μ) is reconstructed as,

$$p_\mu = \sqrt{E_\mu^2 - m_\mu^2}. \tag{6.5}$$

6.7 Vertex, p_μ, θ_μ and q^2 distribution

Figure 6.32 shows the reconstructed vertex distributions of MRD3D-matching events, MRD1L-matching events, EC-stopped events and SciBar-contained events. The reconstructed vertex distribution is well consistent with data and the MC simulation.

Fig. 6.33 shows the distributions of reconstructed muon momentum, muon angle with respect to the beam axis and reconstructed q^2 for these event categories. The q^2 is the reconstructed square of the four-momentum transfer assuming CC-QE, which is defined as

$$q^2 = 2E_\nu(E_\mu - p_\mu \cos\theta_\mu) - m_\mu^2. \tag{6.6}$$

Since it can not be judged whether the track direction is forward or backward, the q^2 is not reconstructed for SciBar-contained events.

In the muon angle distribution of the SciBar-contained events, excess of data to the MC simulation, is seen in large angle region. This excess is due to the contamination of cosmic-rays incident with large angle along the structure of the SciBar detector. as shown in Fig. 6.34. The contamination of cosmic ray events are estimated by data in off-bunch timing, and subtracted in the spectrum measurement as shown in Fig. 7.1.

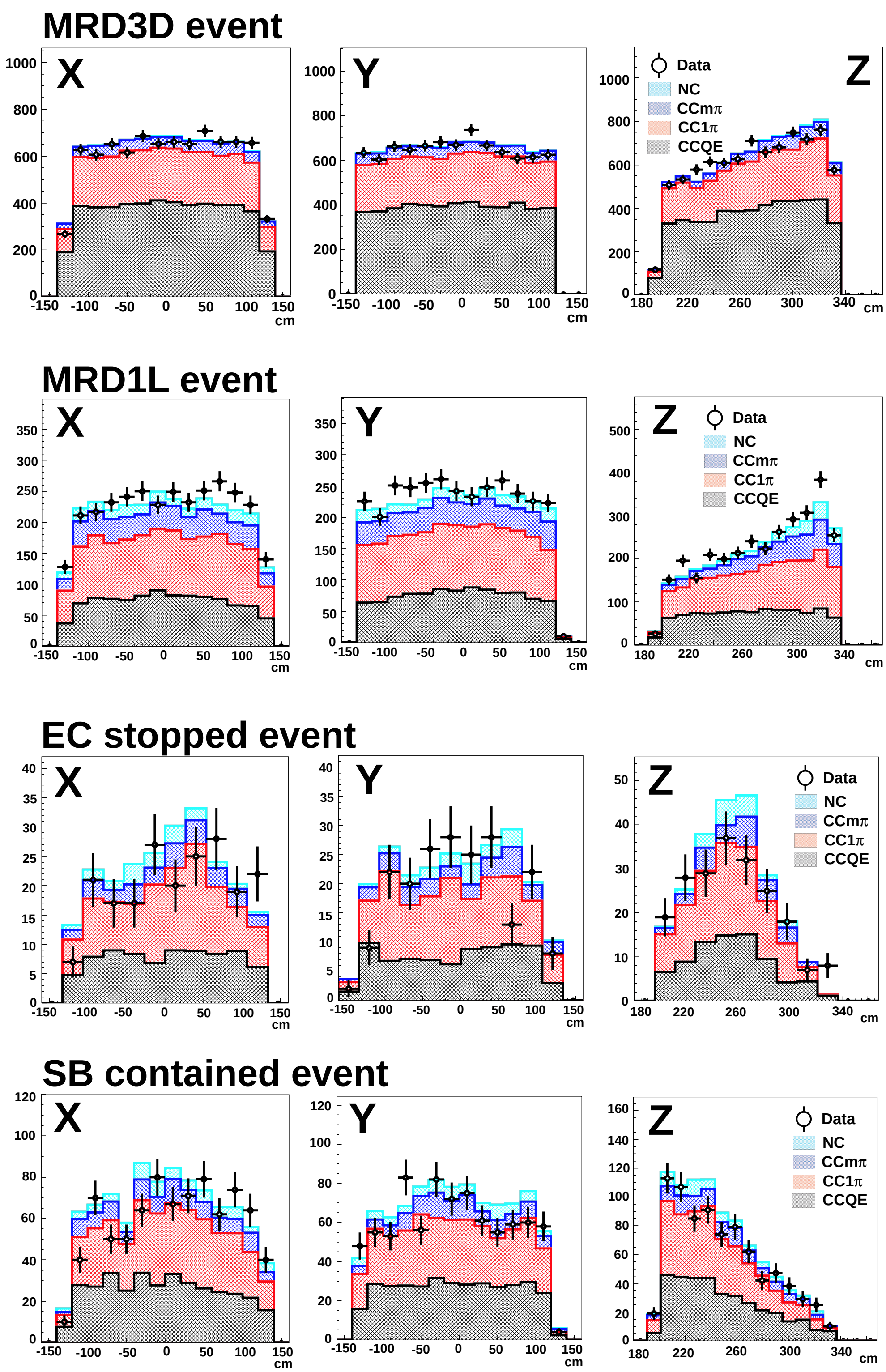

Figure 6.32: The reconstructed vertex distributions of MRD3D-matching events, MRD1L-matching events, EC-stopped events, SciBar-contained events. The normalization between data and MC is done by a number of events of MRD-matching events.

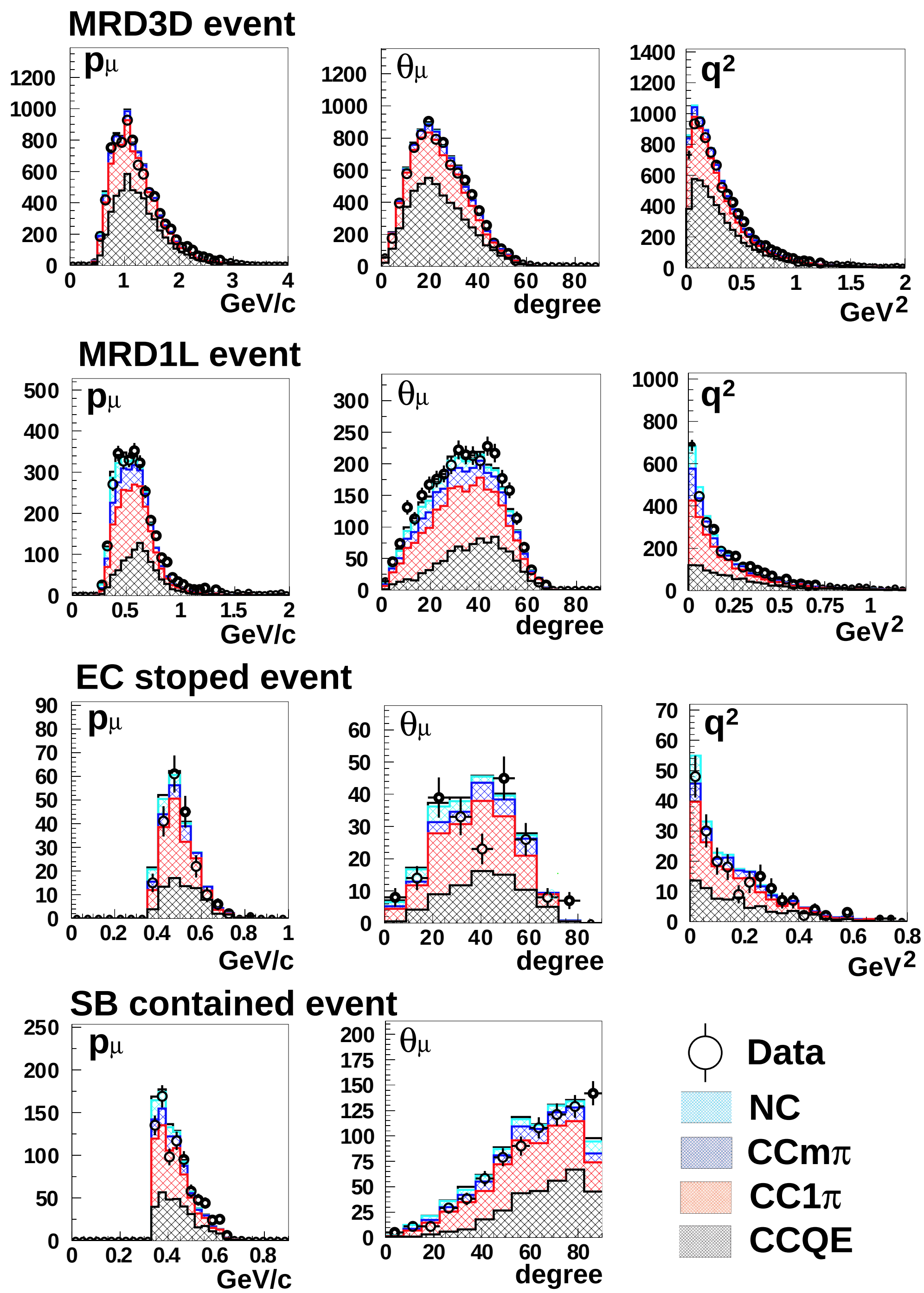

Figure 6.33: The reconstructed muon momentum distribution and muon angle distribution with respect to the beam axis for MRD3D-matching events, MRD1L-matching events, EC-stopped events, SciBar-contained events. The normalization between data and the MC simulation is done by a number of events of MRD-matching events.

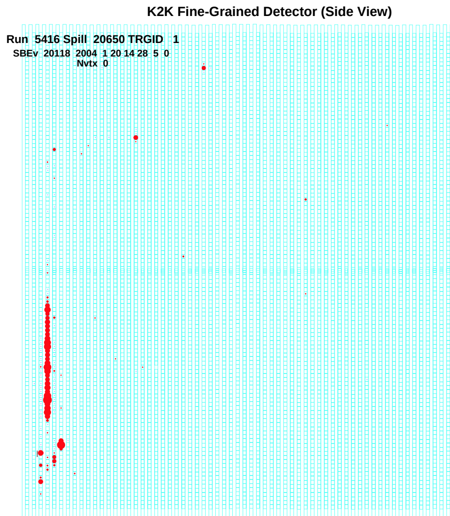

Figure 6.34: Event display of cosmic ray background coming with large angle, which is identified as a SciBar-contained event.

6.8 Efficiency for neutrino events

Figure 6.35 shows the neutrino energy distribution and the efficiency for neutrino events as a function of the neutrino energy, which is estimated by MC simulation. Overall efficiency is about 45%. Although the efficiency is about 60% for neutrinos energy above 2.5 GeV, it decreases in the low energy region.

Figure 6.36 shows the neutrino energy distribution of CC-QE events and the efficiency for CC-QE events as a function of the neutrino energy, which is estimated by MC simulation. The overall efficiency is $\sim$70% and it becomes $\sim$90% for neutrinos of energies above 2.5 GeV. We prepare SciBar-contained events and EC-stopped events to collect low energy CC-QE events. Figure 6.37 shows efficiency for CC-QE events for each event category in low energy region. Low energy CC-QE events from 0.5 GeV to 0.75 GeV, are recovered from 29% to 46% by SciBar-contained events and EC-stopped events, compared to the MRD-matching event only.

The main loss of the low energy CCQE events comes from the events whose muons exit from SciBar to the region out of the MRD acceptance. According to the MC simulation, about 700 CC-QE events below 1 GeV are lost by the reason, which corresponds to 30% of all CC-QE events below 1 GeV in SciBar. Since the muon energy can not be measured, these events are rejected. About 230 events of CC-QE below 1 GeV, which corresponds to about 10% of all CC-QE events below 1 GeV in SciBar, are also lost by the selection of the tracks longer than 100 cm in the SciBar-contained events.

Muons from CC interactions is required to stop in MRD to measure muon momentum, whereas the high energy muons escape from MRD. For this reason, efficiency drop in high energy region is happen.

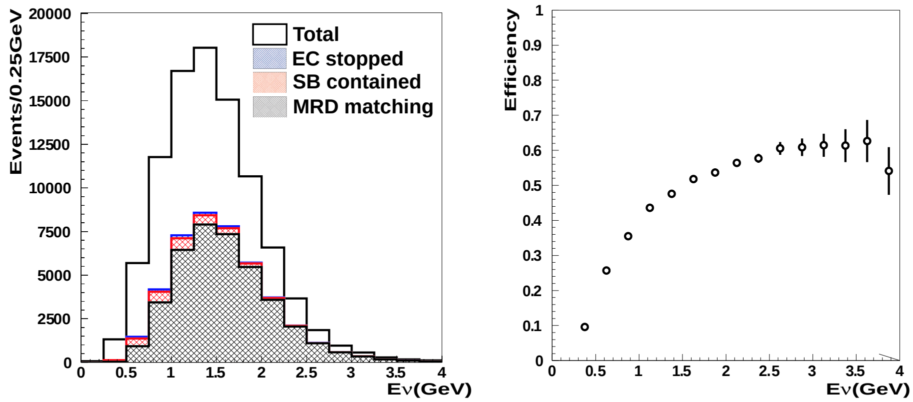

Figure 6.35: The true neutrino energy distribution (left) and the efficiency for neutrino events as a function of the true neutrino energy (right), which is estimated by the MC simulation.

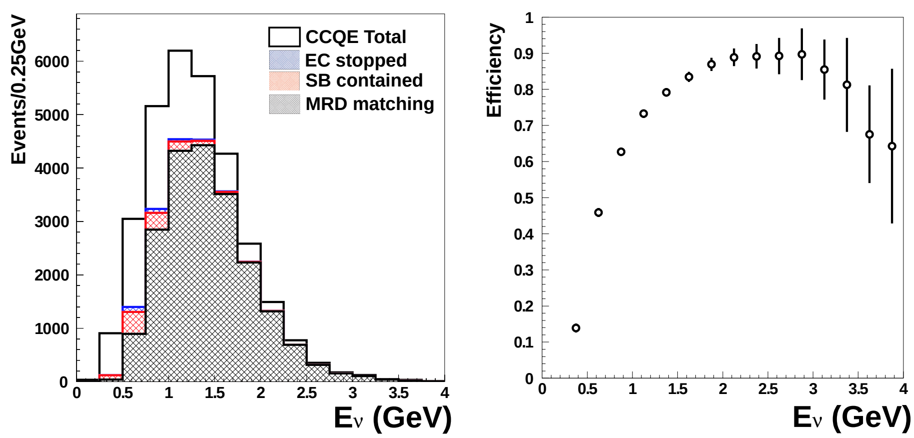

Figure 6.36: The true neutrino energy distribution of CC-QE events (left) and the efficiency for CC-QE events as a function of the true neutrino energy (right), which is estimated by the MC simulation.

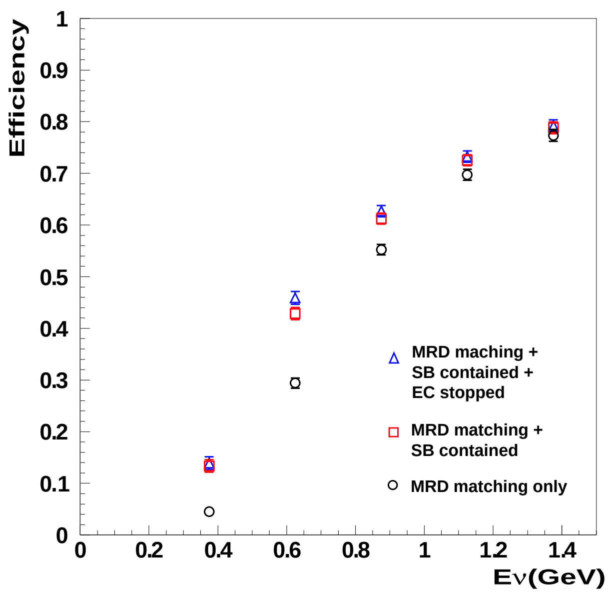

Figure 6.37: Efficiency for CC-QE events for each event category in low energy region, which is estimated by the MC simulation.

Chapter 7

Spectrum Measurement at the Near Site

7.1 Outline of the spectrum measurement

The measurement of neutrino energy spectrum at the near site is performed by the near detectors. The neutrino energy spectrum is measured by using muon momentum and angle from charged current (CC) interaction, since their distributions have information of the parent neutrino energy. In particular, if the effect of the Fermi motion is ignored, the neutrino energy is completely reconstructed for charged current quasi-elastic scattering (CC-QE) by the following equation.

$$E_\nu^{\rm rec} = \frac{m_p^2 - (m_n - V)^2 - m_\mu^2 + 2(m_n - V)E_\mu}{2(m_n - V - E_\mu + p_\mu \cos\theta_\mu)}, \tag{7.1}$$

where m_p, m_n, m_μ, E_μ, θ_μ, and V are the proton mass, neutron mass, muon mass, muon energy, muon angle with respect to the beam, and nuclear potential energy (25 MeV for ^{12}C [79] and 27 MeV for ^{16}O [80]), respectively.

The procedure of the spectrum measurement in this chapter is as follows. At first, the spectrum measurement is performed by using only SciBar data. In particular, the low energy region is investigated by using the low energy samples prepared in Chapter 6. To determine the neutrino spectrum, χ^2 fitting ("spectrum fitting") is applied to the 2-dimensional (p_μ, θ_μ) distribution of data and the MC simulation. Then, the neutrino energy spectrum at the near site, is measured by using all the near detectors.

7.2 Spectrum measurement with SciBar

7.2.1 Event sample

Two data sets in K2K-IIb and K2K-IIc period, are used for SciBar data. For the spectrum measurement, SciBar data is divided into four event samples, which are "1-track sample", "2-track-QE sample" and "2-track-nonQE sample" for SciBar-exiting events (SBEXT) and "SciBar-contained sample" for SciBar-contained events (SBCNT) as described in Chapter 6.

Fig. 7.1 shows the reconstructed p_μ, θ_μ and q^2 distributions of SBEXT 1-track, SBEXT 2-track-QE, SBEXT 2-track-nonQE events and SBCNT events, respectively. In Fig. 7.1, contamination of cosmic ray events estimated by the off-bunch data, is subtracted from the muon angle distribution of SBCNT. All the distributions are consistent with data and the MC simulation even before fitting.

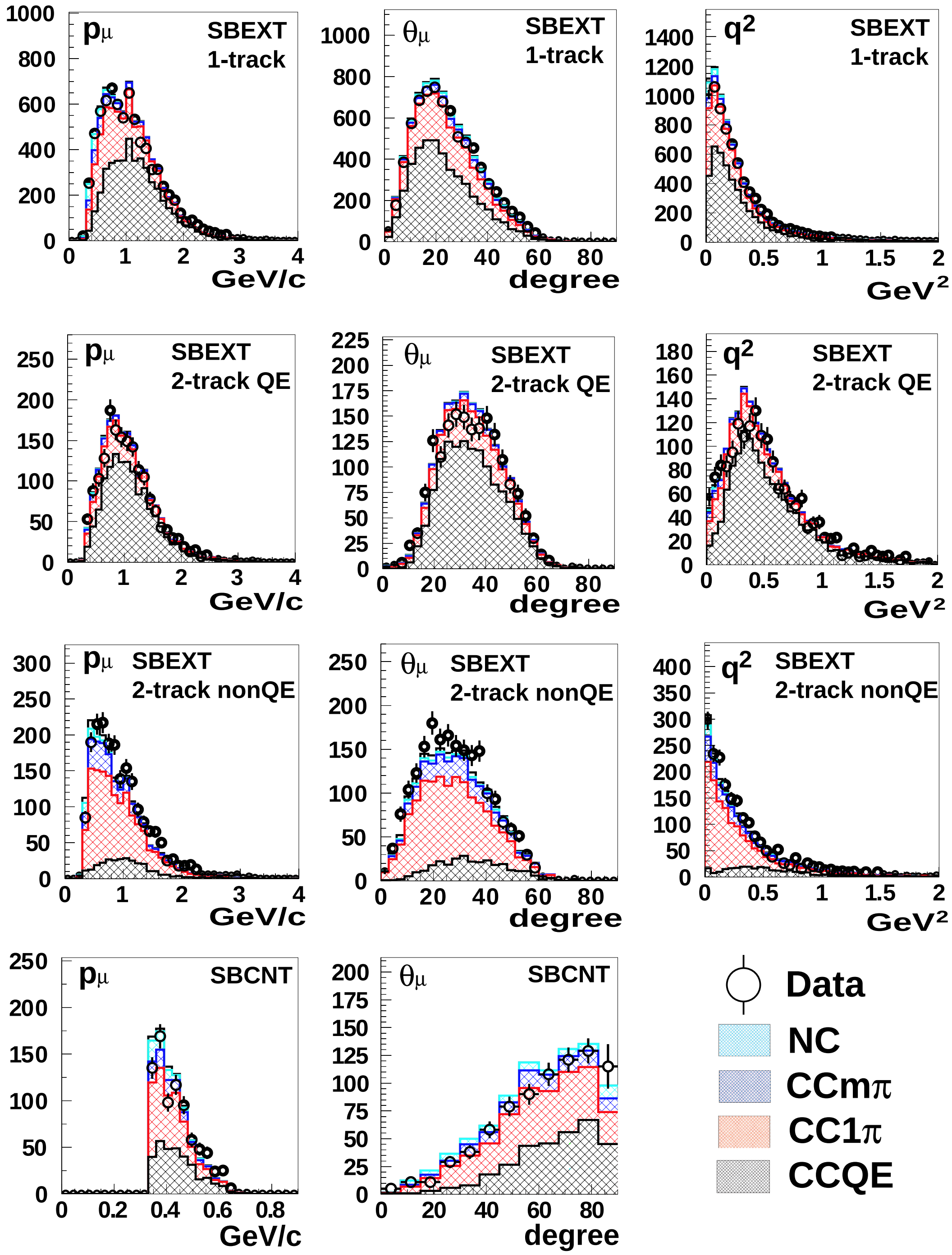

Figure 7.1: The reconstructed p_μ, θ_μ and q^2 distributions of 1-track events, and 2-track-QE events, 2-track-nonQE events and SBCNT events before the spectrum fitting.

Table 7.1: The E_ν interval of each f_i^ϕ bin.

i	1	2	3	4	5	6	7	8
E_ν[GeV]	0.0-0.5	0.5-0.75	0.75-1.0	1.0-1.5	1.5-2.0	2.0-2.5	2.5-3.0	3.0-

7.2.2 Spectrum fitting

The spectrum fitting is applied to the (p_μ, θ_μ) 2-dimensional distribution of data and the MC simulation to determine the neutrino energy spectrum. The MC template of the (p_μ, θ_μ) distribution is prepared for each event sample, which are made for QE and nonQE separately, and divided into each eight E_ν region. The E_ν interval of each f_i^ϕ are listed in Table 7.1. For example, data and the MC template for SciBar-exiting 1-track samples are shown in Fig. 7.2.

The fitting is performed with the parameters of each E_ν bin (f_i^ϕ for i-th bin) and the cross-section ratio of CC-nonQE to CC-QE interaction ($R_{\rm nQE}$). $R_{\rm nQE}$is used as one parameter for all energy region to vary the overall ratio of CC-nonQE to CC-QE. The content in the i-th p_μ and the j-th θ_μ bin of MC histogram is expressed by

$$N^{\rm MC}(i,j) = \sum_{k=1}^{8} f_k^\phi \cdot [N^{\rm MC}_{k,{\rm QE}}(i,j) + R_{\rm nQE} \cdot N^{\rm MC}_{k,{\rm nonQE}}(i,j)], \tag{7.2}$$

where $N^{MC}_{k,{\rm QE}}(i,j)$ and $N^{\rm MC}_{k,{\rm nonQE}}(i,j)$ are the bin contents of QE and nonQE distributions for the k-th E_ν bin, respectively. The χ^2 fitting is done between the observed distribution, $N^{\rm data}(i,j)$ and $N^{\rm MC}(i,j)$, to obtain the best fit parameters. The definition of the (p_μ,θ_μ) distribution and the χ^2 functions is described for the spectrum fitting in this section.

(p_μ, θ_μ) distribution

The (p_μ, θ_μ) distribution for SciBar is binned by 0.1 GeV for p_μ and 10 degree for θ_μ. Fig. 7.2 shows the (p_μ, θ_μ) distribution of SciBar-exiting 1-track sample for data and MC template.

The bin contents of the MC distribution for each event sample is given by

$$N^{\rm MC,1trk}(i,j) = P^{\rm SciBar}_{\rm Norm} \cdot \sum_{k=1}^{8} f_k^\phi \cdot [N^{\rm MC,1trk}_{k,{\rm QE}}(i,j) + R_{\rm nQE} \cdot N^{\rm MC,1trk}_{k,{\rm nonQE}}(i,j)], \tag{7.3}$$

$$\begin{aligned} N^{\rm MC,2trk-QE}(i,j) &= P^{\rm SciBar}_{\rm Norm} \cdot P^{\rm SciBar}_{\rm 2trk/1trk} \\ &\times \sum_{k=1}^{8} f_k^\phi \cdot [N^{\rm MC,2trk-QE}_{k,{\rm QE}}(i,j) + R_{\rm nQE} \cdot N^{\rm MC,2trk-QE}_{k,{\rm nonQE}}(i,j)], \end{aligned} \tag{7.4}$$

$$\begin{aligned} N^{\rm MC,2trk-nonQE}(i,j) &= P^{\rm SciBar}_{\rm Norm} \cdot P^{\rm SciBar}_{\rm 2trk/1trk} \cdot P^{\rm SciBar}_{\rm nonQE/QE} \\ &\times \sum_{k=1}^{8} f_k^\phi \cdot [N^{\rm MC,2trk-nonQE}_{k,{\rm QE}}(i,j) + R_{\rm nQE} \cdot N^{\rm MC,2trk-nonQE}_{k,{\rm nonQE}}(i,j)], \end{aligned} \tag{7.5}$$

$$\begin{aligned} N^{\rm MC,SBCNT}(i,j) &= P^{\rm SciBar}_{\rm Norm} \cdot P^{\rm SciBar}_{\rm EXT/CNT} \\ &\times \sum_{k=1}^{8} f_k^\phi \cdot [N^{\rm MC,SBCNT}_{k,{\rm QE}}(i,j) + R_{\rm nQE} \cdot N^{\rm MC,1trk}_{k,{\rm nonQE}}(i,j)], \end{aligned} \tag{7.6}$$

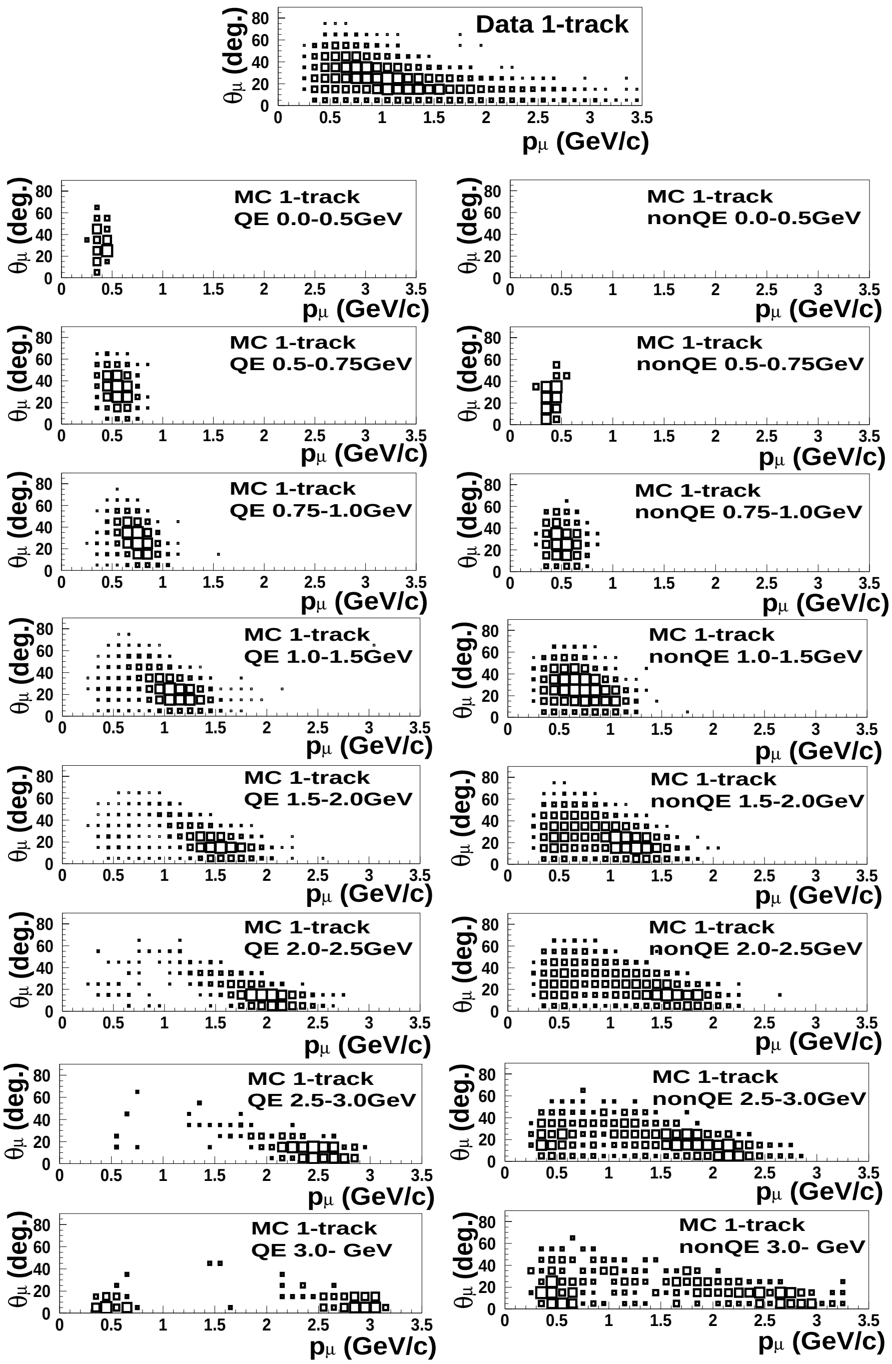

Figure 7.2: The (p_μ, θ_μ) distribution of SciBar-exiting 1-track sample for data and the MC template. The area of each box is proportional to the bin content. The topmost figure shows the observed data, and the others are the MC template for each E_ν bin of QE and nonQE interaction.

where $P^{\rm SciBar}_{\rm Norm}$, $P^{\rm SciBar}_{\rm 2trk/1trk}$, $P^{\rm SciBar}_{\rm nonQE/QE}$ and $P^{\rm SciBar}_{\rm EXT/CNT}$ are the fitting parameters. $P^{\rm SciBar}_{\rm Norm}$ is the normalization factor, which is free variable. $P^{\rm SciBar}_{\rm 2trk/1trk}$ and $P^{\rm SciBar}_{\rm nonQE/QE}$ are the parameters to vary the ratio of the number of 2-track sample to that of 1-track sample ($R^{\rm SciBar}_{\rm 2trk/1trk}$) and the ratio of the number of 2-track-QE sample to that of 2-track-nonQE sample ($R^{\rm SciBar}_{\rm nonQE/QE}$). $P^{\rm SciBar}_{\rm EXT/CNT}$ is the parameter of the normalization ratio between SciBar-exiting sample and SciBar-contained sample. $P^{\rm SciBar}_{\rm 2trk/1trk}$, $P^{\rm SciBar}_{\rm nonQE/QE}$ and $P^{\rm SciBar}_{\rm EXT/CNT}$ vary within their systematic errors.

In addition, the MC distributions are scaled along the p_μ axis by

$$p_\mu \to p'_\mu = \begin{cases} \frac{p_\mu}{P^{\rm SciBar}_{\rm MRD,p-scale}} & \text{(for SBEXT sample)} \\ \frac{p_\mu}{P^{\rm SciBar}_{\rm SB,p-scale}} & \text{(for SBCNT sample)} \end{cases} \tag{7.7}$$

, where $P^{\rm SciBar}_{\rm MRD,p-scale}$ and $P^{\rm SciBar}_{\rm SB,p-scale}$ are momentum scale parameters for SBEXT sample and SBCNT sample, respectively. They are constrained by the systematic terms in χ^2 function.

Definition of χ^2

The χ^2 function for SciBar ($\chi^2_{\rm SciBar}$) is computed from the ratio of Poisson likelihood [93]. In general, the likelihood of the contents in the (i,j)-bin (n_{ij}) with expectation values μ_{ij} at a certain parameter set $\boldsymbol{\theta} = (\theta_1, \theta_2, \cdots, \theta_D)$ is given by

$$f(n;\mu(\theta)) = \prod_{i=1}^{N}\prod_{j=1}^{M} \frac{\mu_{ij}(\theta)^{n_{ij}} \exp[-\mu_{ij}(\theta)]}{n_{ij}!}, \tag{7.8}$$

where M and N are the numbers of bins for the i and j, respectively.

In Fig. 7.2, the MC histograms for the neutrino energy greater than 1.5 GeV have additional event clusters at $p_\mu \sim 0.5$ GeV/c. They are hadrons mis-reconstructed as muons. The amount of hadron contamination is affected by the uncertainties in the hadron production off a nucleus. If we intentionally change pion absorption by ±30%, pion inelastic scattering by ±30%, and proton re-scattering by ±10%, the hadron contamination varies by ±10%. Therefore, we assign the systematic error of 10% to the hadron component. The systematic errors are implemented assuming Gaussian distributions in convolution with Eq. 7.8 as

$$f'(n;\mu(\theta);\sigma) = \prod_{i=1}^{N}\prod_{j=1}^{M} \int_0^{\rm inf} \frac{1}{\sqrt{2\pi}\sigma_{ij}} \exp\left[-\frac{(x-\mu_{ij}(\theta))^2}{2\sigma_{ij}^2}\right] \cdot \frac{x^{n_{ij}} e^{-x}}{n_{ij}!} dx, \tag{7.9}$$

where σ_{ij} is the systematic errors on hadron contamination for each bin. Maximizing this likelihood is equivalent to minimize the quantity as

$$-2\ln\frac{f(n;\mu(\theta))}{f(n;n)} = 2\sum_{i=1}^{N}\sum_{j=1}^{M}\left[\mu_{ij}(\theta) - n_{ij} + n_{ij}\ln\frac{n_{ij}}{\mu_{ij}(\theta)}\right]. \tag{7.10}$$

In the large sample limit, it follows the χ^2 distribution with $(NM - D)$ degrees of freedom. For the calculation of $\chi^2_{\rm SciBar}$, the (p_μ, θ_μ)-bins with more than five entries are used.

Finally, the χ^2_{SciBar} is defined as

$$\begin{aligned}
\chi^2_{\mathrm{SciBar}} &= -2\sum_C \ln \frac{f'(N^{\mathrm{data},C}; N^{\mathrm{MC},C}; \sigma)}{f'(N^{\mathrm{data},C}; N^{\mathrm{data},C}; \sigma)} && (7.11)\\
&+ (\boldsymbol{P}^{\mathrm{SBEXT}} - \langle \boldsymbol{P}^{\mathrm{SBEXT}} \rangle)^T (\boldsymbol{V}^{\mathrm{SBEXT}})^{-1} (\boldsymbol{P}^{\mathrm{SBEXT}} - \langle \boldsymbol{P}^{\mathrm{SBEXT}} \rangle) && (7.12)\\
&+ \sum_S \frac{(P_S^{\mathrm{SciBar}} - \langle P_S^{\mathrm{SciBar}} \rangle)^2}{(\sigma_S^{\mathrm{SBCNT}})^2} && (7.13)\\
C &= \{\text{1trk, 2trk-QE, 2trk-nonQE, SBCNT}\} && (7.14)\\
S &= \{\text{SB p-scale, EXT/CNT}\} && (7.15)
\end{aligned}$$

, where C runs across 1trk, 2trk-QE, 2trk-nonQE and SBCNT. The second and third terms are constraint terms on the systematic parameters for the SBEXT and SBCNT samples, respectively. The systematic errors on the event samples of SBEXT and SBCNT are assumed to be independent of each other.

Systematic term for SciBar-exiting sample

The variables, $\boldsymbol{P}^{\mathrm{SBEXT}}$ and $\langle \boldsymbol{P}^{\mathrm{SBEXT}} \rangle$, in the second term of Eq. 7.15, are the vectors of systematic parameters and their central values for SciBar-exiting sample, respectively. these are defined as

$$\boldsymbol{P}^{\mathrm{SBEXT}} \equiv \begin{pmatrix} P^{\mathrm{SciBar}}_{\mathrm{MRD,p-scale}} \\ P^{\mathrm{SciBar}}_{\mathrm{2trk/1trk}} \\ P^{\mathrm{SciBar}}_{\mathrm{nonQE/QE}} \end{pmatrix}, \qquad \langle \boldsymbol{P}^{\mathrm{SBEXT}} \rangle \equiv \begin{pmatrix} 1 \\ 1 \\ 1 \end{pmatrix}. \tag{7.16}$$

The uncertainty on each parameters are estimated to form constraint terms for the systematic parameters.

The momentum is reconstructed by the range in each detector (SciBar, EC and MRD) as described in Section 6.6. The uncertainty of the energy deposit in MRD is estimated within 2.7%. It is the sum of the errors on density measurement (1.0%) and the difference between the GEANT MC code and the PDG calculation (1.7%) [92]. The systematic error on the stopping power of EC is estimated to be $\pm$10%. The systematic error on the momentum scale in SciBar is estimated within $\pm$1.0% by the beam test as described in Section 4.5.4. Therefore, the systematic error of 2.7% is quoted on the momentum scale for the SciBar-exiting ($P^{\mathrm{SciBar}}_{\mathrm{MRD,p-scale}}$), since the most of the muon energy is deposited in MRD.

Since SBEXT sample is divided into three event samples (1-track, 2-track-QE and 2-track-nonQE) by N_{track} and $\Delta\theta_p$, the uncertainty in the selection causes the migration of events among 1-track, 2track-QE and 2-track-nonQE samples. To estimate the migration effects, we evaluate the errors on the ratio of the number of 2-track events to that of 1-track events ($R^{\mathrm{SciBar}}_{\mathrm{2trk/1trk}}$), and the ratio of the number of 2-track-QE events to the that of 2-track-nonQE events ($R^{\mathrm{SciBar}}_{\mathrm{nonQE/QE}}$). These systematic errors are summarized in Table 7.2, and the details are described later in this section.

The covariance matrix of $\boldsymbol{P}^{\mathrm{SBEXT}}$ ($\boldsymbol{V}^{\mathrm{SBEXT}}$) is estimated as

$$\boldsymbol{V}^{\mathrm{SBEXT}} \equiv \begin{pmatrix} 0.0007 & 0 & 0 \\ 0 & 0.0035 & 0.0003 \\ 0 & 0.0003 & 0.0034 \end{pmatrix}. \tag{7.17}$$

, where $(1,1)$ element is the systematic error on the momentum scale and the other elements are the systematic errors on $R^{\mathrm{SciBar}}_{\mathrm{2trk/1trk}}$ and $R^{\mathrm{SciBar}}_{\mathrm{nonQE/QE}}$. The asymmetric error is averaged, and the correlation is taken into account.

The estimation of the systematic errors on $R^{\rm SciBar}_{\rm 2trk/1trk}$ and $R^{\rm SciBar}_{\rm nonQE/QE}$ is summarized as follows.

Threshold : The hit threshold is set to 2.0 photo-electrons for SciBar. The standard deviation of the light yield for each cell is approximately 15%. In order to study the systematic effect, the threshold is changed by $\pm 15\%$. $R^{\rm SciBar}_{\rm 2trk/1trk}$ varies by $^{+0.7}_{-0.2}\%$, changing the hit threshold 2.3 p.e. and 1.7 p.e., respectively. Thus, the systematic error on $R^{\rm SciBar}_{\rm 2trk/1trk}$ is assigned to be $^{+0.7}_{-0.2}\%$.

Cross-talk : The cross-talk in the MA-PMT is emulated in the MC simulation. The variation of cross-talk is $\pm 50\%$ according to the laboratory measurement. If the parameter of the cross-talk emulation is changed by $\pm 50\%$, $R^{\rm SciBar}_{\rm 2trk/1trk}$ and $R^{\rm SciBar}_{\rm nonQE/QE}$ vary $^{+0.0}_{-1.4}\%$ and $^{+2.3}_{-1.0}\%$, respectively. Therefore, these numbers are assigned as the systematic errors caused by the cross-talk.

Track finding efficiency : The efficiency for the second track is compared between data and the MC simulation as a function of the number of hits. As a result of eye-scanning, $R^{\rm SciBar}_{\rm 2trk/1trk}$ of data and the MC simulation is different by $^{+0.9}_{-4.3}\%$. It is assigned to the systematic error.

Vertex matching efficiency : To obtain the number of tracks associating with the vertex, the matching condition is required in Section 6.5. The uncertainty of $R^{\rm SciBar}_{\rm 2trk/1trk}$ is estimated to be $^{+1.2}_{-2.0}\%$ by changing the track counting condition by $\pm 50\%$.

Angular resolution of a track : The angle resolution of a SciBar track is checked by comparing the angle between SciBar tracks and MRD tracks. Attributing the disagreement of the width between data and the MC simulation to the SciBar track resolution, the angular resolution of SciBar is estimated to be 2.7 degrees. The error on $R^{\rm SciBar}_{\rm nonQE/QE}$ is then obtained to be $^{+1.0}_{-0.0}\%$.

Angle shift : The angle difference between SciBar tracks and MRD tracks are considered as a systematic error on $R^{\rm SciBar}_{\rm nonQE/QE}$. The difference causes the systematic shift in $R^{\rm SciBar}_{\rm nonQE/QE}$ by -0.5% for the first track. For the proton-like tracks, the angular distributions are compared between data and the MC simulation. The angular distribution of the MC simulation shifts by -2.5 degrees from that of data. The angle shift corresponds to the systematic shift on $R^{\rm SciBar}_{\rm nonQE/QE}$ by -0.5% for the first tracks and -2.9% for the second tracks.

Energy scale : Since $\Delta\theta_p$ is calculated from the muon energy as Eq. 6.3, the uncertainty of the energy scale (2.7%) is the source of the error on $R^{\rm SciBar}_{\rm nonQE/QE}$. $R^{\rm SciBar}_{\rm nonQE/QE}$ varies by $^{+0.9}_{-0.6}\%$, shifting the energy scale by $\pm 2.7\%$.

Nuclear effects : Nuclear final state interactions affects the second track. The possible sources are proton re-scattering ($\pm$10%), pion absorption ($\pm$30%) and pion inelastic scattering ($\pm$30%). The uncertainties of them are estimated based on the errors on the past measurements. These effects change $R^{\rm SciBar}_{\rm 2trk/1trk}$ by $^{+4.1}_{-5.9}\%$ and $R^{\rm SciBar}_{\rm nonQE/QE}$ by $^{+5.1}_{-5.8}\%$. The systematic errors on the nuclear effects are summarized in Table 7.2.

Table 7.2: The systematic errors on $R^{\rm SciBar}_{\rm 2trk/1trk}$ and $R^{\rm SciBar}_{\rm nonQE/QE}$.

	$R^{\rm SciBar}_{\rm 2trk/1trk}$[%]		$R^{\rm SciBar}_{\rm nonQE/QE}$[%]	
Threshold	+0.7	-0.2	-	-
Cross-talk	+0.0	-1.4	+2.3	-1.0
Track finding efficiency	+0.9	-4.3	-	-
Vertex matching efficiency	+1.2	-2.0	-	-
Angular resolution	-	-	+1.0	-0.0
Angle shift (1st track)	-	-	-	-0.5
Angle shift (2nd track)	-	-	-	-2.9
Energy scale	-	-	+0.9	-0.6
Proton re-scattering	+2.6	-2.0	+1.2	-3.3
Pion absorption	+1.1	-1.8	+0.5	-2.4
Pion inelastic scattering	+2.4	-1.8	+4.3	-2.8
Total	+4.1	-5.9	+5.1	-5.8

Table 7.3: The central values and errors of the systematic parameters for SBCNT.

	Central value	Error
p-scale	1.	0.010
EXT/CNT	1.	0.066

Systematic term for SciBar-contained sample

The systematic parameters for SciBar-contained sample are $P^{\rm SciBar}_{\rm SB,p-scale}$ and $P^{\rm SciBar}_{\rm EXT/CNT}$, as shown in Eq. 7.15. The uncertainty on the momentum scale in SciBar is estimated within 1%. The normalization ratio between MRD-matching events and SciBar-contained events ($R^{\rm SciBar}_{\rm EXT/CNT}$) may vary by the systematic errors oriented from physics and detector response. The systematic errors on $R^{\rm SciBar}_{\rm EXT/CNT}$ are estimated by comparing SciBar-contained events and MRD-matching events in SciBar-exiting sample. EC-stopped events are ignored in this estimation because the statistical significance of EC-stopped events is not so large in SciBar-exiting sample. The estimation of the systematic errors on $R^{\rm SciBar}_{\rm EXT/CNT}$ are described as bellow.

Cross-talk : The evaluation method is described in the previous section. If the parameter of the cross-talk emulation are changed by $\pm 50\%$, $R^{\rm SciBar}_{\rm EXT/CNT}$ changes $^{+1.2}_{-0.0}$%.

Threshold : The evaluation method is described in previous section. If the threshold of 2.0 photo-electrons is varied by $\pm 15\%$, $R^{\rm SciBar}_{\rm EXT/CNT}$ changes $^{+0.0}_{-1.0}$%.

PMT resolution : PMT resolution is defined as

$$\text{PMT resolution} = \frac{\sigma_{\rm 1p.e.}}{\mu_{\rm 1p.e.}}, \tag{7.18}$$

where $\mu_{\rm 1p.e.}$ and $\sigma_{\rm 1p.e.}$ shows mean and sigma of 1 p.e. peak by Gaussian fitting, respectively. The resolution varies 70% $\sim$ 100% at the operation gain (5.0×10^5) in our measurement, whereas the

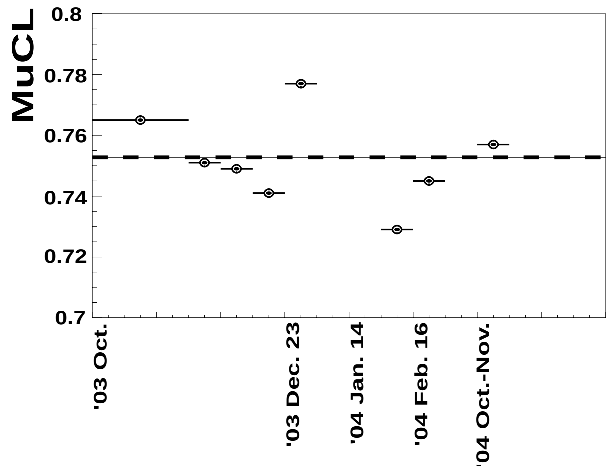

Figure 7.3: The MuCL stability at the threshold value, where satisfies 90% efficiency.

input vale for the MC simulation is 40%. If the resolution is set to 120% as the input value to the MC simulation, $R^{\rm SciBar}_{\rm EXT/CNT}$ decreases by -2.8%. It is assigned to the systematic error.

PID stability : The stability of the MuCL in the period of SciBar data taking is checked, which is defined in Section 6.4.2. The threshold value of the MuCL to satisfy the 90% efficiency for muons are shown in Fig. 7.3 as a function of data-taking period. The MuCL varies from 0.729 to 0.777, therefore $^{+0.5}_{-0.7}$% is assigned as the uncertainty in $R^{\rm SciBar}_{\rm EXT/CNT}$.

MuCL distribution : The MuCL distribution shown in Fig. 6.8 has discrepancy between data and MC simulation. To evaluate the error on $R^{\rm SciBar}_{\rm EXT/CNT}$, the scaling factor is multiplied to the statistical error of each bin in Fig. 6.8 as

$$\sigma(i) = \sigma_{\rm stat}(i) \times (\text{scaling factor}), \tag{7.19}$$

where $\sigma_{\rm stat}(i)$ shows statistical error of the i-th bin. Changing the scaling factor, $\sigma(i)$ to make the probability of χ^2 95% are used. By using the errors, the possible migration to SciBar-contained events from the region of less than 0.1 can be calculated, and ±1.6% is assigned on the error of $R^{\rm SciBar}_{\rm EXT/CNT}$.

Scintillator quenching : The effect of scintillator quenching is observed in the beam test result. By changing the Birk's constant within the measurement error, $R^{\rm SciBar}_{\rm EXT/CNT}$ varies $^{+3.3}_{-3.0}$%.

MRD matching efficiency : MRD matching efficiency is estimated by using EC-matching tracks. The efficiency is 91.7 ± 2.3% for data and 92.4 ± 1.1% for the MC simulation. This 0.7% difference between data and the MC simulation corresponds to ±2.0% error on $R^{\rm SciBar}_{\rm EXT/CNT}$.

Nuclear effect : The evaluation method is described in previous section. The systematic errors on the nuclear effects are summarized in Table 7.4.

M_A (CC-QE, CC1π) : In the MC simulation, M_A value of 1.11 GeV/c^2 is used for CC-QE and CC1π. The uncertainty on $R^{\rm SciBar}_{\rm EXT/CNT}$ is estimated by changing M_A value by ±0.1 GeV/c^2. $R^{\rm SciBar}_{\rm EXT/CNT}$ varies within $^{+0.2}_{-0.5}$% for CC-QE and $^{+1.6}_{-2.1}$% for CC1π.

Table 7.4: The systematic errors on $R^{\mathrm{SciBar}}_{\mathrm{EXT/CNT}}$.

	$R^{\mathrm{SciBar}}_{\mathrm{EXT/CNT}}$ [%]	
M_A(CCQE) (M_A=1.01, 1.21)	$+0.2$	-0.5
M_A(CC1π) (M_A=1.01, 1.21)	$+1.6$	-2.1
π interaction out of nucleus ($\pm$10%)	$+0.5$	-1.3
π inelastic scattering ($\pm$30%)	$+2.2$	-1.7
π absorption ($\pm$30%)	$+1.2$	-1.7
Proton re-scattering ($\pm$10%)	$+1.6$	-0.0
Cross section of NC interaction ($\pm$30%)	$+2.4$	-2.4
PMT resolution (120%)	$+0.0$	-2.8
Cross-talk (1.6%, 4.0%)	$+1.2$	-1.2
Threshold ($+$15%)	$+0.0$	-1.0
PID stability ($\pm$0.03%)	$+0.5$	-0.7
MuCL distribution	$+1.6$	-1.6
Scintillator quenching ($\pm$0.0023%)	$+3.3$	-3.0
MRD matching efficiency	$+2.0$	-2.0
Total	$+6.0$	-6.6

Cross section of NC interaction : The uncertainty of $\pm$30% is assigned to NC cross-section. This uncertainty gives $\pm$2.4% error on $R^{\mathrm{SciBar}}_{\mathrm{EXT/CNT}}$.

The uncertainty on $R^{\mathrm{SciBar}}_{\mathrm{EXT/CNT}}$ is estimated $^{+6.0}_{-6.6}$% as summarized in Table 7.4. The larger value of the systematic errors, 6.6%, is taken for the error on $P^{\mathrm{SciBar}}_{\mathrm{EXT/CNT}}$.

The center values and the systematic errors for $P^{\mathrm{SciBar}}_{\mathrm{SB,p-scale}}$ and $P^{\mathrm{SciBar}}_{\mathrm{EXT/CNT}}$ are summarized in Table 7.3.

7.2.3 Measurement results with SciBar

The spectrum fitting only with SciBar data is carried out to study the effect of low energy samples on the low energy region. Table 7.5 shows the summary of the spectrum fitting for SciBar data. The overall normalization is given by setting f^{ϕ}_4 to unity (constant). The fitting parameters for the energy below 0.5 GeV (f^{ϕ}_1) and above 3 GeV (f^{ϕ}_8) are fixed at the unity in addition to f^{ϕ}_4, since the statistics in the energy bin contents is too small to determine the weighting parameters.

For comparison with various event sample, the fitting result of only MRD events without the correction of multiple scattering effect for MRD1L events as described in Section 6.4.3, is also shown. The fitting error on neutrino energy of 0.5 to 0.75 GeV for combined event sample of SBEXT and SBCNT, gets better from 0.254 to 0.223 comparing to the fitting with only MRD events. Figure 7.4 shows the summary of the best fit parameters for SciBar data. The fitting results are consistent with each others. In addition, the significant shift of the fitting parameters in the low energy sample is not observed.

To check the source of the error on low energy region, the contribution of the statistical error to the low energy region is studied by using the toy-MC simulation. In the-toy MC simulation, the bin contents in the (p_μ, θ_μ) distribution for data is varied with the Poisson function for each spectrum fitting.

Table 7.5: Summary of the spectrum fitting results for SciBar data.

	SBEXT + SBCNT	SBEXT only	MRD only (previous selection)
0.0-0.5	$\mathbf{\equiv 1}$	$\equiv 1$	$\equiv 1$
0.5-0.75	$\mathbf{1.043 \pm 0.223}$	1.040 ± 0.236	1.166 ± 0.254
0.75-1.0	$\mathbf{1.118 \pm 0.131}$	1.130 ± 0.133	1.133 ± 0.136
1.0-1.5	$\mathbf{\equiv 1}$	$\equiv 1$	$\equiv 1$
1.5-2.0	$\mathbf{0.961 \pm 0.069}$	0.974 ± 0.071	0.964 ± 0.070
2.0-2.5	$\mathbf{0.985 \pm 0.082}$	0.989 ± 0.083	0.970 ± 0.083
2.5-3.0	$\mathbf{1.450 \pm 0.195}$	1.470 ± 0.198	1.470 ± 0.198
3.0-	$\mathbf{\equiv 1}$	$\equiv 1$	$\equiv 1$
R_{nQE}	$\mathbf{1.186 \pm 0.086}$	1.197 ± 0.089	1.234 ± 0.096
$P^{\mathrm{SciBar}}_{\mathrm{Norm}}$	$\mathbf{0.997 \pm 0.010}$	0.998 ± 0.010	0.998 ± 0.010
$P^{\mathrm{SciBar}}_{\mathrm{MRD,p-scale}}$	$\mathbf{0.973 \pm 0.004}$	0.973 ± 0.004	0.972 ± 0.004
$P^{\mathrm{SciBar}}_{\mathrm{2trk/1trk}}$	$\mathbf{0.956 \pm 0.022}$	0.956 ± 0.022	0.957 ± 0.024
$P^{\mathrm{SciBar}}_{\mathrm{nonQE/QE}}$	$\mathbf{1.005 \pm 0.040}$	1.001 ± 0.041	0.994 ± 0.043
$P^{\mathrm{SciBar}}_{\mathrm{EXT/CNT}}$	$\mathbf{0.922 \pm 0.032}$	–	–
$P^{\mathrm{SciBar}}_{\mathrm{SB,p-scale}}$	$\mathbf{1.004 \pm 0.007}$	–	–
χ^2/d.o.f	$\mathbf{298.4/255}$	252.4/229	253.5/229
χ^2/Nbins	$\mathbf{298.4/267}$	252.4/239	254.4/239

Fixing all parameters at the best fit values except for the flux of neutrino energy of 0.5 to 0.75 GeV, f_2^{ϕ}, the spectrum fitting is performed to study the contribution of the statistical error on f_2^{ϕ}. Figure 7.5 shows the distribution of the fitting results for f_2^{ϕ}. The fitting results on f_2^{ϕ} distribute like Gaussian function with the standard deviation of 0.18, while the error obtained by the fitting is 0.22. Therefore, the source the error on f_2^{ϕ} is dominated by the statistical error. For more study on f_2^{ϕ}, the spectrum fitting with the toy-MC simulation is performed, increasing the statistics by four times. The error on f_2^{ϕ} becomes about 0.1, reflecting the statistical dependence.

Fig. 7.6 shows the neutrino energy spectrum measured by SciBar, which is obtained by multiplying the cross-section in SciBar to the neutrino flux obtained by beam MC simulation, where the open circle shows the obtained spectrum and the solid line shows beam MC simulation.

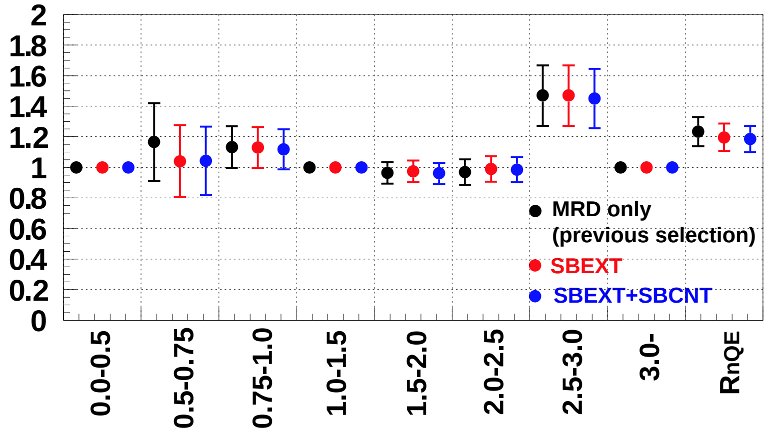

Figure 7.4: Summary of the best fit parameter for the spectrum measurement by SciBar.

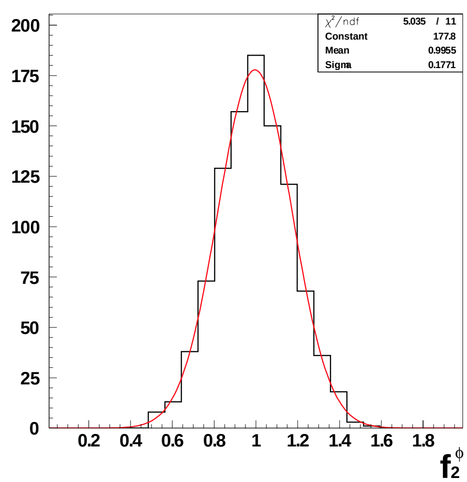

Figure 7.5: A distribution of the fitting results for f_2^{ϕ} by the toy-MC simulation.

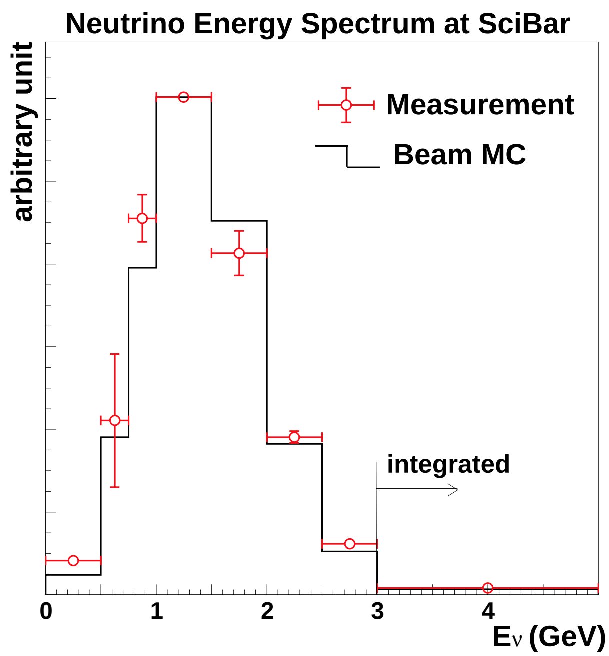

Figure 7.6: A neutrino energy spectrum at the near site measured by SciBar. The open circle shows the obtained spectrum and the solid line shows beam MC simulation.

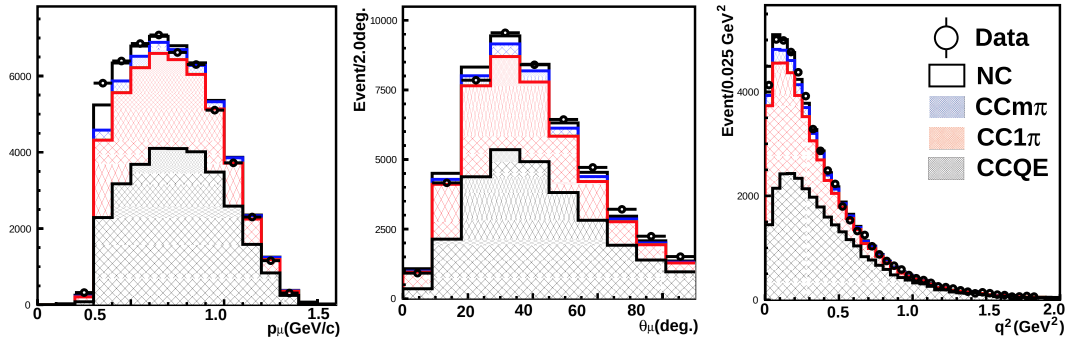

Figure 7.7: The reconstructed p_μ, θ_μ and q^2 distributions of 1KT before the spectrum fitting.

7.3 Spectrum measurement with all near detectors

In this section, the neutrino energy spectrum is measured by using all the near detectors. For the consistency check, the results of the spectrum measurement by each detector are compared. Especially, the energy spectrum in the low energy region is compared with the results of SciBar and 1KT. Finally, the neutrino energy spectrum at the near site is measured by using all the near detectors.

7.3.1 Event sample

To obtain the final results of the spectrum measurement at the near site, the neutrino spectrum is measured by combined data sample of all the near detectors. The data samples for each near detector is summarized below.

1KT

Since the proton momentum from CC-QE interaction is usually below Cherenkov threshold in this experiment, only one-ring muon-like events are suitable for CC-QE selection. In addition, the muon tracks in 1KT are required to be contained within the fiducial volume of 1KT to measure the muon momentum. Those events are used as the fully-contained muon-like (FC1R$_\mu$) sample for the spectrum fitting. The event selection criteria for 1KT is described in Appendix C.1.

Figure 7.7 shows the reconstructed p_μ, θ_μ and q^2 distributions of the FC1Rμ sample. The momentum threshold is approximately 0.3 GeV/c, and muons above 1 GeV/c are almost rejected by the FC requirement. Another feature of 1KT data is the larger angular acceptance than SciBar and SciFi.

SciFi

Two data sets, K2K-Ib (with LG) and K2K-IIa (without LG), are used for SciFi data. In K2K-IIa, there was a four-layer prototype of SciBar (Mini-SciBar) instead of LG. K2K-IIb and K2K-IIc (with SciBar) are not used in this analysis.

Three kinds of CC event categories, K2K-Ib MRD-matching, K2K-Ib LG-stopped and K2K-IIa MRD-matching are selected. For these three categories, 1-track, 2-track-QE and 2-track-nonQE samples are prepared, whose classification is the same as that in SciBar. In total, nine distributions are used for the fitting. The event selection criteria for SciFi is described in Appendix C.2. Figure 7.8 shows the reconstructed p_μ, θ_μ and q^2 distributions of each event sample of SciFi.

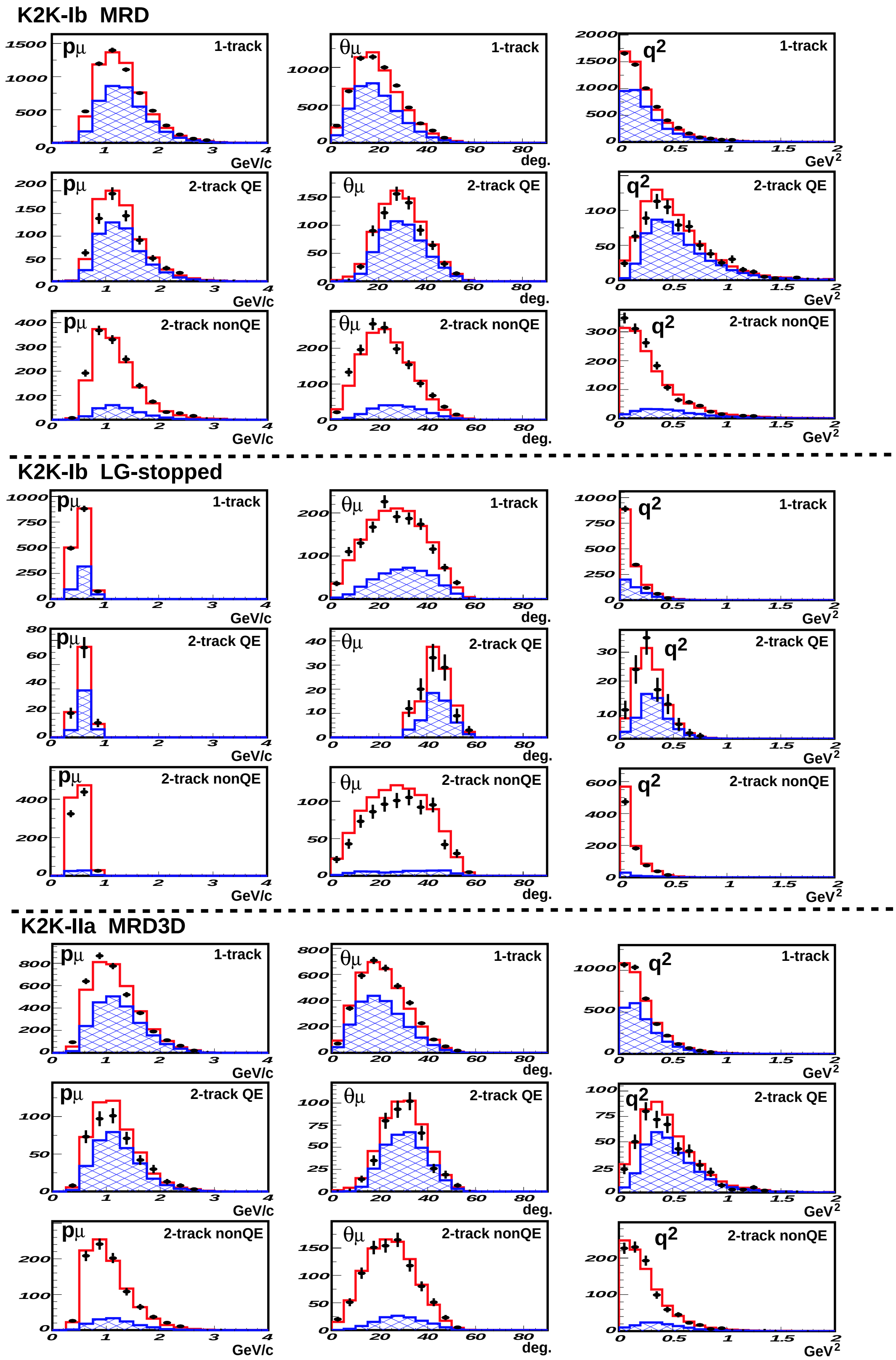

Figure 7.8: The reconstructed p_μ, θ_μ and q^2 distribution of SciFi K2K-Ib MRD-matching events, K2K-Ib LG-stopped events and K2K-IIa MRD-matching events before the spectrum fitting. The hatched region shows the fraction of CCQE.

SciBar

The event samples are prepared in Chapter 6.

7.3.2 Fitting procedure

As the same procedure of the spectrum measurement by SciBar in Section 7.2, the χ^2 fitting is applied to the 2-dimensional (p_μ,θ_μ) distribution between data and the MC simulation by using data samples obtained by each near detector. In total, fourteen distributions are fitted at the same time, which are one sample for 1KT, nine samples for SciFi, and four samples for SciBar. The PIMON result is also employed as the constraint term on f_i^ϕ above 1 GeV.

The χ^2 functions are constructed for each detector, and the final χ^2 function to be minimized is the summation of each χ^2 function expressed as

$$\chi^2 = \chi^2_{\rm 1kt} + \chi^2_{\rm SciFi} + \chi^2_{\rm SciBar} + \chi^2_{\rm PIMON}, \tag{7.20}$$

where $\chi^2_{\rm SciBar}$, $\chi^2_{\rm SciFi}$, $\chi^2_{\rm 1kt}$ and $\chi^2_{\rm PIMON}$ are χ^2 for SciBar, SciFi, 1KT and PIMON data, respectively. They are defined in the following sections.

Some other fitting parameters are introduced to deal with the detector systematics in the MC distribution, which are defined as follows.

- 1KT
  - $P^{\rm 1KT}_{\rm Norm}$: The overall normalization for 1KT
  - $P^{\rm 1KT}_{\rm p-scale}$: The momentum scale in 1KT
- SciFi
  - $P^{\rm SciFi}_{\rm Norm}$: The overall normalization for SciFi
  - $P^{\rm SciFi}_{\rm 2nd-eff}$: The efficiency to find the second track
  - $P^{\rm SciFi}_{\rm rescat}$: The scale factor of the proton re-scattering cross-section
  - $P^{\rm SciFi}_{\rm E-scale}$, $P^{\rm SciFi}_{\rm LG-density}$, $P^{\rm SciFi}_{\rm LG-cluster}$: The energy scale parameters of the measurement by the range in MRD and LG and the LG pulse height of a hit cluster in LG, respectively.
- SciBar
  - The systematic parameters are defined in Section 7.2.

They are restricted within the systematic errors with the additional χ^2 terms. The normalization factor for each detector is a free variable during the fit, because the aim of the fit is to obtain only the shape of the spectrum. The overall normalization is given by setting f_4^ϕ to unity as the fitting with only SciBar. The definition of the χ^2 functions for 1KT, SciFi and PIMON is described in Appendix C.

7.3.3 Measurement results with all near detectors

The spectrum fitting with all data samples, “merged fit”, is performed. Table 7.6 and Fig. 7.9 show summary of the spectrum fitting results. The results are consistent with each detector except for $R_{\rm nQE}$. To study the bias on $R_{\rm nQE}$, the spectrum fitting is performed with several fitting conditions, those are the fitting with only 1KT, only SciFi and only SciBar. Since $R_{\rm nQE}$ has correlation with the other

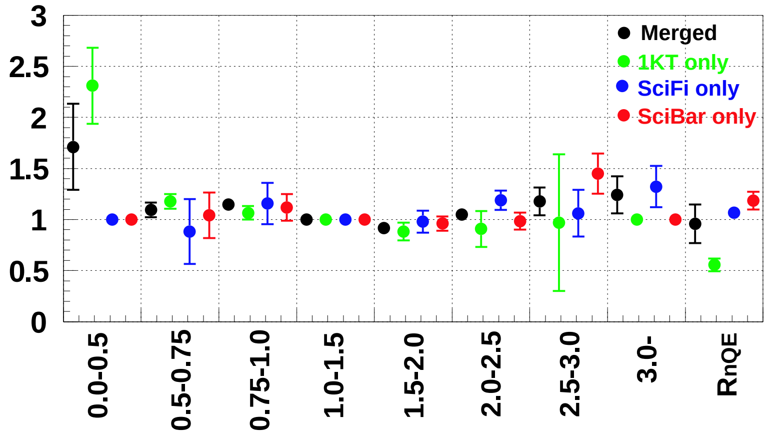

Figure 7.9: Summary of the spectrum fit results.

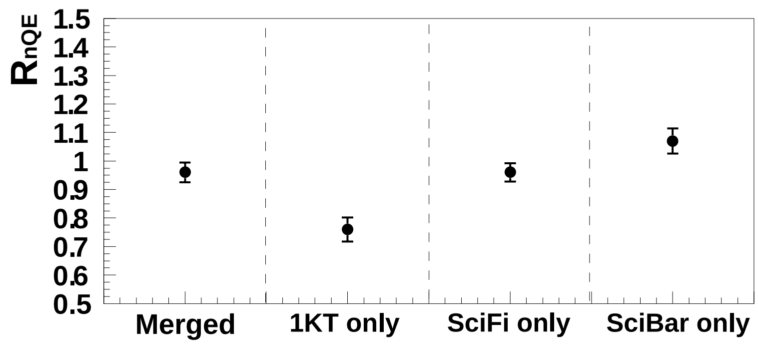

Figure 7.10: Systematic differences of $R_{\rm nQE}$ obtained by each detector.

systematic parameters, all the parameters other than $R_{\rm nQE}$ are fixed at the best fit values to estimate the systematic difference of $R_{\rm nQE}$ in each fitting condition. Figure 7.10 shows systematic difference of $R_{\rm nQE}$ for each fitting condition. Since $R_{\rm nQE}$ varies for each fitting condition within 20% from the fitting result of the merged fit, the additional error of 20% is assigned on $R_{\rm nQE}$.

In the spectrum fitting, the χ^2 function might settle down at the local minimum point. Therefore, the behavior of the χ^2 function around the best fit point as a function of each fitting parameter value, are checked as shown in Fig. 7.11. The minimization of the χ^2 function have been successfully done to find the global minimum point.

Figure 7.12, 7.13 and 7.14 show the reconstructed p_μ, θ_μ and q^2 distributions at the best fit of 1KT, SciFi and SciBar samples, respectively.

In the study of the neutrino oscillation, both the best fit values of f_i^ϕ and $R_{\rm nQE}$ and the error matrix are used, so that the correlations between parameters are taken into account. The systematic error on $R_{\rm nQE}$ is added to the matrix including the correlation. Table 7.6 shows the summary of the best fit values and the error matrix.

Table 7.6: Summary of the spectrum fitting results for all the near detectors.

	Merged	1KT only	SciFi only	SciBar only
0.0-0.5	$\mathbf{1.712 \pm 0.421}$	2.310 ± 0.373	$\equiv 1$	$\equiv 1$
0.5-0.75	$\mathbf{1.095 \pm 0.073}$	1.178 ± 0.071	0.882 ± 0.317	1.043 ± 0.223
0.75-1.0	$\mathbf{1.146 \pm 0.059}$	1.066 ± 0.065	1.157 ± 0.201	1.118 ± 0.131
1.0-1.5	$\mathbf{\equiv 1}$	$\equiv 1$	$\equiv 1$	$\equiv 1$
1.5-2.0	$\mathbf{0.917 \pm 0.040}$	0.882 ± 0.087	0.980 ± 0.107	0.961 ± 0.069
2.0-2.5	$\mathbf{1.051 \pm 0.053}$	0.908 ± 0.176	1.188 ± 0.096	0.985 ± 0.082
2.5-3.0	$\mathbf{1.179 \pm 0.136}$	0.970 ± 0.668	1.062 ± 0.230	1.450 ± 0.195
3.0-	$\mathbf{1.242 \pm 0.180}$	$\equiv 1$	1.323 ± 0.203	$\equiv 1$
$R_{\rm nQE}$	$\mathbf{0.958 \pm 0.035}$	0.556 ± 0.062	1.069 ± 0.060	1.186 ± 0.086
$P^{\rm 1KT}_{\rm Norm}$	$\mathbf{0.953 \pm 0.024}$	1.168 ± 0.047	-	-
$P^{\rm 1KT}_{\rm p-scale}$	$\mathbf{0.984 \pm 0.004}$	0.998 ± 0.006	-	-
$P^{\rm SciFi}_{\rm Norm}$	$\mathbf{1.013 \pm 0.028}$	-	0.925 ± 0.058	-
$P^{\rm SciFi}_{\rm E-scale}$	$\mathbf{0.980 \pm 0.006}$	-	0.980 ± 0.007	-
$P^{\rm SciFi}_{\rm LG-density}$	$\mathbf{0.929 \pm 0.012}$	-	0.927 ± 0.012	-
$P^{\rm SciFi}_{\rm 2nd-eff}$	$\mathbf{0.960 \pm 0.014}$	-	0.932 ± 0.017	-
$P^{\rm SciFi}_{\rm rescat}$	$\mathbf{1.052 \pm 0.055}$	-	0.993 ± 0.062	-
$P^{\rm SciFi}_{\rm LG-cluster}$	$\mathbf{-1.368 \pm 2.488}$	-	-1.859 ± 2.567	-
$P^{\rm SciBar}_{\rm Norm}$	$\mathbf{0.996 \pm 0.010}$	-	-	0.997 ± 0.010
$P^{\rm SciBar}_{\rm MRD,p-scale}$	$\mathbf{0.976 \pm 0.003}$	-	-	0.973 ± 0.004
$P^{\rm SciBar}_{\rm 2trk/1trk}$	$\mathbf{0.951 \pm 0.022}$	-	-	0.956 ± 0.023
$P^{\rm SciBar}_{\rm nonQE/QE}$	$\mathbf{1.092 \pm 0.032}$	-	-	1.005 ± 0.040
$P^{\rm SciBar}_{\rm EXT/CNT}$	$\mathbf{0.923 \pm 0.032}$	-	-	0.922 ± 0.032
$P^{\rm SciBar}_{\rm SB,p-scale}$	$\mathbf{1.005 \pm 0.007}$	-	-	1.004 ± 0.007
χ^2/d.o.f	$\mathbf{728.5/614}$	48.2/74	328.7/273	298.4/255
Goodness [%]	$\mathbf{0.1}$	99.1	1.2	3.2
$\chi^2_{\rm 1KT}$/Nbins	$\mathbf{84.9/80}$	47.7/80	-	-
$\chi^2_{\rm SciFi}$/Nbins	$\mathbf{336.0/286}$		328.7/286	-
$\chi^2_{\rm SciBar}$/Nbins	$\mathbf{298.4/267}$	-	-	298.4/267
$\chi^2_{\rm PIMON}$/Nbins	$\mathbf{0.9/3}$	0.5/3	-	-

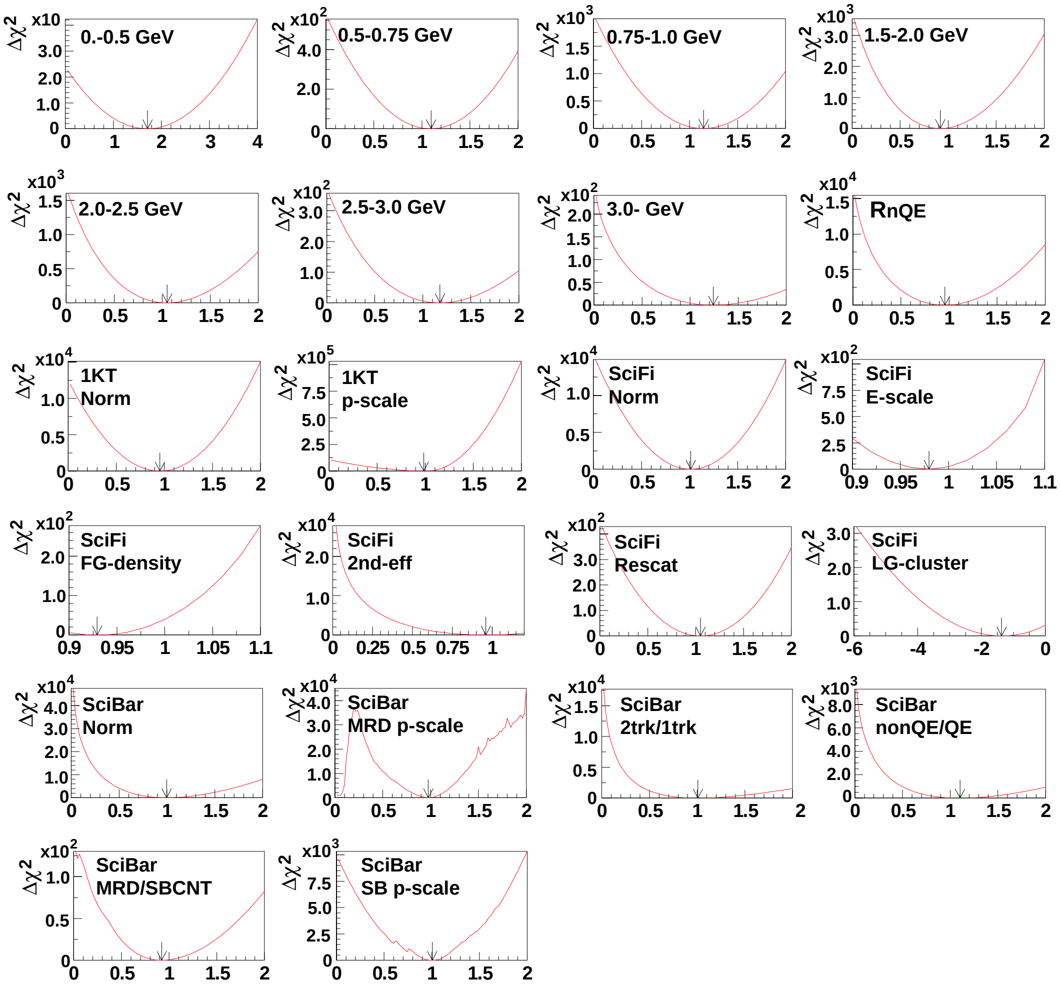

Figure 7.11: Behavior of $\Delta\chi^2$ around the best fit point as a function of each fitting parameter value. In each figure, the other parameters are fixed at the best-fit point. The horizontal and vertical axis shows the parameter values and the $\Delta\chi^2$, which is the difference from the minimum (best-fit) χ^2. The arrow in each figure shows the best-fit point.

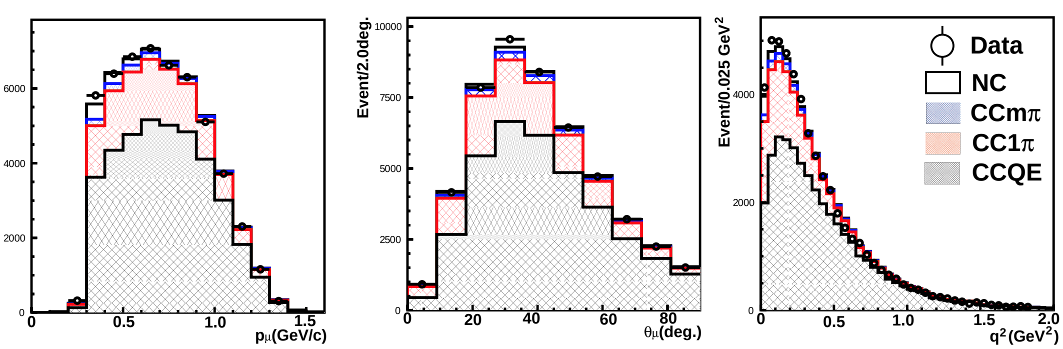

Figure 7.12: The reconstructed p_μ, θ_μ and q^2 distributions of 1KT after the spectrum fitting.

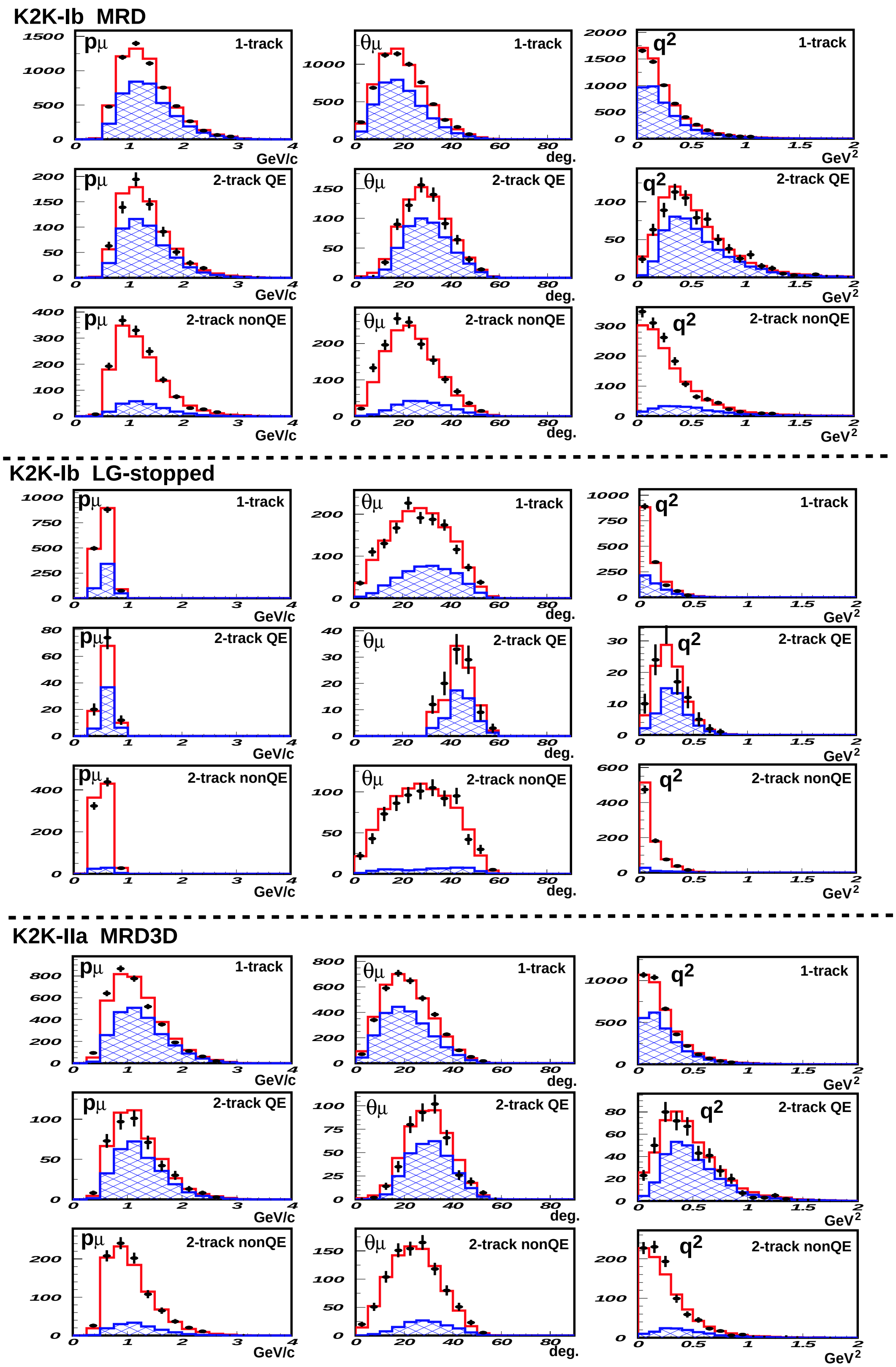

Figure 7.13: The reconstructed p_μ, θ_μ and q^2 distribution at the best fit of SciFi K2K-Ib MRD-matching events, K2K-Ib LG-stopped events and K2K-IIa MRD-matching events. The hatched region shows the fraction of CCQE.

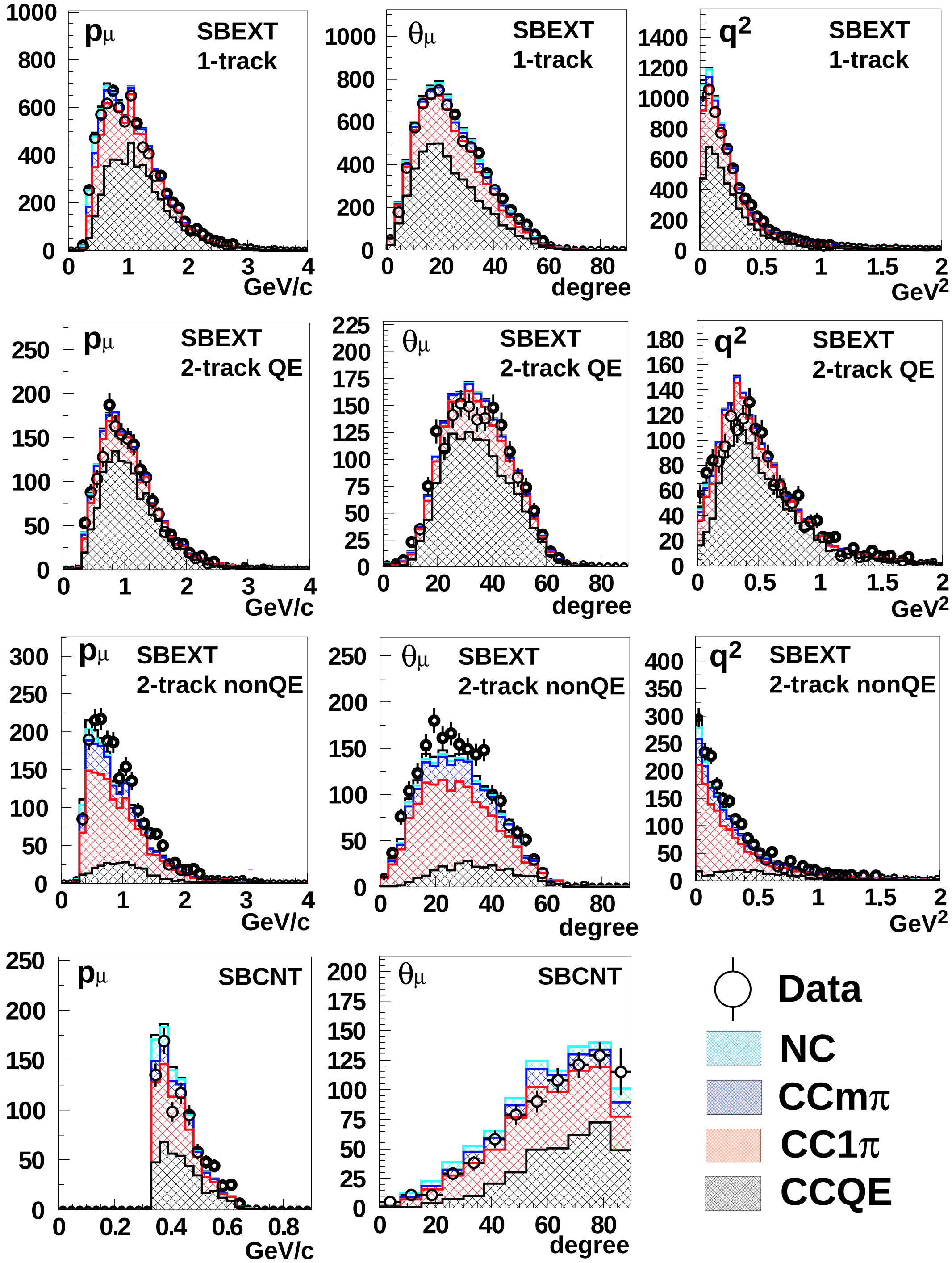

Figure 7.14: The reconstructed p_μ, θ_μ and q^2 distribution at the best fit of SciBar SBEXT 1-track events, and SBEXT 2-track-QE events, SBEXT 2-track-nonQE events and SBCNT events.

Table 7.7: Summary of the best fit values and the error matrix.

	f_1^ϕ	f_2^ϕ	f_3^ϕ	f_4^ϕ	f_5^ϕ	f_6^ϕ	f_7^ϕ	f_8^ϕ	R_{nQE}
Best fit	1.711	1.095	1.146	≡1	0.917	1.051	1.179	1.241	0.958
Error	0.421	0.073	0.059	-	0.040	0.053	0.135	0.179	0.203
f_1^ϕ	1.78×10^{-1}	-5.23×10^{-4}	5.12×10^{-4}	-	-3.60×10^{-4}	-1.02×10^{-4}	-9.24×10^{-4}	-3.75×10^{-4}	-2.26×10^{-2}
f_2^ϕ	-5.30×10^{-4}	5.34×10^{-3}	3.63×10^{-4}	-	3.66×10^{-4}	5.06×10^{-5}	2.07×10^{-4}	3.13×10^{-4}	-4.06×10^{-3}
f_3^ϕ	5.21×10^{-3}	3.63×10^{-4}	3.52×10^{-3}	-	1.14×10^{-3}	2.73×10^{-4}	1.19×10^{-3}	2.29×10^{-4}	-1.24×10^{-3}
f_4^ϕ	-	-	-	-	-	-	-	-	-
f_5^ϕ	-3.60×10^{-4}	3.66×10^{-4}	1.14×10^{-3}	-	1.63×10^{-3}	3.48×10^{-4}	2.03×10^{-3}	5.07×10^{-4}	3.46×10^{-4}
f_6^ϕ	-1.02×10^{-4}	5.06×10^{-5}	2.73×10^{-3}	-	3.48×10^{-4}	2.78×10^{-3}	3.42×10^{-3}	2.64×10^{-3}	1.49×10^{-4}
f_7^ϕ	-9.24×10^{-4}	2.07×10^{-4}	1.19×10^{-3}	-	2.03×10^{-3}	3.42×10^{-4}	1.85×10^{-3}	1.02×10^{-2}	1.28×10^{-3}
f_8^ϕ	-3.75×10^{-4}	3.13×10^{-4}	2.29×10^{-4}	-	5.07×10^{-4}	2.64×10^{-3}	1.02×10^{-2}	3.24×10^{-2}	-4.87×10^{-3}
f_{nQE}	-2.26×10^{-2}	-4.06×10^{-3}	-1.24×10^{-3}	-	3.46×10^{-4}	1.49×10^{-4}	1.28×10^{-3}	-4.87×10^{-3}	4.12×10^{-2}

Finally, the neutrino energy spectrum at the near site is measured by using all the near detectors as shown in Fig. 7.15. It is obtained by multiplying the cross-section in SciBar to the neutrino flux obtained by beam MC simulation, where the open circle shows obtained spectrum and the solid line shows beam MC simulation. In the oscillation analysis, the obtained energy spectrum is employed.

7.4 Summary

In this chapter, the neutrino energy spectrum at the near site is measured by using muon momentum and angle. For the purpose, the χ^2 fitting is applied to the 2-dimensional (p_μ, θ_μ) distribution. Especially, the low energy region below 1 GeV is studied in detail by using SciBar low energy events. The obtained results in this analysis are summarized below.

- The neutrino energy spectrum is measured by using only SciBar. The method to investigate the low energy region by SciBar is established in this study. This enables to measure the neutrino spectrum in the energy region from 0.5 to 3.0 GeV by using only SciBar. With the low energy samples, the measurement error on the neutrino energy of 0.5 to 0.75 GeV is improved from 25.4% to 22.3%, comparing to the previous selection method of the SciBar sample. According to the results of the toy-MC simulation, the error on the low energy region mainly comes from the statistical error.

- The consistency on the neutrino energy spectrum measured by each near detector is checked. Estimating the contamination of nonQE interaction in the fitting samples, the low energy spectrum measured by SciBar is confirmed to be consistent with 1KT.

- The neutrino energy spectrum at the near site is measured by using all the near detectors.

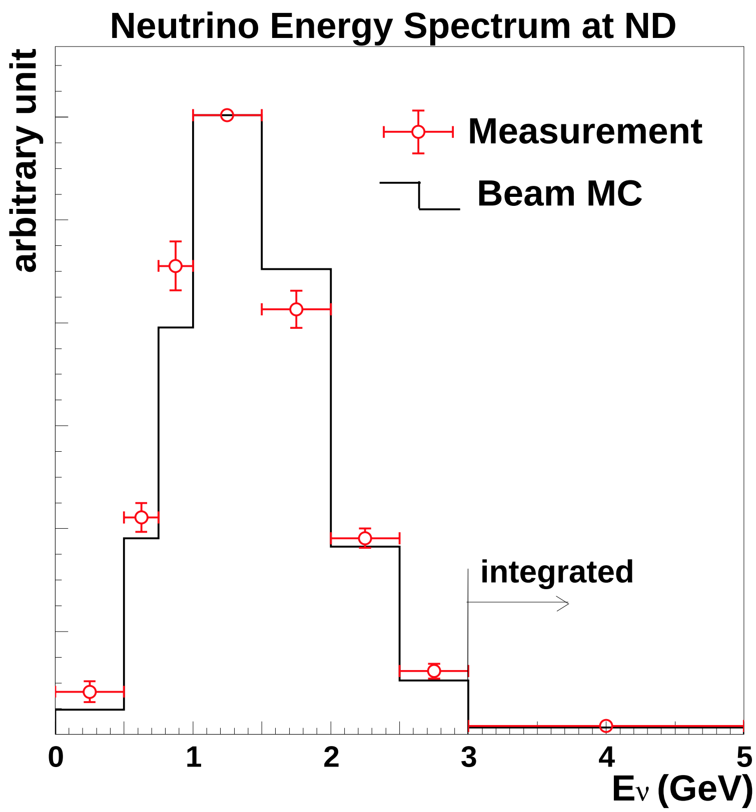

Figure 7.15: Neutrino energy spectrum at the near site. The open circle shows obtained spectrum and the solid line shows beam MC simulation.

Chapter 8

Extrapolation from KEK to SK

To study neutrino oscillation, a number of neutrino events and the energy spectrum observed at SK is compared with the expectation by the measurement at the near detectors (ND). The expected number of events at SK ($N_{\mathrm{SK}}^{\mathrm{exp}}$) is estimated with the neutrino energy spectrum ratio of far to near site ($R^{\mathrm{F/N}}(E_\nu)$) and the number of interaction observed at ND. $R^{\mathrm{F/N}}(E_\nu)$ is calculated by using the MC simulation, whose errors are estimated with results from PIMON measurement. In this chapter, the estimation of $R^{\mathrm{F/N}}(E_\nu)$ and $N_{\mathrm{SK}}^{\mathrm{exp}}$ is described.

8.1 Far/Near spectrum ratio

$R^{\mathrm{F/N}}(E_\nu)$ is evaluated for the following two purpose.

- Extrapolation of the energy spectrum from ND to SK.
- Estimation of the expected number of events at SK.

The generated position of the neutrinos has a finite size for the near detectors due to the long decay volume, whereas it becomes the point source for SK. Therefore, $R^{\mathrm{F/N}}(E_\nu)$ is evaluated by using the MC simulation. For the confirmation and the error estimation of the MC simulation, the neutrino flux at the near site is studied with the measurement of the pion momentum (p_π) and angle with respect to the beam axis (θ_π) by PIMON. Since the neutrinos are generated from the pion decay, the neutrino flux is estimated by distributions of the p_π and θ_π.

8.1.1 Measurement of the (p_π, θ_π) distribution

The PIMON measurements have been performed twice, in June 1999 and November 1999, because the horn configuration was changed as described in Section 3.1.3. The former was done with the single-bunch operation of 7×10^{10} protons per pulse (ppp), while the latter was done with the nine-bunch operation of 7×10^{11} ppp. In the both cases, the proton intensity is lower than the normal run ($\sim 6 \times 10^{12}$ ppp), because the Cherenkov light is too intense to keep the response linearity of the PMTs. The measurement results of the (p_π, θ_π) distribution and errors on them in Nov. 1999 run are shown in Fig. 8.1.

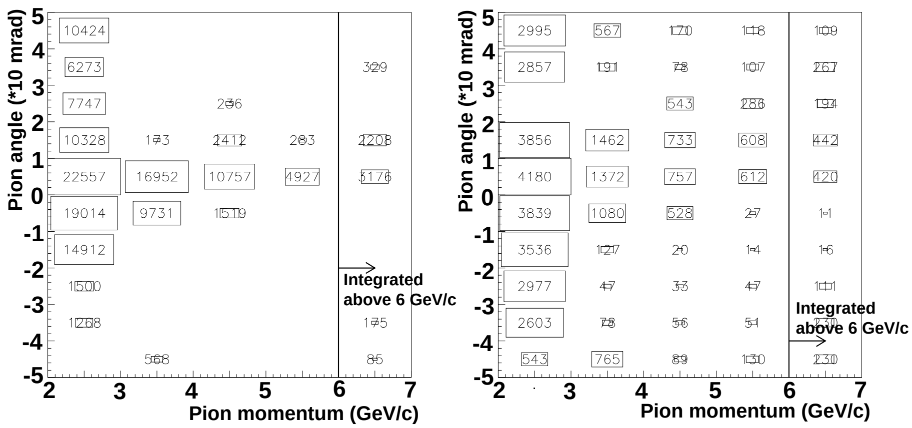

Figure 8.1: The fit result of the (p_π, θ_π) distribution for November 1999 run. The left figure shows the bin content of each bin, and right figure shows the fitting error.

8.1.2 Far/Near spectrum ratio

The expected neutrino spectrum at ND (SK) ($\phi_{i,j}^{\mathrm{ND(SK)}}(E_\nu)$) is calculated by the MC simulation, which is modified with the measurement results of the $(p_\pi,\, \theta_\pi)$ distribution by PIMON. The neutrino energy is binned into 6 bins, which are 0.5 GeV bin up to 2.5 GeV and integrated above 2.5 GeV.

$R^{\mathrm{F/N}}(E_\nu)$ is then calculated by taking the ratio between the spectrum of ND and SK, as follows.

$$R^{\mathrm{F/N}}(E_\nu) = \frac{\Phi^{\mathrm{SK}}(E_\nu)}{\Phi^{\mathrm{ND}}(E_\nu)}. \tag{8.1}$$

The results for the November-1999 run are shown in Fig. 8.2, where the systematic errors on the PIMON measurement are included in the error bars. Since the Cho-CERN pion production model is consistent with the PIMON measurement, it is used to estimate the central value of $R^{\mathrm{F/N}}(E_\nu)$. The errors of the PIMON measurement are used for the error of $R^{\mathrm{F/N}}(E_\nu)$ above 1 GeV. Since PIMON is insensitive to the neutrino energy below 1 GeV, the error in this region is separately estimated with the MC simulation.

8.1.3 Error matrix of the Far/Near ratio

In a study of the neutrino oscillation, the systematic errors on $R^{\mathrm{F/N}}(E_\nu)$ are taken into account including the correlation between E_ν bins. The errors on $R^{\mathrm{F/N}}(E_\nu)$ below 1 GeV are estimated from the beam-MC with several sets of Sanford-Wang parameter values. The error matrix for the neutrino energy below 1 GeV is the sum of the contributions from these error sources. The detail of the calculation is described in [96, 82]. For the neutrino energy above 1 GeV, the error matrix is estimated by the systematic errors on the PIMON measurement. The error matrices for above and below 1GeV, are combined without any correlation between them. The full error matrix is shown in Table 8.1. This is used for a study of the neutrino oscillation.

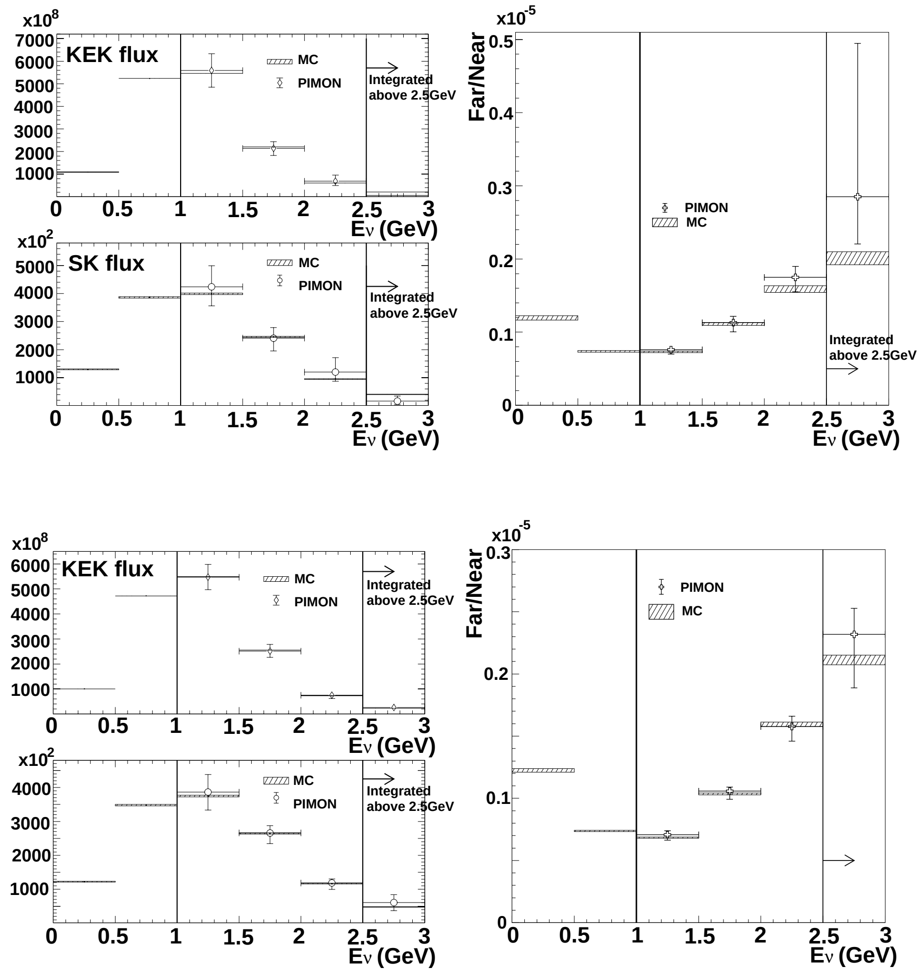

Figure 8.2: The energy spectrum and Far/Near flux ratio measured by PIMON. The upper figures show the results for the June 1999 run, and the lower figures show those for the November 1999 run. The neutrino energy spectrum at the near and far site are shown in the left figures, and the Far/Near ratios are shown in the right figures.

8.2 Expected number of events at SK

In this section, the expected number of events at SK ($N_{\rm SK}^{\rm exp}$) is estimated. To extract $N_{\rm SK}^{\rm exp}$, a number of the interaction in the near detector is evaluated. By using $R^{\rm F/N}(E_\nu)$ obtained in the previous section, $N_{\rm SK}^{\rm exp}$ is estimated for the null oscillation case.

8.2.1 Number of events at the near detector

Detector selection

The neutrino interaction target in 1KT (water) is the same as SK. Therefore, most of the systematic errors on the neutrino interactions for SK and 1KT are canceled out with each other, when we compute the expected number of SK events. For this reason, A number of events at the near detector is measured

Table 8.1: The error matrix of the Far/Near ratio since November 1999. The error is quoted as the square root of the diagonal element.

E_ν [GeV]	0.0-0.5	0.5-1.0	1.0-1.5	1.5-2.0	2.0-2.5	2.5-
Error	0.026	0.043	0.065	0.104	0.111	0.122
0.0-0.5	6.6×10^{-4}	-2.7×10^{-4}	0	0	0	0
0.5-1.0	-2.7×10^{-4}	1.8×10^{-3}	0	0	0	0
1.0-1.5	0	0	4.3×10^{-3}	5.7×10^{-4}	-3.2×10^{-4}	-1.6×10^{-4}
1.5-2.0	0	0	5.7×10^{-4}	1.1×10^{-2}	9.1×10^{-3}	2.5×10^{-3}
2.0-2.5	0	0	-3.2×10^{-4}	9.1×10^{-3}	1.2×10^{-2}	5.2×10^{-3}
2.5-	0	0	-1.6×10^{-4}	2.5×10^{-3}	5.2×10^{-3}	1.5×10^{-2}

by 1KT to estimate a number of interaction in SK. On the other hand, neutral current (NC) interactions are hardly observed by SciFi, while SK and 1KT have a finite efficiency in NC. The SciFi prediction accordingly has the error on the NC cross-section. For SciBar, the neutrino interaction target is (CH)$_n$, whereas that of SK is H_2O. Therefore, the neutrino-nucleus cross-section is slightly different. In addition, if SciBar attempts to select NC interactions, the contamination of the sky-shine neutrons are the source of the systematic error. Although the sky-shine neutrons also strike 1KT, these backgrounds is negligible because the fiducial volume is sufficiently shielded by water.

Event selection

In contrast to the event selection for the neutrino energy spectrum as described in Appendix C.1, all the events reconstructed in the fiducial volume are used to obtain an inclusive event rate. The selection criteria is summarized as below.

- **Energy threshold :**
  To reject low energy background events such as a muon decay of a cosmic ray, the threshold of FADC pulse height is set to 1000 photo-electrons, equivalent to the electron energy of 100 MeV.

- **Fiducial volume cut :**
  Fig. 8.3 shows the vertex distributions of 1KT events. We select the events within the fiducial volume defined as $R < 2$ m and $-2 < Z < 0$ m, where R is the distance from the beam axis and Z is the position along the beam direction originating at the tank center. The definition of the fiducial volume is illustrated in Fig. C.2.

- **Single event selection :**
  1KT often observes two or more detector activities within a beam spill, which is called “multiple events”. Since the vertex reconstruction is difficult for the multiple events, only single events are selected by requiring a number of the FADC peaks to be one. The fraction of spills with multiple events is about 10%, and it is taken into account for the estimation of the total number of the neutrino interaction in 1KT.

The efficiency is estimated as the ratio of a number of reconstructed events to the number of generated events in the fiducial volume by using the MC simulation. The overall efficiency is obtained to be 71% for 1999 data and 75% for the others.

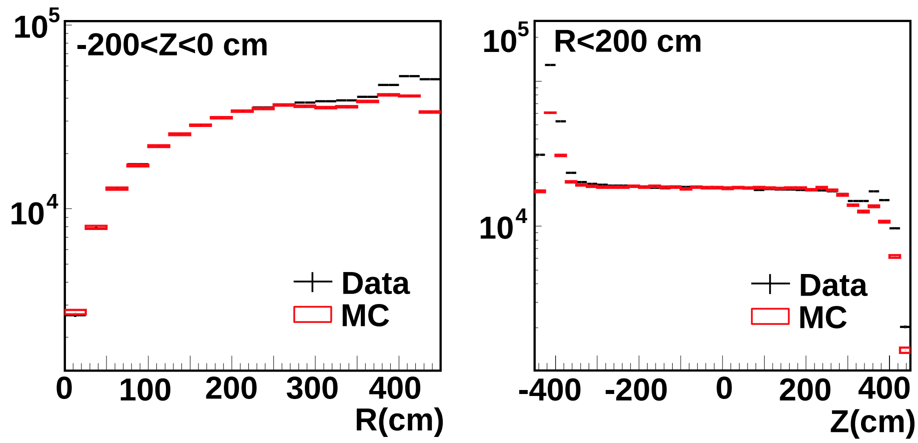

Figure 8.3: The vertex distributions of 1KT. The left figure shows the vertex distribution of R axis for $-200 < Z < 0$ cm and the right figure shows that of Z axis for $R < 200$ cm, where R is the distance from the beam axis and Z is the position along the beam direction originating at the tank center.

Number of interaction in 1KT

A number of interaction in 1 KT ($N^{\rm int}_{\rm 1KT}$) is estimated by using a number of the single-peak events ($N^{1}_{\rm peak}$). For the extrapolation of $N^{\rm int}_{\rm 1KT}$ from $N^{1}_{\rm peak}$, a number of total FADC peaks ($N^{\rm total}_{\rm peak}$) are also counted. Then, $N^{\rm int}_{\rm 1KT}$ is obtained by multiplying the ratio between $N^{\rm total}_{\rm peak}$ and $N^{1}_{\rm peak}$ to the number of selected events ($N^{\rm sel}_{\rm 1KT}$) as

$$N^{\rm int}_{\rm 1KT} = N^{\rm sel}_{\rm 1KT} \cdot \frac{N^{\rm total}_{\rm peak}}{N^{1}_{\rm peak}} \cdot C_{\rm multi} \cdot \frac{1}{1+R_{\rm BG}} \cdot (C_{7\to 9}) \tag{8.2}$$

where the definitions of $C_{\rm multi}$, $R_{\rm BG}$, and $C_{7\to 9}$ are summarized as follows.

Multi-event correction ($C_{\rm multi}$) : The multiple events are sometimes misidentified as the smaller number of events due to the overlapping of the FADC peaks. The multi-event correction factor, $C_{\rm multi}$, is evaluated by the MC simulation. Comparing the number of the peaks with a number of generated events, $C_{\rm multi}$ is estimated to be 1.008.

Background ratio ($R_{\rm BG}$) : The background contamination into $N^{\rm int}_{\rm 1KT}$ are estimated as 1.0% for cosmic ray, 0.5% for neutrino induced muons coming from outside. Since we also have some reflection of the PMT signals at the electronics for 1999 data, the contamination is estimated as 2.6% for the fake events.

Scaling factor from 7 to 9 bunches ($C_{7\to 9}$) : In May and June 2000, the eighth and ninth bunches were sometimes lost, since the timing generators for the FADC became unstable. Therefore, the first to seventh bunches are used for the analysis in this period. The number of events are scaled by the correction factor ($C_{7\to 9}$).

Table8.2 shows the total number of neutrino interaction in 1KT for each period.

Systematic errors on $N_{\mathrm{1KT}}^{\mathrm{int}}$

The total systematic error on $N_{\mathrm{1KT}}^{\mathrm{int}}$ is approximately 5%. It is dominated by the uncertainty of the fiducial volume. The performance of the vertex fitter has been studied by using cosmic ray muons. The reconstructed vertex is found to be biased by 10 cm, that changes $N_{\mathrm{1KT}}^{\mathrm{int}}$ by 3.2%. Shifting the center position of the fiducial volume by ± 50 cm, the number of events changes by 2%. Increasing the radius of the fiducial volume by 20 cm or 40 cm, the number of events per unit mass varies by 1%. These errors are quadratically summed, and the systematic error on the fiducial volume is obtained to be 4.0%.

8.2.2 Expected number of events at SK

The expected number of events at SK without neutrino oscillation ($(N_{\mathrm{SK}}^{\mathrm{exp}})^{\mathrm{null}}$) is calculated by using a number of interaction in KT ($N_{\mathrm{1KT}}^{\mathrm{int}}$) as the following equation.

$$(N_{\mathrm{SK}}^{\mathrm{exp}})^{\mathrm{null}} = N_{\mathrm{1KT}}^{\mathrm{int}} \cdot \frac{\int \Phi^{\mathrm{SK}}(E_\nu) \cdot \sigma_{\mathrm{H_2O}}(E_\nu) \cdot \epsilon_{\mathrm{SK}}(E_\nu) dE_\nu}{\int \Phi^{\mathrm{1KT}}(E_\nu) \cdot \sigma_{\mathrm{H_2O}}(E_\nu) \cdot \epsilon_{\mathrm{1KT}}(E_\nu) dE_\nu} \cdot \frac{M_{\mathrm{SK}}}{M_{\mathrm{1KT}}} \cdot \frac{\mathrm{POT_{SK}}}{\mathrm{POT_{1KT}}} \cdot C_{\nu_e}, \tag{8.3}$$

where $\sigma_{\mathrm{H_2O}}$, $M_{\mathrm{SK(1KT)}}$, $\mathrm{POT_{SK(1KT)}}$, $\epsilon_{\mathrm{SK(1KT)}}$, and C_{ν_e} are the cross-section of the neutrino interaction in water, the fiducial mass of SK (1KT), a number of protons on target used in the analysis in SK (1KT), the neutrino detection efficiency in SK (1KT), and a factor to correct the effect of the electron neutrino component in the beam, respectively.

Since the effect of the electron neutrino component in the beam is not taken into account in $R^{\mathrm{F/N}}(E_\nu)$ and $\epsilon_{\mathrm{1KT(SK)}}$, a factor to correct this effect is multiplied to $(N_{\mathrm{SK}}^{\mathrm{exp}})^{\mathrm{null}}$. C_{ν_e} component is estimated by the MC simulation. If the ν_e component is taken into account, the number of events in SK increases 0.6%, and that in 1KT increases 1.3%. Therefore, C_{ν_e} is obtained as

$$C_{\nu_e} = 1.006/1.013 = 0.996. \tag{8.4}$$

Since this correction makes only tiny effect on $(N_{\mathrm{SK}}^{\mathrm{exp}})^{\mathrm{null}}$, its uncertainty is ignored in the estimation of the systematic errors on $(N_{\mathrm{SK}}^{\mathrm{exp}})^{\mathrm{null}}$. Table 8.3 is the summary of the $(N_{\mathrm{SK}}^{\mathrm{exp}})^{\mathrm{null}}$ for each period. These values are used as the input parameters for a study of the neutrino oscillation in Section 10.1.2.

Table 8.2: A number of the neutrino interactions in the fiducial volume of 25 kt in 1KT.

Period	$\mathrm{POT_{1KT}}(10^{18})$	$N_{\mathrm{1KT}}^{\mathrm{sel}}$	$N_{\mathrm{peak}}^{\mathrm{total}}$	N_{peak}^{1}	$N_{\mathrm{1KT}}^{\mathrm{int}}$
99'Jun	2.6	4,282	109,119	89,782	7,206
99'Nov	2.6	4,923	118,321	96,304	8,351
00'Jan-00'Jun	14.0	25,054	599,102	483,866	45,077
01'Jan-01'Jul	21.6	45,996	1,137,358	895,629	77,428
03'Jan-03'Jun	17.9	43,538	1,061,314	832,112	73,614
03'Oct-04'Nov	16.0	39,991	951,132	756,557	66,654

Table 8.3: The summary of the expected number of events at SK without neutrino oscillation ($(N_{\rm SK}^{\rm exp})^{\rm null}$) for each period.

Period	Horn current	$N_{\rm SK}$	$\sigma_{\rm stat}$	$\sigma_{\rm sys}$	
K2K-Ia	200 kA	4.6	$\pm$0.07	+0.73	-0.62
K2K-Ia	250 kA	75.1	$\pm$0.27	+6.65	-7.42
K2K-IIb	250 kA	76.2	$\pm$0.26	+6.39	-7.13

Systematic errors on $(N_{\rm SK}^{\rm exp})^{\rm null}$

By the estimation of the errors on $(N_{\rm SK}^{\rm exp})^{\rm null}$ for each month, $^{+7.1}_{-7.8}$% and $^{+6.5}_{-7.4}$% is quoted as the systematic error on $(N_{\rm SK}^{\rm exp})^{\rm null}$ in total for K2K-I and K2K-II, respectively. The estimation of the main systematic sources is summarized below. The detail description is found in [82].

Number of interactions in 1KT : The uncertainties on the measurements of the number of neutrino interactions in 1KT is described in Section 8.2.1.

Energy spectrum : The systematic errors on $(N_{\rm SK}^{\rm exp})^{\rm null}$ by the PIMON measurement is assigned as follows.

- The neutrino energy spectrum : $^{+3.6}_{-3.4}$% (K2K-I) and $^{+3.9}_{-3.6}$% (K2K-II)
- The Far/Near ratio : $^{+5.6}_{-7.3}$%

SK event selection : The event selection in SK have some systematic error on $(N_{\rm SK}^{\rm exp})^{\rm null}$. A dominant uncertainty comes from the selection of the fully-contained events in SK. We apply two different vertex fitters to the atmospheric neutrino data and the MC simulation. Comparing with these results, the systematic errors on $(N_{\rm SK}^{\rm exp})^{\rm null}$ is estimated to be $\pm$2%.

Other systematic uncertainties on $(N_{\rm SK}^{\rm exp})^{\rm null}$ come from the event selection for neutrinos in K2K beam (1%) and the statistics of the MC simulation (1%). In total, 3% is quoted as the error on $(N_{\rm SK}^{\rm exp})^{\rm null}$ due to the uncertainties of event selection in SK.

Chapter 9

Far Detector Analysis

9.1 Event selection

For the data analysis of Super-Kamiokande (SK), we select fully-contained events in the fiducial volume (FCFV) of 22.5 ktons by using analysis algorithm similar to the atmospheric neutrino study. Figure 9.1 shows a typical event display of SK. The event selection for FCFV K2K events is summarized below.

9.1.1 Energy threshold

The trigger threshold is 31 (16) PMT hits within 200 nsec time window, which correspond to 50-100 (20-50) photo-electrons for SK-I (SK-II), respectively. We require the visible energy to be greater than 30 MeV, which is the sum of the electron-equivalent energy for each ring. That corresponds to the muon momentum of 197 MeV/c.

9.1.2 Fully-contained event selection

Cosmic rays coming from the outside are removed by the information of the outer detector (OD). A number of hits in the largest OD cluster is required to be less than 10 PMT hits. In addition, we reject the events which have hits greater than 50 within 800 nsec time window. These requirements effectively select FC events.

9.1.3 K2K event selection

Since SK takes the K2K data together with the atmospheric neutrinos, the timing information is used for the identification of the K2K neutrino events. To synchronize SK events with a neutrino beam spill, we use the time information of both the beginning of beam spills ($T_{\rm KEK}$) and SK events ($T_{\rm SK}$) recorded by GPS systems, which is described in Appendix A.4. We define the time difference between $T_{\rm KEK}$ and $T_{\rm SK}$ as

$$\Delta T \equiv T_{\rm SK} - T_{\rm KEK} - TOF, \tag{9.1}$$

where TOF is a time-of-flight of neutrinos from KEK to SK ($\simeq 833$ μsec). K2K events are observed within $0 \leq \Delta T \leq 1.1$ μsec, which is the duration of the beam spill. Fig. 9.2 shows ΔT distributions. K2K events cluster within the beam timing window.

To select the events synchronized with the accelerator, we impose the timing cut of $-0.2 < \Delta T < 1.3$ μsec. Since the uncertainty of the timing information is less than 0.2 μsec, 0.2 μsec margins is

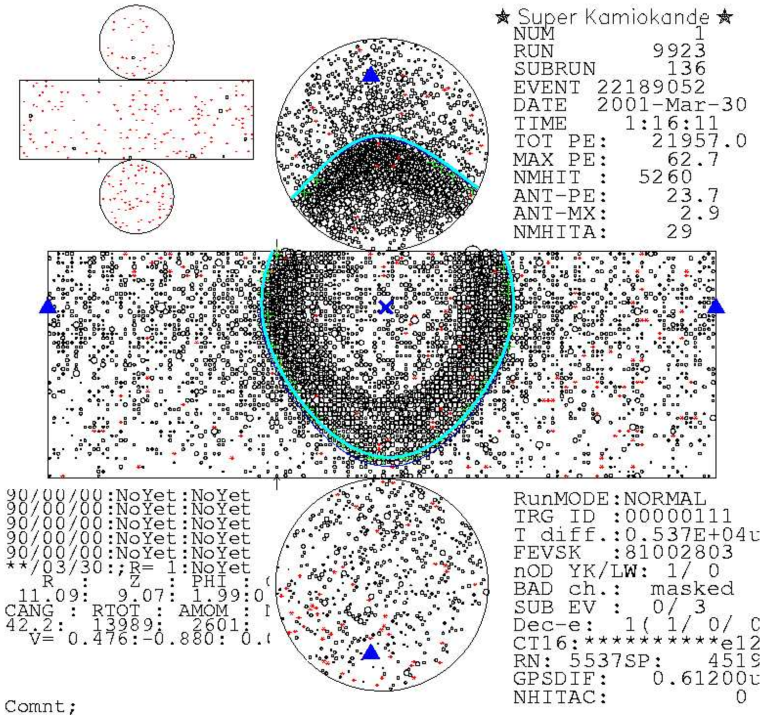

Figure 9.1: Event display of a typical event at Super-Kamiokande.

assigned to the time window before and after the beam. The timing information reduces the background events by six orders of magnitude (1.3(μsec)/2.2(sec) = 0.6×10^{-6}).

9.1.4 Fiducial volume

The reconstructed vertex is required to be within the fiducial volume defined as $D_{\rm wall} \geq 2.0$ m, where $D_{\rm wall}$ is the distance from the vertex to the nearest surface of ID. It corresponds to water mass of 22.5 ktons.

9.2 Event classification

9.2.1 Ring reconstruction

Using the charge and timing information of each PMT, A Cherenkov ring image is obtained by the reconstruction of the ring direction, the outer edge of the most energetic ring, and the vertex position. The edge finding method for SK-II is improved to compensate for the less PMT density than SK-I. By the procedure, we obtained the same performance for electrons, and better performance for muons. The vertex resolution is less than 1 m for both SK-I and SK-II.

More precise fitter is applied to only single-ring events. It uses the PID information in addition to the charge and timing information. The momentum resolution of SK-II is worse than that of SK-I due to the reduction of PMTs, since the momentum is almost linear to a total charge. Nevertheless, the momentum resolution of SK-II is kept as several% level.

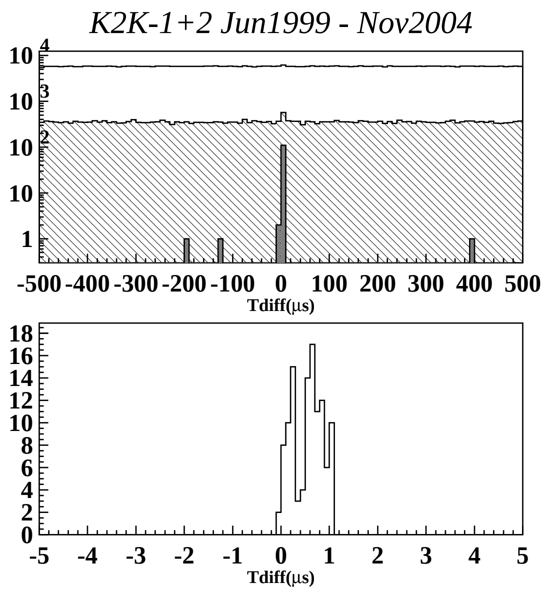

Figure 9.2: ΔT distribution for K2K-I+II. The upper figure shows the events in ± 500 μsec time window after the decay-electron cut (solid lines), after the flashing PMT cut (hatched regions), and after the fiducial volume cut (filled regions). The lower figure shows the final sample within $\pm$ 5 μsec time window.

9.2.2 Ring counting

A number of the reconstructed rings is counted by using the charge pattern with a likelihood method.

9.2.3 Particle identification (PID)

The reconstructed rings are divided into two particle types, μ-like and e-like, by using the ring image and the opening angle. The mis-ID probability is a few % level. Since it is enough smaller than the statistical error, the particle identification is sufficient for the charged-current event selection.

9.2.4 Summary of event classification

Table 9.1 shows a number of selected events for each category and the MC expectation for null oscillation case is also listed. The number of the total observed events are 112, while the expected number of events is 155.9. The number of 1-ring μ-like (1Rμ) events is 58.

The efficiency is estimated as the ratio between a number of the FCFV events and that of the events within the fiducial volume by using the MC simulation. The overall efficiency for SK-I and SK-II are 77.2% and 77.9%, respectively. Regardless of the reduction of PMTs, the efficiency for SK-II is higher than that for SK-I. This is because the improvement of the ring reconstruction method, and the effect of the vertex shift due to the change of the PMT density.

Table 9.1: The summary of observed K2K events at SK.

		K2K-I		K2K-II		Total	
		data	MC	data	MC	data	MC
Total		55	79.7	57	76.2	112	155.9
1 ring	μ-like	30	46.4	28	44.4	58	90.8
	e-like	3	3.8	6	4.4	9	8.2
Multi ring		22	29.5	23	27.4	45	56.9

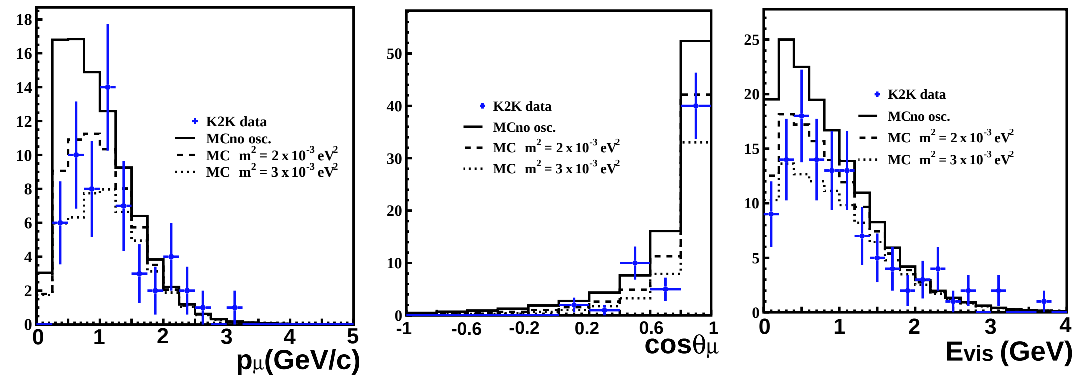

Figure 9.3: Muon momentum (left), muon angle with respect to the beam (center), and visible energy (right) distributions for SK 1Rμ sample. The MC expectation for the neutrino oscillation with the certain oscillation parameters, are also shown.

9.3 Basic distributions

Figure 9.3 shows the muon momentum, muon angle with respect to the beam, and visible energy distributions for SK 1Rμ sample. In the figures, the MC expectation for the neutrino oscillation with the certain oscillation parameters seem to be more consistent with data than the null oscillation case. The effect of the neutrino oscillation is studied in Chapter 10.

9.4 Systematic errors

We evaluate the systematic errors on the energy scale, total number of events, and energy spectrum for 1Rμ event. The estimation of these systematic errors is summarized below.

9.4.1 Energy scale

By using calibration source [101], the difference between data and the MC simulation is within 1.8% (1.9%) for SK-I (SK-II), respectively. In addition to the above calibration sources, the time variation of the energy response is monitored. The RMS of the deviation is 0.9% for both SK-I and SK-II. Finally, we take the quadratic sum of the difference from the MC simulation and the RMS of the time variation. The systematic errors on the absolute energy scale is quoted as 2.0% (2.1%) for SK-I (SK-II), respectively.

Table 9.2: A summary of the systematic errors on the energy spectrum for SK 1Rμ events.

		0-0.5	0.5-1.0	1.0-1.5	1.5-2.0	2.0-
K2K-I	Ring counting [%]	3.4	2.7	3.0	4.5	4.5
	Fiducial volume [%]	2.0	2.0	2.0	2.0	2.0
	PID [%]	0.9	0.3	0.5	0.4	0.4
	Energy scale [%]	2.0	2.0	2.0	2.0	2.0
	Total [%]	4.5	3.9	4.2	5.3	5.3
K2K-II	Ring counting [%]	5.3	4.1	3.7	3.8	3.8
	Fiducial volume [%]	2.0	2.0	2.0	2.0	2.0
	PID [%]	2.6	0.4	0.3	0.6	0.6
	Energy scale [%]	2.1	2.1	2.1	2.1	2.1
	Total [%]	6.6	5.0	4.7	4.8	4.8

9.4.2 Total number of events

We evaluate the uncertainties of the total number of events ($N_{\rm SK}^{\rm obs}$). The main source of the systematic error is the fiducial volume cut, which comes from the difference of the two vertex fitters. For the 1Rμ sample of the atmospheric neutrino data, the number of event in the fiducial volume is compared between the two methods. The difference in data to MC ratio is 2%. The quadratic sum of all the systematic errors is 2.4% for SK-I and SK-II. To be conservative, we assign 3% as the systematic uncertainty in $N_{\rm SK}^{\rm obs}$.

9.4.3 Energy spectrum for 1Rμ events

The 1Rμ sample is used to study the spectrum shape of the neutrino energy. The neutrino energy is divided into six bins, and the systematic error of each bin is estimated, as listed in Table 9.2. The total error is estimated in the quadratic sum of the errors on each source. We summarized the systematic errors as below.

Fiducial volume cut : As described in Section 9.4.2, the systematic error on the fiducial volume is 2.0%. We assign this error on each E_ν bin.

Ring counting : By using the atmospheric neutrino data, the capability of the ring counting is compared with the MC simulation in the energy range up to several GeV. The systematic error corresponding to the difference between data and the MC simulation, is assigned to each E_ν bin.

Particle identification : By using the atmospheric neutrino sample, the difference of the particle identification capability between data and the MC simulation are obtained. The effect of the difference is estimated by the MC simulation, and regarded as a systematic error on the neutrino energy spectrum at SK.

Energy scale : The systematic error of the energy scale is assigned 2.0 and 2.1% for K2K-I and K2K-II, respectively, as estimated in Section 9.4.1.

Chapter 10

Study of the Neutrino Oscillation

The neutrino oscillation is studied by using neutrino events obtained by near detectors (ND) and Super-Kamiokande (SK). To investigate the neutrino oscillation, the shape of the neutrino energy (E_ν) distribution and the number of neutrino events at SK are compared with the expectation by ND measurement. The maximum likelihood method is used to evaluate the effect of the neutrino oscillation. In this chapter, the result of a neutrino oscillation study is described.

10.1 Definition of likelihood

The likelihood function for the neutrino oscillation study is defined as

$$\mathcal{L}(\Delta m^2, \sin^2 2\theta, \boldsymbol{f}) \equiv \mathcal{L}_{\rm shape}(\Delta m^2, \sin^2 2\theta, \boldsymbol{f}) \times \mathcal{L}_{\rm norm}(\Delta m^2, \sin^2 2\theta, \boldsymbol{f}) \times \mathcal{L}_{\rm syst}(\boldsymbol{f}), \qquad (10.1)$$

where $\mathcal{L}_{\rm shape}$, $\mathcal{L}_{\rm norm}$, and $\mathcal{L}_{\rm syst}$ are likelihood functions for the spectrum shape, the number of events ($N_{\rm SK}$), and the constraint on the systematic parameters ($\boldsymbol{f}$), respectively. The oscillation parameters, Δm^2 and $\sin^2 2\theta$, are used as free parameters.

The parameter set ($\boldsymbol{f}$) is introduced to represent the variations of physical quantities within their uncertainties. The contents of the systematic parameters, $\boldsymbol{f}$, are defined as,

$$\boldsymbol{f} \equiv (\boldsymbol{f}^{\phi}, f^{\rm nonQE}, f^{\rm NC}, \boldsymbol{f}^{F/N}, f^{\epsilon_{\rm SK-I}}, f^{\epsilon_{\rm SK-II}}, f^{\rm E-scale}_{\rm SK-I}, f^{\rm E-scale}_{\rm SK-II}, f^{\rm norm}_{\rm K2K-Ia}, f^{\rm norm}_{\rm K2K-Ib}, f^{\rm norm}_{\rm K2K-II}), \qquad (10.2)$$

where each component is summarized below.

- f^{ϕ} : The neutrino energy spectrum measured by ND.
- $f^{\rm nonQE}$: The cross-section ratio of CC-nonQE to CC-QE.
- $f^{\rm NC}$: The cross-section ratio of NC to CC-QE.
- $f^{F/N}$: The Far/Near flux ratio.
- $f^{\epsilon_{\rm SK-I}}$, $f^{\epsilon_{\rm SK-II}}$: The detection efficiency of one-ring μ-like events in SK for SK-I and SK-II, respectively.
- $f^{\rm E-scale}_{\rm SK-I}$, $f^{\rm E-scale}_{\rm SK-II}$: The energy scale of SK for SK-I and SK-II, respectively.

- $f^{\rm norm}_{\rm K2K-Ia}$, $f^{\rm norm}_{\rm K2K-Ib}$, $f^{\rm norm}_{\rm K2K-II}$: The normalization factor relative to the expected number of events for SK-Ia, SK-Ib, and SK-II, respectively.

The each term in the likelihood is described in the following sections.

10.1.1 The spectrum shape term

The spectrum shape term of the reconstructed neutrino energy ($E_\nu^{\rm rec}$), $\mathcal{L}_{\rm shape}$, is expressed as a product of the probability density functions for each one-ring μ-like (1R$_\mu$) event as

$$\mathcal{L}_{\rm shape} = \prod_{i=1}^{N^{1{\rm R}\mu}_{\rm K2K-Ib}} PDF_{\rm I}(E_i^{\rm rec}; \Delta m^2, \sin^2 2\theta, \boldsymbol{f}) \times \prod_{j=1}^{N^{1{\rm R}\mu}_{\rm K2K-II}} PDF_{\rm II}(E_j^{\rm rec}; \Delta m^2, \sin^2 2\theta, \boldsymbol{f}), \quad (10.3)$$

where $N^{1{\rm R}_\mu}_{\rm K2K-Ib}$ and $N^{1{\rm R}_\mu}_{\rm K2K-II}$ are the number of 1Rμ events in K2K-Ib and K2K-II, respectively, and $E_i^{\rm rec}$ is the reconstructed neutrino energy of the i-th 1R$_\mu$ event. Since the number of PMTs is different between SK-I and SK-II, the probability density functions are different. $PDF_{\rm I}$ and $PDF_{\rm II}$, represent the probability density functions of 1R$_\mu$ events with a certain oscillation parameter set for SK-I and SK-II, respectively, as

$$\begin{aligned} & PDF_X(E_\nu^{\rm rec}; \sin^2 2\theta, \Delta m^2, \boldsymbol{f}) \\ \equiv & \int dE_\nu^{\rm true} \cdot \Phi_{\rm SK}(E_\nu^{\rm true}; \sin^2 2\theta, \Delta m^2, \boldsymbol{f}) \sum_{\mathcal{I}} \sigma^{\mathcal{I}}(E_\nu^{\rm true}, \boldsymbol{f}) \cdot r^{\mathcal{I}}(E_\nu^{\rm rec}, E_\nu^{\rm true}, \boldsymbol{f}), \end{aligned} \quad (10.4)$$

where each term is defined as follows.

- x : Indexes of SK-I or SK-II.
- $E_\nu^{\rm true}$: The true neutrino energy.
- $\Phi_{\rm SK}$: The neutrino energy spectrum at SK with the oscillation effect.
- $\mathcal{I}$: Index of each neutrino interaction channel.
- $\sigma^{\mathcal{I}}$: The neutrino-nucleus cross-section.
- $r^{\mathcal{I}}$: The probability density function to be observed a the 1R$_\mu$ event with $E_\nu^{\rm true}$ as neutrino energy of $E_\nu^{\rm rec}$ by SK.

The neutrino flux, $\Phi_{\rm SK}(E_\nu)$, in Eq. 10.4 is defined as

$$\Phi_{\rm SK}(E_\nu^{\rm true}; \Delta m^2, \sin^2 2\theta, \boldsymbol{f}) \equiv f_i^\phi \cdot f_j^{F/N} \cdot P(E_\nu^{\rm true}; \Delta m^2, \sin^2 2\theta) \cdot \Phi_{\rm SK}^{\rm 250kA}(E_\nu^{\rm true}), \quad (10.5)$$

where i and j show the indexes of the corresponding energy bin for the ND energy spectrum (Table 7.7) and the Far/Near flux ratio (Table 8.1), respectively. P is the neutrino oscillation probability defined as

$$P(E_\nu^{\rm true}; \Delta m^2, \sin^2 2\theta) = \begin{cases} 1 - \sin^2 2\theta \cdot \sin^2 \frac{1.27 \cdot \Delta m^2 \cdot L}{E_\nu^{\rm true}} & \text{for CC} \\ 1 & \text{for NC,} \end{cases} \quad (10.6)$$

where L(= 250 km) is the neutrino flight distance. $\Phi_{\rm SK}^{\rm 250kA}$ is the neutrino flux predicted by the MC simulation. The neutrino cross-section term $\sigma^{\mathcal{I}}$ is defined as

$$\sigma^{\mathcal{I}}(E_\nu^{\rm true}, \boldsymbol{f}) = f^{\mathcal{I}} \cdot \sigma^{\rm MC}(E_\nu^{\rm true}), \tag{10.7}$$

where $f^{\mathcal{I}}$ is a fit parameter to vary the cross-section for each interaction channel, and $\sigma^{\rm MC}$ is the neutrino cross-section evaluated by the MC simulation. The definition of $f^{\mathcal{I}}$ is

$$f^{\mathcal{I}} = \begin{cases} 1 & \mathcal{I} = \text{CC-QE} \\ f^{\rm nonQE} & \mathcal{I} = \text{CC-nonQE} \\ f^{\rm NC} & \mathcal{I} = \text{NC} \end{cases}. \tag{10.8}$$

The function of the detector response, $r^{\mathcal{I}}$, is estimated by the MC simulation. To implement the error on the energy scale of SK, the reconstructed neutrino energy with $r^{\mathcal{I}}$ is scaled by $f_{{\rm SK}-X}^{\rm E-scale}$.

10.1.2 Normalization term

The normalization term, $\mathcal{L}_{\rm norm}$, is given by the Poisson probability to observe $N^{\rm obs}$ events with the expected number of events, $N^{\rm exp}$, as

$$\mathcal{L}_{\rm norm} \equiv \frac{[N^{\rm exp}(\Delta m^2, \sin^2 2\theta; \boldsymbol{f})]^{N^{\rm obs}}}{N^{\rm obs}!} \cdot \exp[-N^{\rm exp}(\Delta m^2, \sin^2 2\theta; \boldsymbol{f})], \tag{10.9}$$

$N^{\rm obs}$ and $N^{\rm exp}$ are defined as follows.

$$N^{\rm obs} \equiv N^{\rm obs}_{\rm K2K-Ia} + N^{\rm obs}_{\rm K2K-Ib} + N^{\rm obs}_{\rm K2K-II} = 112, \tag{10.10}$$

$$\begin{aligned} N^{\rm exp}(\Delta m^2, \sin^2 2\theta; \boldsymbol{f}) &\equiv N^{\rm exp}_{\rm K2K-Ia}(\Delta m^2, \sin^2 2\theta; \boldsymbol{f}) \\ &+ N^{\rm exp}_{\rm K2K-Ib}(\Delta m^2, \sin^2 2\theta; \boldsymbol{f}) \\ &+ N^{\rm exp}_{\rm K2K-II}(\Delta m^2, \sin^2 2\theta; \boldsymbol{f}), \end{aligned} \tag{10.11}$$

where each experimental period is indicated by the subscript. The expectation number of events with neutrino oscillation for each period (K2K-Ia, K2K-Ib, K2K-II) is defined as

$$\begin{aligned} & N^{\rm exp}_{{\rm K2K}-X}(\Delta m^2, \sin^2 2\theta; \boldsymbol{f}) \\ & \equiv f^{\rm norm}_{{\rm K2K}-X} \cdot (N^{\rm int}_{\rm 1KT})_{{\rm K2K}-X} \times \frac{M_{\rm SK}}{M_{\rm 1KT}} \cdot \frac{{\rm POT}_{\rm SK}^{{\rm K2K}-X}}{{\rm POT}_{\rm SK}^{{\rm K2K}-X}} \cdot C_{\nu_e} \\ & \times \frac{\int dE_\nu^{\rm true} \cdot \Phi_{\rm SK}^{{\rm K2K}-X}(E_\nu^{\rm true}; \Delta m^2, \sin^2 2\theta, \boldsymbol{f}) \cdot \sum_{\mathcal{I}} \sigma^{\mathcal{I}}(E_\nu^{\rm true}, \boldsymbol{f}) \cdot \epsilon^{\mathcal{I}}_{{\rm SK}-X}(E_\nu^{\rm true})}{\int dE_\nu^{\rm true} \cdot \Phi_{\rm 1KT}^{{\rm K2K}-X}(E_\nu^{\rm true}; \boldsymbol{f}) \cdot \sum_{\mathcal{I}} \sigma^{\mathcal{I}}(E_\nu^{\rm true}, \boldsymbol{f}) \cdot \epsilon^{\mathcal{I}}_{\rm 1KT}(E_\nu^{\rm true})} \\ & \equiv f^{\rm norm}_{\rm 1KT} \cdot (N^{\rm exp}_{\rm SK})^{\rm null}_{{\rm K2K}-X} \\ & \times \frac{\int dE_\nu^{\rm true} \cdot \Phi_{\rm SK}^{{\rm K2K}-X}(E_\nu^{\rm true}; \Delta m^2, \sin^2 2\theta, \boldsymbol{f}) \cdot \sum_{\mathcal{I}} \sigma^{\mathcal{I}}(E_\nu^{\rm true}, \boldsymbol{f}) \cdot \epsilon^{\mathcal{I}}_{{\rm SK}-X}(E_\nu^{\rm true})}{\int dE_\nu^{\rm true} \cdot \Phi_{\rm SK}^{{\rm K2K}-X}(E_\nu^{\rm true}; 0, 0, \boldsymbol{f}) \cdot \sum_{\mathcal{I}} \sigma^{\mathcal{I}}(E_\nu^{\rm true}, \boldsymbol{f}) \cdot \epsilon^{\mathcal{I}}_{{\rm SK}-X}(E_\nu^{\rm true})}, \end{aligned} \tag{10.12}$$

where each term is defined as follows.

- $f^{\rm norm}_{{\rm K2K}-X}$: Defined by Eq. 10.2.

- $(N_{\rm 1KT}^{\rm int})_{{\rm K2K}-X}$: A number of interaction in 1KT estimated in Section 8.2.2.
- $\phi_{\rm SK(1KT)}^{{\rm K2K}-X}$: The neutrino flux at SK (1KT) defined by Eq. 10.14 and 10.14.
- $\sigma^{\mathcal{I}}$: Defined by Eq. 10.7.
- $\epsilon_{{\rm SK}-X({\rm 1KT})}^{\mathcal{I}}$: The detection efficiency for SK (1KT) estimated by the MC simulation.
- $M_{\rm SK(1KT)}$: The fiducial mass of SK (1KT), which is 22.5 ktons (25 tons).
- ${\rm POT}_{\rm SK(1KT)}^{{\rm K2K}-X}$: A number of protons on target for SK (1KT).
- C_{ν_e} : The correction factor for the $\nu_e$component in the beam as described in Section 8.2.2.
- $(N_{\rm SK}^{\rm exp})_{{\rm SK}-X}^{\rm null}$: A expected number of events at SK without neutrino oscillation as shown in Table 8.3.

$\Phi_{\rm SK}^{{\rm K2K}-X}$ and $\Phi_{\rm 1KT}^{{\rm K2K}-X}$ are defined as

$$\Phi_{\rm SK}^{{\rm K2K}-X}(E_\nu^{\rm true};\Delta m^2,\sin^2 2\theta,\boldsymbol{f}) \equiv \begin{cases} P(E_\nu^{\rm true};\Delta m^2,\sin^2 2\theta)\cdot\Phi_{\rm SK}^{\rm 200kA}(E_\nu^{\rm true}) & X = {\rm Ia} \\ \text{Equation 10.5} & X = {\rm Ib, II} \end{cases} \tag{10.13}$$

$$\Phi_{\rm 1KT}^{{\rm K2K}-X}(E_\nu^{\rm true};\boldsymbol{f}) \equiv \begin{cases} \Phi_{\rm 1KT}^{\rm 200kA}(E_\nu^{\rm true}) & X = {\rm Ia} \\ f_i^\phi\cdot\Phi_{\rm 1KT}^{\rm 250kA}(E_\nu^{\rm true}) & X = {\rm Ib, II} \end{cases}, \tag{10.14}$$

where $\Phi_{\rm 1KT}^{\rm 250kA}(\Phi_{\rm 1KT}^{\rm 200kA})$ is the neutrino flux obtained by the MC simulation for the horn current of 250 kA (200 kA), respectively.

10.1.3 Constraint term

The constraint term ($\mathcal{L}_{\rm syst}$) restricts the systematic parameters ($\boldsymbol{f}$) within their systematic errors assuming the Gaussian probability. $\mathcal{L}_{\rm syst}$ is given by

$$\begin{aligned} \mathcal{L}_{\rm syst} \equiv\ & \exp\left[-{}^t\Delta f^{\phi,{\rm nonQE}}\cdot(M^{\phi,{\rm nonQE}})^{-1}\cdot\Delta f^{\phi,{\rm nonQE}} - \frac{(\Delta f^{\rm NC})^2}{2(\sigma^{\rm NC})^2}\right] & (10.15)\\ \times\ & \exp\left[-{}^t\Delta f^{\rm F/N}\cdot(M^{\rm F/N})^{-1}\cdot\Delta f^{\rm F/N}\right] & (10.16)\\ \times\ & \exp\left[-\sigma\frac{(\Delta f_i^{\epsilon{\rm SK}-X})^2}{2(\sigma_i^{\epsilon{\rm SK}-X})^2} - \sigma\frac{(\Delta f_{{\rm SK}-X}^{\rm E-scale})^2}{2(\sigma_{{\rm SK}-X}^{\rm E-scale})^2} - \sigma\frac{(\Delta f_{{\rm K2K}-X}^{\rm norm})^2}{2(\sigma_{{\rm K2K}-X}^{\rm norm})^2}\right], & (10.17)\end{aligned}$$

where Δf is defined as

$$\Delta f \equiv f - \langle f\rangle, \tag{10.18}$$

which is the deviation of f from its central value $\langle f\rangle$. The systematic error of each parameters is summarized as follows.

f^ϕ : The central values and systematic errors are the results of the ND spectrum measurement as shown in Table 7.7.

$f^{\rm nonQE}$: Since $f^{\rm nonQE}$ is determined by the ND spectrum measurement, it varies around the best fit value in terms of the error matrix together with f_i^ϕ. The error on $f^{\rm nonQE}$ is approximately 20%.

f^{NC} : The central value of the NC cross-section parameter (f^{NC}) is unity, whose error is estimated as 15%. The error is the compilation of the error on the NC single-π^0 measurement by 1KT (11%) [99] and the error on the other NC channels (30%).

$f^{\mathrm{F/N}}$: The center values and systematic errors are quoted as the measurement results obtained by PIMON as shown in Table 8.1.

$f^{\epsilon_{\mathrm{SK}}}$: The systematic errors on the selection efficiency for FC1Rμ events is estimated as a function of the incident neutrino energy, which is divided into six bins, corresponding to that of PIMON. The systematic errors come from the uncertainties of the particle identification, ring counting, and energy scale. The estimation results are shown in Table 10.1.

$f_{\mathrm{SK}}^{\mathrm{E-scale}}$: The systematic errors on SK energy scale is assigned to 0.020 and 0.021 for SK-I and SK-II, respectively, as describe in Section 9.4.

f^{norm} : The systematic error on $N^{\mathrm{exp}}_{\mathrm{K2K-Ia}}$ is estimated by taking into account of those on the ND spectrum (f^{ϕ}) and the Far/Near flux ratio ($f^{\mathrm{F/N}}$), since the two systematic parameters are not prepared for K2K-Ia in the oscillation analysis. In total, the systematic error on $N^{\mathrm{exp}}_{\mathrm{K2K-Ia}}$ is obtained to be $^{+17.6}_{-14.9}$%. By using Eq. 10.12, the central value and the error of $N^{\mathrm{exp}}_{\mathrm{K2K-Ia}}$ are calculated to be $4.6^{+0.80}_{-0.68}$ events in the null oscillation case. Although the number of events and its error is expected to become smaller in the oscillation case, $\sigma =^{+0.80}_{-0.68}$ event is used in this analysis.

Since the uncertainties in the Far/Near flux ratio, the neutrino energy spectrum, and the cross-section for each interaction channel are introduced as the systematic parameters, the errors on $f^{\mathrm{norm}}_{\mathrm{K2K-Ib}}$ and $f^{\mathrm{norm}}_{\mathrm{K2K-II}}$ are the quadratic sum of the other uncertainties, which comes from the 1KT event selection, the SK event selection, the POT normalization, and the statistics. The systematic errors on $f^{\mathrm{norm}}_{\mathrm{K2K-Ib}}$ and $f^{\mathrm{norm}}_{\mathrm{K2K-II}}$ are estimated as $\pm 5.1\%$ and $\pm 5.1\%$, respectively.

For $f^{\phi,\mathrm{nonQE}}$ and $f^{F/N}$, the correlations between the parameters are taken into account by using the error matrices ($M^{\phi,\mathrm{nonQE}}$ and $M^{F/N}$), respectively. The central values and the errors for the systematic parameters are summarized in Table 10.1.

10.2 Fitting results

10.2.1 The best fit value

The maximum likelihood fitting with $\mathcal{L}$ is performed to obtain the oscillation parameters, Δm^2 and $\sin^2 2\theta$. The best fit value is obtained as

$$(\Delta m^2, \sin^2 2\theta) = (2.6 \times 10^{-3}[\mathrm{eV}^2], 1.2). \tag{10.19}$$

The value of $\sin^2 2\theta$ is larger than the upper limit of the physical condition ($0 \leq \sin^2 2\theta \leq 1$). If $\sin^2 2\theta$ is restricted within the physical region, the best fit value becomes

$$(\Delta m^2, \sin^2 2\theta) = (2.8 \times 10^{-3}[\mathrm{eV}^2], 1.0). \tag{10.20}$$

The fitting with only shape likelihood ($\mathcal{L}_{\mathrm{shape}}$) is also performed. These results are summarized in Table 10.2 with those of only K2K-I and K2K-II data. Since the normalization likelihood ($\mathcal{L}_{\mathrm{norm}}$) is a single Poisson probability, the fit result with only $\mathcal{L}_{\mathrm{norm}}$ cannot determine two parameters simultaneously.

Table 10.1: A summary of the central values and the errors for the systematic parameters.

	Center	Error		Center	Error
f_1^{ϕ} (0.0-0.5 GeV)	1.712	± 0.421	$f_1^{\epsilon\mathrm{SK-I}}$ (0.0-0.5 GeV)	1.000	± 0.041
f_2^{ϕ} (0.5-0.75 GeV)	1.095	± 0.073	$f_2^{\epsilon\mathrm{SK-I}}$ (0.5-1.0 GeV)	1.000	± 0.034
f_3^{ϕ} (0.75-1.0 GeV)	1.146	± 0.059	$f_3^{\epsilon\mathrm{SK-I}}$ (1.0-1.5 GeV)	1.000	± 0.036
f_4^{ϕ} (1.0-1.5 GeV)	1.000	± 0.000	$f_4^{\epsilon\mathrm{SK-I}}$ (1.5-2.0 GeV)	1.000	± 0.049
f_5^{ϕ} (1.5-2.0 GeV)	0.917	± 0.040	$f_5^{\epsilon\mathrm{SK-I}}$ (2.0-2.5 GeV)	1.000	± 0.049
f_6^{ϕ} (2.0-2.5 GeV)	1.051	± 0.053	$f_6^{\epsilon\mathrm{SK-I}}$ (2.5 GeV -)	1.000	± 0.049
f_7^{ϕ} (2.5-3.0 GeV)	1.179	± 0.136	$f_{\mathrm{SK-I}}^{\mathrm{E-scale}}$	1.000	± 0.020
f_8^{ϕ} (3.0 GeV -)	1.242	± 0.180	$f_1^{\epsilon\mathrm{SK-II}}$ (0.0-0.5 GeV)	1.000	± 0.062
f^{nonQE}	0.958	± 0.035	$f_2^{\epsilon\mathrm{SK-II}}$ (0.5-1.0 GeV)	1.000	± 0.046
f^{NC}	1.000	± 0.421	$f_3^{\epsilon\mathrm{SK-II}}$ (1.0-1.5 GeV)	1.000	± 0.042
$f_1^{\mathrm{F/N}}$ (0.0-0.5 GeV)	1.000	± 0.026	$f_4^{\epsilon\mathrm{SK-II}}$ (1.5-2.0 GeV)	1.000	± 0.043
$f_2^{\mathrm{F/N}}$ (0.5-1.0 GeV)	1.000	± 0.043	$f_5^{\epsilon\mathrm{SK-II}}$ (2.0-2.5 GeV)	1.000	± 0.043
$f_3^{\mathrm{F/N}}$ (1.0-1.5 GeV)	1.000	± 0.065	$f_6^{\epsilon\mathrm{SK-II}}$ (2.5 GeV -)	1.000	± 0.043
$f_4^{\mathrm{F/N}}$ (1.5-2.0 GeV)	1.000	± 0.104	$f_{SK-II}^{\mathrm{E-scale}}$	1.000	± 0.021
$f_5^{\mathrm{F/N}}$ (2.0-2.5 GeV)	1.000	± 0.111			
$f_6^{\mathrm{F/N}}$ (2.5 GeV -)	1.000	± 0.122			
$f_{\mathrm{K2K-Ia}}^{\mathrm{norm}}$	1.000	${}^{+0.80}_{-0.68}\left(\frac{1}{N_{\mathrm{K2K-Ia}}^{\mathrm{exp}}}\right)$			
$f_{\mathrm{K2K-Ib}}^{\mathrm{norm}}$	1.000	± 0.051			
$f_{\mathrm{K2K-II}}^{\mathrm{norm}}$	1.000	± 0.051			

Table 10.2: A summary of the oscillation parameters at the best fit point for each fitting condition. Since the best fit point is unphysical, the best point within the physical region is also listed.

		all region		physical region	
		Δm^2 [eV^2]	$\sin^2 2\theta$	Δm^2 [eV^2]	$\sin^2 2\theta$
K2K-I+II	shape + norm.	2.6×10^{-3}	1.2	2.8×10^{-3}	1.0
	shape only	2.8×10^{-3}	1.3	2.9×10^{-3}	1.0
K2K-I	shape + norm.	2.8×10^{-3}	1.1	2.9×10^{-3}	1.0
K2K-II	shape + norm.	2.4×10^{-3}	1.3	2.6×10^{-3}	1.0

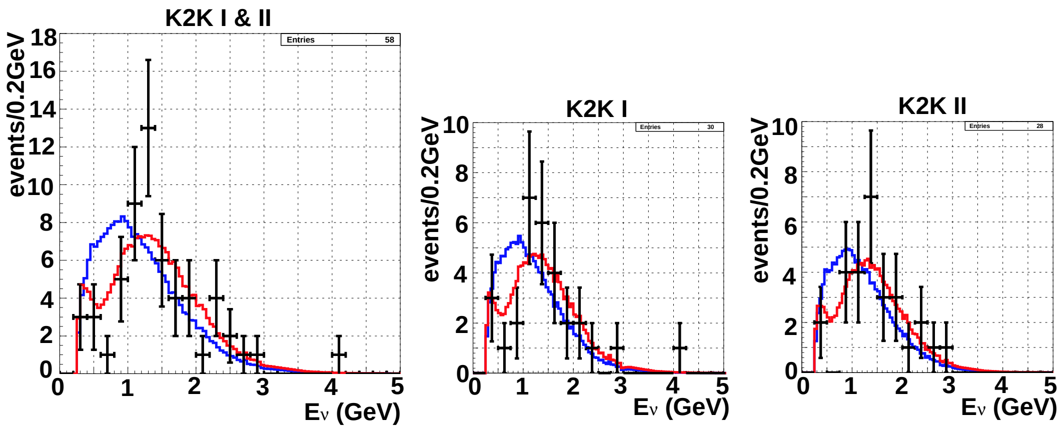

Figure 10.1: $E_\nu^{\rm rec}$distribution of 1Rμ samples at the best fit point in the physical region. K2K-I+II data is plotted in the left figure. Center and right figures show K2K-I and K2K-II sub-samples, respectively. Open circles with error bars are data, and the red lines are the best fit spectra. Blue lines show the spectra in the case of null oscillation.

Table 10.3: A summary of the KS probability for each $E_\nu^{\rm rec}$ distribution.

	Best fit	Null oscillation
K2K-I+II	40%	0.051%
K2K-I	43%	0.062%
K2K-II	35%	0.052%

10.2.2 $E_\nu^{\rm rec}$ distribution

Fig. 10.1 shows the reconstructed neutrino energy distribution measured by SK for the K2K-I+II data set. In this figure, the fit function with the best fit value and null oscillation case $[(\Delta m^2, \sin^2 2\theta) = (0,0)]$, are overlaid. The clear dip around 0.6 GeV can be seen in the data, which is expected by the neutrino oscillation hypothesis.

10.2.3 Kolmogorov-Smirnov test

Consistency check with data and the fitting results is performed by Kolmogorov-Smirnov test (KS-test) [98]. The confidence probability is summarized in Table 10.3. The KS-probability is 40% for the spectrum shape of the best fit value, and 0.05% for null oscillation case. Each sub-sample favors the best fit point.

10.3 Null oscillation probability

The probability for null oscillation case is calculated with the maximum likelihood in the physical region ($\mathcal{L}_{\rm max}^{\rm phys}$) and that of null oscillation case ($\mathcal{L}_{\rm null}$).

Table 10.4: A summary of the null oscillation probability.

	K2K-I+II	K2K-I only	K2K-II only
Shape + Norm	**0.0029**%	0.025%	0.069%
Shape only	**0.55**%	8.6%	5.7%
Norm. only	**0.18**%	0.87%	3.9%

If $\Delta \ln \mathcal{L}_{\rm null}$ is defined as

$$\Delta \ln \mathcal{L}_{\rm null} \equiv \ln \frac{\mathcal{L}^{\rm phys}_{\rm max}}{\mathcal{L}_{\rm null}} = \ln \mathcal{L}^{\rm phys}_{\rm max} - \ln \mathcal{L}_{\rm null}, \tag{10.21}$$

the probability for the null oscillation case is calculated as

$$\text{probability} = exp(-\Delta \ln \mathcal{L}), \tag{10.22}$$

assuming the likelihood ($\mathcal{L}$) follows a two-dimensional Gaussian of the (Δm^2, $\sin^2 2\theta$). From the logarithm of the likelihood ratio ($\Delta \ln \mathcal{L}_{\rm null} = 10.4$), the null oscillation probability is evaluated to be 0.0028%, corresponding to 4.3 standard deviations. The null oscillation hypothesis is excluded with 99.998% confidence level (C.L.). The null oscillation probability for each sub-sample or for each likelihood term is summarized in Table 10.4. Both the fitting with the likelihood of the shape only and normalization only, reject the null oscillation hypothesis with 99% C.L.. This strong rejection power of the $E_\nu^{\rm rec}$ shape term is an indication of the E_ν dependence on the oscillation probability.

10.4 Allowed region for oscillation parameters

The allowed region is evaluated by using the logarithm of the likelihood ratio,

$$\Delta \ln \mathcal{L}^{\rm phys}_{\rm max}(\Delta m^2, \sin^2 2\theta) \equiv \ln \left(\frac{\mathcal{L}^{\rm phys}_{\rm max}}{\mathcal{L}(\Delta m^2, \sin^2 2\theta)} \right) \equiv \ln \mathcal{L}_{\rm max} - \ln \mathcal{L}(\Delta m^2, \sin^2 2\theta), \tag{10.23}$$

where $\mathcal{L}(\Delta m^2, \sin^2 2\theta)$ is the likelihood at (Δm^2, $\sin^2 2\theta$) and $\mathcal{L}^{\rm phys}_{\rm max}$ is the maximum likelihood in physical region of $[(\Delta m^2, \sin^2 2\theta) = (2.8 \times 10^{-3}, 1.0)]$. The certain probability corresponding to the $\Delta \ln \mathcal{L}$ threshold (C) covers the parameter region for

$$\Delta \ln \mathcal{L}(\Delta m^2, \sin^2 2\theta) \leq C. \tag{10.24}$$

Since the best fit value for $\sin^2 2\theta$ is out of the physical region, the coverage probability is calculated in the physical region. Fig. 10.2 shows the allowed region for the oscillation parameters. The allowed region is studied by using log-likelihood for the normalization and spectrum shape separately, as shown Fig. 10.3. The both 90% C.L. allowed regions contain the best fit point for the physical region, $(\Delta m^2, \sin^2 2\theta) = (2.8 \times 10^{-3}, 1.0)$. Fig. 10.4 shows the ΔL behavior as a function of Δm^2 at $\sin^2 2\theta = 1.0$, and that of $\sin^2 2\theta$ at $\Delta m^2 = 2.8 \times 10^{-3}$.

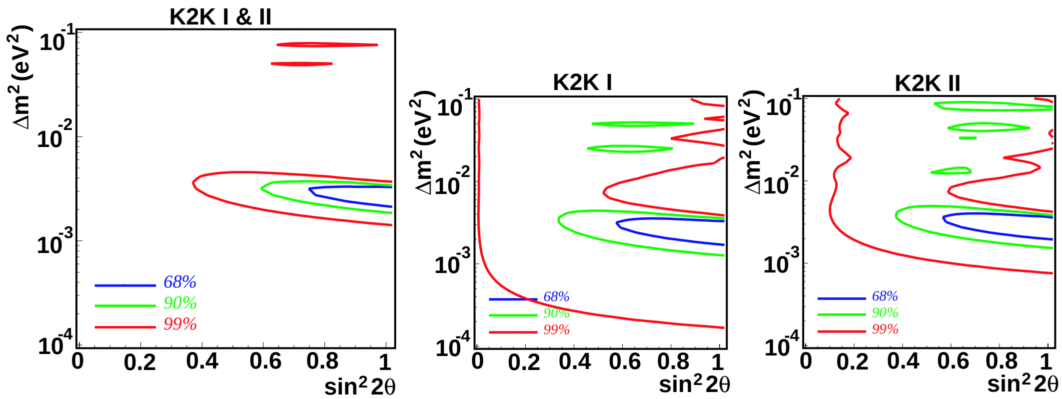

Figure 10.2: Allowed region for the oscillation parameters for K2K-I&II, K2K-I only, and K2K-II only. Blue, green, and red lines show 68%, 90% and 99% C.L. contours, respectively.

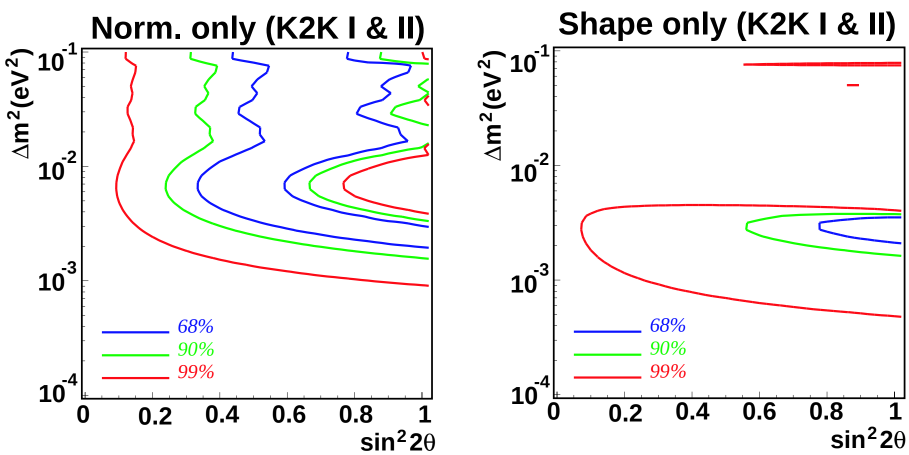

Figure 10.3: Allowed region for the oscillation parameters for the fitting with the likelihood of the normalization only and shape only. Blue, green , and red lines show 68%, 90% and 99% C.L. contours, respectively.

10.5 Summary of the neutrino oscillation study

The effect of the muon neutrino oscillation is studied with a maximum likelihood method. In the likelihood function, the uncertainties in the ND measurements, Far/Near flux ratio and SK systematics are properly taken into account, including the error cancellation in the normalization term.

The best fit value for the oscillation parameter is obtained $(\Delta m^2, \sin^2 2\theta) = (2.8 \times 10^{-3}[\mathrm{eV}^2], 1.0)$ in physical region. The KS probability for the E_ν^{rec} spectrum is 36% at the best fit point in the physical region, and the expected number of events (155.9) agrees with data (112) within the statistical error. Consequently, the observation is consistent with the neutrino oscillation.

On the other hand, the observation does not agree with the null oscillation case, which is excluded with 99.998% C.L. (4.3 standard deviations) by using the likelihood ratio method. The fitting with only E_ν^{rec} shape likelihood also excludes the null oscillation hypothesis, that indicates the E_ν dependence of the oscillation probability.

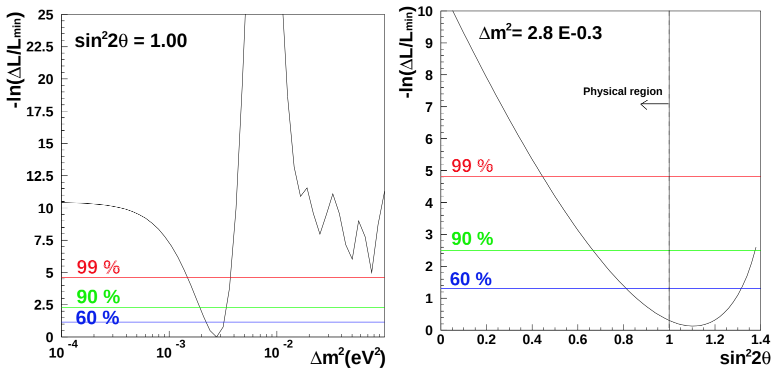

Figure 10.4: The log-likelihood curve as a function of Δm^2 along the axis of $\sin^2 2\theta = 1$ (left), and as a function of $\sin^2 2\theta$ along the axis of $\Delta m^2 = 2.8 \times 10^{-3}$ [eV^2] (right). The vertical axis shows the difference from the log-likelihood at the best fit point. Blue, green, and red lines show 68%, 90% and 99% C.L., respectively.

Finally, our results are compared with the atmospheric neutrino experiment. In the recent study of the atmospheric neutrino by SK, the 90% C.L. allowed parameter region has been obtained as ($1.5 \times 10^{-3} < \Delta m^2 < 3.4 \times 10^{-3}$ [eV^2], $\sin^2 2\theta > 0.92$). This region is consistent with our result (Fig. 10.4). Therefore, our measurement confirms the neutrino oscillation observed by the atmospheric neutrino experiments.

Chapter 11

Conclusions

The KEK-to-Kamioka (K2K) experiment is a long baseline neutrino oscillation experiment by using an accelerator, which was performed to confirm muon neutrino oscillation observed by the study of atmospheric neutrinos in Super-Kamiokande. In the K2K experiment, a number of the neutrino events and the energy spectrum were measured by the near detectors at KEK site and Super-Kamiokande. As an effect of neutrino oscillation, decrease of neutrino events and distortion of energy spectrum are observed at SK, comparing to the expectation by measurement of the near detectors. In particular, distortion of the energy spectrum is expected to become significant in low energy region below 1 GeV. Therefore, precise spectrum measurement in low energy region at the KEK site is necessary for the confirmation of neutrino oscillation. For this purpose, a full active scintillator bar (SciBar) detector was constructed and installed in the summer of 2003. The data of 2.04×10^{19} protons on target (POT) were taken by the SciBar detector, while a total of 9.2×10^{19} POT had been taken for the K2K experiment from June 1999 to November 2004.

In this thesis, the neutrino oscillation is studied with the measurement of the low energy neutrino spectrum by SciBar. The results in this analysis are described below.

- **Selection of the low-energy neutrino events in SciBar :**
  To improve the accuracy on the low-energy neutrino spectrum in SciBar, the low energy events (SciBar-contained events and EC-stopped events) are selected. Since background events synchronizing to the accelerator cycle (sky-shine backgrounds) and neutral current (NC) events contaminate in the low energy sample, the difficulties of these events are studied. Finally, the low energy sample is prepared by reducing the sky-shine backgrounds and NC events with the observed range. The fraction of CC-QE events in the low energy region below 1 GeV is increased by a factor of 30% with the low energy sample, comparing with the event sample of MRD-matching events only.

- **Study of the energy spectrum by SciBar:**
  The energy spectrum, especially in the low energy region, is measured by using SciBar. The systematic uncertainty in the neutrino energy spectrum ranging from 0.5 to 0.75 GeV with the low energy sample gets better from 25.4% to 22.3%, comparing to the previous analysis of the spectrum measurement in SciBar. The error on the low energy region mainly comes from the statistical error. In this study, the method to investigate the low energy region by SciBar is established.

- **Spectrum measurement at the near site :**

The spectrum measurement is performed with each near detector separately to check the consistency of the measurement. Although 1KT has good efficiency for the low energy region, it cannot separate QE interactions from nonQE interactions in its analysis. Therefore, estimating contamination of nonQE interactions, the low energy spectrum measured by 1KT is confirmed by SciBar. Since the measurement results are consistent with that of each detector, the energy spectrum at the near site is measured by using combined data of all the near detectors.

- **Study of the neutrino oscillation :**
  Finally, the neutrino oscillation is studied to investigate oscillation parameters observed by the atmospheric neutrino study in SK. Our best fit parameters are obtained to be $(\Delta m^2, \sin^2 2\theta) = (2.8 \times 10^{-3}[\mathrm{eV}^2], 1.0)$ in the physical region, which is consistent with the 90% C.L. allowed parameter region obtained at Super-Kamiokande, $(1.5 \times 10^{-3} < \Delta m^2 < 3.4 \times 10^{-3}$ [eV^2], $\sin^2 2\theta > 0.92$).

Appendix A

The Experimental Components

Although the setup for the K2K experiment is summarized in Chapter 3 briefly, some experimental components are supplemented in this chapter. At first the secondary beam monitors (the pion monitor and muon monitor) are described. Then, the far detector (Super-Kamiokande) are explained. Finally, the GPS system for the timing synchronization between KEK site and Super-Kamiokande is described.

A.1 Pion monitor (PIMON)

The momentum and the divergence of pions are measured by the pion monitor (PIMON) [96], which is located just after the second horn magnet. In this section, the detector characteristics and the measurement of the secondary pions are described.

A.1.1 Detector characteristics

The PIMON is a gas Cerenkov detector, which consists of a gas vessel, a spherical mirror, and a photo detector as shown in Fig. A.1.

The gas vessel of the PIMON is a cylinder of 91 cm in diameter and 90 cm in length, attached to the edge of an approximately 3 m arm. Cherenkov lights generated in the gas are reflected by a pie-shaped spherical mirror at the beam line, and detected by a photo detector at the focal plane. The gas vessel is made of 5 mm thick stainless steel, which has aluminum beam windows at the beam entrance and exit. The thickness of aluminum beam windows is 1 mm, which corresponds to 0.01 radiation length and 0.0025 interaction length. An aluminum foil of 50 μm thickness is located at 23 cm in front of the mirror to define the fiducial area of Cherenkov light emission. The gas vessel is filled with freon gas R-318 (C_4F_8) for its high refractive index to measure pion momentum as low as possible. For rejection of sever background from the primary protons, the refractive index should be lower than 1.00264 as shown in Fig. A.2. The momentum threshold of the pions is determined 2 GeV, which corresponds to 1 GeV for neutrinos.

A spherical mirror focuses Cherenkov photons emitted by particles with the same beta and angle, onto the same ring at the focal plane, being independent of its emission point. The radius of the curvature is 6 m and the size is 60 cm $\times$ 15 cm. Its thickness is about 8 mm. It is made of Pyrex glass which is partially coated with aluminum and frosted by sand to make a pie-shape.

Twenty photo-multiplier (PMTs) are used to detect the photons on the forcal plane of the spherical mirror. PMTs are located far away from the beam line, as shown in Fig. A.1, in order to avoid the

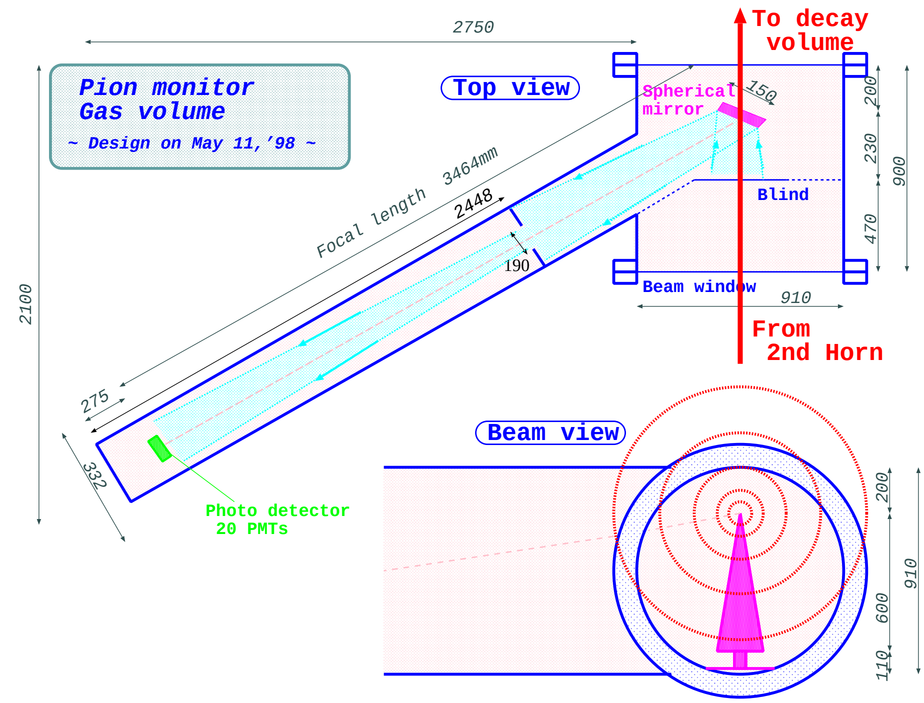

Figure A.1: A schematic view of the pion monitor (PIMON).

radiation damage. The PMTs are aligned along the vertical direction with 35 mm interval. The type of the PMT is modified R5600-01Q made by Hamamatsu Photonics Corporation. The diameter of the outer socket is 15.5 mm and that of the photo cathode is 8 mm. The radiation hardness was tested at KEK-PS K3 beamline [96, 22].

A.1.2 Measurement of the (p_π, θ_π) distribution

We took data with nine sets of the refractive indices. To obtain a fine Cherenkov image, data was taken with a half PMT interval for each refractive index. Additional data was taken, removing the mirror from the PMT array to make low background condition. The background coming from a electro-magnetic shower is estimated by the MC simulation which is tuned by the data of the lowest refractive index. Fig. A.3 shows the Cherenkov light distribution for each refractive index after the background subtraction in November 1999 data.

A χ^2 fitting is employed to extract the (p_π, θ_π) distribution from the Cherenkov light distributions with various reflective indices. The (p_π, θ_π) distribution is binned into 5×10 bins, which are 5 bins for p_π above 2 GeV/c with 1 GeV/c step ($p_\pi > 6$ GeV/c is integrated) and 10 bins for θ_π from -50 to 50 mrad with 10 mrad step. A MC template of the Cherenkov light intensity on the l-th PMT ($N^{\rm MC}_{k,l}(i,j)$) in k-th refractive index, is calculated for each (p^i_π, θ^j_π)-bin. The observed Cherenkov light distribution for the k-th refractive index ($N^{\rm data}_{k,l}(i,j)$) is fitted by the χ^2 function with the MC template as

$$\chi^2 = \sum_k \left(\sum_{l=1} \frac{N^{\rm data}_{k,l}(i,j) - W_{i,j} \cdot N^{\rm MC}_{k,l}(i,j)}{\sigma^2_{k,l}} \right), \qquad \text{(A.1)}$$

where $W_{i,j}$ is a weighting factor on $N^{\rm MC}_{k,l}(i,j)$ and $\sigma_{k,l}$ is the measurement error on the l-th PMT. $W_{i,j}$

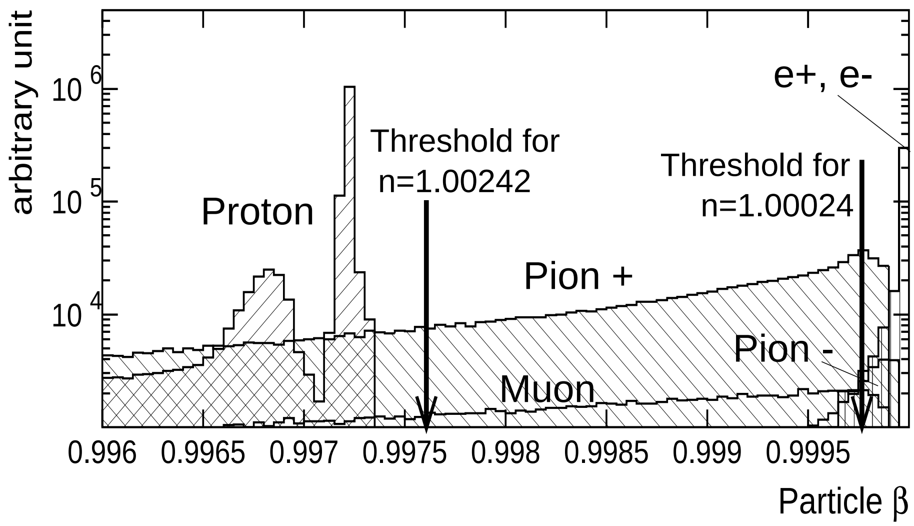

Figure A.2: Distributions of beta for protons, pions, muons and electrons after the second horn.

is a fitting parameter of the χ^2 function.

The expected neutrino spectrum at ND (SK) ($\phi_{i,j}^{\mathrm{ND(SK)}}(E_\nu)$) is calculated with the neutrino spectrum of the (p_π^i, θ_π^j)-bin obtained by the MC simulation and their weighting factor ($W_{i,j}$), as follows.

$$\Phi^{\mathrm{ND(SK)}}(E_\nu) = \sum_{i=1}^{5}\sum_{j=1}^{10} W_{i,j} \cdot \Phi_{i,j}^{\mathrm{ND(SK)}}(E_\nu). \tag{A.2}$$

A.2 Muon monitor (MUMON)

Muon monitor (MUMON) is placed in a pit at the downstream of the beam dump (Fig. A.4). It consists of two detector parts, an ionization chamber (ICH) and a silicon solid detector (SSD) array.

Since the energy loss in the beam dump is about 5.5 GeV for a minimum ionizing particle, only 2.1 % of muons can reach the MUMON. Fig. A.5 shows the momentum distributions of pions, muons and neutrinos before the beam dump. The beam profile measured by MUMON works as a good indicator of the overall beam steering towards SK, since high energy muons are more sensitive to the beam direction.

Ionization chamber

The ionization chamber (ICH) is a segmented ionization chamber like SPIC in the primary beamline. The cross section is 190 cm × 175 cm to measure the broad muon profile at the beam dump. There are three planes inside the gas vessel filled with Ar gas. The gap between two planes is 1 cm. Each readout plane is segmented into 5 cm × 200 cm strip lines to measure muon density distributions. The readout planes have 36 channels in the horizontal direction and 32 channels in the vertical direction. Each plane is divided into six sheets with a size of 60×90 cm^2, due to the difficulty to make a large sheet. The corresponding horizontal (vertical) readout strips in the vertically (horizontally) adjoining sheets are connected electrically. A typical muon profiles measured by ICH after gain correction are shown in Fig. A.6.

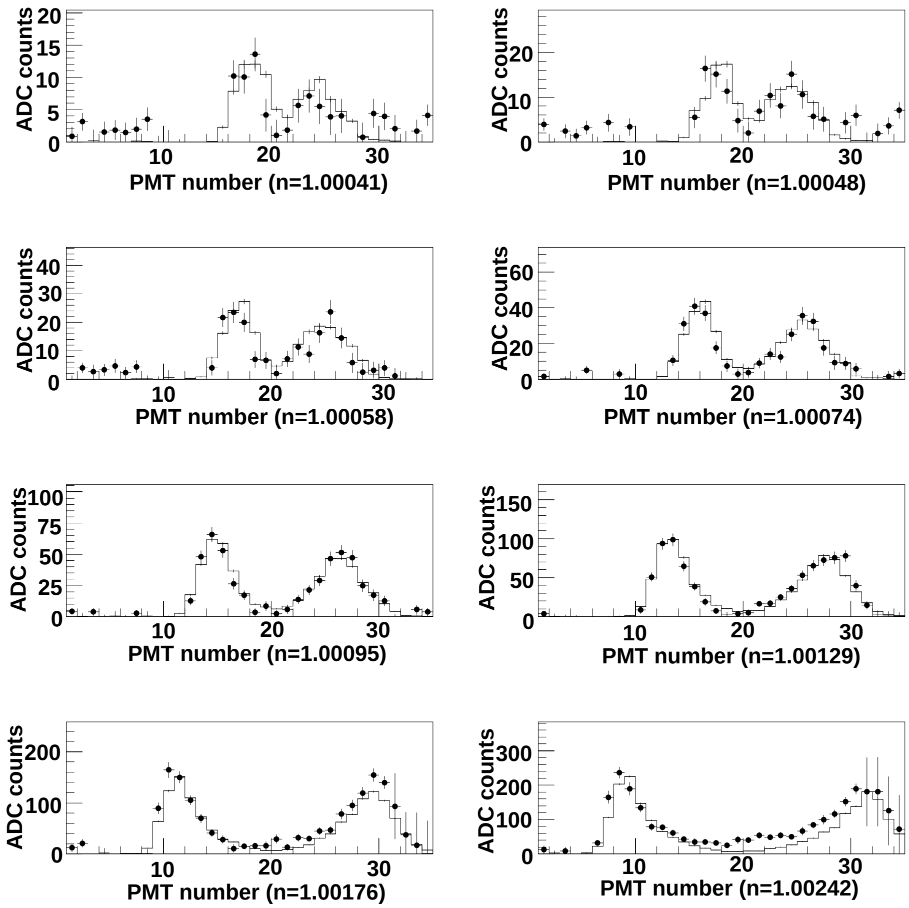

Figure A.3: The Cherenkov light distribution for each refractive index (n) after the background subtraction in November 1999 data.

Silicon detector array

The silicon detector (SSD) array is installed for redundancy. It gives the 2-dimensional information of the muon profile of 280 cm $\times$ 280 cm area. 17 small silicon detectors are installed along the horizontal and the vertical axis, which is 1 cm $\times$ 2 cm with 300 μm of depletion layer. 9 large silicon detectors are installed as diagonal array, which is 3.4 cm $\times$ 3.05 cm with 375 μm of depletion layer.

A.3 Super-Kamiokande

Super-Kamiokande (SK) is 250 km far from KEK, $36^\circ\ 25'$N in latitude and $137^\circ\ 18'$E in longitude. It is located 1000 m underground below the peak of Mt. Ikenoyama, which is equivalent to 2700 m of water level, and the detector site is about 2 km away horizontally from the entrance of the mine. The detector is filled with natural underground water flowing plentifully near the detector site. The temperature in the mine is about 10 $^\circ$C stably all through the year.

SK is an imaging water Cherenkov detector, which detects Cherenkov light photons generated by charged particles propagating in the water. The threshold momentum for the Cherenkov radiation are

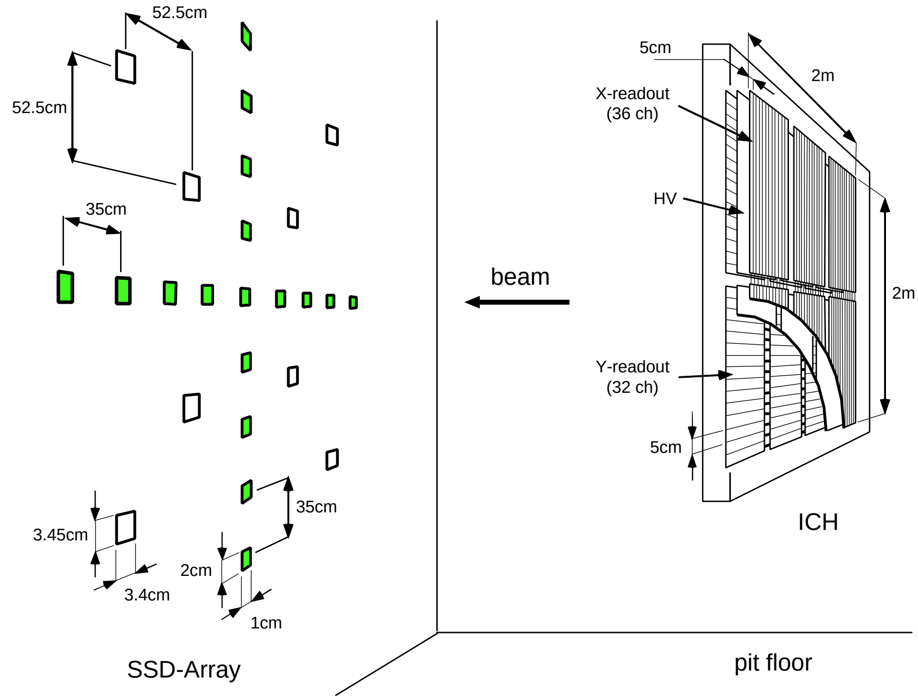

Figure A.4: A schematic view of the MUMON, silicon solid detectors (SSD) array and ionization chamber (ICH).

0.58, 120, 153 MeV/c for electrons, muons and pions, respectively. The Cherenkov light is emitted in a cone of half angle θ toward the direction of the particle track. The Cherenkov angle, θ, is defined as,

$$\cos\theta = \frac{1}{n\beta}, \tag{A.3}$$

where $\beta = v/c$, c is the light velocity and n is the refractive index of the medium ($n = 1.33$ for water). θ is about 42 degree in the water for a relativistic charged particle. The spectrum of the Cherenkov light as a function of the wavelength λ is expressed as,

$$\frac{dN}{d\lambda dx} = \frac{2\pi\alpha}{c}\left(1 - \frac{1}{n^2\beta^2}\right)\frac{1}{\lambda^2}, \tag{A.4}$$

where α is the fine structure constant and x is the track length of the charged particle. About 390 photons/cm are emitted in water, whose wavelength is $300 \sim 700$ nm.

The SK is a cylindrical water tank whose size is 41.4 m in height and 39.3 m in diameter, instrumented with photomultiplier tubes (PMTs), electronics, online data acquisition systems and a water purification system. The water tank to be filled with 50,000 tons of pure water, is made of stainless steel. The detector has two PMT layers, inner detector (ID) and outer detector (OD). The ID is 33.8 m in diameter and 36.2 m in height. The total mass is 32 kton. 11,146 20-inch PMTs are used for the ID. The PMTs are placed at intervals of 70 cm grid and the gaps are lined with black polyethlene therephthalate sheets (black sheets). The photocathode coverage is about 40%.

The OD surrounds the inner detector completely, whose thickness is 2.0 m for the side and 2.2 m for the top and bottom. 1,885 8-inch PMTs are mounted, which have 60×60 cm^2 square collar plate

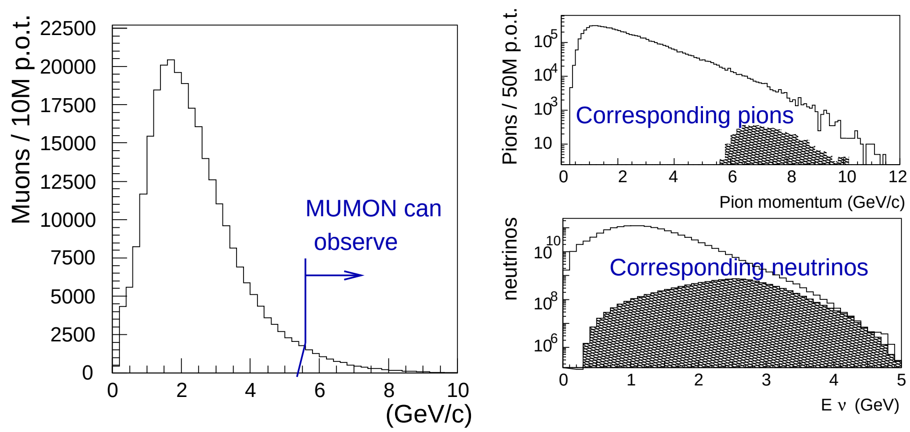

Figure A.5: The momentum distribution of muons, pions, and neutrinos before the beam dump, which is estimated by Monte Carlo simulation. The left figure shows the muon momentum distribution just before the beam dump. Only the muons above 5.5 GeV/c can reach the MUMON. The right figures show the momentum distributions of the generated pions (top) and neutrinos (bottom) in the beam line. The hatched histogram in these figures are corresponding pions and neutrinos to the muons above 5.5 GeV/c.

of wavelength shifter to increase the light collection efficiency. Tyvek sheets cover the inner surface of the OD to enhance the light collection efficiency. The OD is used as a veto counter for background rejection, which identifies incoming cosmic ray muons. In addition to that, 2 m thickness of the water in the OD, reduces gamma-ray and neutron backgrounds from the surrounding rock. These two detector volumes are optically isolated by black sheets and Tyvek sheets.

The photomultiplier tubes (PMTs) 20-inch in diameter were originally developed by Hamamastu Photonics Company in cooperation with members of Kamiokande. The photo-cathode is made of bialkali (Sb-K-Cs). The quantum efficiency is 21% at the wave length $\lambda = 400$ nm, which is the typical wave length of Cherenkov light. The average collection efficiency is more than 70%. The average PMT gain is about 10^7 with applied high voltage of 2 kV.

The PMT used for OD is 8-inch in diameter Hamamatsu R1408 PMT, which is recycled from the IMB experiment. The size of wavelength shifter which collars the outer PMT is 60 cm on each side and 1.3 cm thick. It absorbs ultraviolet light and re-radiates blue light. Consequently, the light collection efficiency increases by 60%.

The SK detector has 3 type of triggers for the ID, which are named as high energy trigger (HE), low energy trigger (LE) and super low energy trigger (SLE). For OD, outer detector trigger (OD) is also prepared. The HE trigger is used mainly to identify K2K beam neutrinos, cosmic ray muons, atmospheric neutrino and proton decay candidates. The LE trigger is for solar neutrino analysis above $5 \sim 6$ MeV in the energy. The OD trigger is for the rejection of the cosmic ray muons. The SLE trigger started from May 1997 in order to push the analysis threshold of solar neutrino energy spectrum down to 4.6 MeV.

The water purification system circulates 50 m^3 of pure water per hour to keep its quality. The water purification system removes the radioactive materials and bacteria from the water. After the water purification, the concentration of radon, which is 10^4 Bq/m^3 in the mine primary water, is reduced to less than 10 mBq/m^3. The light attenuation length is kept to about 100 m at wavelength of 420 nm.

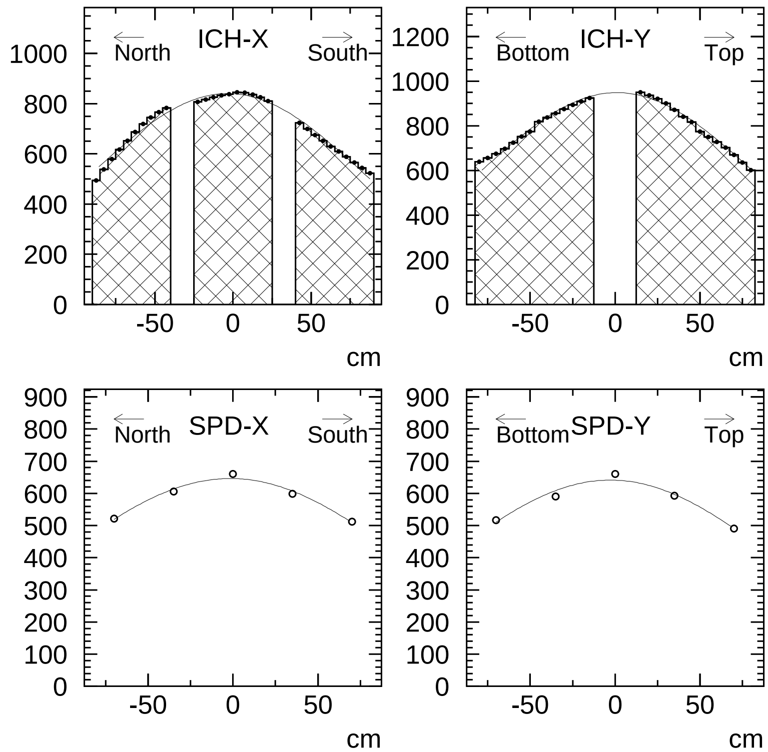

Figure A.6: Typical muon profiles measured by ionization chamber (ICH) and silicon pad detector arrays (SPD). Upper two figures are of ICH in the horizontal (left) and the vertical (right) directions. Gaps shown in these figures are corresponding to the insensitive regions of ICH as described in the text. Lower two are of SPD also in the horizontal (left) and the vertical (right) directions.

A.4 GPS system

GPS is a Satellite Navigation System founded and controlled by the U.S. Department of Defense (DOD). There are 24 satellites in six orbital planes. Each satellite has an atomic clock, which refers to the master clock at the U.S. Naval Observatory (USNO) and steered to Universal Time Coordinate (UTC). These satellites send information of their time and position by radio wave. A GPS receiver calculates its precise position and time by using the information from 4 satellites at the same time.

GPS system in the K2K experiment consists of GPS receivers, a VME receiver, and a 50 MHz 32-bit local time clock (LTC) as shown in Fig. A.7. Two independent GPS receivers (GPS1 and GPS2) in both KEK and SK are used in parallel for the hardware backup as well as their quality check with each other. The GPS receiver provides UTC time stamps every 1 sec and 1 Hz logic pulses, whose leading edges are synchronized to UTC. Its accuracy is better than 40 nsec in average and 150 nsec at the worst. UTC time stamp of GPS receiver is sent to and decoded by the VME receiver. LTC is a free-running 50 MHz 32-bit clock counter. The UTC time stamp and the current count of LTC are recorded when it receives an event trigger signal. UTC time stamp and LTC counters are read by the online computer. The synchronization of GPS receivers at KEK and SK had been taken by using an atomic clock. The timing difference of these two GPS with respect to the atomic clock was measured to be 115 $\pm$ 142 nsec (syst.).

The principle to determine the event triggered time is also shown in Fig. A.7. When event trigger

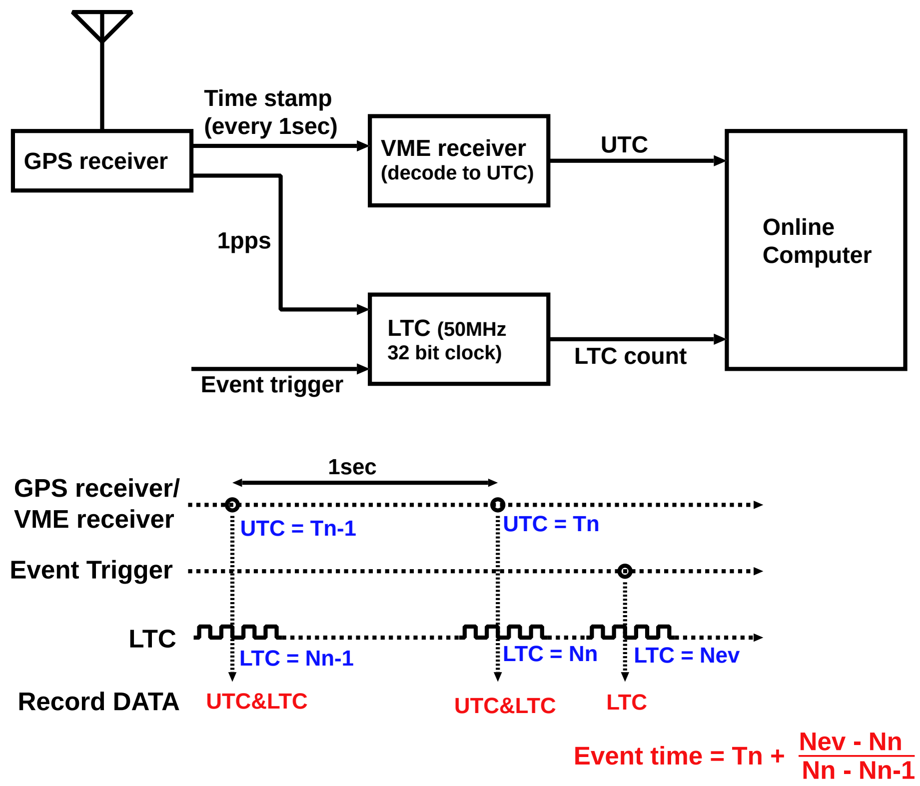

Figure A.7: A schematic view of GPS system in the K2K experiment.

is generated, the LTC count at the trigger timing (N_{ev}) is recorded. By looking at the latest two GPS-data, two sets of UTC time stamp and LTC count, (T_{n-1}, N_{n-1}) and (T_n, N_n), are known. The trigger timing, T_{ev}, is obtained by the linear interpolation as,

$$T_{ev} = T_n + \frac{N_{ev} - N_n}{N_{ev} - N_{n-1}}. \tag{A.5}$$

Two independent GPS were compared and agreed with each other within 100 nsec (FWHM). The stability of the system is continuously monitored in SK site by looking at LTC count in 1 sec, $N_n - N_{n-1}$.

Appendix B

Physics Formula for Monte Carlo Simulation

B.1 Pion production

For Sanford-Wang, Cho-ANL and Cho-CERN model, Sndford-Wang formula is employed to fit the experimental data. In Sanford-Wang formula, the differential yield of the secondary particles is given as follows.

$$\frac{d^2n}{d\Omega dp} = C_1 p^{C_2}\left(1 - \frac{p}{p_B - 1}\right)\exp\left(-\frac{C_3 p^{C_4}}{p_B^{C_5}} - C_6\theta(p - C_7 p_B \cos^{C_8}\theta)\right), \tag{B.1}$$

$\frac{d^2n}{d\Omega dp}$: Particle yield per interacting proton
θ : Angle of the secondary particle with respect to the beam axis in the laboratory frame
p : Momentum of the secondary particle
p_B : Momentum of the incident proton
C_i : Fitting parameters

The fit results of the positive pion production for Sanford-Wang, Cho-ANL, and Cho-CERN compilations are summarized in Table B.1. Fig. B.1 shows the differential cross-section of positive pion production in past experiments and fitted curves with the Cho-CERN compilation.

In Sanford-Wang, Cho-ANL and Cho-CERN, the hadron production is reproduced by Eq. B.2 for only a proton with the energy more than 10 GeV, and interactions for lower energy are simulated by the GCALOR model. For kaon production, the parameters described in [83], are employed.

Table B.1: Fitted parameters of Sanford-Wang formula for the positive pions in Sanford-Wang, Cho-ANL, and Cho-CERN compilations.

	C_1	C_2	C_3	C_4	C_5	C_6	C_7	C_8
Sanford-Wang	1.09	0.65	4.05	1.63	1.66	5.03	0.17	82.7
Cho-ANL	0.96	1.08	2.15	2.31	1.98	5.73	0.13	24.1
Cho-CERN	1.05	1.01	2.26	2.45	2.12	5.66	0.14	27.3

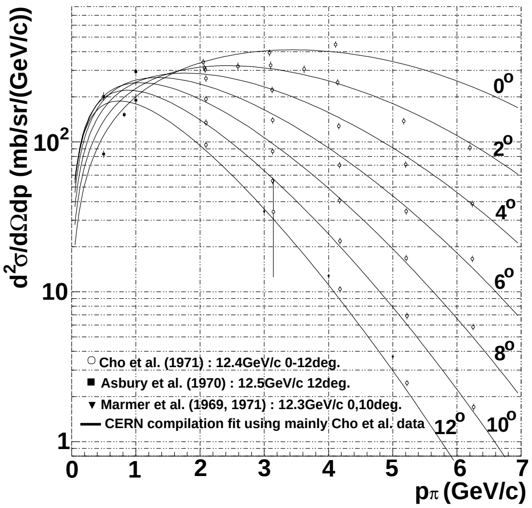

Figure B.1: The differential cross-section of positive pion production in past experiments and fitted curves of the Cho-CERN compilation.

B.2 Neutrino interaction

B.2.1 CC quasi-elastic scattering and NC elastic scattering

In Llewellyn Smith's formula [90], the amplitude for the charged-current quasi-elastic (CC-QE) is described as a product of hadronic and leptonic weak currents as following equation.

$$T = \frac{G_F}{\sqrt{2}} \bar{u}(k_2)\gamma^\mu(1-\gamma^5)u(k_1)\langle N'(p_2)|J_\mu^{\mathrm{had}}|N(p_1)\rangle, \tag{B.2}$$

where G_F is the Fermi coupling constant, p_1 (p_2) is the initial (final) nucleon four-momentum, and k_1 (k_2) is the initial (final) lepton four-momentum. The hadronic current, $\langle N'|J^{\mathrm{had}}|N\rangle$, can be expressed as function of four-momentum transfer, $Q^2 \equiv -q^2 = -(p_1 - p_2)^2$, as

$$\langle N'|J^{\mathrm{had}}|N\rangle = \cos\theta_c \bar{u}(N') \left[\gamma_\lambda F_V^1(Q^2) + \frac{i\sigma_{\lambda_\nu} q^\nu \xi F_V^2(Q^2)}{2m_N} + \gamma_\lambda\gamma_5 F_A(Q^2)\right] u(N), \tag{B.3}$$

where θ_c is the Cabbibo angle, and m_N is the nucleon mass. The vector form factors, F_V^1 and F_V^2, are represented as follows.

$$F_V^1(Q^2) = \left(1 + \frac{Q^2}{4m_N^2}\right)^{-1} \left[G_E^V(Q^2) + \frac{Q^2}{4m_N} G_M^V(Q^2)\right], \tag{B.4}$$

$$\xi F_V^2(Q^2) = \left(1 + \frac{Q^2}{4m_N^2}\right)^{-1} [G_M^V(Q^2) - G_E^V(Q^2)], \tag{B.5}$$

$$G_E^V(Q^2) = \frac{1}{\left(1 + \frac{Q^2}{M_V^2}\right)^2}, \quad G_M^V(Q^2) = \frac{1+\xi}{\left(1 + \frac{Q^2}{M_V^2}\right)^2}, \tag{B.6}$$

where $\xi (\equiv \mu_p - \mu_n = 3.71)$ is the difference of anomalous magnetic dipole moments between a proton and neutron, and the vector mass in the dipole parameterization, M_V, is set to be 0.84 GeV/c. The axial form factor, F_A, is given by

$$F_A(Q^2) = \frac{-1.23}{\left(1+\frac{Q^2}{M_A^2}\right)^2}, \tag{B.7}$$

where M_A is the axial vector mass.

Finally, the differential cross section is expressed by

$$\frac{d\sigma}{dQ^2} = \frac{m_N^2 G_F^2 \cos^2\theta_c}{8\pi E_\nu^2}\left[A(Q^2 \mp B(Q^2)\frac{(s-u)}{m_N^2} + C(Q^2)\frac{(s-u)^2}{m_N^4}\right] \tag{B.8}$$

$$\begin{aligned} A(Q^2) &\equiv \frac{(m_l^2+Q^2)}{4m_N^2}\left[\left(4+\frac{Q^2}{m_N^2}\right)|F_A|^2 - \left(4-\frac{Q^2}{m_N^2}\right)|F_V^1|^2 + \frac{Q^2}{m_N^2}|\xi F_V^2|^2\left(1-\frac{Q^2}{4m_N^2}\right)\right. \\ &\quad \left. + \frac{4Q^2 F_V^1 \xi F_V^2}{m_N^2} - \frac{m_l^2}{m_N^2}(|F_V^1+\xi F_V^2|^2 + |F_A|^2)\right], \end{aligned} \tag{B.9}$$

$$B(Q^2) \equiv -\frac{Q^2}{m_N^2}F_A(F_V^1+\xi F_V^2), \tag{B.10}$$

$$C(Q^2) \equiv \frac{1}{4}\left(|F_A|^2 + |F_V^1|^2 + \frac{Q^2}{m_N^2}\left|\frac{\xi F_V^2}{2}\right|^2\right), \tag{B.11}$$

$$(s-u) \equiv 4m_N E_\nu - Q^2 - m_l^2, \tag{B.12}$$

where E_ν is the incident neutrino energy, and m_l is the lepton mass. The sign of $B(Q^2)$ in Eq. B.12 is "$-$" for neutrinos and "$+$" for anti-neutrinos.

Fig. B.2 shows the quasi-elastic cross section as a function of E_ν with M_A = 0.91, 1.01, 1.11 GeV/c^2 [47]. They are consistent with various measurement of bubble chamber around 1 GeV [46, 47, 48, 49].

The cross section of the NC elastic scattering is derived from following relations [51].

$$\sigma(\nu p \to \nu p) = 0.153 \times \sigma(\nu n \to e^- p), \tag{B.13}$$

$$\sigma(\nu n \to \nu n) = 1.5 \times \sigma(\nu p \to \nu p). \tag{B.14}$$

B.2.2 Resonance production channel

The differential cross-section for the single resonance production with the mass (M) is written as

$$\frac{d^2\sigma}{dQ^2 dE_\nu} = \frac{1}{32\pi m_N E_\nu^2}\cdot\frac{1}{2}\cdot\sum_{\text{spins}}|T(\nu N \to lN^*)|^2 \cdot \delta(W^2-M^2), \tag{B.15}$$

where W is the invariant mass of the hadron system, and the width of the resonance decay is neglected. The amplitude of the resonance production, $T(\nu N \to lN^*)$, is calculated according to the FKR (Feynman-Kislinger-Ravndal) baryon model [53]. This model includes vector and axial-vector form factors by using dipole parameterization with the same M_V and M_A values as CC-QE. The differential cross-section for the resonance production with a finite decay width, Γ, is derived by replacing the δ-function in Eq. B.15 with a Brei-Wigner formula as

$$\delta(W^2-M^2) \to \frac{1}{2\pi}\frac{\Gamma}{(W-M)^2+\Gamma^2/4}. \tag{B.16}$$

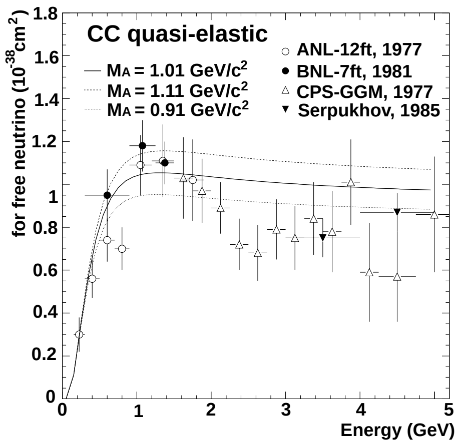

Figure B.2: The cross-section of CC-QE interaction on free neutron in NEUT as a function of the incident neutrino energy, together with the results of measurements by bubble chamber experiments. The solid, dashed, and dotted lines show the calculation of the cross-section in NEUT with $M_A =$ 1.01, 1.11, and 0.91 GeV/c, respectively. Data points are from ANL [46], BNL [47], GGM [48], and Serpukhov [49].

In NEUT, Δ(1232) and the other 17 resonance states with $W < 2.0$ GeV/c^2, are taken into account. Fig. B.3 shows our calculation results of the cross-section for each fianl state with $M_A = 1.01$ GeV/c^2 and experimental data [54, 55, 56].

The decay kinematics of Δ(1232) is calculated by the Rein-Sehgal model. For the other resonance states, the angular distribution of generated mesons is set to be isotropic in the rest frame of the resonance state.

B.2.3 Coherent pion production

The coherent pion production has been measured in a number of experiments [58, 59, 60, 61], providing a test of the partially conserved axial-vector current (PCAC) hypothesis [62]. The existing data agree with the Rein and Sehgal model [57] based on the PCAC hypothesis in the neutrino energy region from 7 to 100 GeV, while there is no measurement available at lower energies. Therefore, the coherent pion production in a few GeV region, was searched for by using SciBar [63] detector with K2K-IIb data.

Fig. B.4 shows the reconstructed q^2 distribution for SciBar CC coherent pion enriched sample. For MC simulation of CC coherent pion production, Rein and Sehgal model is employed [57] in NEUT. In low q^2 region less than 0.1 (GeV/c)^2, clear discrepancy between data and MC simulation is observed. The cross-section ratio of CC coherent pion production to the total CC interaction is measured to be $(0.04 \pm 0.29(\mathrm{stat.})^{+0.32}_{-0.35}(\mathrm{syst.})) \times 10^{-2}$. This result is consistent with the non-existence of CC coherent pion production at K2K neutrino beam energies, and hence we set an upper limit on the cross-section ratio at 90% C.L. to be

$$\sigma(\text{CC coherent } \pi)/\sigma(\nu_\mu(\mathrm{CC})) < 0.60 \times 10^{-2}. \tag{B.17}$$

The obtained upper limit is inconsistent with the model prediction by Rein and Sehgal of 2.67×10^{-2}. Assuming the cross-section relation $\sigma(\mathrm{CC}) = 2\sigma(\mathrm{NC})$ derived from isospin relations,

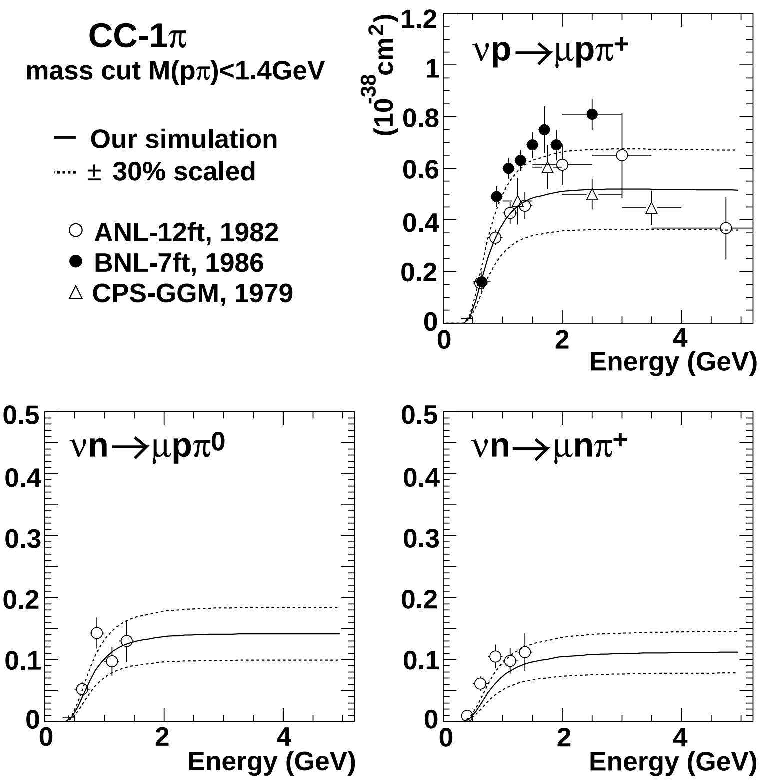

Figure B.3: The cross-section of CC resonance production channel in NEUT, together with experimental results. Solid lines show our calculation, and dashed lines show the cross-section scaled by $\pm 30\%$, where $M_A = 1.01$ GeV/c^2. The experimental results are from ANL [54], BNL [55], and GGM [56].

B.2.4 Deep inelastic interaction

The cross-section of CC-DIS is calculated based on Bjorken scaling [65] as follows.

$$\begin{aligned}
\frac{d^2\sigma}{dxdy} &= \frac{G_F^2 m_N E_\nu}{\pi} \cdot \left[(1 - y + \frac{1}{2}y^2 + C_1)F_2(x) + y(1 - \frac{1}{2}y + C_2)(xF_3(x))\right], \quad \text{(B.18)} \\
C_1 &= \frac{m_l^2(y-2)}{4m_N E_\nu x} - \frac{m_N x y}{2E_\nu} - \frac{m_l^2}{4E_\nu^2}, \\
C_2 &= -\frac{m_l^2}{4m_N E_\nu x}, \\
x &= Q^2/(2m_N(E_\nu - E_\mu) + m_N^2) \\
y &= (E_\nu - E_l)/E_\nu
\end{aligned}$$

m_N: Nucleon mass

m_l: Lepton mass

E_ν: Neutrino energy

E_l: the energy of the final state lepton,

where x and y are the Bjorken scaling parameters. The nucleon structure functions, F_2 and xF_3, are given by GRV94 [66], which is modified by Bodek and Yang [67]. The Bodek-Yang modification

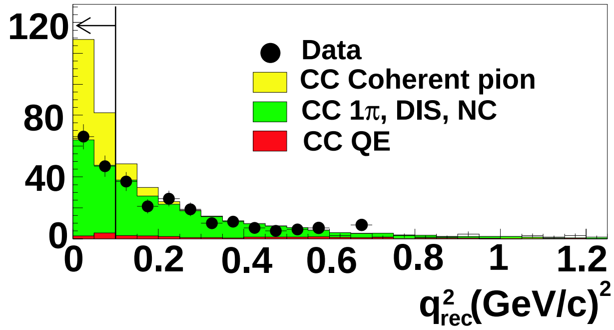

Figure B.4: The reconstructed q^2 distribution for SciBar CC coherent pion enriched sample.

effectively changes the cross-section by a Q^2-dependent factor as

$$\frac{d^2\sigma}{dxdy} \to \frac{Q^2}{Q^2 + 0.188} \cdot \frac{d^2\sigma}{dxdy}. \tag{B.19}$$

This treatment reduces the cross-section in low Q^2 region, which is favored by our previous analysis.

The kinematics of the hadronic system is simulated by two different methods depending on the range of its invariant mass, W. For $1.3 < W < 2.0$ GeV/c^2, only pions are considered as outgoing mesons. The mean multiplicity of pions, $\langle n_\pi \rangle$, is estimated from the result of 15-foot hydrogen bubble chamber experiment at Fermilab [68]. Assuming $\langle n_{\pi^+} \rangle = \langle n_{\pi^-} \rangle = \langle n_{\pi^0} \rangle$,

$$\langle n_\pi \rangle = 0.09 + 1.83 \ln W^2. \tag{B.20}$$

The number of pions for each event is determined by using KNO (Koba-Nielsen-Olesen) scaling [69]. The forward-backward asymmetry of pion multiplicity in the hadron center-of-mass system is included according to the results from the BEBC experiment at CERM-SPS [70] as

$$\frac{\langle n_\pi^F \rangle}{\langle n_\pi^B \rangle} = \frac{0.35 + 0.41 \ln W^2}{0.50 + 0.09 \ln W^2}. \tag{B.21}$$

In the region of $W > 2.0$ GeV/c^2, the kinematics of the hadronic system is calculated by JETSET/PYTHIA package [71].

For the NC deep inelastic scattering, the ratio of NC to CC is assumed by the experimental results [72] as,

$$\frac{\sigma(\mathrm{NC})}{\sigma(\mathrm{CC})} = \begin{cases} 0.26 & (E_\nu < 3\mathrm{GeV}) \\ 0.26 + 0.04(E_\nu/3 - 1) & (3 < E_\nu < 6\mathrm{GeV}) \\ 0.30 & (E_\nu > 6\mathrm{GeV}) \end{cases}. \tag{B.22}$$

Appendix C

The Spectrum Analysis with Near Detectors

The neutrino energy spectrum at the near site is measured by using all near detectors with measurement results of PIMON. In this chapter, we describe the event selection criteria and the definition of the χ^2 function for the spectrum fitting by the other detectors than SciBar.

C.1 1KT part

C.1.1 Event selection

Since the proton momentum in CC-QE is usually below the Cherenkov threshold, only one-ring muon-like events are suitable for CC-QE selection. In addition, the muon should be fully contained within the inner detector of 1KT to measure the muon momentum. Therefore, fully-contained single-ring muon-like (FC1Rμ) events are used for the measurement of the neutrino energy spectrum. Fig. C.1 shows an event display of a typical FC1Rμ event. The selection efficiency for the CC-QE interaction is estimated to be 53%. The fraction of CC-QE in the FC1Rμ sample is 58%. The selection procedure for FC1Rμ events is summarized below, and more detail description is found in [82].

Energy threshold

To reject low energy background events such as a muon decay of a cosmic ray, the threshold of FADC pulse height is set to 1000 photo-electrons, equivalent to the electron energy of 100 MeV.

Fiducial volume cut

The reconstructed vertex is required to be within a fiducial volume. The fiducial volume is defined as a cylindrical volume with a radius of 2 m and a length of 2 m,. as shown in Fig.C.2. It is oriented along the beam and shifted by 1 m upstream from the center of the tank. The fiducial mass is 25 tons.

Ring reconstruction

Using the charge and timing information of each PMT, Cherenkov ring image is obtained by reconstructing the ring direction, the outer edge of the most energetic ring, and the vertex position. For a

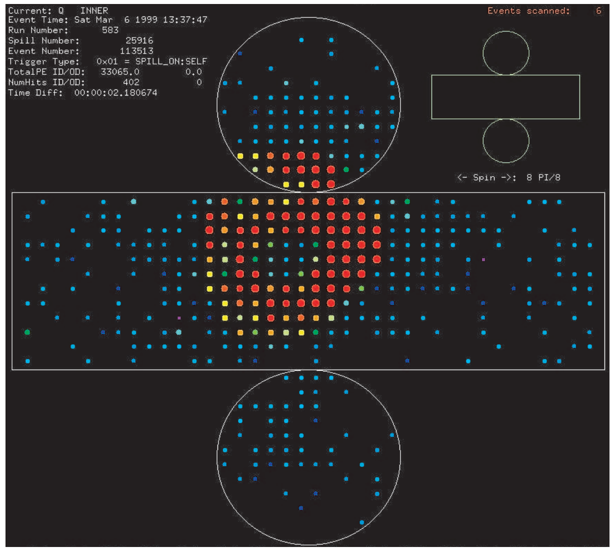

Figure C.1: Event display of typical FC1Rμ event for 1KT.

single-ring event, the another vertex finding algorithm is applied to improve the precision of the vertex position.

The vertex resolution is estimated by the distance between a reconstructed vertex and a true vertex by using the MC simulation. The angular resolution is similarly obtained from the angle between a reconstructed direction and a MC true direction. The vertex and angular resolutions are 17.3 cm and 1.8 degree for FC1Rμ events.

The vertex and angular resolution are also estimated by using cosmic ray. The vertex is found to be shifted by 10 cm toward the particle direction only for data. The angular resolution of the MC simulation is 2.5 degrees, and that of data is 4.1 degrees.

Fully-contained one-ring μ-like event selection

For the analysis, fully-contained one-ring μ-like (FC1Rμ) events are selected. The selection procedure is summarized as follows.

- Fully-contained event selection :
  To identify FC events, the number of photo-electrons in a PMT located within 20 degrees around the particle direction, POMAX20deg, is used. Fig. C.3 (left) shows the POMAX20deg distribution. POMAX20deg less than 200 photo-electrons is identified as fully-contained (FC) events, because the number of Cherenkov photons becomes larger at the exiting point of an outgoing muon.

- One-ring event selection :
  With likelihood method, the number of rings ($N_{\rm ring}$) is determined. Fig. C.3 (right) shows $N_{\rm ring}$ distribution of 1KT FC sample. Only one-ring events are used for the analysis.

- μ-like event selection :
  A ring is identified as μ-like or e-like by using the ring image and opening angle. Both a muon and charged pion make a sharp ring edge (μ-like), since it travels almost straight in a matter. On

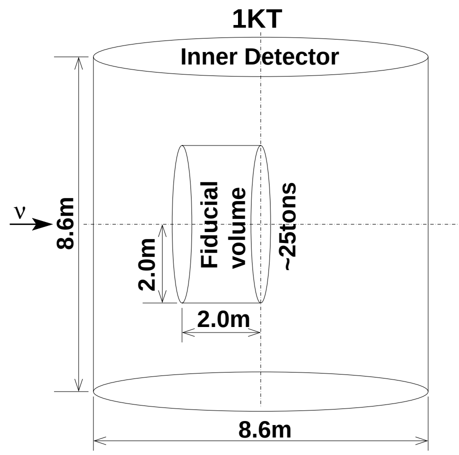

Figure C.2: The definition of the fiducial volume of 1KT. It is a cylindrical region which has a radius of 2 m and a length of 2 m.

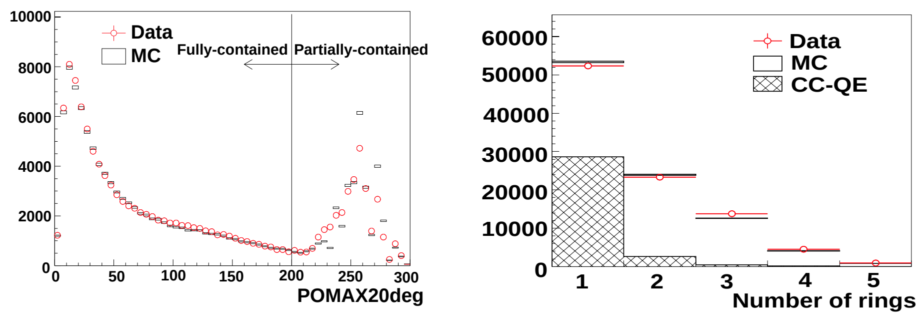

Figure C.3: The POMAX20deg distribution (left) and the number of ring, N_{ring}, distribution of 1KT FC sample (right).

the other hand, both an electron and a gamma ray make a fuzzy ring (e-like), because a cascade shower is created. According to MC simulation, 0.7% of muon neutrino events with single ring is mis-identified as e-like events, and 3.7% of electron neutrino events with single-ring are mis-identified as μ-like events.

C.1.2 Definition of χ^2

(p_μ, θ_μ) distribution

The bin width of the (p_μ, θ_μ) distribution of 1KT is the same as that of SciBar, except that the events above 90 degrees are integrated into one angular bin. The contents of the ith $p_\mu$and the jth $\theta_\mu$bin for MC simulation, is given by

$$N^{\text{MC}}(i,j) \equiv P^{\text{1KT}}_{\text{Norm}} \cdot \sum_{k=1}^{8} f_k^{\phi} \cdot [N^{\text{MC}}_{k,\text{QE}} + R_{\text{nQE}} \cdot N^{\text{MC}_{k,\text{nonQE}}}], \tag{C.1}$$

where $P^{\text{1KT}}_{\text{Norm}}$ is a free parameter for the normalization.

To implement the systematic error on the muon momentum scale, that of the MC simulation is modified into

$$p'_\mu = \frac{p_\mu}{P^{\mathrm{1KT}}_{\mathrm{p-scale}}}, \tag{C.2}$$

where $P^{\mathrm{1KT}}_{\mathrm{p-scale}}$ is a fitting parameter.

χ^2 function

The χ^2 of 1KT data is defined as

$$\chi^2_{\mathrm{1KT}} \equiv \sum_{i,j} \frac{[N^{\mathrm{data}}(i,j) - N^{\mathrm{MC}}(i,j)]^2}{[\sigma^{\mathrm{data}}_{\mathrm{stat}}(i,j)]^2 + [\sigma^{\mathrm{MC}}_{\mathrm{stat}}(i,j)]^2 + [\sigma_{\mathrm{syst}}(i,j)]^2} + \frac{(P^{\mathrm{1KT}}_{\mathrm{p-scale}} - 1)^2}{(\sigma^{\mathrm{1KT}}_{\mathrm{p-scale}})^2}, \tag{C.3}$$

where $\sigma^{\mathrm{data}}_{\mathrm{stat}}(i,j)$ and $\sigma^{\mathrm{MC}}_{\mathrm{stat}}(i,j)$ are the statistical errors of data and MC simulation, respectively. The bin-by-bin systematic errors, $\sigma_{\mathrm{syst}}(i,j)$, are also put into χ^2_{1KT}. The second term in Eq. C.3 is the constraint term for the momentum scale.

Systematic term 1KT

The central value of $P^{\mathrm{1KT}}_{\mathrm{p-scale}}$ is unity, and the error, $\sigma^{\mathrm{1KT}}_{\mathrm{p-scale}}$, is $^{+2.0}_{-2.3}$%. The error sources of $\sigma_{\mathrm{syst}}(i,j)$ are summarized below.

Vertex reconstruction : In cosmic ray data, a discrepancy of the reconstructed vertex position between data and the MC simulation is found, whose the difference is 10 cm. Therefore, changing the size and position of the fiducial volume by 10 cm, the systematic error is estimated to be the deviation of each bin content.

Angle resolution : The angular resolution of data is worse by 1.6 degrees than the MC simulation. The systematic error of 2.0 degrees, are assigned to the angular resolution. θ_μ is smeared for the MC simulation by 2.0 degrees, and the systematic error is evaluated as the difference by the smearing.

Ring counting : To select single-ring events, events with the ring counting likelihood is used. The systematic error which comes from discrepancy of the likelihood between data and MC simulation is estimated, changing cut position within the uncertainty. The systematic error is quoted as the function of each bin.

Particle identification : The particle identification is applied to select a μ-like ring. Removing this requirement, the difference is quoted as the systematic error.

C.2 SciFi part

Two data sets, K2K-Ib (with LG), and K2K-IIa (without LG), are used for SciFi data. In K2K-IIa, there was a four-layer prototype of SciBar (Mini-SciBar) instead of LG. Although K2K-IIb and K2K-IIc (with SciBar) is not used in the present analysis.

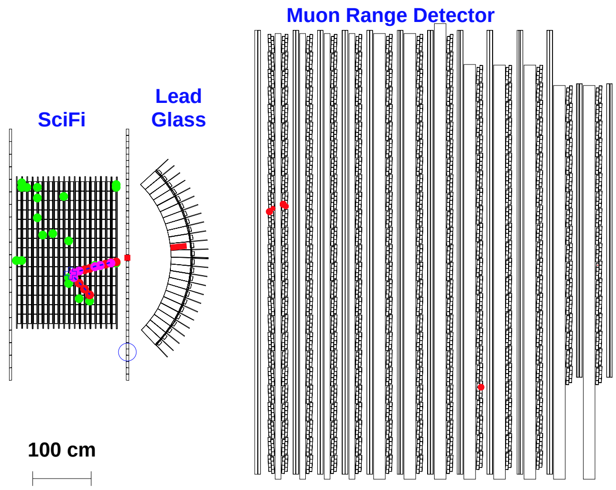

Figure C.4: Event display of typical CC-QE candidate for SciFi.

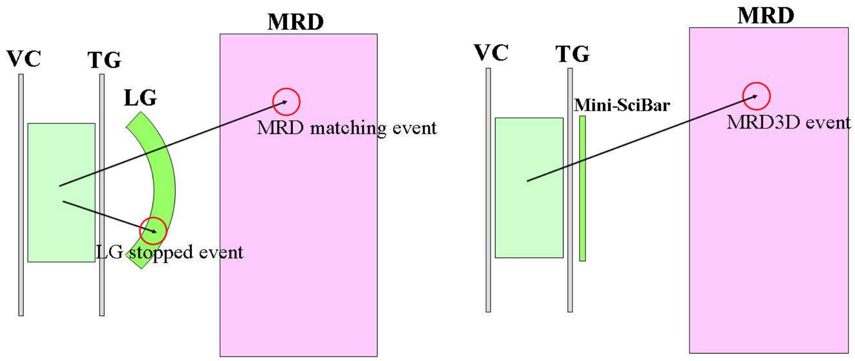

Figure C.5: Schematic view for each event type of SciFi in K2K-Ib (left) and K2K-IIa (right).

C.2.1 Event sample

Event selection

The charged current (CC) events of SciFi are selected with the similar way as SciBar. A typical CC-QE event is shown in Fig. C.4.

Fig. C.5 shows the schematic view for each event type of SciFi. Two types of MRD-matching events, “MRD 3D track (MRD3D) matching” and “MRD fist layer (MRD1L) matching events”, are used for SciFi data, whose definition is the same as SciBar. If a SciFi track matches to an LG cluster without any associate MRD hits, the track is identified as an “LG-stopped” events. For K2K-Ib, MRD-matching events and LG-stopped events are used for K2K-Ib. For K2K-IIa, only MRD-3D events are used, since hadrons contaminate in the other event samples due to a small amount of material between SciFi and MRD.

The fiducial volume is defined as the 2.2×2.2 m^2 region of X-Y view and the first to seventeenth layer of the water tank, corresponding to 5.9 tons. However, for 1-track events of LG-stopped events, the vertex is required to be only from the first to fourteenth tank, for rejection of backward neutrino events occurred in LG to enter SciFi.

Table C.1: Summary of the number of events in each event category of SciFi for the spectrum fitting.

	K2K-Ib	K2K-IIa
Detector Configuration	SciFi+LG+MRD	SciFi+MRD
MRD3D	6,935	5,188
MRD1L	1,403	-
LG-stopped	2,666	-

The detail descriptions of SciFi events selection are found in [94, 95].

Muon energy reconstruction

The muon energy is calculated as the summation of deposit energy in each detector.

- **K2K-Ib MRD-3D, 1L :** $E_\mu = E_\mu^{\rm SciFi} + E_\mu^{\rm TG} + E_\mu^{\rm LG} + E_\mu^{\rm MRD}$,
- **K2K-Ib LG-stopped :** $E_\mu = E_\mu^{\rm SciFi} + E_\mu^{\rm TG} + E_\mu^{\rm LGcluster}$,
- **K2K-IIa MRD-3D :** $E_\mu = E_\mu^{\rm SciFi} + E_\mu^{\rm TG} + E_\mu^{\rm Mini-SciBar} + E_\mu^{\rm MRD}$,

where $E_\mu^{\rm SciFi}$, $E_\mu^{\rm TG}$, $E_\mu^{\rm LG}$, $E_\mu^{\rm MRD}$, and $E_\mu^{\rm Mini-SciBar}$ are the energy deposit in SciFi, the trigger counter, LG, MRD, and Mini-SciBar, respectively, which are obtained by the muon range. $E_\mu^{\rm LGcluster}$ is also the energy deposit in LG, which is measured by the pulse height information of the cluster.

Event classifi cation

The SciFi events are classified into 1-track, 2-track-QE, and 2-track-nonQE samples in the same way as SciBar. 2-track events are divided into QE-like or nonQE-like by using $\cos\Delta\theta_p$ as shown in Fig. C.6, respectively. If $\Delta\theta_p$of a 2-track event is less than 25 degrees, it is classified as the QE enriched sample. If $\Delta\theta_p$ is more than 25 degrees, the event is categorized as the nonQE enriched sample. Table C.1 summarizes number of events for each event category. In total, 16,192 events are prepared for the spectrum fitting.

C.2.2 Definition of χ^2

(p_μ, θ_μ) distribution

The (p_μ, θ_μ) distribution for SciFi is binned into the same intervals as E_ν(Table 7.1) for $p_\mu$and every 10 degrees for θ_μ.

The definitions of MC (p_μ, θ_μ) distributions are as follows.

$$N^{\rm MC,1trk}(i,j) = P_{\rm Norm}^{\rm SciFi} \cdot \sum_{k=1}^{8} f_k^\phi \cdot [N_{k,\rm QE}^{\rm MC,1trk}(i,j) + R_{\rm nQE} \cdot N_{k,\rm nonQE}^{\rm MC,1trk}(i,j)], \tag{C.4}$$

$$N^{\rm MC,2trk-QE}(i,j) \quad = \quad P_{\rm Norm}^{\rm SciFi} \cdot \sum_{k=1}^{8} f_k^\phi \cdot [N_{k,\rm QE}^{\rm MC,2trk-QE}(i,j)$$

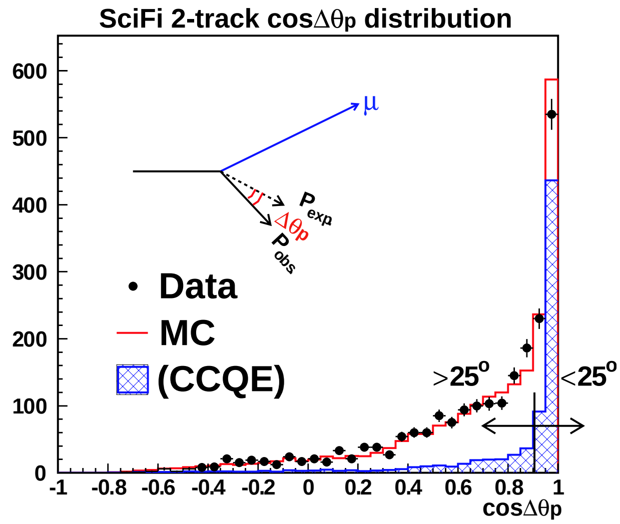

Figure C.6: The $\cos\Delta\theta_p$ distribution for SciFi 2-track data.

$$
\begin{aligned}
&+ \frac{R^{\rm SciFi}_{\rm rescat}}{1-R^{\rm SciFi}_{\rm rescat}}(1-P^{\rm SciFi}_{\rm rescat})\cdot N^{\rm MC,2trk-QE}_{k,\rm QE}(i,j) \\
&+ R_{\rm nQE}\cdot N^{\rm MC,2trk-QE}_{k,\rm nonQE}(i,j)], \qquad \text{(C.5)}
\end{aligned}
$$

$$
\begin{aligned}
N^{\rm MC,2trk-nonQE}(i,j) &= P^{\rm SciFi}_{\rm Norm}\cdot\sum_{k=1}^{8} f_k^{\phi}\cdot[N^{\rm MC,2trk-nonQE}_{k,\rm QE}(i,j) \\
&+ \frac{R^{\rm SciFi}_{\rm rescat}}{1-R^{\rm SciFi}_{\rm rescat}}(1-P^{\rm SciFi}_{\rm rescat})\cdot N^{\rm MC,2trk-nonQE}_{k,\rm QE}(i,j) \\
&+ R_{\rm nQE}\cdot N^{\rm MC,2trk-nonQE}_{k,\rm nonQE}(i,j)], \qquad \text{(C.6)}
\end{aligned}
$$

where $P^{\rm SciFi}_{\rm Norm}$ and $P^{\rm SciFi}_{\rm rescat}$ are the fitting parameters. The overall normalization is adjusted by $P^{\rm SciFi}_{\rm Norm}$, and the proton re-scattering cross-section is tuned by $P^{\rm SciFi}_{\rm rescat}$. The second term in Eq. C.5 and C.6 represent the migration between 2-track-QE and 2-track-nonQE samples due to the proton re-scattering. Here, $R^{\rm SciFi}_{\rm rescat}$ is the proton re-scattering probability in the CCQE interaction, estimated to be 0.33 by the NEUT MC simulation. The proton re-scattering cross-section is found to be $(87\pm10)\%$ of our simulation according to an electron scattering experiment Therefore, the central value of $P^{\rm SciFi}_{\rm rescat}$ is set to 0.87 with the systematic error of 0.10.

The systematic error on the second track finding efficiency is taken into account. The migration between the three categories is implemented by

$$N'^{\rm MC,1trk}(i,j) = (1-P^{\rm SciFi}_{\rm 2nd-eff})\cdot\left[N^{\rm MC,2trk-QE}(i,j)+N^{\rm MC,2trk-nonQE}(i,j)\right], \qquad \text{(C.7)}$$

$$N'^{\rm MC,2trk-QE}(i,j) = P^{\rm SciFi}_{\rm 2nd-eff}\cdot N^{\rm MC,2trk-QE}(i,j), \qquad \text{(C.8)}$$

$$N'^{\rm MC,2trk-nonQE}(i,j) = P^{\rm SciFi}_{\rm 2nd-eff}\cdot N^{\rm MC,2trk-nonQE}(i,j), \qquad \text{(C.9)}$$

where $P^{\rm SciFi}_{\rm 2nd-eff}$ is the fitting parameter to vary the second track finding efficiency. The central value of $P^{\rm SciFi}_{\rm 2nd-eff}$ is unity, and the systematic error on $P^{\rm SciFi}_{\rm 2nd-eff}$ is 5%.

The systematic errors on $E_\mu^{\rm MRD}$, $E_\mu^{\rm LG}$, and $E_\mu^{\rm LGcluster}$, are separately taken into account by three fitting parameters, $P^{\rm SciFi}_{\rm E-scale}$, $P^{\rm SciFi}_{\rm LG-density}$ and $P^{\rm SciFi}_{\rm LG-cluster}$, respectively. In the fitting, the reconstructed energy of the observed data is shifted as

$$\begin{array}{ll} \text{K2K-Ib MRD-3D, 1L :} & E'_\mu = E_\mu^{\rm SciFi} + E_\mu^{\rm TG} + E_\mu^{\rm LG}\cdot P^{\rm SciFi}_{\rm LG-density} + E_\mu^{\rm MRD}\cdot P^{\rm SciFi}_{\rm E-scale} \\ \text{K2K-Ib LG-Stopped :} & E'_\mu = E_\mu^{\rm SciFi} + E_\mu^{\rm TG} + E_\mu^{\rm LGcluster}\cdot P^{\rm SciFi}_{\rm LG-cluster} \\ \text{K2K-IIa MRD-3D :} & E'_\mu = E_\mu^{\rm SciFi} + E_\mu^{\rm TG} + E_\mu^{\rm Mini-SciBar} + E_\mu^{\rm MRD}\cdot P^{\rm SciFi}_{\rm E-scale} \end{array} \quad \text{(C.10)}$$

Definition of χ^2

The χ^2 for the SciFi data is defined as

$$\begin{aligned} \chi^2_{\rm SciFi} &= 2\sum_\tau\sum_C\sum_{i,j}\left[N'^{{\rm MC},\tau,C}(i,j) - N'^{{\rm data},\tau,C}(i,j) + N'^{{\rm data},\tau,C}(i,j)\ln\frac{N'^{{\rm data},\tau,C}(i,j)}{N'^{{\rm MC},\tau,C}(i,j)}\right] \\ &+ \sum_S\frac{(P_S^{\rm SciFi}-\langle P_S^{\rm SciFi}\rangle)^2}{(\sigma_S^{\rm SciFi})^2} \qquad \text{(C.11)} \\ \tau &= \{{\rm K2K-Ib-MRD, K2K-Ib-LG, K2K-IIa-MRD}\}, \\ C &= \{\text{1trk, 2trk-QE, 2trk-nonQE}\}, \\ S &= \{\text{E-scale, LG-density, LG-cluster, rescat, 2nd-eff}\}. \end{aligned}$$

The first term represents the χ^2 function between data and the MC simulation based on Eq. 7.8. The second term is the constraint term for the systematic parameters..

Systematic term for SciFi

The systematic errors on $E_\mu^{\rm LG}$, $E_\mu^{\rm LGcluster}$, and $E_\mu^{\rm MRD}$, have the dominant error on E_μ. The systematic error on $E_\mu^{\rm MRD}$ is 2.7% as descibed in Section 7.2.2. The energy deposit in LG was studied by a beam test (KEK-PS T501). As a result, observed $E_\mu^{\rm LG}$ is 5% smaller than the GEANT MC expectation with the error of $\pm$5% to $E_\mu^{\rm LG}$. Therefore, the factor of 0.95 is multiplied to $E_\mu^{\rm LG}$, and the systematic error of $\pm$5% is assigned. Since the conversion factor of the LG pulse height to the energy deposit is different by 30 MeV between data and the MC simulation in the T501 experiment, the systematic error on $E_\mu^{\rm LGcluster}$ is quoted as ± 30 MeV.

The central value ($\langle P_S^{\rm SciFi}\rangle$) and the systematic error of each systematic parameter ($\sigma_S^{\rm SciFi}$) are summarized in Table C.2.

C.3 PIMON part

The information from PIMON is employed to constrain the $E_\nu$spectrum shape (f_i^ϕ). The spectrum shape of $E_\nu > 1$ GeV is obtained by the measurement of secondary pions above 2 GeV/c. The PIMON spectrum parameters are expressed as $f^{\rm PIMON}$ ($i = 4,5,6,7$), where the subscript i indicates the same $E_\nu$bin as f_i^ϕ. The eighth bin ($f_8^{\rm PIMON}$) does not exist, because the neutrino flux above 2.5 GeV is integrated in the PIMON measurement. $f_4^{\rm PIMON}$ is set at unity, so that $f_i^{\rm PIMON}$ is written as

$$f_i^{\rm PIMON} = \frac{\Phi_i^{\rm PIMON}/\Phi_i^{\rm MC}}{\Phi_4^{\rm PIMON}/\Phi_4^{\rm MC}} \qquad (i = 5,6,7), \qquad \text{(C.12)}$$

Table C.2: The central values and errors of the systematic parameter for SciFi.

Parameter	Central value	Error
$P^{\mathrm{SciFi}}_{\mathrm{E-scale}}$	1.00	0.027
$P^{\mathrm{SciFi}}_{\mathrm{LG-density}}$	0.95	0.05
$P^{\mathrm{SciFi}}_{\mathrm{LG-cluster}}$ [MeV]	0.00	30.
$P^{\mathrm{SciFi}}_{\mathrm{rescat}}$	0.87	0.10
$P^{\mathrm{SciFi}}_{\mathrm{2nd-eff}}$	1.00	0.05

Table C.3: The input values to compute the χ^2 of PIMON. The units of Φ_i^{PIMON} and Φ_i^{MC} are arbitrary.

E_ν [GeV] (index i)	1.0-1.5 ($i=4$)	1.5-2.0 ($i=5$)	2.0-2.5 ($i=6$)	2.5- ($i=7$)
Φ_i^{PIMON}	6.30	3.21	1.01	0.427
Φ_i^{MC}	6.19	3.35	1.05	0.396
f_i^{PIMON}	$\equiv 1$	0.941	0.945	1.059
$\sigma_i^{\mathrm{PIMON}}$	-	$^{+10.7}_{-9.9}\%$	$^{+12.1}_{-17.7}\%$	$^{+47.7}_{-34.0}\%$

where Φ_i^{PIMON} and Φ_i^{MC} are the neutrino fluxes of the PIMON measurement and the MC simulation, respectively. The χ^2 of the PIMON part is given by

$$\chi^2_{\mathrm{PIMON}} = \sum_{i=5}^{7} \frac{(f_i^{\phi} - f_i^{\mathrm{PIMON}})^2}{(\sigma_i^{\mathrm{PIMON}})^2}, \tag{C.13}$$

where $\sigma_i^{\mathrm{PIMON}}$ is the error onn f_i^{PIMON}. In this equation, f_8^{ϕ} is combined into f_7^{ϕ}. The input values into Eq. C.12 and C.13 are summarized in Table C.3.

Appendix D

Test for Physics Beyond the Standard Model

The possibility of physics beyond the standard model is studied, which causes discrepancy between the observation and expectation for muon neutrinos. In this chapter, two physic modes, "neutrino decay" and "neutrino decoherence", are investigated.

D.1 Neutrino decay

If ν_2 and ν_3 are the mass eigenstates, there are two kinds of models for the non-radiative decays of ν_2 to ν_3 according to the neutrino types (Dirac or Majorana) as below.

- Dirac neutrino : $\nu_{2L} \to \bar{\nu}_{3R} + \phi$,
  where $\bar{\nu}_{3R}$ is a right-handed SU(2)-doublet and ϕ is a complex scaler field with the lepton number of -2, isospin of 0 and hypercharge of zero. In this case, the final state particles are sterile.

- Majorana neutrino : $\nu_{2L} \to \nu_{3R} + J$,
  where J is a Majoron which is a Gold-stone boson followed by the lepton number violation.

If we assume ν_2 neutrino is the only unstable state and decay into ν_3 with a rest-frame lifetime τ_0, the ν_μ survival probability is

$$
\begin{aligned}
P(\nu_\mu \to \nu_\mu) &= \sin^4\theta + \cos^4\theta \exp\left(-\frac{m_2}{\tau_2}\frac{L_\nu}{E_\nu}\right) && \text{(D.1)} \\
&= 2\sin^2\theta\cos^2\theta \exp\left(-\frac{m_2}{2\tau_2}\frac{L_\nu}{E_\nu}\right)\cos\left(\frac{\Delta m^2 L_\nu}{2E_\nu}\right), && \text{(D.2)}
\end{aligned}
$$

where m_2 and τ_2 are the mass and the lifetime of ν_2, θ is mixing angle, and $\Delta m^2 (= m_3^2 - m_2^2)$ is squared mass difference between ν_2 and ν_3. In the case of $\tau_2 \to \infty$, Eq. D.2 becomes normal neutrino oscillation case.

When ν_2 decay into a new (sterile) neutrino, Δm^2 can be very small. If $\Delta m^2 \to 0$, the survival probability is given by

$$
P(\nu_\mu \to \nu_\mu) = \left[\sin^2\theta + \cos^2\theta \exp\left(-\frac{m_2}{2\tau_2}\frac{L_\nu}{E_\nu}\right)\right]^2. \qquad \text{(D.3)}
$$

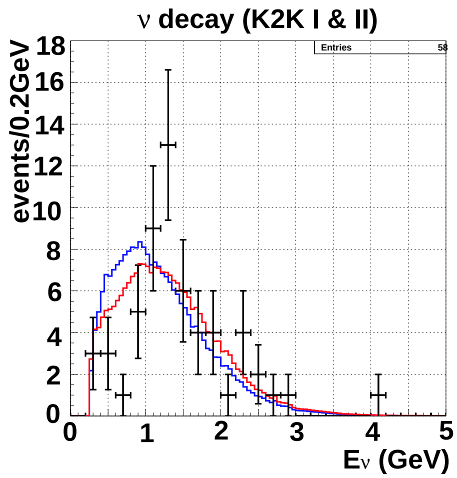

Figure D.1: $E_\nu^{\rm rec}$ distribution of 1Rμ samples at the best fit point in the physical region. Open circles with error bars are data, and the red lines are the best fit spectrum obtained by the neutrino decay model. Blue lines show the spectra in the case of null oscillation.

Assuming $\Delta m^2 \to 0$ with Eq. D.3, the expectation by the neutrino decay is compared with the observation at SK. The best fit parameter is obtained as $(m_2/\tau_2, \sin^2\theta) = (2.7 \times 10^{-3}, 1.0)$ in the physical region. Fig. D.1 shows the $E_\nu^{\rm rec}$ distribution of 1Rμ samples at the best fit point in the physical region. In this model, the dip in the $E_\nu^{\rm rec}$ distribution is not reproduced. The KS-probability for the spectrum shape is 2.4% at the best fit value.

D.2 Neutrino decoherence

Decoherence effect allows neutrino to take mixing state [103, 104]. Quantum gravity suggested by Hawiking in the context of black-hole thermodynamics [102], is possible source of decoherence. The effect of the neutrino decoherence is parameterized by $\gamma = \gamma_0(E_\nu/\mathrm{GeV})^n$, and the survival probability of ν_μ is as follow.

$$P(\nu_\mu \to \nu_\mu) = 1 - \frac{1}{2}\sin^2 2\theta \left[1 - \exp(-\gamma L_\nu)\cos\left(\frac{\Delta m^2 L_\nu}{2E_\nu}\right)\right]. \tag{D.4}$$

γ is a decoherence term defined as

$$\gamma = \gamma_0(E_\nu/\mathrm{GeV})^n, \tag{D.5}$$

where γ_0 is a constant value, and n is a integer number which shows dependence of γ on the energy variation. When $\gamma \to 0$, the normal neutrino oscillation formula is obtained.

Since n is strongly constrained in the results from SK [104], we assume the most possible case, $n = -1$, and that deficit comes from only decoherence effect. If $n = -1$ and $\Delta m^2 \to 0$, the survival probability is given by

$$P(\nu_\mu \to \nu_\mu) = 1 - \frac{1}{2}\sin^2 2\theta \left[1 - \exp\left(-\gamma_0 \frac{L_\nu}{E_\nu}\right)\right]. \tag{D.6}$$

By using Eq. D.6, the expectation by the neutrino decoherence is compared with the observation at SK. The best fit parameter is obtained as $(\gamma_0, \sin^2 2\theta) = (6.1 \times 10^{-3}, 1.0)$ in the physical region.

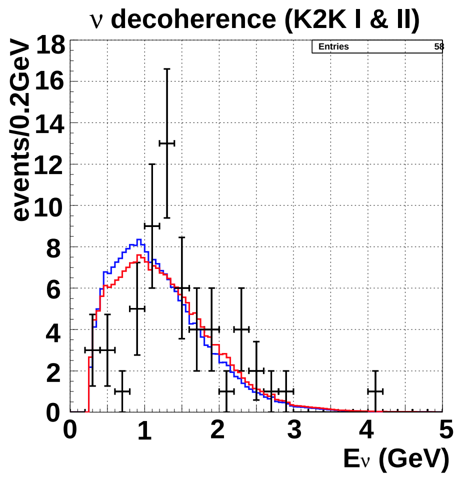

Figure D.2: E_ν^{rec}distribution of 1Rμ samples at the best fit point in the physical region. Open circles with error bars are data, and the red lines are the best fit spectrum obtained by the neutrino decoherence model. Blue lines show the spectra in the case of null oscillation.

Fig. D.2 shows the E_ν^{rec} distribution of 1Rμ samples at the best fit point in the physical region. As the neutrino decay, the dip around 0.6 GeV in the E_ν^{rec} distribution is not reproduced. The KS-probability is 0.49% for the spectrum shape of the best fit value.

Bibliography

[1] Z. Maki, M. Nakagawa and S. Sakata, Prog. Theor. Phys. **28**, 870 (1962).
[2] Y. Fukuda *et al.*, Phys. Rev. Lett. **81**, 1562 (1998).
[3] S. P. Mikheev and A. Y. Smirnov, Sov. J. Nucl. Phys. **42**, 913 (1985) [Yad. Fiz. **42**, 1441 (1985)]; L. Wolfenstein, Phys. Rev. **D17**, 2369 (1978).
[4] S. Fukuda *et al.*, Phys. Lett. **B539**, 179 (2002).
[5] B. Aharmim *et al.*, Phys. Rev. **C72**, 055502 (2005).
[6] B. Aharmim *et al.*, Phys. Rev. Lett. **92**, 181301 (2004).
[7] T. Araki *et al.*, hep-ex/0406035.
[8] A. Aguilar *et al.*, Phys. Rev. **D64**, 112007 (2001).
[9] Y. Ashie *et al.*, Phys. Rev. **D71**, 112005 (2005).
[10] S. H. Ahn *et al.*, Phys. Lett. B **511**, 178 (2001);
[11] M. H. Ahn *et al.*, Phys. Rev. Lett. **90**, 041801 (2003).
[12] M. H. Ahn *et al.*, Phys. Rev. Lett. **93**, 051801 (2004).
[13] Y. Yamanoi *et al.*, IEEE Trans. on Applied Superconductivity **10**, 252 (2000);
M. Kohama, Master thesis, Kobe University (1997), in Japanese;
Y. Yamanoi *et al.*, KEK-preprint 97-225 (1997);
Y. Yamanoi *et al.*, KEK-preprint 99-178 (1999).
[14] K.H. Tanaka *et al.*, KEK-preprint 91-27 (1991).
[15] T. Maruyama, Ph.D. thesis, Tohoku University (2000).
[16] T. Inagaki, Master's thesis, Tokyo University (1998), in Japanese.
[17] A. Suzuki *et al.*, Nucl. Instrum. Meth. **A453**, 165 (2000).
[18] B.J. Kim *et al.*, hep-ex/0206041.
[19] S. Kawabata *et al.*, Nucl. Instrum. Meth. **A270**, 11 (1988).
[20] M. Yoshida, Ph.D thesis, Osaka University (2001).
[21] T. Ishii *et al.*, Nucl. Instrum. Meth. **A482**, 244 (2002), hep-ex/0107041.
[22] T. Inagaki, Ph.D thesis, Kyoto University (2001).
[23] Y. Fukuda *et al.*, Nucl. Instrum. Meth. A **501**, 418 (2003);
[24] H. G. Berns and R. J. Wilkes, IEEE Trans. Nucl. Sci. 47, 340 (2000), hep-ex/9909021. S. Yamada, Ph.D thesis, University of Tokyo (2003).
[25] A. Pla-Dahnau, FERMILAB-Conf-00/343 (2001).
[26] The MINOS Collaboration, "Technical Design Report" NuMI-L-337 (1998).
[27] T. Morita, Master thesis, Kyoto University (2004) in Japanese;
T. Morita, Proc. Scintillating crystals, KEK Proceedings 2004-4 H, 227 (2004).
[28] T. Sasaki, Master thesis, Kyoto University (2004) in Japanese;
[29] M. Hasegawa, Master thesis, Kyoto University (2003) in Japanese;
M. Hasegawa, Proc. Scintillating crystals, KEK Proceedings 2004-4 H, 243 (2004).
[30] S. Yamamoto, Master thesis, Kyoto University (2003) in Japanese;
S. Yamamoto, Proc. Scintillating crystals, KEK Proceedings 2004-4 H, 257 (2004).

[31] Y. Arai, M. Ikeno, S. Iri, T. Sofue, M. Sagara and M. Ohta, IEEE Trans. Nucl. Sci. **49**, 1164 (2002);
[32] S. Buontempo *et al.*, Nucl. Instrum. Meth. A **349**, 70 (1994);
[33] N. Armenise *et al.*, CERN-SPSC/90-42; M. de Jong *et al.*, CERN-SPSC/93-134.
[34] Y. Takubo, Proc. Scintillating crystals, KEK Proceedings 2004-4 H, 263 (2004).
[35] S. Eidelman et al., Phys. Lett. B 592, 245 (2004);

[36] H. Maesaka, Ph.D thesis, Kyoto University (2005).
[37] H. Maesaka, Master thesis, Kyoto University (2001) in Japanese.
[38] T. A. Gabriel, J. D. Amburgey, and B. L. Bishop (1997), ORNL/TM-5619.
[39] C. Zeitnitz and T. A. Gabriel, Nucl. Instrum. Meth. A **349**, 106 (1994);
[40] *GEANT - Detector Description and Simulation Tool*, Application Software Group, Computing and Networks Division, CERN (1993), CERN Program Library Long Writeup W5013.
[41] R. A. Lundy *et al.*, Phys. Rev. Lett. **14**, 504 (1966).
[42] D. Dekkers *et al.*, Phys. Rev. Lett. **137**, B962 (1965).
[43] W. F. Baker *et al.*, Phys. Rev. Lett. **7**, 101 (1961).
[44] Y. Hayato, Nucl. Phys. Proc. Suppl. *112*, 171 (2002).
[45] K. Okumura, Ph.D thesis, University of Tokyo (1999);
M. Shiozawa, Ph.D thesis, University of Tokyo (1999);
K. Ishihaa, Ph.D thesis, University of Tokyo (1999);

[46] S. J. Barish *et al.*, Phys. Rev. D **16**, 3103 (1977).
[47] N. J. Baker *et al.*, Phys. Rev. D **23**, 2499 (1981).
[48] S. Bonetti *et al.*, Nuovo Cim. A **38**, 260 (1977).
[49] S. V. Belikov *et al.*, Z. Phys. A **320**, 625 (1985).
[50] F. A. Brieva and A. Dellafiore, Nucl. Phys. A **292**, 445 (1977).
[51] L. A. Ahrens *et al.*, Phys. Rev. Lett. **56**, 1107 (1986) [Erratum-ibid. **56**, 1883 (1986)];
C. H. Albright, C. Quigg, R. E. Shrock and J. Smith, Phys. Rev. D **14**, 1780 (1976).
[52] D. Rein and L. M. Sehgal, Annals Phys. **133**, 79 (1981);
D.Rein, Z. phys. C **35**, 43 (1987).
[53] R. P. Feynman, M. Kislinger and F. Ravndal, Phys. Rev. D **3**, 2706 (1971).
[54] G. M. Radecky *et al.*, Phys. Rev. D **25**, 1161 (1982) [Erratum-ibid. D **26**, 3297 (1982)].
[55] T. Kitagaki *et al*, Phys. Rev. D **34**, 2554 (1986).
[56] M. Pohl *et al*, Lett. Nuovo Cim. **24**, 540 (1979).
[57] D. Rein and L. M. Sehgal, Nucl. Phys. **B223**, 29 (1983).
[58] CHARM-II Collaboration, P. Vilain *et al.*, Phys. Lett. **313**, 267 (1993).
[59] BEBC WA59 Collaboration, P. Marage *et al.*, Z. Phys. **C31**, 191 (1986); **C43**, 523 (1989)
[60] SKAT Collaboration, H. J. Grabosch *et al.*, Z. Phys. **C31**, 203 (1986).
[61] FNAL E632 Collaboration, S. Willocq *et al.*, Phys. Rev. **D47**, 2661 (1993).
[62] S. L. Adler, Phys. Rev. **131**, B963 (1964).
[63] M. Hasegawa *et al.*, hep-ex/0506008.
[64] H. Faissner *et al.*, Phys. Lett. **B125**, 230 (1983).
[65] C. H. Albright and C. Jarlskog, Nucl. Phys. B **84**, 467 (1975).
[66] M. Fluck, E. Reya and A. Vogt, Z. Phys. C **67**, 433 (1995).
[67] A. Bodek and U. K. Yang, Nucl. Phys. Proc. Suppl. **112**, 70 (2002).
[68] M. Derrick *et al*, Phys. Rev. D **17**, 1 (1978).
[69] H. Sarikko, Proc. of NEUTRINO'79, 507 (1979).
[70] S. Barlag *et al* (Amsterdam-Bologna-Padua-Pisa-Saclay-Turin), Zeit. Phys. **C11**, 283 (1982).

[71] T. Sjostrand, CERN Report No. CERN-TH-7112-93 (1994), hep-th/9508391.
[72] P. Musset and J. P. Vialle, Phys. Rept. **39**, 1 (1978);
J. E. Kim, P. Langacker, M. J. Vicente-Vacas and H. H. Williams, Rev. Mod. Phys. **53**, 211 (1981).
[73] L. L. Salcedo, E. Oset, M. J. Vicente-Vacas and C. Garcia-Recio, Nucl. Phys. A **484**, 557 (1988).
[74] C. H. Q. Ingram *et al.*, Phys. Rev. C **27**, 1578 (1983).
[75] H. W. Bertini, Phys. Rev. C **6**, 631 (1972).
[76] S. J. Lindenbaum *et al.*, Phys. Rev. **105**, 1874 (1957).
[77] K. V. Alanakian *et al.*, Phys. Atom. Nucl. **61**, 207 (1998) [Yad. Fiz. **61**, 256 (1998)].
[78] T. S. Kosmas and E. Oset, Phys. Rev. C **53**, 1409 (1996).
[79] H. Budd, A. Bodek and J. Arrington, hep-ex/0308005.
[80] J. Engel *et al.*, Phys. Rev. **D48**, 3048 (1993).
[81] M. H. Ahn *et al.*, Phys. Rev. Lett. **90**, 041801 (2003).
[82] I. Kato, Ph.D thesis, Kyoto University (2004).
[83] J. R. Sanford and C. L. Wang, Brookhaven National Laboratory, AGS internal report, (1967), unpublished;
C. L. Wang, Phys. Rev. Lett. **25** 1068 (1970);
C. L. Wang, Phys. Rev. D **16** 2196 (1977).
[84] A. Yamamoto, KEK Report 81-13 (1981).
[85] Y. Cho *et al.*, Phys. Rev. **D4**, 1967 (1971).
[86] Private communication with W. Gajewski, a K2K collaborator;
J. Hill, K2K internal note BEAM/BMMC/00-001 (2000).
[87] G. J. Marmer *et al.*, Phys. Rev. **179**, 1294 (1969);
G. J. Marmer and D. E. Lundquist, Phys. Rev. **D3**, 1089 (1971).
[88] J. F. Asbury *et al.*, Phys. Rev. **178**, 2086 (1969).
[89] J. V. Allaby *et al.*, CERN Report No. CERN-TH-70-12 (1970), unpublished.
[90] C. H. L. Smith, Phys. Rept. **3**, 261 (1972).
[91] V. Bernard, L. Eluadrhiri and U. G. Meissner, J. Phys. G **28**, R1 (2002).
[92] S. Eidelman et al., Phys. Lett. B 592, 1 (2004);

[93] S. Eidelman et al., Phys. Lett. B 592, 275 (2004);
S. Baker and R. D. Cousins, Nucl. Instrum. Meth. A 221, 437 (1984).
[94] T. Iwashita, Ph. D thesis, Kobe University (2003).
[95] H. Yokoyama, Ph. D thesis, Tokyo University of Science (2004).
[96] T. Maruyama, Ph. D thesis, Tohoku University (2000).
[97] A. Shima, Master thesis, Kyoto University (2001) in Japanese.
[98] W. H. Press *et al.*, Numerical Recipes in C, Second edition, 620 (1992), Cambridge University Press.
[99] S. Nakayama *et at.* arXiv:hep-ex/0408134.
[100] Y. Ashie *et al.*, Phys. Rev. Lett. **93**, 101801 (2004);
[101] M. Ishitsuka, Ph. D thesis, University of Tokyo (2004).
[102] S. W. Hawking, Commun. Math. Phys. **43**, 199 (1975);
Commun. Math. Phys. **87**, 395 (1982);
Phys. Rev. D **14**, 2460 (1976).
[103] V. Barger *et al.*, Phys. Rev. Lett. **29**, 2640 (1999);
Phys. Lett. B **462**, 109 (1999);
[104] E. Lisi *et al.*, Phys. Rev. Lett. **85**, 1166 (2000);